Studying VHE Blazars with VERITAS and the Detection of VHE Emission from OJ 287

The thesis is submitted to University College Dublin in fulfilment of the requirements for the degree of Doctor of Philosophy.

School of Physics

Head of School: Prof. Martin Grunewald

Supervisor: Dr. John Quinn

Stephan O'Brien, BSc

10350535

September 2018

Contents

List of Figures

List of Tables

Abstract

In this thesis blazars, a type of active galactic nuclei, are studied at very high energies (VHE), using observations taken by VERITAS. As the current population of VHE blazars is small and heavily biased, a list of six promising candidate VHE blazars is compiled based on their multiwavelength properties. Deep exposures of these objects show a promising excess of gamma-ray events, however they do not yield a significant detection at VHE. Upper limits on the integral VHE flux of these objects are calculated and found to on the order of 1% of the Crab Nebula flux.

Observations of one blazar, OJ 287, were taken during a period of enhanced multiwavelength activity, during which the X-ray flux reached a historic peak in *Swift*-XRT observations. Multiwavelength data is analyzed from X-ray to TeV energies. The broadband spectral energy distribution is observed to be shifted to higher energies, with respect to previous observations. A discrete correlation function analysis is performed between UVOT and X-ray light curves. Significant correlation between all bands is obseved, with the exception of the hard X-ray (3-10 keV) band. The correlation is consistent with a time-lag of 0 days. A likelihood-based correlation analysis was performed between the X-ray and VHE light curves, with the VHE emission found to be more strongly correlated to the soft (0.3-1 keV) and moderate (1-3 keV) X-ray bands than the hard X-ray band, indicating the emission may be due to multiple regions.

Finally, the energy spectra of known VHE blazars, including OJ 287, are used to perform a likelihood-based analysis of the Extragalactic Background Light (EBL). A joint-likelihood fit to the intrinsic spectra of the sources was performed assuming theoretical models of the EBL with a normalization (β_{scale}) applied. Comparing the best-fit normalization to a "no EBL" hypothesis ($\beta_{scale} = 0$) fails to show a significant improvement. Upper limits on the normalization are obtained and found to be consistent with upper limits derived from observations of the most distant VHE detected active galactic nuclei.

Statement of Original Authorship

I hereby certify that the submitted work is my own work, was completed while registered as a candidate for the degree stated on the Title Page, and I have not obtained a degree elsewhere on the basis of the research presented in this submitted work.

I am a member of the VERITAS Collaboration[1], a collaboration of ~100 scientists responsible for the maintenance, operation and data taking of the VERITAS instrument. The data taking and operation of a ground-based gamma-ray observatory requires a lot of manpower. As part of the collaboration, each member is expected to partake in data taking shifts at the observatory. While not all the data taken in this thesis was directly collected by myself, I have played an active role in the data taking operations of VERITAS. To analyze data taken by VERITAS, the VERITAS Collaboration maintains two analysis software packages. While I did not contribute to the initial development of the software package used in this thesis, I have contributed to the development of the package used in this work as part of my graduate studies. In order analyze gamma-ray data, VERITAS requires Monte Carlo simulations of gamma-ray showers. These simulations where performed by members of the VERITAS collaboration, with the results being used in the analysis of this thesis. The VERITAS collaboration also requires that all results be confirmed by an independent analysis. For this VERITAS collaborators have performed so-called "secondary analyses" of the VERITAS results presented here.

All the data presented in this thesis is my own work with some notable exceptions. Firstly, the analysis of *Swift*-UVOT data was performed by a VERITAS collaborator Dr. Karlen Shahinyan (University of Minnesota). Secondly the data quality management and initial stage data processing of several sources used in the EBL analysis was performed by Dr. Patrick Moriarty (National University of Ireland Galway). Finally modelling of the broadband SED of OJ 287 was performed by Dr. Olivier Hervet (University of California Santa Cruz), while the results are not presented here, the model used by Dr, Hervet and preliminary results are discussed.

In summary, the operation and maintenance of the VERITAS instrument and analysis software is performed by the VERITAS Collaboration, of which I am a member. The data analyzed, and results and conclusions derived from the data are my own. Some notable exceptions are highlighted where appropriate.

[1] https://veritas.sao.arizona.edu/

Summary of Thesis

This thesis layout is as follows. In Chapter 1 an introduction to the field of very-high-energy blazars and a discussion of the imaging atmospheric-Cherenkov technique in given. In Chapter 2 the physical concepts relating to the very-high-energy gamma-ray emission of blazars are discussed and the basic components of the emission models are given. In Chapter 3 the instrumentation using in this thesis are described. In Chapter 4 the analysis of data taken by the instruments discussed in Chapter 3 is discussed. In Chapter A the implementation of a binned-likelihood analysis into the VERITAS analysis chain is discussed, with the verification of this method also presented. In Chapter 6 the analysis of six promising candidate very-high-energy blazars is presented and upper limits on their intrinsic flux is determined. In Chapter 7 the discovery of very-high-energy emission from OJ 287 is presented, with multiwavelength data taken during a period of enhanced multiwavelength activity analyzed. In Chapter 8 using the methods implemented in Chapter A, a joint-likelihood analysis of the Extragalactic Background Light using very-high-energy observations of blazars is performed. Finally, in Chapter 9 some concluding remarks on the results presented here are made and the prospects of futures studies are discussed.

Acknowledgements

This thesis would not be possible without the support of my Family. They have always encouraged me to pursue my curiosities. My friends, from both Churchtown and Waffle House, who have always kept me on my toes with “well can your science explain...”. Emma McCann, who was always up for a chat. Cat Crotty, who has kept me sane over the last few years, listening to my thesis induced rants.

I would like to thank my supervisor John Quinn for all his advice, encouragement, guidance and pool lessons. Elisa Pueschel for showing me the ropes with Event Display, and always offering a “have you tried...”. All my UCD colleagues, past and present, Sean Mooney, Ralph Bird and Eddie Collins-Hughes, and everyone in the School of Physics, in partiuclar Emma Sokell, Baibre Fox and Paul Hanratty.

As part of my studies I undertook two trips to VERITAS basecamp. I would like to thank Wystan Benbow for the opportunity to visit and study at VERITAS. I would also like to thank Michael Daniel, and Gareth Hughes for all their help while at basecamp and for answering any and all of my stupid questions. I’d like to express my gratitude to all the staff at basecamp, in particular Jack Musser, George Jones and Ceser Lopez, for making my time at basecamp feel like home.

I have produced this work as part of the VERITAS Collaboration. I have enjoyed being part of this fantastic group of people. I would particularly like to thank Amy Furniss, for all her help and advice. Maria Krause and Gernot Maier for all their assistance with Event Display. Olivier Hervet, Karlen Shahinyan, Jodi Christiansen and Marcos Santander for all their assistance with OJ 287 and other projects. All the senior VERITAS members for their advice, comments and, most importantly, constructive criticisms over the years, in particular David Williams, Lucy Fortson and all the members of the Blazar Working Group. Rita Wells and Ben Zitzer for all our rambling discussions.

And finally, to Kevin, woof grrrrr, bark bark, woof.

Acronyms

1/2/3FHL First/Second/Third Fermi Hard Point Sorce Catalog

1/2/3FGL First/Second/Third Fermi Point Sorce Catalog

BDT Boosted Decision Tree

BL Lac BL Lacertae Object

BLR Broad-Line Region

CAT Cherenkov Array at Themis

CFD Constant Fraction Discriminator

CL Confidence Level

Crab Crab Nebula Flux (unit)

CTA Cherenkov Telescope Array

DAQ Data Acquisition

EAS Extensive/Electromagnetic Air Shower

EBL Extra Galactic Background Light

EC Extrenal Compton

ED Event Display

FACD Flash-Analogue-to-Digital Converters

Fermi-LAT Fermi Large Area Telescope

FOFA First Order Fermi Acceleration

FoV Field of View

FSRQ Flat Spectrum Radio Quasar

HAWC High Altitude Water Cherenkov (Observatory)

HBL High Frequency-Peaked BL Lacertae Object

HE High Energy

H.E.S.S. High Energy Stereoscopic System

HV High Voltage

IACT Imaging Atmospheric Cherenkov Technique/Telescope

IBL Intermediate Frequency-Peaked BL Lacertae Object

IC Inverse Compton

IRF Instrument Response Functions

LBL Low Frequency-Peaked BL Lacertae Object

LRT Likelihood Ratio Test

MAGIC Major Atmospheric Gamma Imaging Cherenkov Telescopes

MLE Maximum Likelihood Estimator

NSB Nigh Sky Background

MSCW/L Mean Scaled Width/Length

NLR Narrow-Line Region

PC Photon Counting

PMT Photo-Multiplier Tube

PSF Point Spread Function

RHV Reduced High Voltage

SED Spectral Energy Distribution

SHV Standard/Nominal High Voltage

SOFA Second Order Fermi Acceleration

SSC Synchrotron Self-Compton

Swift-XRT Swift X-ray Telescope

Swift-UVOT Swift Ultraviolet Optical Telescope

TD Threshold Discriminator

ToO Targe of Opertunity (Observations)

TS Test Statistic

VDAQ VME Data Acquisition

VEGAS Veritas Gamma-ray Analysis Suite

VERITAS Very Energetic Radiation Imaging Telescope Array System

VHE Very High Energy

VPM VERITAS Pointing Monitor

WT Window Timing

ZCD Zero-Crossing Discriminator

List of Publications

Lead Author

1. Allen, C., et al. "Very-High-Energy γ-Ray Observations of the Blazar 1ES 2344+ 514 with VERITAS." MNRAS 471.2 (2017): 2117-2123.

2. O'Brien, S., et al. "VERITAS detection of VHE emission from the optically bright quasar OJ 287" arXiv preprint arXiv:1708.02160 (2017).

Significant Contribution

1. **Secondary Analysit:** Abeysekara, A. et al. "Multiwavelength observations of the blazar BL Lacertae: a new fast TeV gamma-ray flare", ApJ 856 (2018): 95

In Preparation

1. **Lead-Author, VERITAS/*Swift*-XRT Analyst:** Multiwavelength observations of OJ 287.

2. **Lead-Author:** Stand-alone likelihood-based EBL analysis using VERITAS data.

3. **Co-Author:** VERITAS blazar upper limits paper.

4. **Co-Author, VERITAS/*Swift*-XRT Analyst:** Multiwavelength observations of H 1426+428.

5. **Co-Author, *Swift*-XRT Analyst:** Multiwavelength observations of 1ES 0033+596.

6. **VERITAS Analyst:** VERITAS EBL constraints paper.

Chapter 1

Studying Active Galactic Nuclei at Very High Energies

1.1 Overview

In this chapter I provide the reader with an introduction to the field of Active Galactic Nuclei (AGN), particularly in the very-high-energy (E >100 GeV, VHE) gamma-ray regime. To study these objects, this work utilizes the imagining atmospheric-Cherenkov technique. The key concepts of the imagining atmospheric-Cherenkov technique will be discussed, with an overview of current, and future, ground-based gamma-ray observatories also given.

1.2 Active Galactic Nuclei

1.2.1 What are Active Galactic Nuclei?

An Active Galactic Nucleus (AGN) is a type of galaxy which has a central core, or nucleus, region which dominates the emission of the overall galaxy. At the centre of an AGN is a compact region, with size on the order of milliparsecs, in which lies a super massive black hole (SMBH) with mass typically in the range $10^4 - 10^8$ $M_\odot$ (where $M_\odot$ is a solar mass). While it is expected that most, if not all, galaxies will have a SMBH at their centre (for example, in the Milky Way, Sgr A*), AGN show intense activity from these central regions. The broad emission lines (broad due to Doppler broadening of emission lines) observed from these regions, indicate that matter is rapidly rotating about the centre of the region. This suggests that the SBMH is "actively" accreting matter from a circumstellar disk. While normal or non-active galaxies may also have an accreting SMBH at their centre, in AGN the emission of the accreting central SMBH dominates the total output of the galaxy.

1.2.2 Anatomy of an AGN and the Unified AGN Model

A schematic diagram of the different components of an AGN is shown in Figure 1.1. A generic spectral energy distribution (SED) of AGN is shown in Figure 1.2, with the components of a jet-dominated and accretion-dominated AGN SEDs overlaid.

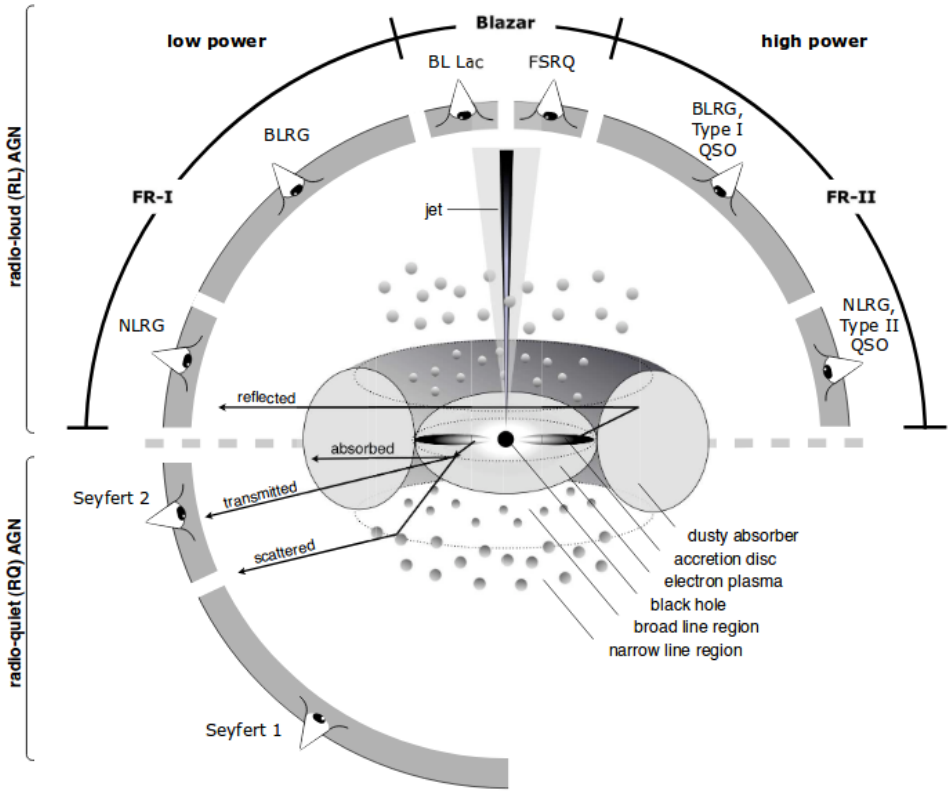

Figure 1.1: Schematics of a unified view of AGN. Different forms of AGN can be explained as arising from variations in the observing angle, whether the AGN is jetted and the relative dominance of the jet. Image credit Beckmann & Shrader (2013).

At the centre of the AGN lies the SMBH. This SMBH will accrete matter from its accretion disk. This accretion of matter results in strong emission in the UV-optical range and is commonly known as the "Big Blue Bump". Surrounding the accretion disk lies a dusty region known as the "dusty torus" or "dusty absorber". This dusty torus may act to obscure a view of the central engine when viewed from certain angles. Some of the emission from the accretion process will be absorbed and reemitted by the dust in the dusty torus. This results in prominent emission in the IR region.

Blobs of gas located between the accretion disk and the wall of the dusty torus are illuminated and ionized by emission from the accretion disk. This gas typically has velocities on

the order of ~1000 km s^{-1}, resulting in broad emission lines occurring in the spectra of some sources. This region is therefore known as the broad-line region (BLR), with "broadness" of the emission lines measured as the full-width at half maximum (FWHM) of the emission lines. Further out from the SMBH (on the order of 100s of parsecs) there is a region of slower moving gas with velocities on the order of 300-1000 km s^{-1}. This region is known as the narrow-line region (NLR).

Finally, some AGN exhibit a collimated jet of relativistic plasma emitted perpendicular to the accretion disk. The high collimation of the jet occurs due to intense toroidal magnetic fields and is "fed" by the accretion process. This relativistic jet is of particular interest to this work as the observed TeV emission is expected to originate from within this jet.

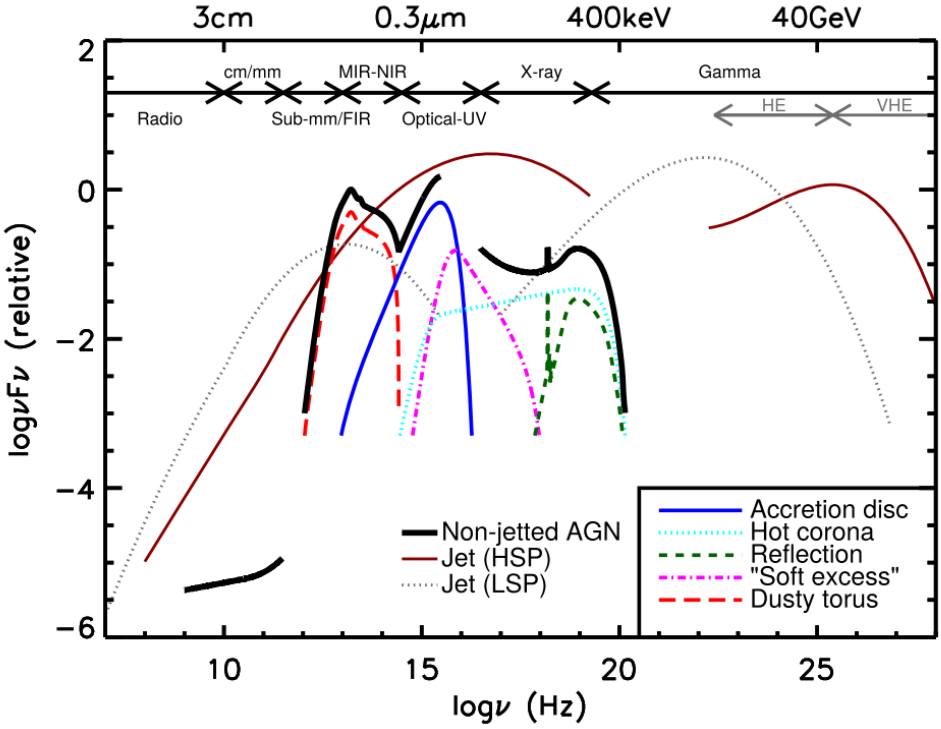

Figure 1.2: Contribution to the SED of different AGN components. The relative dominance of the different components are dependent of AGN type (see Figure 1.1). Image credit Padovani et al. (2017).

Blazars refer to a group of jetted AGN in which, by chance, their jet is closely orientated towards Earth ($\theta \lessapprox 10°$, see Figure 1.1). As the jet is closely orientated towards the observer, the emission from the jet is Doppler boosted (see Section 2.2). The energy spectrum of Blazars shows a non-thermal, jet-dominated SED (see Figure 1.2) which shows a double-peak structure. The lower-energy peak is due to synchrotron emission from relativistic electrons. The higher-energy peak, while somewhat debated, is generally attributed to inverse-Compton

scattering of a soft photon field off the same population of relativistic electrons (see Section 2.6 for a discussion of the emission processes of blazars). Flux variability has been observed from blazars on time scales ranging from years to minutes, across all wavelengths (radio-gamma ray). The rapid nature of this variability suggests that the emission originates from a compact region within the jet.

The blazar subclass is further divided into BL Lacertae objects (BL Lacs) and Flat Spectrum Radio Quasars (FSRQ). The historical definition is based on the equivalent width (EW) of their emission lines. BL Lacs typically show a featureless optical continuum, with little or no emission lines detectable ($EW < 5$Å). FSRQs on the other hand show broad-emission lines ($EW > 5$Å). FSRQs show more powerful and more luminous jets than BL Lacs, with the Compton peak of the SED more luminous than the synchrotron peak.

BL Lacs are further divided into 3 categories based on the location of the synchrotron peak, Low-frequency-peak BL Lacs (LBLs, also referred to radio-selected BL Lacs, RBLs, or low-synchrotron peaked, LSP), intermediate-frequency-peaked BL Lacs (IBLs) and high-frequency-peaked BL Lacs (HBLs, also referred to X-ray selected BL Lacs, XBLs, or high-synchrotron peaked, HSP).

Radio galaxies can be considered jetted AGN. These galaxies are classified based on their surface brightness profile, with the classification known as the Fanaroff-Riley classification (Fanaroff & Riley, 1974). A Class I (FR I) galaxy is a galaxy whose jet is brighter towards the core, with the surface brightness decreasing towards the edges. A Class II (FR II) galaxy is a galaxy whose jet shows increasing brightness away from the core, either showering limb-brightening or enhanced emission within the jet structure. See Peterson (1997) for a discussion of the morphological differences between FR Is and FR IIs. The differences in the radio morphology of the jets is related to power of the emitting jet, with FR II galaxies AGN with more powerful jets. In the context of blazars, BL Lacs are believed to be FR I galaxies with their jets closely orientated to Earth, while FSRQs are believed to be FR II galaxies.

1.2.3 Blazars in the Very-High-Energy Gamma-Ray Regime

At the time of writing the VHE gamma-ray sky (see Figure 1.3) contains 212 known TeV emitters.[1] Of these sources, 75 are AGN, making them the dominant single source class of TeV objects. Of the AGN, ~80% are BL Lacs, ~10% are FSRQs and ~5% are blazars with an unclear classification. The remaining 4 objects are jetted radio galaxies with jets closely orientated towards Earth, these are often referred to as "mis-aligned" blazars. See Padovani et al. (2017) for a recent review of extragalactic TeV astronomy.

[1] http://tevcat.uchicago.edu/

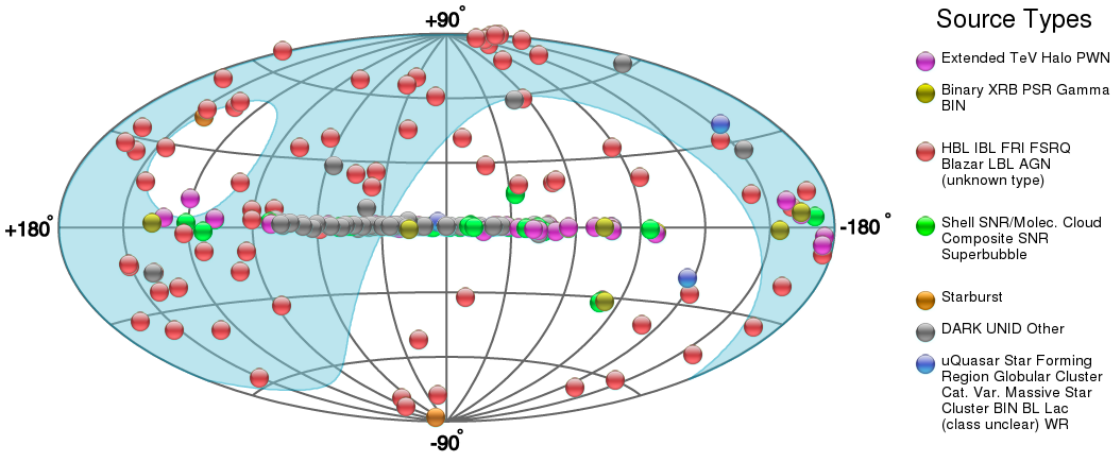

Figure 1.3: Sky map of all known TeV emitters at the time of writing. The shaded region corresponds to the section of the sky visible to VERITAS under nominal observing conditions. This figure was generated using the tools available on TeVCat (Wakely & Horan, 2008).

The subclass of VHE BL Lac objects are dominated by HBLs. HBLs show an inverse-Compton peak in the gamma-ray regime, this results in a hard TeV spectrum, which is favorable for TeV-detection. While HBLs are the dominated class, FSRQs are the most distant detected objects in the TeV sky, with the three most distant TeV-detected blazars (S3 0218+35, z = 0.954 (Ahnen, M. L. et al., 2016); PKS 1441+25, z = 0.939 (Abeysekara et al., 2015; Ahnen et al., 2015); Ton 599, z=0.725 (Mirzoyan, 2017; Mukherjee et al., 2017)) all being FSRQs. A limit on the distance from which TeV emission may be observed from an object arises due to the energy and distance dependent attenuation of VHE photon flux due to photon-photon interactions with the Extragalactic Background Light (EBL, see Chapter 8). Nonetheless, the cosmological distance of blazars and their TeV emission, make them excellent cosmological probes.

The current population of blazars largely corresponds to either bright, nearby objects or objects that have undergone period of intense flaring. For this reason, the current sample of TeV-blazars in highly biased, with a significant proportion of the sources only visible during such a-typical flaring events. This prevents unbiased population studies being performed with the current sample of blazars.

In the high-energy (HE 100 MeV - 100 GeV) gamma-ray regime, *Fermi*-LAT (see Section 3.3.1) has been instrumental in detecting and studying blazars at gamma-ray energies. *Fermi*-LAT is a space-based gamma-ray telescope which operates in survey mode, allowing for the entire sky to be sampled every $\sim$ 3 hours. At the time of writing, *Fermi*-LAT has detected 1959 AGN at HE.[2] Of these objects 536 are FSRQs, 687 are BL Lacs, 15 are radio galaxies

[2] http://www.ssdc.asi.it/fermiagn/

and 75 are AGN of an unknown or unclear classification. As with the VHE sky, the most distant AGN detected at HE are FSRQs, which have been detected out to redshifts beyond $z = 3$ (2FGL J1405.1+0405, $z = 3.215$ (Nolan et al., 2012; Yang et al., 2009)). The most distant BL Lac however is 3FGL J1450.9+5200 which is at a redshift of $z = 2.471$ (Acero et al., 2015).

1.3 Ground Based Gamma-ray Observatories

To understand how gamma-rays are detected by ground-based instruments, we must first understand how gamma rays interact with the Earth's atmosphere. There are two important concepts needed here. The first is that charged relativistic particles can induce the emission of a blue-ish light known as Cherenkov emission. This is discussed in Section 1.3.1. Secondly, a high-energy photon, or particle, impacting the Earth's atmosphere will produce a shower of particles in the Earth's atmosphere. This is discussed in Section 1.3.2. Ground based gamma-ray detectors utilize these two facts to indirectly measure incident gamma rays by observing the Cherenkov emission produced by the charged particles in the extensive air shower.

1.3.1 Cherenkov Radiation

A charged particle traveling with a velocity v in a dielectric medium with speed of light in the medium c/n, where c is the vacuum speed of light and n is the refractive index of the medium, will induce a polarization in the medium. This polarization occurs due to the local molecules in the medium being attracted/repelled by the charged particle. As the particle moves by a local polarization, the medium will return to an unpolarized state, causing the molecules to radiate. If the particle is traveling at velocities less than c/n, the net intensity of the radiated emission, when viewed from far away, will be zero. This is due to the symmetry of the system. If, however the particle is traveling with a velocity greater than c/n, the system will no longer be symmetric about the particle's trajectory, hence the net field intensity will no longer be zero. This effect, where a relativistic charged particle induces the emittance of radiation from a dielectric medium, is known as Cherenkov radiation (see, Jelley, 1955, for a full description of Cherenkov radiation). The light emitted appears as a brief pulse of UV-optical radiation, emitted in a cone, as shown in Figure 1.4, with an angle:

$$\theta = \cos^{-1}\left(\frac{1}{\beta n}\right), \tag{1.1}$$

where $\beta = v/c$. This is known as the Cherenkov relation and leads to an energy threshold for Cherenkov radiation of:

$$\beta \geq \frac{1}{n}. \tag{1.2}$$

For an electron (electrons and positrons, $e^{\mp}$) traveling at sea level ($n = 1.00029$, Grieder, 2010) this corresponds to an threshold energy of 21 MeV.

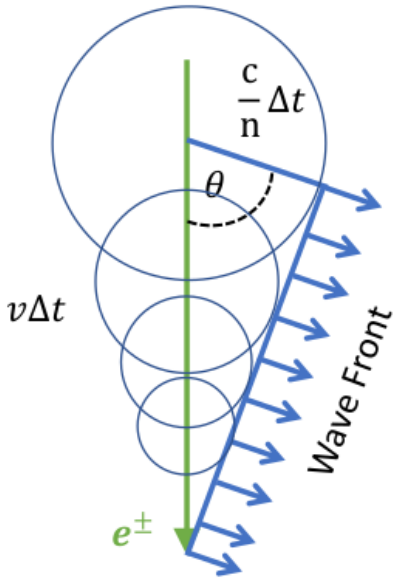

Figure 1.4: Cherenkov Angle. The green line corresponds to the trajectory of the charged particle (for example $e^{\pm}$) traveling at a speed v, which travels a distance of $v\Delta t$ in the time period Δt. The blue circles correspond to the individual wavelets. The first wavelet will emit a photon which travels with a speed c/n and travels a distance of $c\Delta t/n$ in the time period Δt. The individual wavelets coherently interfere to produce a wave front which will be emitted at an angle θ with respect to the particle's trajectory.

1.3.2 Extensive Air Showers

Extensive air showers (EAS) are showers of particles produced by gamma rays, leptons or hadrons as they enter the atmosphere. As a gamma ray enters the atmosphere it will travel, on average, one radiation length before interacting with the atmosphere via the pair-production process. This produces an electron-positron pair with energy, on average, equally shared between the two particles, and with direction approximately equal to the incident gamma ray. These electrons and positrons will travel again, on average, one radiation length before producing secondary gamma rays by the bremsstrahlung process, emitted at angles $\propto m_e c/E$ rad (Weekes, 1988), where E is the energy of the electron/positron and m_e is the rest mass of

the electron. The secondary gamma ray will go on to produce more electron-positron pairs, which produce additional gamma rays and so on. This process continues until the ionization energy losses are equal to the radiation losses. At this point the number of particles in the shower reaches a maximum and is therefore referred to as "shower max". After reaching shower max, the number of particles in the shower will decrease and the cascade will die off. In the case of a leptonically-induced EAS the initial interaction will be a bremsstrahlung interaction producing a gamma ray, which continues to produce a shower as described above.

The radiation length, X_0, is defined as the mean scale length (measured in g cm^{-2}) over which an electron loses all but $(1/e)$-th of its energy due to bremsstrahlung. This is also 7/9-th of the mean free path for pair production. In air the radiation length is $X_{0,air} = 37.1$g cm^{-2} (Grieder, 2010), with the total thickness of the atmosphere being ~ 1000g cm^{-2}, corresponding to about 27 radiation lengths. This suggest that only the most energetic showers will be directly detectable at sea level, requiring one to go to high altitudes to directly detect the shower particles.

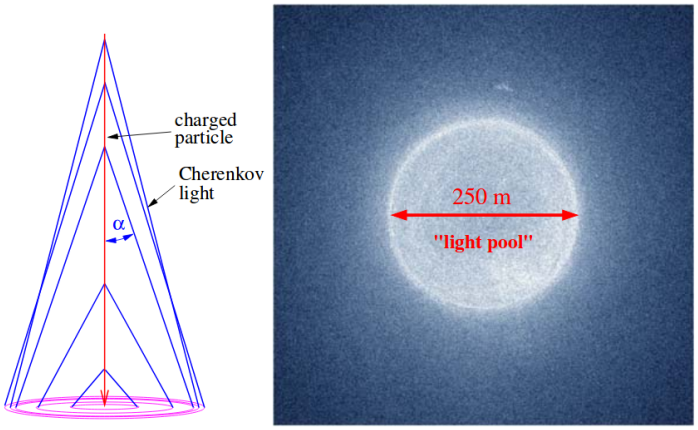

Figure 1.5: (Left) Variation in the angle of emitted Cherenkov radiation with altitude ($\theta = \alpha$). (Right) Resulting light pool as viewed from an observed on the ground. Image credit Völk & Bernlöhr (2009).

Charged particles within the shower, above the Cherenkov energy threshold, will induce Cherenkov emission. This emission will radiate in the forward direction, with an angle $\theta \sim 1.3°$ at sea level (Weekes, 1988). For an EAS, this results in a tight pool of Cherenkov radiation arriving on the ground with a temporal spread on the order of 3-5 ns. As the refractive index will decrease with altitude, so too will the angle of Cherenkov emission. This variation in the refractive index results in the light pool observed from the ground forming a ring-like structure with radius on the order of 100m, centered around the shower axis. This is illustrated in Figure 1.5. Telescopes placed within this radius will be able to detect photons

from the shower.

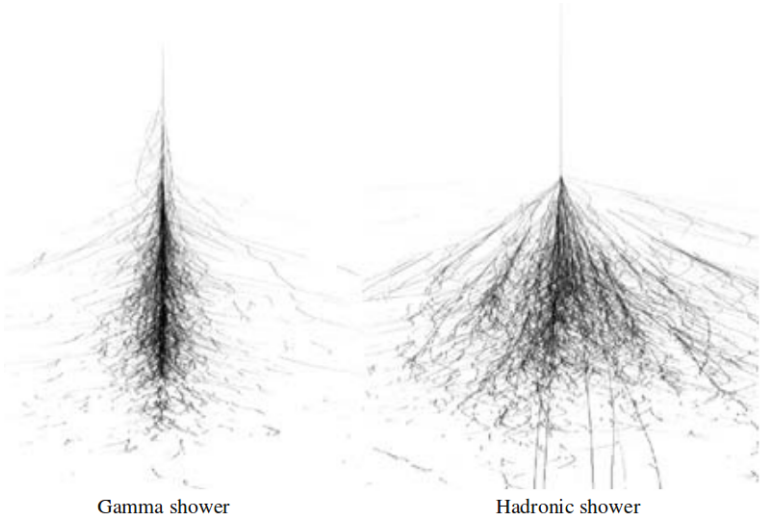

Figure 1.6: Comparison between showers produced by a gamma ray induced shower (left) and a hadron induced shower (right). Image credit Völk & Bernlöhr (2009).

Air showers produced by hadrons will also occur as cosmic rays impact the atmosphere. These showers result in hadronic interactions producing pions and kaons. These particles have a significant component of transverse momentum, resulting in a broadening of the shower. These particles go on to produce more particles via hadronic interactions and methods described above. The net result is that hadronic showers tend to have a larger transverse spread with clumpy shower components, and photon arrival times on the order of 10 ns. A comparison between electromagnetic and hadronic induced air showers is shown in Figure 1.6. The different structure of the shower types can be used to discriminate between hadronic and electromagnetic showers based on the shape of the shower and the temporal spread in the arrival time of Cherenkov photons. This will be used in Section 4.2.6 to remove hadronic events from the background.

1.3.3 Current-Generation Ground-Based Gamma-ray Observatories

The current generation of ground-based gamma-ray detectors can be classified as either imaging atmospheric-Cherenkov telescopes (IACTs)[3] or water-Cherenkov detectors. IACTs use telescopes with large collection areas and rapid cameras to detect the nano-second pulses of Cherenkov radiation emitted by EAS traveling within the atmosphere. IACTs are pointing

[3]Note: The acronym IACT is commonly used interchangeably to refer to either imaging atmospheric-Cherenkov technique, or to a telescope which uses this technique, an imaging atmospheric-Cherenkov telescope.

instruments and typically have a field of view on the order of $3° - 5°$. As a result IACTs have a greater sensitivity and angular resolution than their water-Cherenkov counterparts. Due to the production of the EAS, the effective area for a single IACT telescope will be on the order of 10^4 m^2, as suggested by a light pool of radius ~100 m. This result is independent of the size of the telescope mirror, with the mirror limiting the number of photons from the shower detected, hence introducing a lower-energy threshold due to the brightness of showers. Modern IACT arrays utilize effective areas on the order of 10^5 m^2.

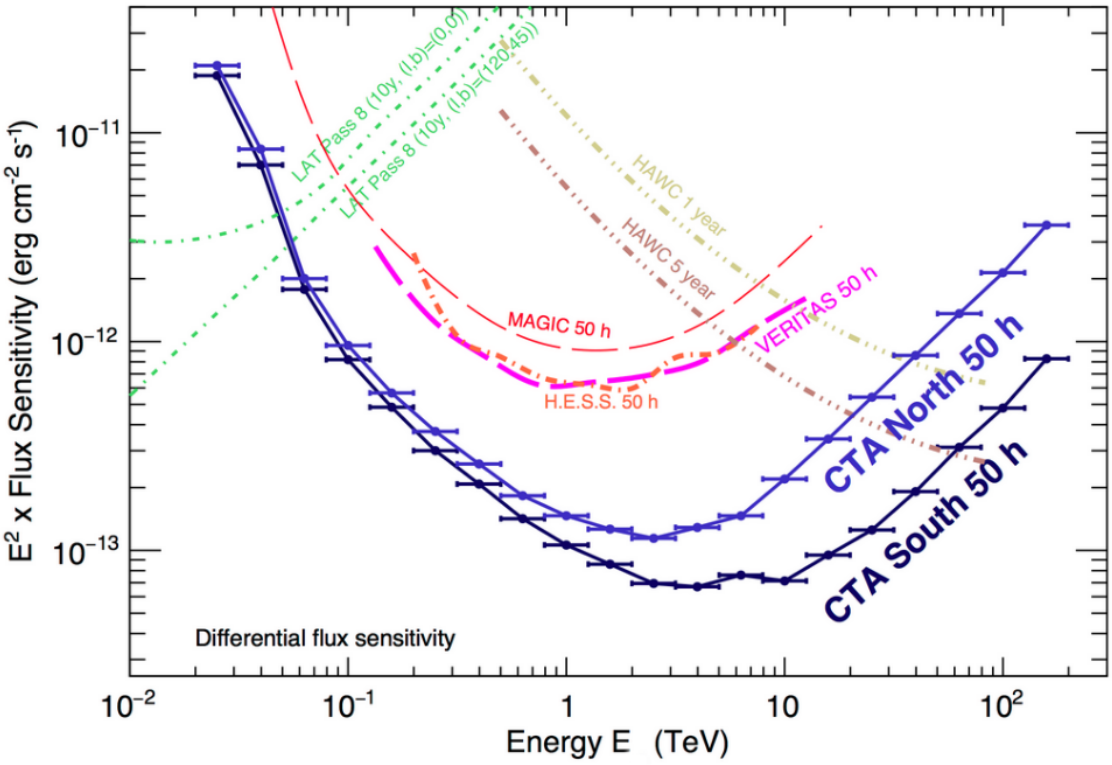

Figure 1.7: Differential flux sensitivity of current and future gamma-ray instruments. Note: the sensitivity curve for H.E.S.S. corresponds to the H.E.S.S.-1 (4-telescope) array. Image taken from CTA performance website.[4]

Water-Cherenkov detectors on the other hand use pools of water to detect the Cherenkov emitted due to charged-relativistic particles of an EAS which pass through the pool. Water-Cherenkov detectors operate as surveying instruments, with a wide ($\sim$ 1.5 str) field of view. Water-Cherenkov detectors typically have a lower sensitivity than IACTs. However, as water-Cherenkov detectors do not require pointed observations, they can regularly monitor a large number of sources. This makes them ideal for unbiased surveys.

[4] https://www.cta-observatory.org/science/cta-performance/

A comparison of the sensitivity of current generation and future gamma-ray instruments is shown in Figure 1.7.

Imaging Atmospheric-Cherenkov Telescopes

There are three (major) current generation IACTs in operation, namely H.E.S.S., MAGIC and VERITAS.

The High Energy Stereoscopic System (H.E.S.S., Aharonian et al., 2006) is an array of five IACTs located in the Khomas Highlands of Namibia (23° 16′ 17″S, 16° 30′ 00″E, at 1.8 km above sea level (a.s.l.)). The H.E.S.S.telescopes array comprises four 12m telescope and a fifth 28m telescope. The large 28m telescope allows H.E.S.S. to reach lower-energy showers, pushing the energy threshold of the array down to $\sim$ 30 GeV. This results in a sensitivity to gamma rays in the ~30 GeV to >10 TeV energy range. Being located in the Southern Hemisphere, H.E.S.S. is optimally situated to observe the Galactic Plane, with a survey of the Galactic Plane being a key legacy product of H.E.S.S. (Abdalla et al., 2018).

The Major Atmospheric Gamma Imaging Cherenkov Telescopes (MAGIC, Aleksić et al., 2016) is an array of two 17m telescopes located in La Palma, Spain (28° 45′ 43′N, 17° 53′ 42′W, 2.2 km a.s.l.). The large mirrors and high elevation of MAGIC make it ideal for detecting lower-energy EAS, while slightly sacrificing sensitivity to higher energy events. Consequently MAGIC is sensitive to gamma rays in the ~50 GeV to >10 TeV energy range.

The Very Energetic Radiation Imaging Telescope Array System (VERITAS, Holder, 2011) is an array of four 12m IACTs located at the Fred Lawrence Whipple Observatory (FLWO) in southern Arizona U.S. (31° 40′ 30″N, 110° 57′ 07″W, 1.3km a.s.l.). VERITAS is sensitive to photons in the ~85 GeV to >30 TeV energy range. VERITAS is the primary instrument used in this thesis and is described in more detail in Sections 3.2 and 4.2.1.

Water Cherenkov Detectors

The High Altitude Water Cherenkov ((HAWC, Abeysekara et al., 2013)) observatory is a current generation water-Cherenkov detector located in central Mexico (18° 59′ 41″N, 97° 18′ 30.6″W, 4.1km a.s.l.). It consists of 300 water-Cherenkov detectors, each consisting of a water bladder and four photomultiplier tubes. HAWC is sensitive to gamma rays in the ~1 TeV to ~100 TeV energy range. Due to HAWC's high altitude, it is able to sample the EAS by observing the Cherenkov emission emitted by relativistic particles in the shower, as they pass through the detector, hence allowing for an estimate of the energy and origin of the gamma ray. HAWC's large field of view (> 1.5 str) allows it to sample a large portion of the sky at any given time. This makes HAWC an ideal instrument for monitoring sources over

long timescales. Its sensitivity, however, limits such studies to brighter objects.

1.3.4 Cherenkov Telescope Array

The Cherenkov Telescope Array (CTA, Acharya et al., 2017), is a planned array of IACTs with two sites located in the northern (La Palma, Spain) and southern (Paranal, Chile) hemispheres sensitive to gamma rays in the 20 GeV to > 300 TeV energy range. To achieve this sensitivity, CTA will comprise three different size telescopes. The large size telescope (LST) will utilize a large mirror to detect light from faint, low-energy showers, allowing for the detection of gamma rays down to 20 GeV. The medium size telescope (MST) will be of comparable size to current generation IACT telescopes and largely operate over the same energy range (80 GeV - 50 TeV). The highest energy showers will be detected by the 4m small size telescopes (SST), which will provide sensitivity in the 1 TeV - 300 TeV energy range. A combination of the different telescope sizes and different combinations those telescope at each of the sites will provide orders of magnitude improvement in sensitivities compared to current generation instruments (see Figure 1.7).

1.4 Summary

In this thesis blazars are studied in the VHE regime, primarily using observations taken by the IACT VERITAS. In this work I firstly attempt to expand the catalog of known VHE blazars. To do this a list of promising candidate VHE blazars is compiled based on their multiwavelength properties and the reanalysis of archival VERITAS data. Additional VERITAS observations are obtained, analyzed and presented as part of this thesis. In absence of strong VHE detections, upper limits on the VHE emission of these sources are obtained. The results of these observations can allow for constraints on the VHE emission processes of the sources to be placed and may act as a *path finder* study for a future searches by CTA.

One peculiar blazar is detected, OJ 287. Multiwavelength data spanning X-ray to TeV energies is analyzed during an exceptional period of multiwavelength activity. This period resulted in the historical peak in the X-ray light curve and the first detection of this object at VHE energies.

To optimize the scientific output from the analysis of these blazars, a binned-likelihood method is implemented into the VERITAS data analysis chain. This provides the first analysis of VERITAS data using a binned-likelihood analysis. A joint-likelihood analysis of the EBL is performed by combining observations of OJ 287 with data from other known VHE blazars. The dataset presented as part of this EBL analysis corresponds to ~20% of the total VERITAS

EBL dataset (see, Pueschel, 2017) and represents the first likelihood-based EBL analysis performed using VERITAS data.

Chapter 2

Gamma-Ray Emission From Blazars

2.1 Overview

The broadband SEDs of blazars are characterized by a double-peaked structure. The lower-energy peak, spanning radio-X-ray energies, is widely attributed to synchrotron radiation from relativistic electrons. The higher-energy peak, spanning from X-ray-gamma-ray energies is somewhat debated. The process generally attributed to this emission is inverse-Compton scattering of low-energy photons by relativistic electrons. The source of these photons varies and may be the same photons as those produced by the synchrotron process, or due to an external photon field, for example the broad line region, dusty torus, etc. (see Section 1.2).

Hadronic models have also been used to model blazar emission. In hadronic models relativistic protons produce synchrotron emission and also produce pions. These pions decay to secondary particles such as gamma rays and leptons (which may also produce synchrotron emission). The higher-energy peak is therefore attributed to synchrotron radiation from protons and gamma rays produced by pion decay.

2.2 Special Relativity in Astronomy

2.2.1 Doppler Factor

Consider a particle, observed in the laboratory rest frame, traveling relativistically with a velocity $\beta = v/c$, emitting a photon of energy, as measured in the rest frame, E. Let the co-moving frame be defined as a frame traveling parallel to the particle at a velocity β, with quantities measured in the co-moving frame denoted by a prime ($'$). In this frame the particle is instantaneously at rest. Let the Lorentz factor of the particle be defined as:

$$\gamma = \frac{1}{\sqrt{1-\beta^2}}. \tag{2.1}$$

The energy of the photon, as measured in the co-moving frame, will be E', with transform between the two frames given by

$$E = \frac{E'}{\gamma(1-\beta\mu)}, \tag{2.2}$$

or in terms of frequency:

$$h\nu = \frac{h\nu'}{\gamma(1-\beta\mu)}, \tag{2.3}$$

where $\mu = \cos\theta$ and θ is the angle at which the photon is emitted as observed in laboratory frame. This gives the definition of the Doppler factor:

$$\delta = \frac{1}{\gamma(1-\beta\mu)}. \tag{2.4}$$

Hence we have $E = \delta E'$, suggesting that the energies of the photons emitted in by the particle will be boosted/deboosted by a factor of δ as observed by an observer in laboratory frame.

Consider the two extreme cases when a particle is moving towards and away from the observer. When the particle is moving towards the observer (i.e. $\mu = 1$):

$$\delta_{forward} = \frac{1}{\gamma(1-\beta)} \tag{2.5}$$

$$\delta_{forward} = \frac{1+\beta}{\gamma(1-\beta^2)}, \tag{2.6}$$

where in the relativistic case ($\beta \to 1$):

$$\delta_{forward} \approx 2\gamma. \tag{2.7}$$

When the particle is moving away from the observer (i.e. $\mu = -1$):

$$\delta_{back} = \frac{1}{\gamma\,(1+\beta)}, \tag{2.8}$$

which in the relativistic case ($\beta \sim 1$):

$$\delta_{back} = \frac{1}{2\gamma}, \tag{2.9}$$

This shows that a particle traveling at relativistic speeds, emitting isotropically in its rest frame, will have the energy of its emitted photons in the forward direction increased by a factor of $\sim 2\gamma$, while the radiation emitted in the backwards direction will be decreased by a factor of $\sim 1/2\gamma$. This process is known as "boosting" (or deboosting in the case of emission

in the backwards direction).

The transformation of the angle at which the photon is emitted as is given by:

$$\mu' = \frac{\mu - \beta}{1 - \beta\mu}, \tag{2.10}$$

$$\mu = \frac{\mu' + \beta}{1 + \beta\mu'}. \tag{2.11}$$

If we consider the case of a photon emitted at an angle $\theta' = 90°, \mu' = 0$,

$$\cos\theta = \beta = \left(1 - \frac{1}{\gamma^2}\right)^2. \tag{2.12}$$

In the relativistic case $\gamma \gg 1$, hence $\beta \sim 1$. Therefore, expanding both sides of Equation 2.12, one obtains:

$$\theta = \frac{1}{\gamma}. \tag{2.13}$$

This suggests that the emission observed by an observer in the laboratory frame will be beamed into an angle of $\sim 1/\gamma$. This relativistic effect is known as beaming. Combining this effect with the boosting effect we have the interesting effect that a relativistic particle emitting isotropically in its rest frame, will have the energy of its emission boosted by a factor of δ and its emission concentrated into an open angle of $\sim 1/\gamma$ when viewed from an observer in the laboratory frame. The combination of these effects plays an important role in the emission of blazars, whose emission is due to relativistic particles traveling with a bulk relativistic motion.

2.2.2 Effects on the Energy Flux Distribution

The spectral flux density[1] (or distribution) is given by:

$$F(\nu) = \frac{h\,\nu\,d^3N_{ph}}{dt\,dA\,d\nu}, \tag{2.14}$$

where d^3N_{ph} is the number density of photons in the $[\nu, \nu + d\nu]$ interval and is Lorentz invariant. An area element dA can be related to a solid angle element by introducing the distance to the observer D such that:

$$dA = D^2 d\Omega, \tag{2.15}$$

where the $d\Omega = d\theta d\phi$ and $d\Omega = \delta^2 d\Omega'$.

[1] This is also referred to as the "specific" flux density as it is the flux density in the frequency interval $d\nu$.

In order to obtain a transformation between the flux emitted by a particle, or system of particles, we can take the ratio of the two fluxes such that:

$$F(\nu) = F'(\nu')\frac{\nu}{\nu'}\frac{d\nu'}{d\nu}\frac{d\Omega'}{d\Omega}\frac{dt'}{dt}. \tag{2.16}$$

We can therefore write a transformation between fluxes by considering the transforms between the two frames:

$$F(\nu) = F'(\nu')\delta^3. \tag{2.17}$$

Similarly, the energy flux density (given as $\mathcal{F} = \int F(\nu)d\nu$)[2], can be transformed as:

$$\mathcal{F} = F(\nu)\Delta\nu = \delta^3 F'(\nu')\Delta\nu, \tag{2.18}$$

$$\mathcal{F} = \delta^4 F'(\nu')\Delta\nu' = \delta^4\mathcal{F}'. \tag{2.19}$$

This allows for a transformation between luminosities

$$L = \delta^4 L', \tag{2.20}$$

where luminosity is defined as

$$L = 4\pi D\mathcal{F}. \tag{2.21}$$

A flux density emitted by a relativistic particle, when viewed by an observer in the laboratory frame, will be boosted by a factor of δ^3. For a power-law of frequencies emitted, $F(\nu) \propto \nu^{-\alpha}$, Equation 2.17 can be written more generally as:

$$F(\nu) = F'(\nu)\delta^{3+\alpha}, \tag{2.22}$$

where in the above the flux is measured at the flux observed in the laboratory frame, ν.

2.2.3 Size of the Emission Region

If we consider that the emission region is optically thin at the observed frequencies, one obtains a simple estimate of the size of the region by assuming the timescale for emission to change is related to the light travel time:

$$\Delta t' = \frac{R}{c}, \tag{2.23}$$

[2]This is also referred to as the bolometric flux.

where R is the radius, or "size"[3] of the emission region. To determine how the interval Δt transforms, we need to account for two factors. Firstly any time interval in the co-moving frame will be observed by the observer in the rest frame to dilated such that $\Delta t = \gamma \Delta t'$. Secondly the blob has transversed a distance $\beta\mu$ during the period, this results in the time between the pulse observed at the start and end of the interval to appear shorter by a factor of $1 - \beta\mu$. This has the net effect:

$$\Delta t = \Delta t' \gamma (1 - \beta\mu) = \Delta t' \delta^{-1}. \tag{2.24}$$

Therefore the minimum variability timescale observed in the laboratory frame can be used to place constraints on the size of the emission region:

$$R \leq c \Delta t_{min} \delta. \tag{2.25}$$

In this work Δt_{min} shall be defined as the minimum flux doubling time, that is the minimum timescale on which the flux doubles.

2.3 Particle Acceleration

In this section different purposed particle acceleration mechanisms are discussed. For a review of acceleration mechanisms in blazars the reader is referred to Rieger et al. (2007); Tammi & Duffy (2009); Madejski & Sikora (2016).

2.3.1 First Order Fermi Acceleration

Fermi acceleration was first purposed by Enrico Fermi as a process by which cosmic rays could be accelerated by interstellar magnetic fields (Fermi, 1949). In this process, a particle is scattered off a turbulent magnetic structure. A particle will either gain energy, if it undergoes a head on collision, or lose energy, if it undergoes a following collision. In the context of first order Fermi acceleration, particles interact with a (non-relativistic) shock moving within a jet with velocity $v = v_u - v_d$, where $v_{u/d}$ correspond to the up-/down-stream velocities. A particle approaching the shock from the down-stream direction will be scattered and accelerated such that:

$$E_2 = E_1 + \vec{P} \cdot \vec{v}, \tag{2.26}$$

[3] Assuming a spherical blob.

where $E_{1/2}$ is the energy before/after the scatter. In the rest frame of either side of the shock, the shock is seen to always be approaching with a velocity v, hence all collisions are head on, resulting in a gain in energy for each scatter event. For a head on scatter we have:

$$\frac{\Delta E}{E} = \beta, \tag{2.27}$$

where β is the relativistic velocity of the shock, $\beta = v/c$. The averaged change in energy due to a shock crossing is obtained by averaging over interaction angle:

$$\langle \frac{\Delta E}{E} \rangle = \frac{2}{3}\beta. \tag{2.28}$$

The change in energy is linear in β hence it is commonly referred to as First Order Fermi Acceleration (FOFA).

Higher-energy particles require additional shock crossings in order to be accelerated to higher energies, with the probability of escaping the shock region being independent of energy ($\mathcal{P}_{esc} = 4v_d/c$). Hence the probability of particles being accelerated to higher energies drops as a function of energy. This results in the accelerated population of particles being described by a power-law distribution (Bruggen & Rosswog, 2007):

$$n(E) \propto E^{-p} dE, \tag{2.29}$$

where the spectral index can be related to the probability of remaining in the acceleration region, $\mathcal{P} = 1 - \mathcal{P}_{esc}$:

$$p = 1 - \frac{\log \mathcal{P}}{\log \tilde{\beta}}. \tag{2.30}$$

$\tilde{\beta}$ is the fractional energy gain by a particle undergoing a round trip:

$$\tilde{\beta} = 1 + \frac{4}{3}\beta. \tag{2.31}$$

The power-law index p can be related to the shock compression (Krymsky, 1977; Axford et al., 1977; Bell, 1978; Blandford & Ostriker, 1978):

$$p = \frac{\kappa + 2}{\kappa - 1}, \tag{2.32}$$

where $\kappa = v_u/v_d$, is the shock compression ratio and lies in the range $(1, 4]$. For a "strong" shock, $\kappa \sim 4$ the accelerated distribution tends to a power law of index ~ 2. This important result suggests an upper limit on the hardness on the particle distribution responsible for the

observed VHE emission, and therefore on the hardness of the VHE emission.

2.3.2 Second-Order Fermi Acceleration

Fermi acceleration may occur as a more stochastic process when there is no dominant shock structure. In this case the shock centres move with random velocities, resulting in the particle undergoing both head-on and following collisions. As head-on collisions are more likely (if $\gamma_{particles} > \Gamma_{medium}$) this process results in a net gain in energy such that (Rieger et al., 2007):

$$\langle \frac{\Delta E}{E} \rangle \propto \beta^2. \tag{2.33}$$

As the energy gain is proportional to the second power of β, this is referred to as Second-Order Fermi Acceleration (SOFA). SOFA generally tends to a power-law distribution of particles. The index of this distribution tends to be softer than that of FOFA.

As SOFA doesn't require a shock front for acceleration to occur, this could be a dominant process of accelerating particles within the jet. Particles may be injected in the base of the jet and undergo some FOFA, before traveling through jet and undergoing further acceleration due to SOFA.

2.3.3 Shear Acceleration

Shear acceleration is a form of acceleration similar to SOFA. In this scenario, a particle traveling in a jet is traveling in a semi-homogeneous manner, in the sense that the scattering centres, which typically could result in SOFA, have a rest frame velocity approximately equal to that of the particle ($\gamma_{particles} \approx \Gamma_{medium}$), hence the acceleration due to SOFA is negligible. In this case acceleration occurs due to a shear in the background flow.

Rieger & Duffy (2004) discuss different environments which may result in shear acceleration. Longitudinal shear acceleration would be expected to occur at the boundary between two flows of the jet. This could be either a boundary between the jet and the ambient medium, or due to a spine-sheath structure within the jet (see, for example, Sikora et al., 2016). Transverse shear acceleration would be expected to occur due to a transverse change in the jet flow. Such a change in the flow would be expected due to a kink in the jet or due to a helical jet structure.

The acceleration timescale of a particle due to a longitudinal shear is inversely proportional to the mean free path of the particle ($t \propto 1/\lambda$). This suggests that shear acceleration of electrons would be rather ineffective. When compared with synchrotron loss timescales ($t_{cool} \propto 1/\lambda$) this would only result in a marginal net acceleration. However, for protons the

mean free path is much larger, suggesting that this process could be very efficient for protons. Rieger & Duffy (2004) suggest that a gradual longitudinal shear acceleration of protons could occur along the jet, where the seed protons would be accelerated by SOFA processes.

2.3.4 Magnetic Reconnection

Acceleration due to reconnection of magnetic-field lines has been developed in the study of gamma-ray burst and solar flares. Such acceleration process have been invoked in an attempt to explain minute scale TeV variability observed from a number of TeV sources (see, for example, Mrk 501 and PKS 2155-304, Albert et al., 2007; Aharonian et al., 2007, respectively). In magnetic reconnection, the magnetic field is not "frozen" into the plasma, rather the magnetic field can move through the plasma (see, for example, Böttcher et al., 2012, for a detailed description). A reconnection event can be viewed as the re-joining of two magnetic-field lines such as that shown in Figure 2.1. This results in a rapid change in the topology of the magnetic field, dissipating energy in the form of heating the plasma and accelerating particles to relativistic energies.

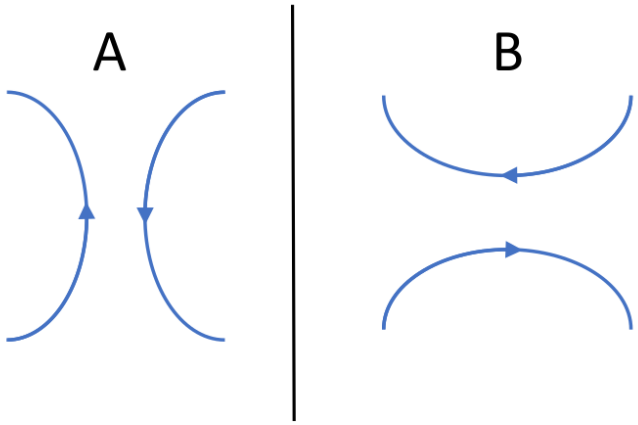

Figure 2.1: Diagram of adjectant magnetic field before (A) and after (B) a reconnection event.

Giannios et al. (2009) propose a "jets-in-a-jet" model to explain minute-timescale TeV variability. In this model, the jet is characterized by a Poynting flux-dominated flow. In such a jet a significant fraction of the jet luminosity may be dissipated in reconnection events. Giannios et al. (2009) consider relativistically traveling blobs within the jet that may be accelerated at a reconnection site. The material leaving the reconnection site would then undergo an emission process similar to a synchrotron self-Compton or external-Compton process (see Section 2.6).

Discussion

In the context of blazar emission, the most efficient and likely acceleration process is FOFA. In this scenario, seed particles would be inserted into the jet. They would travel within the jet before meeting a shock front. Such a shock front could arise due to a change in the relative speed of the jet due to, for example, a change in the ambient medium or a change in the magnetic field. This is supported by the observations of knots observed in VLBI imaging, from which brightening correlated with multiwavelength flaring has been observed.

It is likely however that some, if not all, of these processes play roles in the acceleration within the jet. While FOFA may likely be responsible for emission observed about knots, SOFA and shear acceleration might play a significant role downstream of the jet, which could attribute some of the outer jet emission.

Tammi & Duffy (2009) discuss the different acceleration time scales for particles in the context of TeV blazar flaring. Tammi & Duffy (2009) suggest that both FOFA and (to a lesser extent) SOFA processes could accelerate particles to sufficiently high energies, in a sufficiently short period of time, to account for minute-scale variabilities observed at TeV. However, Giannios et al. (2009) suggest that such variability requires that the bulk Lorentz factor of the jet would need to be on the order of $\Gamma \sim 50$ in order for such TeV variability to be observed, this is inconsistent with the observed values of $\Gamma \sim 10$. Marscher (2016) postulates that such minute scale variability, which requires ultra-high Lorentz factors, is not a continuous process, rather they represent occasional and extreme events within the jet, a view consistent with the "jets-in-a-jet" model of Giannios et al. (2009).

It is evident that a complete, unified model of blazar emission needs to consider multiple acceleration processes, with different acceleration processes attributed to the particle energies at different locations of the jet.

2.4 Synchrotron Emission

While not the process responsible for gamma-ray emission observed by VERITAS and *Fermi*-LAT, synchrotron radiation plays an important role and is largely responsible for the radio-X-ray emission observed from blazars. Synchrotron radiation is emitted by a charged particle traveling relativistically in a magnetic field. In the case of blazars, the radio-X-ray emission is considered to be due to a population of relativistic electrons.

2.4.1 Observed Frequency

A charged particle traveling in a magnetic field will encounter an acceleration perpendicular to the direction of travel and the magnetic field B. This will cause the particle to "gyrate" about its trajectory, resulting in the particle following a helical path. The frequency of this gyration is known as the gyro-frequency and is given by (Longair, 2011):

$$\omega_g = \frac{qB}{\gamma m} \sin\theta, \tag{2.34}$$

where q is the charge of the particle, m is the particle's mass and θ is the pitch angle between the magnetic field and the particle's trajectory. Radiation will be emitted by the particle primarily at this frequency, however radiation may also be emitted at harmonics of this frequency. In the non-relativistic case ($\gamma = 1$), higher-order harmonics provide an insignificant contribution to the emitted spectrum. In the ultra-relativistic case ($\gamma \gg 1$), higher-order harmonics begin to play a significant role in the spectrum of the emitted radiation. This results in a smearing or spread of frequencies being emitted.

Full derivation of the synchrotron spectrum can be found in Longair (2011), however in deriving the synchrotron spectrum, Longair (2011) defines the critical angular frequency as:

$$\omega_c = \frac{3}{2}\frac{\gamma^2}{\beta}\omega_g \sin\theta. \tag{2.35}$$

The form of the energy spectrum emitted by a single particle is shown in Figure 2.2. One can see that most of the emission occurs for frequencies $\omega \leq \omega_c$. Indeed, the peak intensity occurs for $\omega = 0.29\omega_c$. Longair (2011) shows that the spectrum can be asymptotically approximated as

$$I(\omega) \propto F\left(\frac{\omega}{\omega_c}\right) = \begin{cases} \left(\frac{\omega}{\omega_c}\right)^{\frac{1}{3}}, \omega \ll \omega_c, \\ \left(\frac{\omega}{\omega_c}\right)^{\frac{1}{2}} exp^{-\frac{\omega}{\omega_c}}, \omega \gg \omega_c. \end{cases} \tag{2.36}$$

One can see from Equation 2.36 that as ω tends to values much greater than ω_c the intensity of the flux is suppressed by the exponential cutoff.

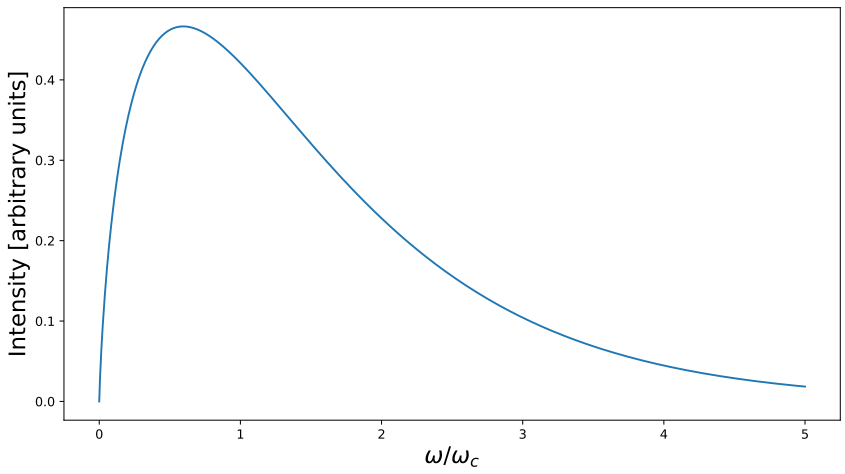

Figure 2.2: Synchrotron spectrum of a single electron.

2.4.2 Power Emitted by Synchrotron Radiation

The power radiated due to synchrotron emission is given by (Longair, 2011):

$$P_{sync} = -\frac{dE}{dt} = \frac{4}{3}\sigma_T \beta^2 \gamma^2 c U_B, \tag{2.37}$$

where σ_T is the Thompson cross-section and U_B is the energy density of the magnetic field.

From the above we can see that the synchrotron "cooling" timescale, that is the typical timescale in which a particle loses its energy due to synchrotron emission, will be:

$$\tau = \frac{E}{dE/dt} \propto \frac{E}{B^2\gamma^2} \propto \frac{E}{B^2E^2} \propto \frac{1}{B^2E}. \tag{2.38}$$

2.4.3 Synchrotron Emission From a Population of Electrons

For simplicity, assume that the energy distribution of the relativistic electrons is described by a power law of the form:

$$N(\gamma)d\gamma = \kappa\gamma^{-p}d\gamma. \tag{2.39}$$

The energy spectrum of radiation emitted by a power-law distribution of electrons, as given by Equation 2.36 requires a rather cumbersome derivation. A full derivation is given in Longair (2011) and shows the proportionality:

$$F(\nu) \propto \nu^{-\frac{(p-1)}{2}} B^{\frac{(p+1)}{2}}, \tag{2.40}$$

where p is the power-law index of the electron distribution.

2.5 Inverse-Compton Scattering

Inverse-Compton emission occurs when relativistic electrons up-scatter low-energy photons to high energies. In this section let the energy of the incident photon (ϵ) and scattered photon (ϵ_s) be normalized by the electron rest energy such that:

$$\epsilon = \frac{h\nu}{m_e c^2}, \tag{2.41}$$

$$\epsilon_s = \frac{h\nu_s}{m_e c^2}, \tag{2.42}$$

where ν and ν_s are the frequencies of the incident and scattered photons respectively. Additionally, it is convenient to consider the rest-frame of the electron in the following calculation. Let the primed values correspond to the values measured in the rest frame of the electron, with the unprimed values corresponding to the values as measured in the stationary laboratory frame. In this section the key results of the inverse-Compton process are presented. A full derivation and discussion of inverse-Compton scattering can be found in text books, such as Böttcher et al. (2012).

2.5.1 Energy Change due to a Single Scatter

In the rest frame of the electron, the energy of the scattered photon is given by:

$$h\nu'_s = \frac{h\nu'}{\frac{h\nu'}{m_e c^2}(1 - \cos\theta'_s) + 1}, \tag{2.43}$$

where θ'_s is the scatter angle.

To determine the energy change due to a single scatter event we consider the interaction in the rest frame of the electron and use the energy transformations previously shown in Section 2.2 (see Figure 2.3 for a definition of the different angles):

$$\epsilon' = \epsilon\gamma(1 - \beta\mu), \tag{2.44}$$

$$\epsilon_s = \epsilon'_s\gamma(1 + \beta\mu'_s). \tag{2.45}$$

where the energy of the scattered photon in the laboratory frame (ϵ_s) is what we are particularly interested in. In the Thomson regime the scattering will be elastic ($\epsilon' \ll 1$, see Section

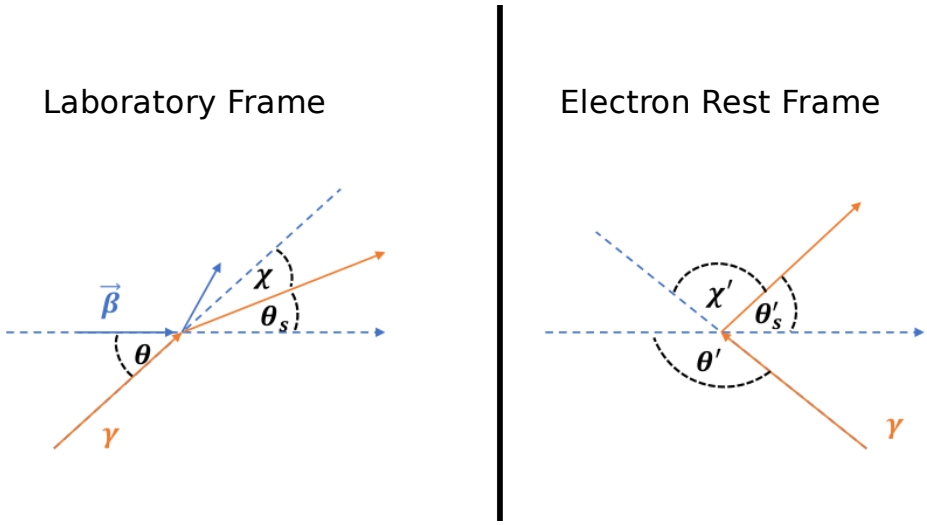

Figure 2.3: Definition of angles the laboratory frame (left, unprimed values) and electron rest frame (right, primmed values). θ is the angle of incidence of the photon, θ_s is the angle of the scattered photon, χ is the angle through which the photon has been scattered with respect to its initial trajectory.

2.5.2), giving $\epsilon'_s \approx \epsilon'$. Hence:

$$\epsilon_s \quad = \epsilon'_s \gamma(1 + \beta\mu'_s) = \epsilon' \gamma(1 + \beta\mu'_s). \tag{2.46}$$

Using Equation 2.45, ϵ'_s can be transformed back into the laboratory frame:

$$\epsilon_s = \epsilon\gamma^2(1 - \beta\mu)(1 + \beta\mu'_s). \tag{2.47}$$

Therefore, the upper limit on the energy transfer is:

$$\epsilon_s \leq 4\epsilon\gamma^2. \tag{2.48}$$

The averaged value is found by averaging over incidence and scattering angles:

$$< \epsilon_s >= \frac{4}{3}\epsilon\gamma^2. \tag{2.49}$$

Therefore the increase in photon energy scales as

$$\epsilon_s \sim \epsilon\gamma^2. \tag{2.50}$$

Hence in the Thomson regime a photon will be up-scatted by a factor of γ^2.

In the Klein-Nishina regime ($\epsilon' \gg 1$, see Section 2.5.2) the energy of the scattered photon can be obtained by considering Equation 2.43. Taking $\epsilon' \gg 1$ or $h\nu' \gg m_e c^2$ one obtains

$$\epsilon_s \approx \gamma. \tag{2.51}$$

This suggests a maximum energy that can be obtained via inverse-Compton scattering.

2.5.2 Klein-Nishina Cross-Section

The differential Compton cross-section is also known as the differential Klein-Nishina cross-section and is given by (Böttcher et al., 2012):

$$\frac{d\sigma_c}{d\Omega_s' d\epsilon_s'} = \frac{r_e^2}{2}\left(\frac{\epsilon_s'}{\epsilon'}\right)\left(\frac{\epsilon_s'}{\epsilon'} + \frac{\epsilon'}{\epsilon_s'} - \sin^2\chi\right) \times \delta\left(\epsilon_s' - \frac{\epsilon'}{1+\epsilon'\left[1-\cos\chi\right]}\right), \tag{2.52}$$

where χ is the angle of scatter and $r_e = e^2/m_e c^2$ is the classical radius of a electron. The Klein-Nishina cross-section is obtained by integrating Equation 2.52 over solid angle and incident photon energy (Böttcher et al., 2012):

$$\sigma_c(\epsilon') = \frac{\pi r_e^2}{\epsilon'^2}\left[4 + \frac{2\epsilon'^2(1+\epsilon')}{(1+2\epsilon')^2} + \frac{\epsilon'^2 - 2\epsilon' - 2}{\epsilon'}\ln\left(1+2\epsilon'\right)\right]. \tag{2.53}$$

The low- and high-energy behavior can be examined by considering the asymptotic limits of the Klein-Nishina cross-section:

$$\sigma_c(\epsilon') = \begin{cases} \sigma_T\left(1 - 2\epsilon' + \frac{26}{5}\epsilon'^2\right), \epsilon' \ll 1; (\text{ or } h\nu \ll m_e c^2), \\ \frac{3\sigma_T}{8\epsilon'}\left(\ln\left(2\epsilon'\right) + \frac{1}{2}\right), \epsilon' \gg 1; (\text{ or } h\nu \gg m_e c^2). \end{cases} \tag{2.54}$$

In the lower-energy limit, i.e. when the energy of the photon is much less than the electron rest mass, the Klein-Nishina cross-section is approximately constant and tends to the Thomson cross-section. This is referred to as the Thomson Regime. An important result of the Thomson Regime is that the scatter process is elastic. This suggests that, in the electron rest frame, the energy of the incident photon is approximately equal to the energy of the scattered photon ($\epsilon_s' \approx \epsilon'$).

In the higher-energy limit, i.e. when the energy of the photon is much greater than the electron rest mass, the Klein-Nishina cross-section is no longer approximately constant with energy, rather it decreases. The decrease in the cross-section is roughly proportional to the inverse of the incident photon energy. This limit is known as the Klein-Nishina Regime. The full Klein-Nishina cross-section and the approximations in the Thomson and Klein-Nishina

regimes are plotted in Figure 2.4.

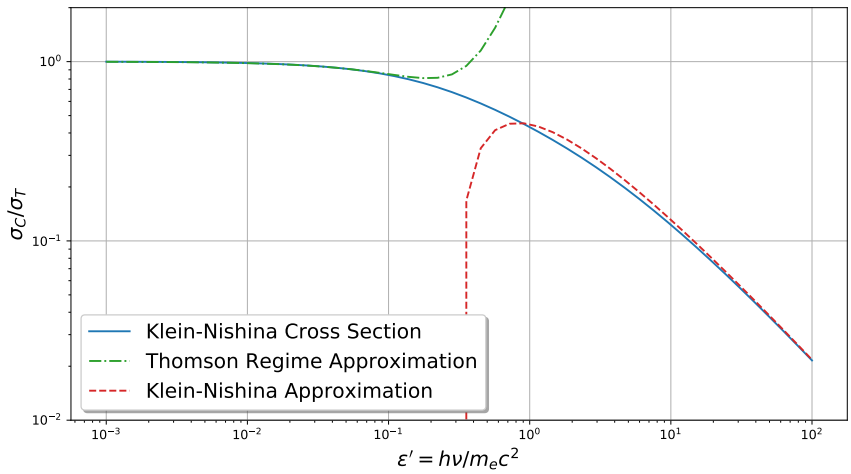

Figure 2.4: Klein-Nishina cross-section, normalized by the Thomson cross-section. The limits shown in Equation 2.54 are also plotted.

2.5.3 Power Emitted due to Inverse Compton Scattering

It can be shown (see Böttcher et al., 2012) that the power emitted due to inverse-Compton scattering of photons in the Thomson regime is given by:

$$P_{Comp,Thom,iso} = \frac{4}{3}\sigma_T\gamma^2\beta^2 U_\gamma. \tag{2.55}$$

This is similar to the power emitted due to synchrotron radiation. Comparing the Equations 2.37 and 2.55 we obtain a useful relation to compare the synchrotron and inverse-Compton luminosities:

$$\frac{L_{sync}}{L_{Comp,Thom,iso}} = \frac{P_{sync}}{P_{Comp,Thom,iso}} = \frac{U_{mag}}{U_\gamma}. \tag{2.56}$$

This shows the ratio of the two luminosities is simply the ratio of the magnetic energy density to the photon field energy density

Equation 2.55 gives the power radiated by to a single electron. In general for an electron energy distribution which is described by a power law (γ^{-p}) the energy radiated due to inverse-Compton scattering takes the form $\epsilon^{-(p-1)/2}$ where p is the power-law index of the electron distribution.

Assuming the relativistic electrons are accelerated by FOFA processes, as discussed in Section 2.3, they are power-law distributed with an upper limit on the spectral index of $p \geq 2$. This would suggest an upper limit on the hardness of the observed IC emission of 0.5 or in a dN/dE representation $\Gamma > 1.5$. This assumes that IC occurs in the Thomson regime, in the Klein-Nishina regime the cross section is suppressed with increasing energy. In addition, the scattering is non-elastic, hence the energy transferred to the electron is non-negligible. This suggests that there are firstly fewer photons being scattered and secondly that the up-scatter is not as efficient. This would result in a cut off in the observed spectrum from blazars. For these reasons an upper limit on the spectra hardness of $\Gamma > 1.5$ is a conservative limit based on the physics of electrons up-scattering a soft photon field, with harder photon fields suggesting a softer spectral index. This results will be used in Section 8.

2.6 Blazar Emission Models

Emission models of blazars can generally be divided into two categories, leptonic (see, for example, Böttcher et al., 2013; Böttcher & Chiang, 2002; Sikora et al., 2009) and (lepto-) hadronic models (see, for example, Böttcher et al., 2013). In leptonic models, lepton pairs (e^+, e^-) are accelerated to relativistic energies. The leptons then produce synchrotron and inverse-Compton emission as described in the previous sections. In a hadronic model, highly relativistic protons produce both synchrotron radiation and electromagnetic cascades. For a review of emission models of blazars see Böttcher (2012).

2.6.1 Leptonic Models

In leptonic models relativistic electrons (e^+, e^-), in the presence of a magnetic field, emit synchrotron radiation in the radio-X-ray regime. The same population of relativistic electrons then up scatter a soft photon field to X-ray to gamma-ray energies via the inverse-Compton process. The origin of this soft photon field may be the synchrotron photons (synchrotron self-Compton, SSC) or due to an external photon field (external-Compton, EC). The external photon field may originate from a number of sources such as the accretion disk, the dusty torus, broad-line region, etc. EC models will naturally have an SSC component due to the presence of the synchrotron photons, however the EC component will dominate at the higher-energy SED peak.

SSC models are rather simple models, which, in their simplest manifestations, require only a handful of parameters, all of which can be constrained using simultaneous observations (see, Ghisellini et al., 1996; Tavecchio et al., 1998, for a discussion of SSC models for TeV

blazars). In order to reproduce the observed synchrotron peak of blazar SEDs, this emission would have to originate from a relativistic population of electrons, described by a broken power law with spectral indices n_1 and n_2, such that:

$$N(\gamma) = \begin{cases} K\gamma^{-n_1}, \text{ if } \gamma < \gamma_b, \\ K\gamma_b^{n_2-n_1}\gamma^{-n_2}, \text{ if } \gamma > \gamma_b, \end{cases} \tag{2.57}$$

where K is the normalization and γ_b is the break energy. In this scenario the synchrotron peak observed at frequency ν_{sync} is emitted by electrons with energies γ_b, such that (Ghisellini et al., 1996):

$$\nu_{sync} \approx \frac{1}{1+z}\frac{4}{3}\nu_B\gamma_b^2\delta, \tag{2.58}$$

where $\nu_B = 2.8 \times 10^6 B$ Hz is the Larmor frequency. As the IC-peak occurs due to the same population of electrons scattering the synchrotron photons to higher energies, the location of the IC-peak is due to the photons at frequency ν_{sync} being up scattered by the electrons at energies γ_b. The averaged frequency of these photons, up-scattered by electrons with energy γ_b, will be given by:

$$\nu_{Comp} = \frac{4}{3}\gamma_b^2\nu_{sync}. \tag{2.59}$$

This can be rearranged to obtain an expression for γ_b:

$$\gamma_b = \left(\frac{3\nu_{Comp}}{4\nu_{sync}}\right)^{1/2}. \tag{2.60}$$

Inserting Equation 2.60 into Equation 2.58 one gets a relation for the magnetic field and Doppler factor:

$$B\delta = (1+z)\frac{\nu_{sync}^2}{2.8 \times 10^6 \nu_{Comp}} \tag{2.61}$$

The rising and falling edges of the synchrotron peak ($\nu < \nu_{sync}$ and $\nu > \nu_{sync}$) can be described by power laws with spectral indices α_1 and α_2 respectively. As shown in Section 2.4 these are related to the spectral indices of the electron distribution such that:

$$\alpha_{1/2} = \frac{-(n_{1/2}-1)}{2}, \tag{2.62}$$

which will also describe the rising and falling edges of the IC peak ($\nu < \nu_{Comp}$ and $\nu > \nu_{Comp}$). This provides motivation for the observed correlation between the rising/falling side of the synchrotron peak with the rising/falling side of the IC peak, and allows for an estimation of

the spectral shape parameters of the electron distribution.[4]

The total synchrotron and Compton luminosities ($L_{sync,Comp}$) can be related to the peak luminosities via:

$$L_{sync,Comp} = f(\alpha_1, \alpha_2)\, \nu_{sync,Comp}\, L_{sync,Comp}\,(\nu_{sync,Comp}), \tag{2.63}$$

where $L_{sync,Comp}(\nu_{sync,Comp})$ is the peak luminosity, and :

$$f(\alpha_1, \alpha_2) = \frac{1}{1-\alpha_1} + \frac{1}{\alpha_2 - 1}. \tag{2.64}$$

Recalling the relationship between the synchrotron and Compton luminosities (Equation 2.56), one obtains:

$$\frac{L_{sync}}{L_{Comp}} = \frac{\nu_{Comp}\, L_{Comp}(\nu_{Comp})}{\nu_{sync}\, L_{sync}(\nu_{sync})} = \frac{U'_\gamma}{U'_B} = \frac{2\,\nu_{sync}\, L_{sync}(\nu_{sync})\, f(\alpha_1, \alpha_2)}{R^2\, c\, \delta^4\, B^2}, \tag{2.65}$$

where the energy density of the photon field being up-scattered is the synchrotron photon field ($U_\gamma = U_{sync}$) such that ($L = \delta^4 L'$):

$$U'_{sync} = \frac{L_{sync}}{4\pi R^2 c \delta^4}. \tag{2.66}$$

Constraints on the size of the emission region can be obtained from the minimum variability time scale (see Section 2.2.3). Taking account for cosmological expansion Equation 2.25 becomes:

$$R \leq c \Delta t_{min} \delta (1+z)^{-1}. \tag{2.67}$$

Inserting Equation 2.67 into Equation 2.65 an additional relation for B and δ can be obtained.

$$B\delta^3 \leq (1+z)\left(\frac{2[\nu_{sync}\, L_{sync}(\nu_{sync})]^2 f(\alpha_1, \alpha_2)}{c^3\, \Delta t^2_{min}\, \nu_{Comp}\, L_{Comp}(\nu_{Comp})}\right)^{1/2}. \tag{2.68}$$

Hence using a handful of observable parameters, one can place firm constants on the parameters of a SSC model. However given the variable nature of blazars, simultaneous observations are required for the SSC model discussed above to be valid. This can largely be achieved using observations in the UV-X-ray band (for example using an instrument such as *Swift*-UVOT

[4]This relation will hold in the regime such that the rising edge of the synchrotron spectrum isn't significantly affected by synchrotron self-absorption, and the falling edge of the IC peak doesn't result from IC scattering in the Klein-Nishina regime. For HBLs in particular this generally isn't an issue as despite the scattering process potentially occurring in the Klein-Nishina regime, the synchrotron peak occurs in the X-ray band, a band which is typically well-covered observationally, allowing for estimation of α_2.

and *Swift*-XRT) and observations in the gamma-ray band (using instruments such as *Fermi*-LAT and VERITAS).

Single-zone leptonic models generally provide an adequate fit to the observed broadband SED of blazars. HBLs are generally well fit by a pure SSC model, FSRQs generally require a significant EC component to fully explain their emission, while IBLs/LBLs require an increasing EC component. This suggests a progression in the blazar sequence based on the degree of EC contributing to the SED. FSRQs typically requiring a larger EC component is consistent with the strong emission lines observed, suggesting a dusty region about the jet. In addition, the more powerful jets of FSRQs could be attributed the region about the jet being denser, suggesting higher accretion rates.

In general, models single-zone models are rather successful, however rapid variability observed in TeV energies are difficult to explain. Rapid TeV variability has been observed to the scale of minutes (Albert et al., 2007; Aharonian et al., 2007). This suggests an exceptionally small emission region with a high bulk Lorentz factor. As discussed in Section 2.6, different acceleration processes have been invoked to explain such variability. In addition to this, models more complicated than a single-zone model have been implemented to explain previously unexplainable SEDs. For example, Tavecchio & Ghisellini (2008) invoke a spine-sheath layer model to explain the peculiar SED features of M 87. In this model, the jet shows a spine-sheath structure, where the emission from the spine layer and the sheath layer both contribute to the overall SED.

2.6.2 (Lepto-) Hadronic Models

It is believed that in addition to leptons, protons will also be present in the jet. This is supported by observations of orphan flares from blazars such as 1ES 1959+650 (see, for example, Reimer et al., 2005) and the recent observation of an ICE-Cube neutrino event coincident with a flaring blazar (see Section 2.6.3). If a significant portion of the jet's power is converted into accelerating protons, a significant component of the SED can be due to hadronic emission. In particular if the protons are accelerated to energies greater than the $p\gamma$ pion energy threshold, protons will have enough energy to produce pions. These will decay to produce secondary particles, such as gamma rays ($\pi^0 \rightarrow 2\gamma$) and leptons such as electrons, muons and neutrinos ($\pi^{\pm} \rightarrow \mu^{\pm} + \nu_{\mu}^{\pm}$, $\mu^{\pm} \rightarrow e^{\pm} + \nu_{e}^{\pm}$). These secondary particles will also produce synchrotron radiation in the radio-X-ray regime. While the synchrotron emission of the secondary particles is non-negligible, the dominant components of the lower-energy SED peak is still expected to be due to synchrotron radiation from electrons. The higher-energy peak is attributed to synchrotron radiation of the relativistic protons and the

gamma-ray emission from pion decay. These features result in the smooth double peaked SED observed from blazars.

Typically hadronic models require extreme power requirements, with magnetic fields on the order of $\sim$ 10 G (for example see, Böttcher, 2012, for a discussion of a discussion of the requirements of the hadronic models of RX J0648+152 and RBS 0413). Such magnetic fields would result in synchrotron cooling time scales on the order of days, hence rapid TeV emission is difficult to reproduce in such a model.

2.6.3 Discussion

While it has been mentioned that blazars are generally well described by leptonic-models, and that SSC models generally provide an adequate fit to HBLs, this is not the case for all sources. For example, the HBLs RX J0648.7+1516 and RBS 0413 cannot be well described by a SSC model (as discussed by Böttcher, 2012). Rather these sources are adequately described by hadronic models.

The recent detection of a neutrino event, correlated spatially and temporally with a gamma-ray flare of the blazar TXS 0506+056 (see Ahnen et al., 2018; Abeysekara et al., 2018b; Aartsen et al., 2018), suggests that TeV blazars may also be sources of astrophysical neutrinos. High-energy neutrinos are expected to be emitted in hadronic models due to charged pion decay. Such a correlation may suggest a hadronic origin to the gamma-ray emission. In the evolving era of multi-messenger astronomy development of hadronic models will be of great importance.

While the models discussed here take a rather extreme view of the emission origin, it is likely that blazar emission is due to (in the leptonic case) both SSC and EC mechanisms. It is also likely that the emission originates from both leptonic and hadronic processes. Observations however suggest that leptonic emission generally dominates over the hadronic emission. While within leptonic emission, the relative dominance of the external photon field may be linked to the blazar class type.

2.7 Summary

As discussed in the previous sections, there are a number of different proposed acceleration and emission processes which result in the observed emission from blazars. In Section 2.3 the different acceleration processes were discussed and the different locations of acceleration highlighted. This suggests that acceleration might not be solely due to a single process, rather the location and environment of the accelerating particles may play a role in the relative

dominance of an acceleration process.

In Section 2.6 different emission models were discussed, building on the basic emission mechanisms discussed is Sections 2.4 and 2.5. While simplistic single-zone SSC models have been successful in describing HBLs, FSRQs and LBL/IBLs generally need EC components. Furthermore, some sources have diverged from this general trend, with multi-zone and hadronic models showing better agreement.

To truly characterize the broadband SED, simultaneous multiwavelength observations are crucial. Variability and spectral studies at multiwavelength allow for one to test different hypotheses for the emission processes and the environment.

Chapter 3

Instrumentation

3.1 Overview

In this chapter the different instruments used in thesis are introduced. In Section 3.2 VERITAS and its operations are discussed. As VERITAS is the primary instrument using in this thesis, it shall be discussed in detail. The analysis of VERITAS data and, in general, IACT data will be discussed in Chapter 4. In Section 3.3 the key concepts of the *Fermi* Large Area Telescope (*Fermi*-LAT) are discussed. In Section 3.4 the *Swift* X-Ray Telescope (*Swift*-XRT) is discussed.

3.2 VERITAS

3.2.1 Overview

The **V**ery **E**nergetic **R**adiation **I**maging **T**elescope **A**rray **S**ystem, VERITAS [1], is an array of four 12m IACTs, located at the Fred Lawrence Whipple Observatory in southern Arizona, USA (31° 40′ 30″N, 110° 57′ 07″W, 1.3km a.s.l.) (Holder, 2011). Each of the four telescopes has a Davies-Cotton-design segmented mirror dish, consisting of 350 individual hexagonal mirrors giving a total mirror area of ∼110 m^2 (Holder et al., 2006). VERITAS has been operating with the full four-telescope array since 2007. Since its commissioning VERITAS has undergone a number of upgrades to improve its sensitivity and performance. In 2009, telescope 1 (T1), the original prototype telescope, was relocated to improve the symmetry of the array, increase the effective area of the array and reduce the background rates due to local muons (Perkins et al., 2010). In 2012 the L3 trigger system (see Section 3.2.4) was upgraded (Zitzer, 2013) and the original photomultiplier tubes (PMTs) were replaced with higher quantum efficiency PMTs (Otte et al., 2011).

In its current configuration VERITAS can indirectly detect gamma rays with energies

[1] veritas.sao.arizona.edu

between 85 GeV and > 30 TeV and has an energy resolution of 15-25%[2] for a 1 TeV photon. The effective collection area (see Section 4.2.8) for a 1 TeV photon is on the order of 10^5 m^2. The angular resolution (68% containment radius) of an individual 1 TeV photon is $\sim 0.1^\circ$. VERITAS can detect a source with flux equal to 1% of the Crab Nebula flux at 5 standard deviations above background (σ) in ~25 hours of observations. See Park et al. (2015) and references therein for a detailed study of the current performance of the VERITAS instrument.

To differentiate between the different array configurations used in this work, 3 data taking epochs are defined:

- **V4**: Data taken in the original 4-telescope configuration (2007-2009).
- **V5**: Data taken after the relocation of the T1 but before the camera upgrade (2009 - 2012).
- **V6**: Data taken after the camera upgrade (2012 - Present).

In addition, since 2012 VERITAS has been operating under reduced high voltage (RHV, hereinafter observations taken using the standard high voltage configuration shall be referred to as SHV) during moderate-moonlight conditions (see Archambault et al., 2017). During these observations the voltage applied to each PMT is reduced hence preventing damage to, and increased degradation of, the PMT. This reduces the chances of a lower-energy, and hence dimmer, shower triggerings the telescope, hence increasing the energy threshold to $\sim$ 150 GeV.

Southern Arizona experiences an annual monsoon season, during which heavy rainfall and lightning storms are a near daily occurrence. As operating in such conditions would be dangerous to the observers, maintenance staff and the telescope itself, VERITAS ceases observations during the monsoon period. A typical monsoon period lasts from early July to late August/ early September. Hence in this work a typical VERITAS observing season is defined as starting in September and ending in July.

3.2.2 VERITAS Mirrors

Each of the VERITAS telescopes is of Davis-Cotton design (Davis & Cotton, 1957). The dish of each telescope consists of a segmented mirror made up of 350 hexagonal mirrors. The segmented mirrors combine to generate a mirror aperture of 12m, giving a total collection area of ~110m^2. The mirror focuses the collected image onto the camera located at the focal plane. This camera is supported by a quadrupod structure, where the weight of the camera

[2]The range arises due to effects such as, different analysis cuts (see Section 4.2.6 and observation conditions.

results in zenith angle dependent distortions of the optical support structure and pointing inaccuracies. The distortion of the optical structure results in a distortion of the PSF, which, in addition to the pointing offset, is regularly monitored, allowing for corrections to be applied.

3.2.3 VERITAS Cameras

Each VERITAS camera, located at the focal plane of each dish, consist of 499 photo-multiplier tubes (PMTs), with each PMT having a field of view (FoV) of $\sim 0.1^\circ$ giving a total FoV of 3.5°. To reduce the dead space between pixels, a set of Winston (1970) design light cones are mounted on the face of the camera (see Figure 3.1). This has the added effect of reducing background contamination by blocking light arriving from large angles. In its original configuration, the VERITAS camera utilized Photonis XP2970 PMTs, which were replaced as part of the V6 upgrade to Hamamatsu R10560-100-20 MOD PMTs. The upgraded PMTs produce a signal which has a full width at half maximum (FWHM) of 4.2 nanoseconds, which is 40% narrower than the Photonis models. The Hamamatsu PMTs also have a higher quantum efficiency. Otte et al. (2011) estimate that the improved quantum efficiency yields a 35% improvement to the detection of Cherenkov photons. For a full discussion of the PMTs used in the VERITAS camera see Otte et al. (2011).

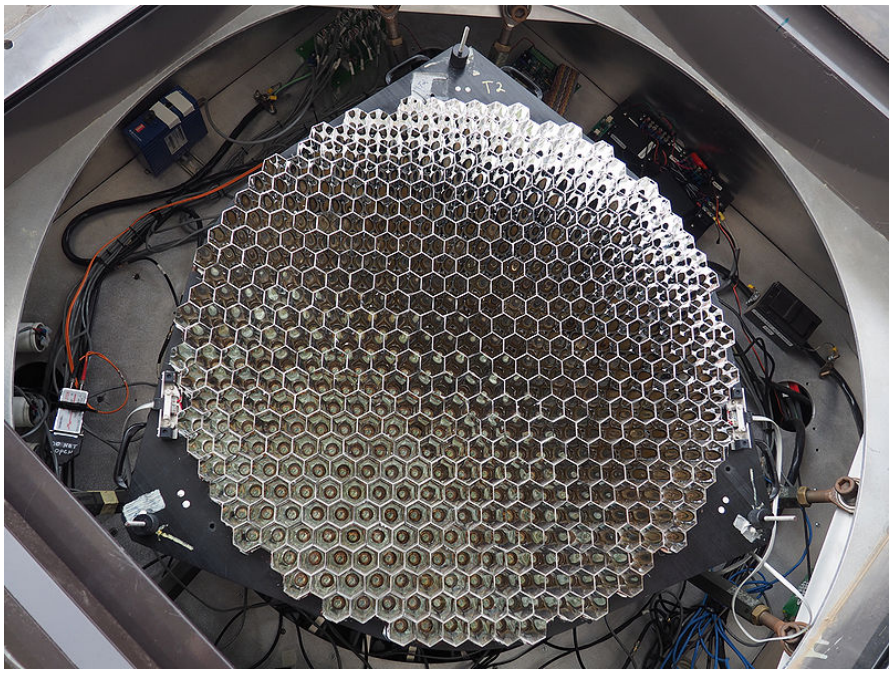

Figure 3.1: VERITAS Camera. Image credit: M. Hütten.

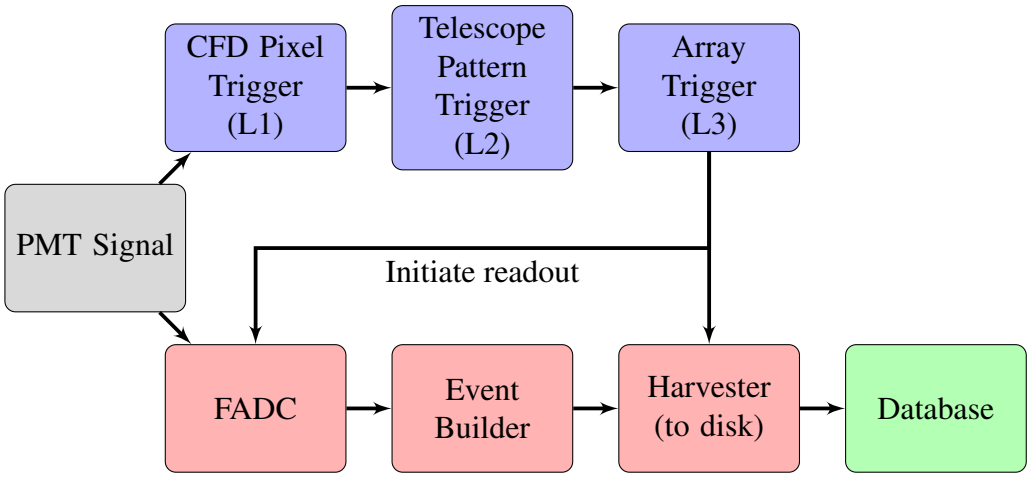

Figure 3.2: Flow chart of the VERITAS trigger and DAQ systems. Components highlighted in dark blue correspond to the trigger system. Components highlighted in red correspond to DAQ components.

3.2.4 VERITAS Trigger System

VERITAS utilizes on a three-level trigger system. The first trigger level (L1), referred to as the pixel trigger, corresponds to the voltage recorded by each individual PMT (hereinafter pixel). The signal received by each pixel is passed to a constant fraction discriminator (CFD) (see Hall et al., 2003). The CFD duplicates the signal into three components. The first signal passes through a threshold discriminator (TD), where the threshold voltage is programable and specific to the observing conditions. The second and third signals are used to create a zero-crossing discriminator (ZCD). This is done by inverting and delaying the second signal and attenuating the third signal by a fraction. The two signals are then added to find the time at which the signal reaches a threshold of given fraction of the total signal. In addition to this, a rate feedback loop is applied to allow dynamic real-time adjustments to the CFD trigger level by applying a voltage offset which is a function of trigger rate. This has the effect of adjusting the CFD threshold for increasing night sky background (NSB). This feedback loop accounts for changes in the NSB on the timescales of $\sim$ 1s. Hence the ZCD determines the time at which $f * V(t) - V(t+\tau) - V_{RFB} = 0$, where $V(t)$ is the voltage of the pixel signal, f is the fraction of the maximum signal we wish to trigger at, τ is the time delay and V_{RFB} is the CFD correction determined by the rate feedback loop. Utilizing both a ZCD and TD, the CFD provides both the timing of a pixel signal and whether the signal is large enough to trigger.

If the voltage measured by the CFD passes a predetermined discriminator voltage then the PMT will be consider to be a triggered pixel. For nominal observation conditions the CFD

threshold level is set to ~45mV. For observations taken under low-moonlight conditions the CFD threshold level are set to ~65mV. During moderate-moonlight conditions (i.e. RHV) the CFD threshold level is set to ~25mV. A higher CFD threshold has the effect of reducing the rate of false triggers due to increasing NSB at the cost of not triggering on dimmer showers, hence increasing the energy threshold.

The second trigger level (L2) is referred to as a pattern trigger or telescope-level trigger (for a detailed discussion see Zitzer, 2013). The outputs from each pixel's CFD channel is sent to a topological trigger system which searches for patterns of 3 or more triggered pixels which are adjacent to each other, within a coincidence window of $\sim$ 6 ns. This requirement reduces the effects of NSB fluctuations, background cosmic ray events and stars on the trigger rate.

The third trigger level (L3), referred to as the array-level trigger, requires that two or more L2 triggers occur within a coincidence window of around ~50 ns.[3] This requirement has the effect of rejecting false triggers due to single telescope events such as local background muons and variations in the NSB. Upon a L3 trigger occurring, a signal is sent to each telescope to initiate the data readout processes (see Section 3.2.5). A bias curve, obtained by observing a dark patch of sky and adjusting the CFD threshold voltage, is shown in Figure 3.3. Under nominal operations the L2 trigger rate varies from telescope to telescope, but is on the order of $\sim 10^3$ Hz. The L3 rate for nominal observational conditions is around 200-400 Hz. The L3 rate for RHV observations is around 100-200 Hz.

[3]This time accounts for the transit time of signals between the telescopes and the central trigger machine. It also takes into account the pointing of the array, and therefore, the expected delay between photon arrival times.

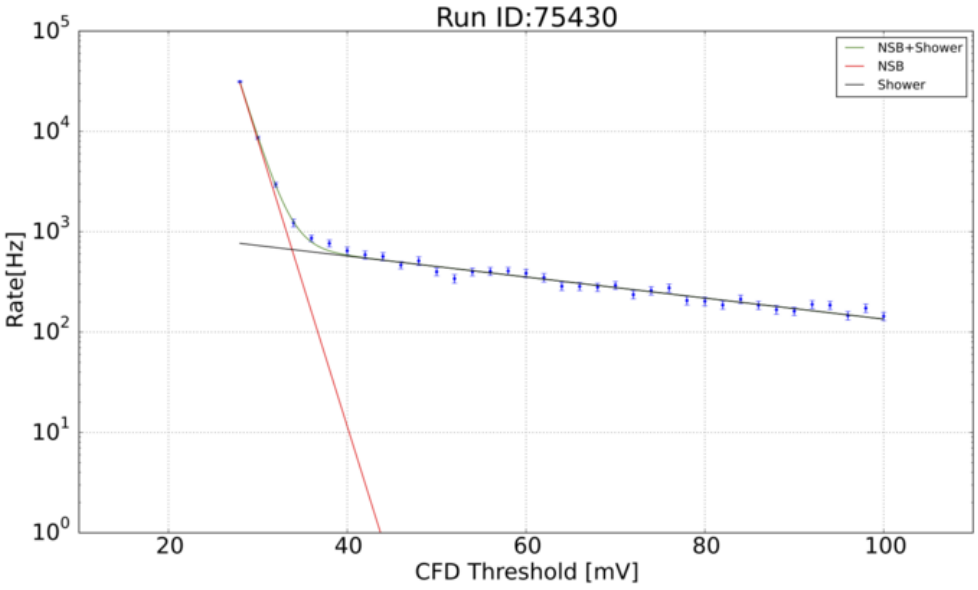

Figure 3.3: Typical Bias curve obtained by observing a dark patch of sky and adjusting the CFD threshold voltage. The red line corresponds to the contribution to the trigger rate due to NBS variations. The black line corresponds to triggers due to shower events. The effect of NSB is negligible above ~45 mV. These observations were taken under dark observing conditions.

3.2.5 Data Acquisition System

The VERITAS Data Acquisition System (DAQ, see Hays, 2008), operates on a telescope-level and array-level. At the telescope-level, two components, namely VME Data Acquisition (VDAQ) and the Event Builder, operate to build a telescope-level event. In order to read the signal received from each pixel, each telescope utilizes custom-built flash-analogue-to-digital converters (FADCs) (see Rebillot et al., 2003). In parallel to the triggering procedure, the signal from each pixel is fed into a dedicated FADC. The FADC continuously digitizes the pixel signal at a rate of 500 millisamples per second or 2 nanoseconds per sample. Prior to digitization the signal is fed into two channels. The first channel applies a "High" gain level to the signal, while the second channel delays the signal and applies a "Low" gain level. The digitized pixel signals are stored in a ring buffer which has a memory depth of 32 μs. If the "High" gain channel is saturated an internal switch is thrown and the delayed "Low" gain signal is written to the buffer memory. This has the effect of extending the range of the FADCs from 256 to 1500 digital counts. The FADCs are hosted in a FADC board which have 10 individual FADC channels. The FADC boards are mounted in VME crates, which allow for the transfer of data to the VDAQ system.

Upon receiving a L3 trigger, the VDAQ is sent an event number and event type (for example pedestal events, see Section 4.2.2). The VDAQ system consists of five VME crates, four of which house FADC boards and one acting as an auxiliary crate, handling information such as event numbers and types. The VDAQ reads out data from the FADC board via a serial communications interface (SCI) and buffers these fragmented events before transferring them in blocks to the telescope-level Event Builder. In addition to this, the VDAQ transfers the event number and event type, and other information such as CFD trigger rates. These data transfers account for the majority of the array deadtime, which is dependent on the L3 trigger rate. For nominal observations the array deadtime is typically 10-15%. The Event Builder combines the events from individual VME crates to create a telescope-level event. The telescope-level event is then transferred to the array-level Harvester via a gibabit ethernet connection. The Harvester combines the data recorded by each telescope to create an array-level event. In addition to creating array-level events the Harvester also does some preliminary tests on the data, for example checking the telescope participation rates and searching for missing events. The Harvester also provides a basic "Quicklook" analysis, giving observers a real-time view of the data and allowing for an estimate of the source's flux. The events recorded in a single run (typical duration of 15-30 minutes) are stored by the Harvester in a custom data format (VERITAS Bank File, VBF, see Hays (2008)), which combines the event data with other metadata such as UTC timing and trigger rates. The VBF file is then saved locally and archived on two dedicated external servers operated by the VERITAS collaboration, each containing a independent copy of the data to prevent data losses due to RAID failures.

3.2.6 Flasher Calibration

During each night of observations, and for each specific observation mode (i.e. SHV and RHV), a Flasher observation is taken (see, Hanna, 2008). A Flasher is typically a 2 minute long run during which the camera of each telescope is flashed by a LED flasher. The LED flasher is designed to deliver a cycle of pulses of a known brightness at programmable rate. While the LED flasher is illuminating the telescope camera, the system is forced to trigger at the same rate. This allows for the recording of the flasher pulses. Since the duration, timing and brightness of each flash is known, the data read out can be used to adjust the relative gains between pixels, correct for any timing difference between pixels (due to, for example, different cable lengths) and determine the absolute gain of the PMTs. See Section 4.2.3 for a more detailed discussion on how these calibrations are implemented into the analysis chain.

The absolute gain of a PMT is an important characteristic of a PMT, which relates the

observed signal to the incident light. This makes knowledge of the absolute gain of the PMTs critical in estimating the brightness of the shower. The absolute gain is regularly monitored by measuring the PMTs response to low light levels. This is done by placing so-called "holey plates", that is a plate with small holes drilled at the locations of the PMTs, over the camera and exposing the camera to light of varying intensities using the flasher described above. As the number of photo-electrons will be Poisson distributed, the number of photo electrons observed will be:

$$\mu = G\, N_{PE}, \tag{3.1}$$

where μ is the mean of the distribution, N_{PE} is the number of photo-electrons arriving at the first dynode of the PMT and G is the absolute gain. As the distribution is Poisson, this can be related to the width of the distribution, σ, to provided an estimate of the absolute gain:

$$G = \frac{\sigma^2}{\mu}. \tag{3.2}$$

As the PMTs age the absolute gain will decrease, it is important to monitor the absolute gains and increase the high-voltage levels as is required, in order to keep the absolute gain within an acceptable range. Absolute gain measurements are typically taken during each dark run and the high-voltages are typically reviewed at the start of each season.

3.2.7 Monitoring Subsystems

To assist with data taking and data quality monitoring, VERITAS has a number of subsystems located on site. These systems range from monitoring how the atmosphere is changing, to monitoring how the telescope's systems are behaving. In this section some of the key subsystems will be discussed.

VERITAS Pointing Monitor (VPM): A key subsystem of VERITAS is the VPM. As the name suggests, the VPM provides monitoring of the pointing of each telescope. The VPM has a hardware and software component. Each telescope has two cameras mounted on the optical support system. The first camera is focused on the location of the sky at which the telescope is pointing. The VPM software compares the location of stars in images taken by this camera to known reference stars. This gives accurate and real-time measurements of the elevation and azimuthal offset from the desired pointing. Knowledge provided by the VPM reduces the pointing uncertainty to less than 25 arcseconds.

VERITAS Secondary Monitoring Camera: The second camera is focused on the telescope's camera. The primary goal of the second camera is to provide calibration measurements related to the performance of the telescope's structure and optics. Calibrations such as

mirror reflectivity measurements and monitoring of the telescope point spread function (PSF) are regularly taken throughout an observing season.

Current Monitor Boards (IMon): Custom-built current monitors allow for the monitoring of the current output of each PMTs. When combined with software developed by the VERITAS collaboration, observers can monitor the currents and HV level of each pixel. The IMon software also has a safety feature in which if the current measured by a single PMT reaches a threshold then the HV to that pixel is turned off. This helps protect the PMTs from potential damage.

Far Infrared Radiation Pyrometer (FIR): VERITAS has 3 Heitronics KT15.82 Infrared Radiation Pyrometers[4] located around the site. Two of the FIRs are mounted on telescopes T2 and T3, which are co-aligned with the telescope's optical axis. The third FIR is mounted on a nearby building pointing upwards to zenith. These FIRs are designed to detected cloud cover by measuring the relative change in the temperature of the sky (see Figure 3.4). Mounting FIRs on the telescopes and pointing at zenith give an accurate estimate of the cloud cover in the FoV and overhead.

Light Detection and Ranging (LIDAR): A Vaisala LIDAR system[5] is installed at the VERITAS site. The LIDAR system measures back-scatter of light due to scattering agents in the atmosphere such as smoke, dust, haze, fog and clouds. This is done by emitting short pulses of light and measuring the time until back-scatter is detected. The LIDAR allows for a 2-dimensional profile through the atmosphere to be recorded.

Weather Station: The weather station located at the VERITAS site gives the observers an up-to-date measurement of the weather conditions. Measurements such as wind speeds and direction, humidity and temperature are recorded by the weather station. There is also an all-sky monitoring camera located at the weather station, which has an adjustable exposure time to give a current view of the total night's sky.

3.2.8 Database and Data Quality Monitoring

An online database is operated by the VERITAS collaboration. This database acts as an archive for the observations. The database stores details of observations, for example observing target, L2 and L3 rates and observing mode (SHV/RHV). In addition, the database stores information relating to the observing conditions, for example, coordinates tracked, FIR measurements, NSB levels and observer comments. The database in an integral part of VERITAS

[4] http://www.heitronics.com/en/infrarot-messtechnik/produkte/radiation-thermometers/universelle-spezialisten/kt15ii-serie/models/

[5] https://veritas.sao.arizona.edu/documents/CL51_B210861EN-A-LoRes.pdf

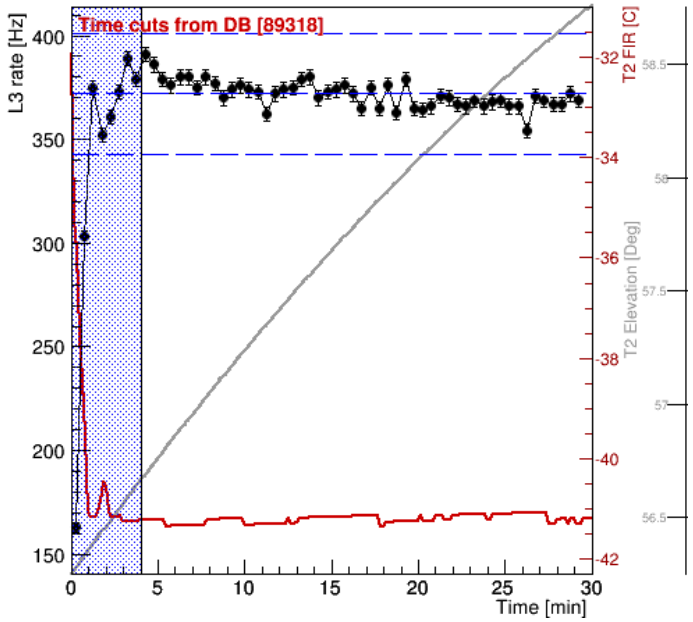

Figure 3.4: DQM plot for a VERITAS run. The black points show the measured L3 rate, with the solid and dashed lines corresponding to the mean and 1σ error on mean of the L3 rate, respectively. The red line is the temperature measured from the T2 FIR. The gray line shows the elevation of the telescope. The shaded blue region shows a data-quality time cut recorded in the database.

operations, forming a crucial bridge between observers and data analysts. The database also stores data quality monitoring (DQM) information. DQM is undertaken every date after observations are taken by a member of the VERITAS collaboration. The DQM processes help to monitor the health and performance of the telescopes and to flag any poor quality data.

Figure 3.4 shows an example typically DQM plot. In this run in particular the T2 FIR detected a change in temperature at the start of the run. At the same time, the L3 trigger rates were far lower than the mean, and showed strong fluctuation. This might correspond to a cloud passing across the FoV, resulting in a momentary drop in L3 rate. The DQMer flagged this data as affected by weather and put a timecut in the database. While this is done on a daily basis, I have also performed my own DQM on each run used in this analysis.

3.3 *Fermi*-LAT

3.3.1 Overview

The *Fermi* Gamma-ray Space Telescope (*Fermi*) is a space-based observatory designed to observe the sky in energies from $\sim$ 10 keV to >300 GeV. On board *Fermi* are two instruments,

the Gamma-ray Burst Monitor (GBM, Meegan et al., 2009) and the Large Area Telescope (LAT, Atwood et al., 2009). As only data taken by *Fermi*-LAT is used in this work, only *Fermi*-LAT will be discussed. *Fermi* was launched in June 2008 with full science operations beginning on 4th August 2008. The data taken by *Fermi* is made publically available via the *Fermi* Science Support Centre (FSSC)[6]. The FSSC also maintain publically available analysis software for analysing data products of the *Fermi* Mission (*Fermi* Science Tools[7]).

3.3.2 *Fermi*-LAT

Fermi-LAT is a gamma-ray telescope sensitive to gamma-rays in the range $\sim$ 20 MeV to $>$ 300 GeV. *Fermi*-LAT is a pair-conversion telescope meaning that it utilizes the pair production process to detect and measure the energy and trajectory of incoming gamma rays. In this method an incoming gamma ray has energy greater than twice the rest mass of an electron, therefore the energy of the gamma ray can be converted into an electron-positron pair. Pair production becomes the dominate mechanism for photon interaction above $\sim$10 MeV. To identify gamma-ray photons, *Fermi*-LAT has three components. The first component is the Anticoincidence detector (ACD). The ACD is a layer of segmented plastic scintillators on the outer side of the space craft. The plastic scintillators are made of a low-Z material and produce a flash of light when a charged particle passes through them. The choice of a low-Z material reduces the attenuation of the gamma rays passing through the scintillator. A signal from the plastic scintillators suggests that the particle passing through the ACD, and into the inner components of the telescope, is a charged particle and not a gamma ray. This allows for the event to be vetoed instead of being classified as a gamma-ray like event.

After passing through the ACD, the gamma ray will then pass into the Tracker (TKR), The TKR is made up of 16 Precision Si-strip Tracker modules. Each module contains 18 layers of paired x-y silicon strip detectors (SSD) planes, with layers of tungsten foil on top of each SSD pair. The tungsten pair is a high Z material which has a higher cross-section for the production of electron-positron pairs. The excess energy of the gamma ray is carried away by the electron-positron pair. The SSD planes measure the x-y coordinates of the electron-positron pairs created when the gamma ray is destroyed as it passes through the tungsten foil. This allows for the flight paths of electron-positron pairs to be estimated and hence the incidence direction of the gamma ray to be determined.

To determine the energy of the incoming gamma ray, *Fermi*-LAT uses an electromagnetic calorimeter (CAL) which consists of an array of CsI(Tl) scintillation crystals. The CAL

[6] https://fermi.gsfc.nasa.gov/ssc/
[7] https://fermi.gsfc.nasa.gov/ssc/data/analysis/software/

is a 3D imaging calorimeter, which in addition to measuring the energy deposited in the calorimeter, also provides 3D imaging of the electromagnetic shower development within the calorimeter. The electromagnetic shower is produced in a similar manner as the extensive air showers as discussed in Section 1.3.2. Imaging of the shower development allows for an estimate of the initial photon trajectory; this estimate can be used as a sanity test when combined to the trajectory determined by TKR.

The combination of the ACD, TKR and CAL allow for the determination of the trajectory and energy of the event, as well as providing a discriminator for charged particle events and events in which overlapping events occur within the same event readout window (i.e. temporally coincident events). The classification and reconstruction of events software has undergone a number of incremental improvements since launch (see Ackermann et al., 2012a, for a detailed discussion of the post flight calibration and details of the "Pass 6" and "Pass 7" event reconstruction techniques). The most recent improvement to the event reconstruction is known as "Pass 8" (Atwood et al., 2013). Pass 8 introduces a number of improved analysis techniques for event reconstruction such as tree-based tracking for the TKR module and cluster analysis for the CAL module. Pass 8 results in improvements in the overall instrument acceptance, with an estimated ~25% improved sensitivity to high-energy events and the lower-energy acceptance improving by a factor as high as 3 (Atwood et al., 2013).

The analysis presented in this work uses Pass 8 analysis. In addition, the analysis is done using the fermipy package (Wood et al., 2017). The fermipy package is a python framework which builds on the *Fermi* Science Tools package.

3.4 *Swift*-XRT

3.4.1 Overview

The *Swift* Gamma-Ray Burst Explorer (*Swift*, Gehrels et al., 2004), is a space-based observatory which was launched on the 20th of November 2004. The primary goal of *Swift* is to detect and provided rapid follow up observations of gamma-ray bursts (GRBs). To facilitate this, *Swift* has 3 onboard instruments: the gamma-ray Burst Alert Telescope (BAT, Barthelmy et al., 2005), the X-Ray Telescope (XRT, Burrows et al., 2005) and the Ultraviolet/Optical Telescope (UVOT, Roming et al., 2005). *Swift*-BAT is a large field of view instrument (FoV of 1.4 sr), which has the primary goal of detecting X-ray emission in the 15 - 150 keV range from GRBs and determining their location with arcminute accuracy within 1-2 minutes of the initial GRB detection. Upon detecting a GRB, *Swift*'s onboard computer quickly determines if observations of the source are viable, if so it will quickly slew to the

source location, allowing observations to be made with the two narrow FoV instruments, *Swift*-UVOT and *Swift*-XRT. *Swift*-UVOT is an optical-UV (170-600 nm) telescope with a FoV of 17x17 arcmin^2. *Swift*-UVOT is designed to study the early light from GRBs and their environment, provide sub arcsecond localization of GRBs, to provide photometric redshift measurements and to study the temporal evolution of the GRBs optical-UV flux. Observations taken by *Swift*-XRT have been analyzed and will be presented as part this work. For this reason, *Swift*-XRT will be discussed in detail in Section 3.4.2.

When not observing GRBs, *Swift* observes a number of astrophysical source types. As part of a joint campaign, VERITAS and *Swift* regularly monitor a number of known TeV blazars. This results in large multiwavelength datasets from optical-UV to TeV for a number of TeV blazars. *Swift* also operates a target of opportunity (ToO) program. This program is open to the wider astronomical community, allowing astronomers to request time be taken on a source which is of current scientific interest. Observations taken on OJ 287 (see Chapter 7) were taken as part of a ToO request. Data taken by *Swift* is made available to the public via an online data archive[8]. Analysis of these observations is made possible by publically available tools developed and maintained as part of the *HEAsoft* software package[9]. Note in this work the latest (as of November 2017) version of *HEAsoft*, v6.22.1, is used for all *Swift*-XRT analysis.

3.4.2 *Swift*-XRT

Swift-XRT is a X-ray telescope sensitive to X-rays in the range 0.2-10 keV. It has an effective area for 1.5 keV photons of $\sim$ 125 cm^2 and the energy resolution (at launch) was 140 eV at 5.9 keV (Burrows et al., 2005), whereas more recent estimates (2009)[10] put the energy resolution at 260 eV at 5.9 keV. The energy resolution of the telescope is expected to slowly degrade due to the incident protons creating electron traps in the CCD's silicon lattice, degrading the charge transfer efficiency (see Section 4.3.2.4 of Burrows et al., 2005). The telescope's mirror system consists of 12 concentric gold-coated electroformed Ni shells or length 600 mm and with diameters in the range 191 - 300 mm. This gives a focal length of 3.5 m. The system utilizes a Wolter-I, grazing incidence design. This design uses two mirrors positioned at a shallow angles to the incident X-ray, so that the X-ray grazes off the first mirror then off the second causing it to be focused onto the CCD. Figure 3.5 shows a schematic view of a Woltzer-I design, such as that implemented by *Swift*-XRT.

[8] http://www.swift.ac.uk/archive/
[9] https://heasarc.nasa.gov/lheasoft/
[10] http://www.swift.ac.uk/analysis/xrt/modes.php

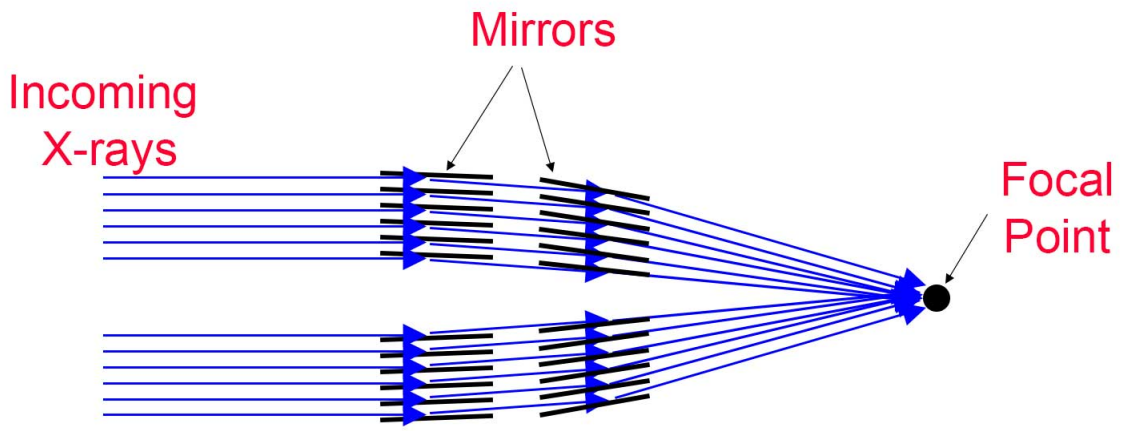

Figure 3.5: Schematic design of a Woltzer-I grazing incidence mirror design such as that used by *Swift*-XRT. Image credit NASA's Imagine the Universe https://imagine.gsfc.nasa.gov/science/toolbox/xray_telescopes1.html.

The CCD detector is an e2v CCD-22, the imaging section is a 600 X 600 array of 40 X 40 μm^2 pixels, with a pixel scale of 2.36″ per pixel giving an effective FoV of 23.6 × 23.6 arcminutes. The CCD detector is intentionally located slightly offset along the optical axis from the best on-axis focus (Moretti et al., 2004). This has the result of slightly blurring the on-axis PSF and giving a more uniform PSF over a larger portion of the FoV. This design is to take into account that observations might not be taken with the source located in the centre of the FoV (note: the BAT location uncertainty is on the order of arcminutes), hence a comparable PSF over a larger portion of the FoV is preferable.

The principle goal of *Swift*-XRT is to provide detailed spatial, spectroscopic and flux measurements of GRBs over orders of magnitude and to within sub-millisecond timing resolution. To achieve this *Swift*-XRT has four different operating modes, namely Imaging mode, Photo Diode mode (disabled since May 2005), Photon Counting (PC) mode and Window Timing (WT) mode. Each of the different observing modes have their own strengths and weaknesses. For observations of blazars used in this work, only data taken in WT modes were analyzed. For a detailed discussion of the other data taking modes (see Section 4.7 of Burrows et al., 2005). A detailed description of the analysis of *Swift*-XRT data is given in Section 4.4.

3.5 Summary

In this section I have introduced the key instruments that shall be used in this thesis. These instruments represent the state-of-the art current generation instruments currently being used to study astrophysical phenomena. Future missions such as CTA and ATHENA[11] will build on the success (and shortcomings) of the instruments discussed in this section, to provide improved sensitivities in their respective energy bands.

[11] X-ray mission proposed by the European Space Agency, http://www.the-athena-x-ray-observatory.eu/

Chapter 4

Data Analysis Methodology

4.1 Overview

In this section the analysis techniques for data taken by the instruments used in this thesis will be discussed. As the majority of this thesis focuses on the reduction, processing and analysis of VERITAS data, the VERITAS analysis chain will be discussed in detail in Section 4.2.1. In Sections 4.3 and 4.4 the analysis of data taken with the *Fermi*-LAT and Swift-XRT instruments respectively will be discussed. Rather than a detailed description of the step-by-step analysis process, a overview of the key elements of the analysis is discussed. Non-standard details, such as the choice of energy cuts values, are discussed where relevant.

4.2 VERITAS Analysis

4.2.1 VERITAS Analysis Chain

To analyse data taken by the VERITAS array, two semi-independent analysis packages have been written and are maintained by the VERITAS collaboration. These packages are ***E**vent**D**isplay* (ED, Maier & Holder, 2017) and ***VE**ritas **G**amma-ray **A**nalysis **S**uite* (VEGAS, Cogan, 2007). As ED was used for the analysis of VERITAS data in this thesis, only ED shall be discussed here. It is worth noting that it is common practice within the VERITAS collaboration for analysis to be verified by both ED and VEGAS before being submitted for publication. All VERITAS results presented in this thesis have been verified using both analysis packages.

ED was initially developed as a method to display events recorded by the original prototype one-telescope array. ED has since evolved into a complete analysis suite for multi-telescope IACT data, allowing temporal, spectral, flux and morphological studies to be performed on IACT data. Due to its scalability, ED has also been adapted to analyse CTA data. In the following sections the ED analysis chain will be discussed.

4.2.2 Trace Integration

The Cherenkov photons arriving from an EAS are detected by the camera's PMTs and are recorded as a voltage-vs-time signal by the FADCs (see Section 3.2.5). The pulse measured by each PMT is recorded as an FADC trace (see Section 3.2.5). The arrival time, T_0, is defined as the time at which the signal rises to 50% of its maximum value. A typical FADC trace is shown in Figure 4.1. The FADC is deliberately offset by a programmable hardware value known as the pedestal value. This offset applied due to the signal measured by the FADC being AC-coupled. The offset allows for the measurement of a signal which fluccuates about the pedestal value. This accurately represents the natural variability of the signal due to electronic noise and NSB variations. Due to this variability it is convenient to define the pedestal variance (pedvar). The pedvar is a measure of the NSB and is measured by artificially injecting triggers, in the absence of a triggering event, during VERITAS data taking at a rate of 3 Hz. These are known as pedestal events. The pedestal events provide a measurement of the brightness of the sky as measured by the PMTs. The pedvar is estimated from the 3 minute average of these events.

To optimize the signal-to-noise ratio, VERITAS utilizes a double-pass trace integration method (see Holder, 2005). During the first pass, a wide integration window of typically 16 ns (8 samples) is used to determine the integrated charge and T_0 of each pixel. The image is then cleaned and parametrized as described in Sections 4.2.3 and 4.2.4. Using the parameterized shower information, a linear fit to the pulse arrival time as a function of position along the image axis is obtained. The time gradient (slope of the fit) is used to obtain a new T_0 for each pixel. This new T_0 is then used in conjunction with a smaller integration window of typically 12 ns (6 samples). Figure 4.2 shows the linear fit, obtained from the shower shown in Figure 4.3, from which the location of the second pass integration window is determined. From the second-pass time window, the integrated charge is obtained and a correction for the relative gain of the pixel is applied. The image is then cleaned and parametrized as described in Sections 4.2.3 and 4.2.4.

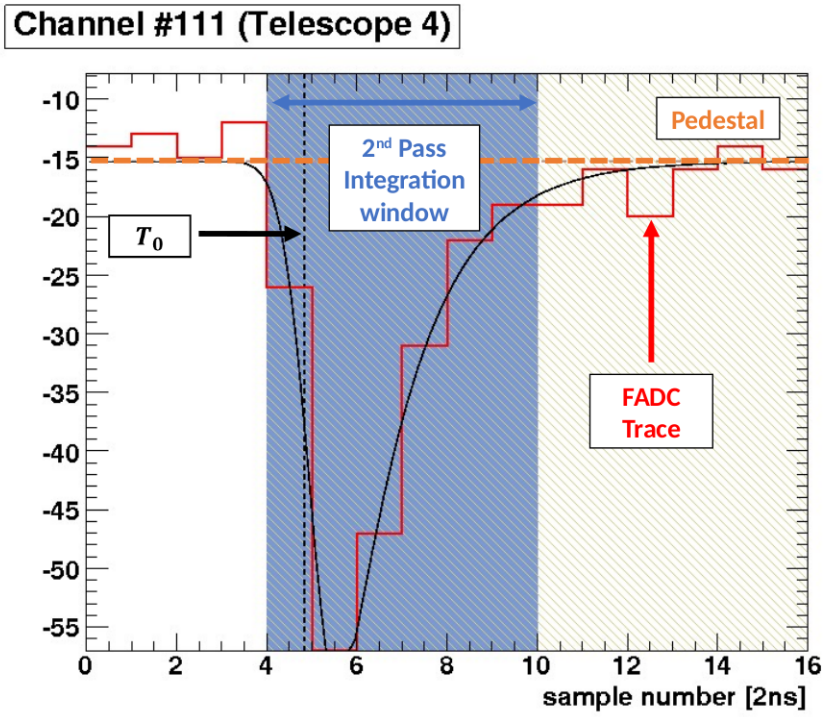

Figure 4.1: A PMT signal as measured by a FADC for a typical event. The red line shows the FADC trace measured by the FADC in units of digital counts (dc). The dashed black line shows T_0. The dashed orange line shows the pedestal level. The shaded blue region shows the integration window over which the integrated charge is calculated.

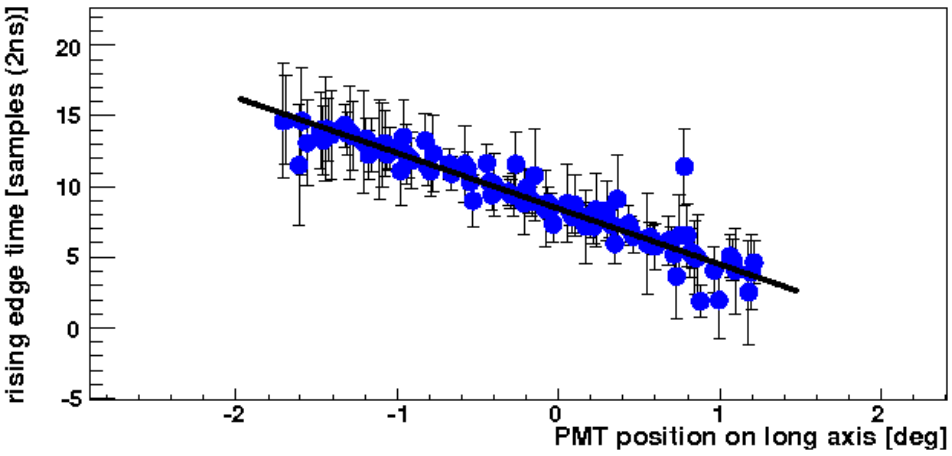

Figure 4.2: Linear fit applied to the arrival time as a function of position along the image axis for the shower shown in Figure 4.3.

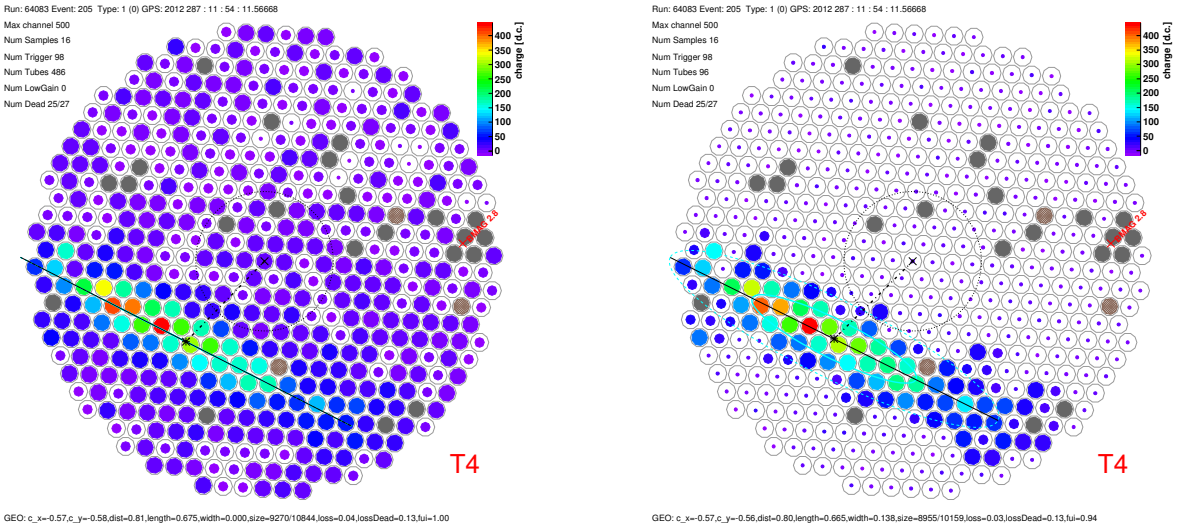

Figure 4.3: Image of a bright shower recorded by VERITAS before (left panel) and after (right panel) picture-boundary threshold are applied. Pixels shown as filled gray circles are pixels which have been flagged as bad pixels. These include a grouping of pixels on the right side of both images which have been suppressed due to the presence of a bright star (located at the red cross). The black line denotes the image axis.

4.2.3 Image Cleaning

To clean images, VERITAS uses an island cleaning method as described by Bond et al. (2003). This method searches for significant islands of signal, significant with respect to the pedvar value, within the camera image. The pedvar is an estimate of the variance of the mean pedestal value. This allows the signal recorded in a PMT to be quantified in terms of the pedvar. An island is defined as a "picture" pixel which is surrounded by "boundary" pixels. A picture pixel is defined as a pixel in which the integrated charge is 5 times its pedvar. A boundary pixel is defined as pixel in which the integrated charge is 2.5 times its pedvar and is adjacent to a picture pixel. Pixels failing to meet these thresholds as well as picture pixels which don't have any surrounding boundary pixels are removed. The remaining pixels are considered images of the Cherenkov showers from an EAS and are used to parameterize the shower (see Section 4.2.4). Figure 4.3 shows an image recorded by VERITAS of a particularly bright shower before and after image cleaning.

4.2.4 Image Parameterization

The image recorded after cleaning is interpreted as the 2-dimensional projection of the EAS. The shape of the image is generally ellipsoidal in the case of a gamma-ray induced shower. To parameterize the image a moment analysis developed by Hillas (1985) is used. The so-called

"Hillas" parameters are a set of parameters which provide powerful tools to discriminate between gamma-ray induced and cosmic ray induced EAS. A detailed summary of the Hillas parameters, and modifications to them which are still in use by modern IACTs, is given in Fegan (1997). The key parameters used in this analysis are shown in Figure 4.4 and are described below:

- **Centroid**: The coordinates of the centre of gravity of the image.
- **Width**: The root mean squared (RMS) spread of light along the minor axis of the ellipse. This is a measurement of the lateral development of the shower.
- **Length**: The RMS spread of light along the major axis of the ellipse. This is a measurement of the vertical development of the shower.
- **Size**: The total integrated charge of the image. This is a measurement of the brightness of the shower measured by the telescope. Also written as S.
- **Distance**: The distance between the centroid of the image and the centre of the FoV.
- **Loss**: The fraction of the Size parameter contained by pixels on the edge of the camera. This parameter allows for the rejection of showers which are truncated by the edge of the camera.

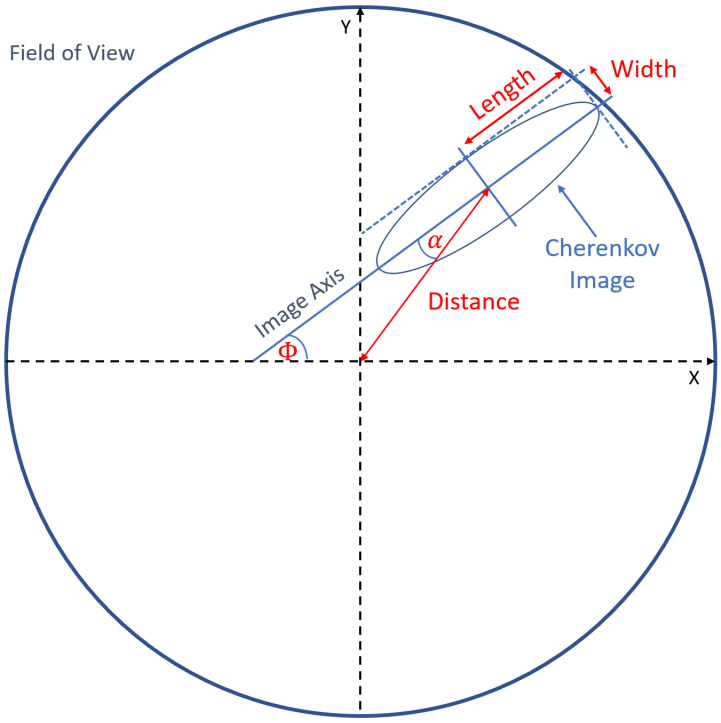

Figure 4.4: Hillas parameters used when characterising a Cherenkov image.

4.2.5 Stereoscopic Reconstruction

Cleaned and parameterized images from each telescope are combined on an event-by-event basis to allow for stereoscopic reconstruction of the shower. Stereoscopic reconstruction provides a significant improvement over single-telescope reconstruction by providing multiple images of the same shower as viewed from different angles. The first step of this process is applying cuts to the events based on the observed images. It is required that an image has a minimum number of picture/boundary pixels (`MINTUBES` >5), that the total integrated charge in an image meets a threshold (`MINSIZE` >100 dc) and that the shower isn't truncated due to its location on the camera (`MAXLOSS` <0.2). In addition to this, it is required that at least 2 telescopes have images which pass these thresholds (`nTels` >2).

Shower Origin and Core Location

As the shower will develop in the direction of the incident gamma ray, the origin of the shower in the sky plane lies along the major axis of the image. The origin of the shower can be determined by observing two images of the same shower and finding the intersection point of the shower axes observed by the images, overlaid in the sky plane of a single camera's FoV. ED uses algorithm 1 of Hofmann (1999) to determine the shower origin. In this method the shower origin is calculated as the mean origin obtained by each pair of telescopes, weighted

by the angle between the two images, the size of the images and the ratio of width to length of the images:

$$weight_{1,2} = \left(\frac{1}{Size_1} + \frac{1}{Size_2}\right)^{-1} \times \left(\frac{Width_1}{Length_1} + \frac{Width_2}{Length_2}\right)^{-1} \times \sin(\theta_{1,2}), \tag{4.1}$$

where $\theta_{1,2}$ is the angle between the image axes of the images.

Similarly the location at which the shower would have impacted the ground can be obtained by finding the intersection of the shower images in the "ground" plane. This gives the location of the shower core in the ground plane from which the so-called *impact parameter* (R) can be calculated. The impact parameter is a measurement of the perpendicular distance between the shower core and the telescope. As a shower will appear dimmer for a larger impact parameter, a larger impact parameter will affect the error on the reconstruction process. Hence a cut on the impact parameter is applied to the data.

Emission Height

The emission height (H_{emis}) of the shower can be estimated using the centroid of the images, the impact parameter and the source location (see Aharonian et al., 1997). H_{emis} is estimated as the average emission height obtained by each pairwise combination of images, weighted by the image size. The χ^2-value is also obtained and can be used to reject poorly reconstructed showers. As hadron induced showers are generally produced deeper into the atmosphere, H_{emis} can be used to as an effective parameter for rejecting cosmic ray induced showers.

Energy Estimation

The energy of the incident gamma ray can be estimated by comparing the brightness of the shower, which is measured by the total integrated charge in an image (S), to the impact parameter (R). This method utilizes the fact that the brightness of the shower depends on the distance to the shower and the energy of the incident gamma ray, or simply put a shower will appear brighter when more energetic or closer to the observer. To estimate the energy of the gamma ray, lookup tables —which estimate the energy as a function of R and S—are used. These lookup tables are filled by analyzing Monte Carlo simulations of gamma-ray events for different combinations of NSB, zenith angle and wobble offsets. In addition to storing the median energy estimate (E) of the simulated showers, the 90% width of the energy distribution (σ_E) is also recorded. The median energy and the 90% distribution width are used to reduce the effect of outliers on the energy estimation. Examples of these lookup tables are shown in Figure 4.5. The weighted mean shower energy is determined by taking the mean E estimated by each telescope, weighted by the square of σ_E:

$$E = \frac{\sum_i^N \frac{E_i}{\sigma_{E,i}^2}}{\sum_i^N \frac{1}{\sigma_{E,i}^2}}, \tag{4.2}$$

where N is the number of reconstructed images.

A χ^2-value on the energy estimation can be calculated as:

$$\chi_E^2 = \frac{1}{N-1} \sum_{i=1}^{N} \left(\frac{E - E_i}{\sigma_{E,i}^2} \right). \tag{4.3}$$

Due to the irregular shape of hadron induced showers, χ_E^2 can be used to reject poorly reconstructed events.

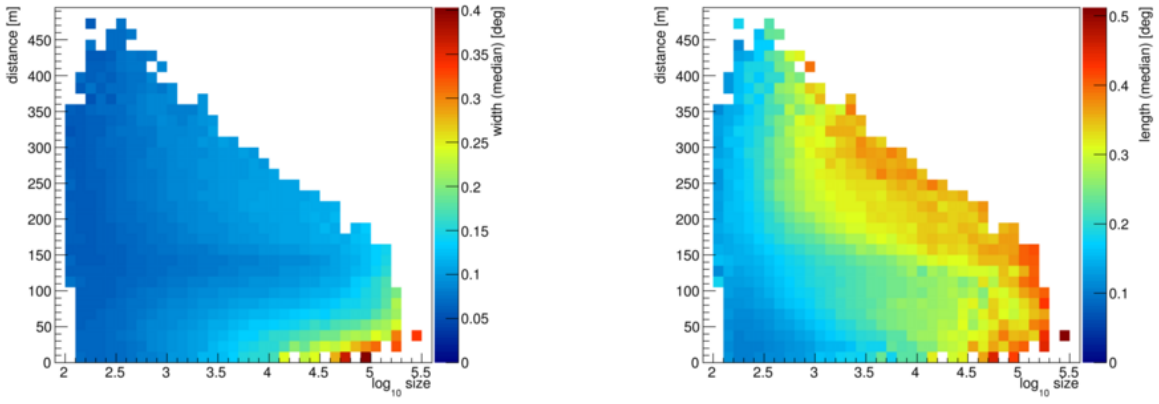

Figure 4.5: Example of the mean scaled width (left) and length (right). The x-axis shows the size of the shower plotted in log space, y-axis shows the distance to the shower. The color map corresponds to the median value of the mean scaled width/length. Image credit The VERITAS Collaboration.

4.2.6 Gamma/Hadron Separation

Shower Shape Parameters

After event reconstruction, the data is still be dominated by cosmic ray events. To attempt to separate the gamma-ray events from the cosmic ray events, cuts are applied to the shape of the showers. The shower shape parameters, mean scaled width/length (MSCW/L) (Krawczynski et al., 2006), exploit the advantage of imaging the shower from multiple angles. Whereas a cosmic ray shower may appear gamma-ray-like when viewed from one angle, it may appear more cosmic-ray-like when viewed from another. This fact is reflected

in calculating the mean scaled parameters, defined as:

$$MSCW = \frac{1}{N}\sum_{i=1}^{N}\left(\frac{width_i - w(R,S)}{\sigma_w(R,S)}\right) \tag{4.4}$$

and

$$MSCL = \frac{1}{N}\sum_{i=1}^{N}\left(\frac{length_i - l(R,S)}{\sigma_l(R,S)}\right), \tag{4.5}$$

where $w/l(R,S)$ and $\sigma_{w/l}(R,S)$) are the median width/length and 90% width of the width/length distributions derived from Monte Carlo simulations of gamma-ray showers. These values are obtained from lookup tables which are filled in a similar manner to the energy lookup tables. Figure 4.6 shows an example of MSCW/L distributions. For gamma-ray events, one would expect these distributions to be centred on 0, however cosmic ray events, which may appear more diffuse, occasionally show clumpier showers (see Section 1.3.2), and will therefore have larger MSCW/MSCL values. The is evident in Figure 4.6, where the "On" distribution is characterized by a peak at 0 due to gamma-ray events and a tail extending to higher values due to the cosmic ray background events.

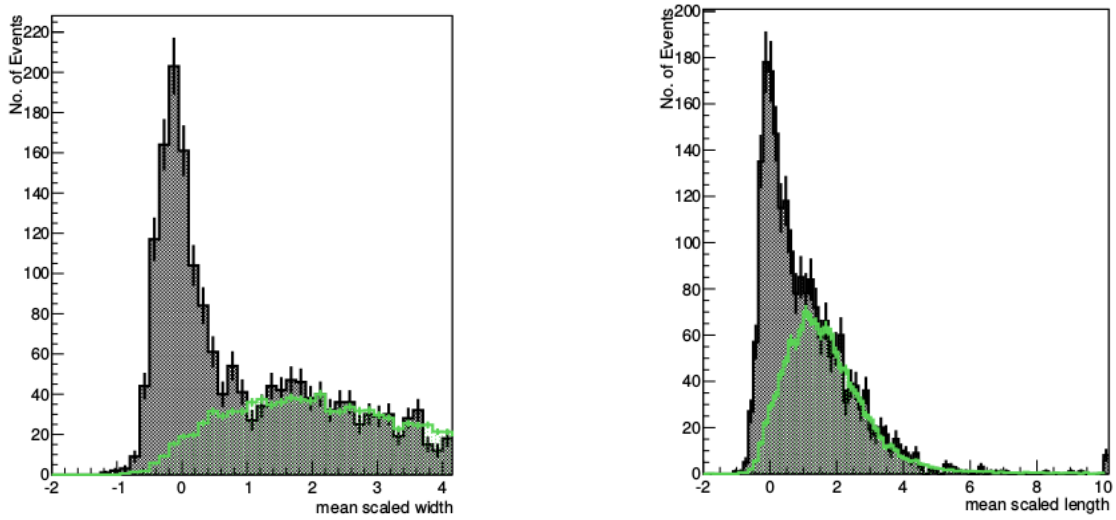

Figure 4.6: Example of the mean scaled width (left) and length (right) distributions. The gray shaded region corresponds to events from the On region, while the shaded green region corresponds to events from the Off region.

Gamma-Hadron Cuts

A set of cuts based on the parameters previously defined are used to differentiate between gamma-ray and cosmic ray events. These cuts are optimised to improve the significance

of the source signal (see Section 4.2.7). The optimization process is done a priori, on a separate dataset and verified on previously published datasets to ensure consistency. Different flavors of cuts have been optimised for different source types. These cuts are defined as "Soft", "Moderate" and "Hard". The Soft, Moderate and Hard definitions refer to the spectral hardness of the source they've been optimised for. For example, Soft cuts are optimised for sources with a soft spectral (power-law index $\Gamma > 3.5$), whereas Hard cuts are optimised for hard spectrum sources ($\Gamma < 2.0$). Soft cuts have a lower energy threshold and 'looser' cuts designed to allow more gamma-ray events which appear cosmic-ray-like. This increases the signal at lower energies at the cost of also increasing the background.

Two types of cuts are used in the VERITAS analysis chain. "Box" cuts apply strict cuts on a number of parameters, essentially drawing a box in the parameter space. Typical MSCW/MSCL cuts used for Moderate cuts would be $-1.2 < MSCW < 0.5$ and $-1.2 < MSCL < 0.7$. Boosted decision tree (BDT) based cuts (Krause et al., 2017) attempt to classify an event as either a gamma ray or a cosmic ray using a series of decision trees. The BDTs are trained using gamma-ray simulations and FoVs which have no known gamma-ray emitters as background and are validated using real data. The "boosted" aspect of BDTs refers to an iterative process in which the misclassified events are reweighted during each iteration of the optimization process. BDTs make use of the wider parameter space of the shower properties to attempt to pick out cosmic-ray-like gamma-ray events. BDTs provide improved performance over standard box cuts (Krause et al., 2017) and are the type of cuts used in this thesis.

4.2.7 Signal Extraction

After Gamma-Hadron cuts are applied to the dataset, there will still be cosmic ray events present. This is due to the presence of cosmic ray electrons and gamma-ray-like hadronic showers. To subtract away the remaining background events, the isotropic nature (on the scale of the telescope FoV) of the cosmic ray flux is exploited. This is done by defining two regions, an "On" region and an "Off" region. The number of excess events can be calculated as:

$$N_{excess} = N_{On} - \alpha N_{Off}, \tag{4.6}$$

where N_{On} and N_{Off} are the number of events in the On and Off regions respectively and α is the normalization between the On and Off exposures. In general, α is a function of the On and Off exposure time, the energy of the event and the location in the FoV. If the On and Off regions are chosen from locations in FoV with different responses, it is important to take into account the radial response of the camera, that is the relative change in acceptance to gamma-

ray-like events as a function of radial distance from the camera centre. Radial acceptances can be generated by analyzing observations from presumed gamma-ray-dark fields. In this analysis, a reflected region estimation (see below) method is used. This ensures that the On and Off regions are taken from regions with similar radial response, removing the need for a radial acceptance correction to be applied.

Different methods used to estimate the background contributions are discussed in Berge et al. (2006) and are summarized below.

On-Off Background Estimation

For On-Off background estimation, an On-source observation is taken, followed by an Off-source observation. The Off-region is typically an observation taken under similar observation conditions (e.g. similar zenith angle, azimuth angle and NSB level). Using this method offers accurate background estimation, in particular for sources with a complex FoV such as extended sources or the Galactic Centre. This method relies heavily on separate observations and therefore requires a significant amount of time.

Ring Background Estimation

In this method the array may either be pointing directly at the region of interest (On source) or at a location offset from the region of interest by a small angle (wobble angle, typically 0.5°). The ring background method defines the On region, for point-like sources, as a circular region of radius comparable to the instrument PSF and the Off regions as a annulus in which the inner radius is chosen so as to not overlap with the inner on region, as shown in left panel of Figure 4.7. The Off region used excludes known gamma-ray emitters, with bright stars also being excluded. The large Off region selected allows for a firm estimate of the background and reduces the effect of statistical fluctuations. When calculating α one needs to consider the radial acceptance of the camera and its energy dependence. The energy dependence of the radial acceptance is difficult to study as one would need a source of gamma rays with known energy spectrum and spatial profile. In practice this isn't feasible, and the radial acceptance is calculated assuming no energy dependence. This increases the systematic uncertainty in any energy related measurement such as the energy spectrum or a flux measurement.

Reflected Region Background Estimation

In this method wobble observations are taken (typically with a wobble angle of 0.5° from the source of interest). This pointing configuration allows for the simultaneous observations of the source and estimation of the background. In this method On and Off regions are defined as circular regions with radii comparable to the instrument PSF. Off-regions are selected as regions in the FoV which are located at the same distance from the centre of the FoV as the source, are free of any known gamma-ray emitter and are free of any bright stars. An

example of the region selection is shown in the right panel of Figure 4.7. As the On and Off regions are at the same distance from the centre of the FoV, the camera acceptances are equal and hence $\alpha = 1/N_{regions}$. The lack of energy dependence in α makes this method preferable for spectral analysis. As this method relies on the offset from the centre to define background regions, it is not suitable for analysis of sources close to the pointing direction. Complex fields of view such as those with a large number of bright stars or other gamma-ray sources may reduce the number of background regions available for analysis. In this thesis all presented sources are the only known gamma-ray source in their FoV and a sufficient number of background regions ($N_{regions} \geq 6$) remain after removing regions with bright stars. Reflected region background estimation is used in this analysis.

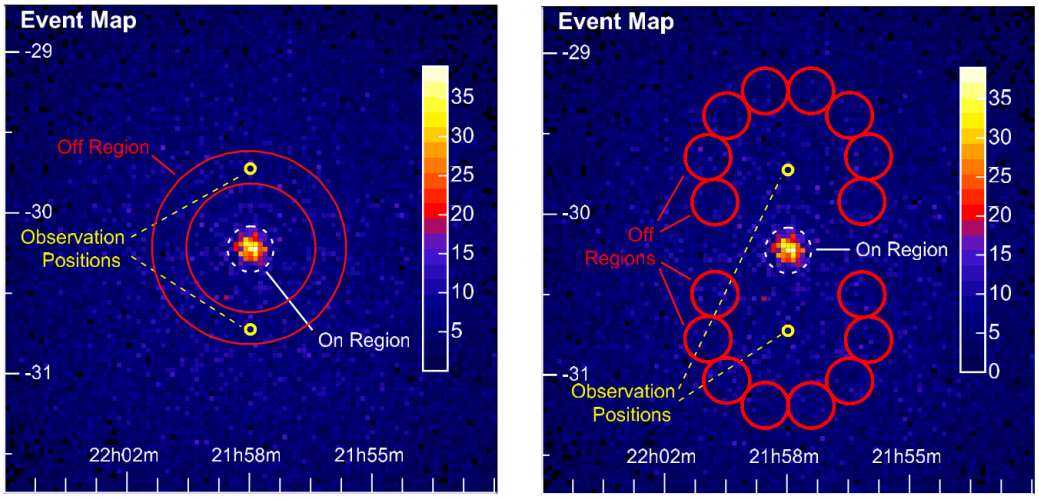

Figure 4.7: Ring (left) and reflected-region (right) background estimation models, taken from Berge et al. (2006). In this example observations are taken in wobble mode to allow for simultaneous estimation of the background.

Significance Calculation

The statistical significance of the excess can be calculated using the generalized Equation 17 of Li & Ma (1983) which is given by (Aharonian et al., 2004):

$$S = \sqrt{2}\left[\sum_i N_{On,i} \log\left(\frac{\sum_i N_{On,i}}{\sum_i \frac{\alpha_i}{1+\alpha_i}\left(N_{On,i}+N_{Off,i}\right)}\right) + \sum_i N_{Off,i} \log\left(\frac{\sum_i N_{Off,i}}{\sum_i \frac{1}{1+\alpha_i}\left(N_{On,i}+N_{Off,i}\right)}\right)\right]^{1/2}, \tag{4.7}$$

where the summation over i results from the different observing conditions of the data were taken under. It is common to define the required threshold for claiming the detection of a new gamma-ray source to be 5 standard deviations above the background (or 5σ). When claiming

a detection, the VERITAS Collaboration requires the detection of a new source to be verified using two independent analyses (i.e. using both ED and VEGAS). In this thesis a source is required to have a post-trials significance of 5σ for it to be considered a gamma-ray emitter.

4.2.8 Advanced Analysis

Sky Maps

A sky map can be obtained by converting the camera coordinates into sky coordinates. The significance sky map (see Figure 4.8) is calculated by correlating the significance at each location of the sky map. The correlated significance is obtained correlating the yet uncorrelated On and Off gamma-ray-like event sky maps, assuming a Gaussian PSF. This takes into account correlation between adjacent points due to the PSF. These correlated events maps are used to obtain the correlated excess and significance maps using Equations 4.6 and 4.7, respectively. The significance distribution, as shown in the right panel of Figure 4.8 is the distribution of the significances for all points of the sky map. For a field with no gamma-ray emitter, one would expect this distribution to be Gaussian distributed with a mean of 0 and RMS of 1. This provides a useful tool for testing for additional sources, or "holes" within the FoV or regions which should be excluded (for example due to a bright star in the case of a hole).

Effective Areas

So far we have dealt purely with counts. To calculate astrophysical properties such as energy spectra and flux measurements the effective area needs to be accounted for. The effective area is the area over which incident gamma rays will be recorded by the detector. The effective area is determined by the Cherenkov angle, the air shower development and the geometry of the detector (see Section 1.3). VERITAS calculates its effective areas by analyzing Monte Carlo simulations of gamma-ray events which are reconstructed using the VERITAS analysis chain. This results in the effective areas being a function of the array geometry, the energy of the incident gamma-ray and the analysis reconstruction efficiency. Effective areas are generated for all array configurations (all observational epochs, all 3-telescope configurations and SHV/RHV high voltage configurations) and for a wide range of observation parameters (NSB, zenith angle, Winter/Summer atmospheres, etc). In general VERITAS effective areas are calculated as:

$$A_{eff}(E,\Gamma) = A_0 C(E,\Gamma)\left(\frac{N_{\gamma,rec}(E)}{N_{\gamma,sim}(E)}\right), \tag{4.8}$$

where $A_0 = \pi R^2$ is an area of radius R centred on the detector over which simulated

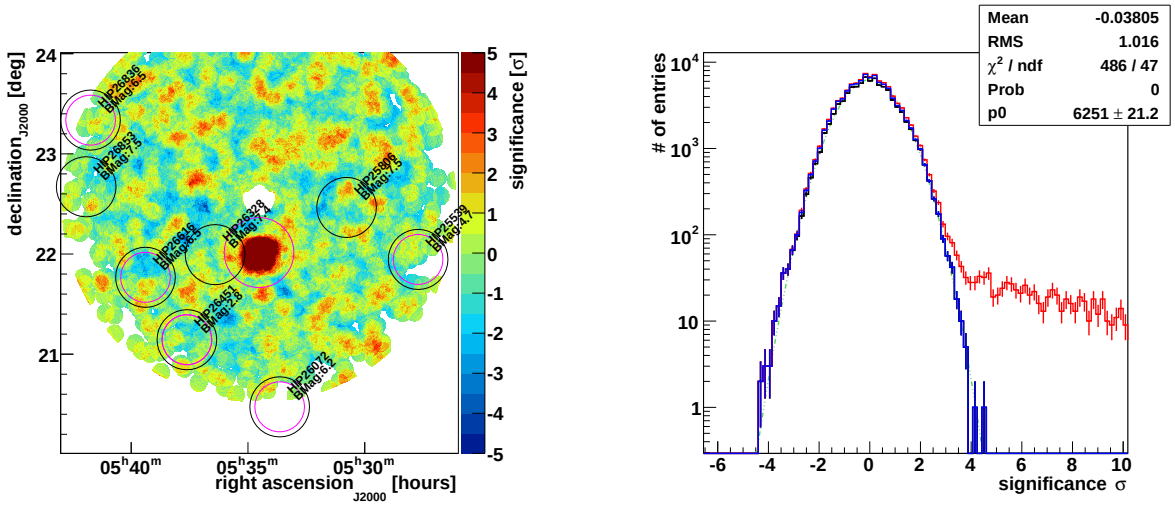

Figure 4.8: The left panel shows the significance sky map obtained from one 20 minute observation of the Crab Nebula. The Crab is clearly visible as the highly significant point at the centre of the sky map. The black circles denote the locations of bright stars within the FoV while the pink circles denote regions excluded from the background analysis. The right panel shows the significance distribution obtained from the sky map on the right panel. The red line shows the significance distribution of the entire sky map, the blue line shows the significance distribution with the source region excluded and the black line, which lies underneath the blue line, shows the significance distribution with the source and any other excluded regions removed. The green dashed line shows a Gaussian with mean of 0 and RMS of 1.

gamma-ray showers are "thrown", $N_{\gamma,sim}(E)$ is the number of simulated gamma rays, $N_{\gamma,rec}(E)$ is the number of reconstructed gamma rays and $C(E,\Gamma)$ is a correction applied due to the finite energy resolution of the instrument, the binning process and the effect of the spectral index on the binning process and Γ is the spectral index of the source. $C(E,\Gamma)$ is determined as:

$$C_i(E,\Gamma) = \frac{N_{\gamma,MC,i}(E)}{N_{\gamma,rec,i}(E,\Gamma)}, \tag{4.9}$$

where i refers to the i-th energy bin, $N_{\gamma,MC,i}(E)$ is the number of events in the Monte Carlo (true) energy scale and $N_{\gamma,rec,i}(E,\Gamma)$ is the number of events in the reconstructed energy scale. The Γ dependency is due to the effect of the spectral shape on the centre of mass of the energy bin. Forward folding methods can be implemented to account for the effect of spectral model on the energy reconstruction process and will be discussed in Chapter A.

Figure 4.9 shows an example of an effective area plot. The low energy threshold of VERITAS analysis is evident from Figure 4.9 and arises due to the lack of statistics at lower

[1] https://veritas.sao.arizona.edu/about-veritas-mainmenu-81/veritas-specifications-mainmenu-111

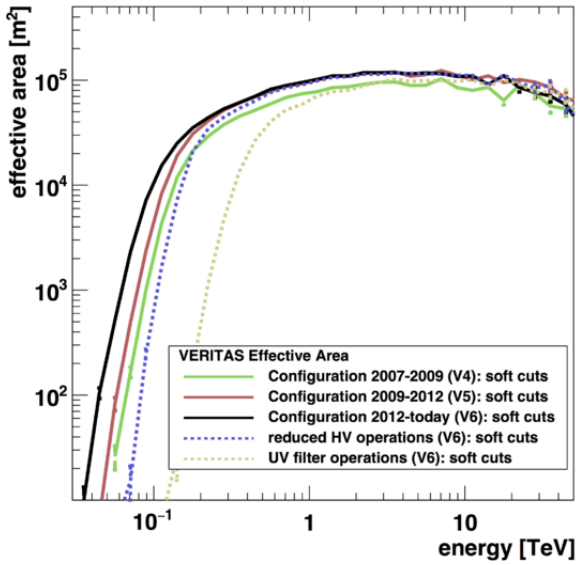

Figure 4.9: Comparison of the VERITAS effective areas for different observation epochs and observing conditions. Image credit The VERITAS Collaboration.[1]

energies as the dimmer simulated showers are poorly reconstructed. At higher energies the error on the effective areas becomes large, this is largely due to poorer statistics for high-energy showers (simulated gamma-ray showers are generated from a power law distribution of $\Gamma = 2$) and high-energy reconstruction issues such as camera saturation. Figure 4.9 also shows the effect of different high voltage configurations. The energy threshold is higher for RHV observations, this is due to lower energy showers having a brightness comparable to the NSB variations and are therefore not distinguishable from the NSB. At higher energies ($E > 250$ GeV) the effective areas for SHV and RHV observations are comparable and are on the order of 10^5 m for a 1 TeV photon.

Spectral Analysis

By accounting for the effective areas, the energy spectrum can be obtained as:

$$\frac{dN}{dE}(E) = \frac{N_{excess}(E)}{\tau A_{eff}(E,\Gamma) dE} \text{ cm}^{-2} \text{ s}^{-1} \text{ TeV}^{-1}, \tag{4.10}$$

where τ is the deadtime corrected exposure and dN/dE (E) is generally described by a power law model:

$$\frac{dN}{dE}(E) = N_0 \left(\frac{E}{E_0}\right)^{-\Gamma}, \tag{4.11}$$

where N_0 is the normalization at the normalization energy E_0. Standard analysis requires one to perform an iterative fitting procedure during which the input Γ used in the effective area calculation is modified until the best-fit reconstructed energy spectrum matches the input Γ.

A likelihood based forward folding spectral fitting method will be discussed in Chapter A.

Flux Determination

The integral gamma-ray flux above a given threshold E_{thresh}, can be determined as:

$$\phi(E > E_{thresh}) = \frac{N_{excess}(E > E_{thresh})}{N_{theory}(E > E_{thresh})} \int_{E_{thresh}}^{\infty} \frac{dN}{dE}(E)dE, \tag{4.12}$$

where

$$N_{theory}(E > E_{thresh}) = \tau \int_{E_{thresh}}^{\infty} \frac{dN}{dE}(E)A_{eff}(E, \Gamma)dE. \tag{4.13}$$

Therefore, the integral flux calculation is heavily dependent on the assumed spectral model. In this thesis a light curve shall be defined as the integral flux obtained in a series of temporal bins. For VERITAS these are obtained by applying the methods discussed above to temporally binned observations.

Upper Limits

Unless otherwise stated, upper limits on the integral flux are calculated using the method described by Rolke et al. (2005). In this method the upper limit is obtained assuming a set of On and Off data, giving an upper limit on the excess counts. This upper limit can be used in Equations 4.10 and 4.13 to obtain upper limits on the differential and integral flux.

4.3 Fermi-LAT

4.3.1 *Fermi*-LAT Analysis

In this section the *Fermi*-LAT analysis chain will be discussed. For the analysis presented in this thesis the `fermipy` (Wood et al., 2017) analysis suite is used. This analysis suite simplifies *Fermi*-LAT analysis by providing user-level tools to automate many functions of the `Science Tools`[2] software package and by simplifying the analysis chain where suitable. In this analysis `Science Tools` v10r0p5 and `fermipy` v0.14.1 are used. In this section the general steps needed to reduce *Fermi*-LAT data and extract results using a binned-likelihood analysis, will be discussed. A detailed discussion on the *Fermi*-LAT data analysis pipeline can be found in the online Cicerone documentation.[3] The general steps involved in performing *Fermi*-LAT analysis are as follows:

1. Generate source model.

2. Apply data quality cuts and perform event selection.

[2] https://fermi.gsfc.nasa.gov/ssc/
[3] https://fermi.gsfc.nasa.gov/ssc/data/analysis/documentation/Cicerone/

3. Obtain good time intervals.
4. Obtain counts cube.
5. Obtain live time cubes.
6. Obtain exposure cubes.
7. Obtain source maps.
8. Perfmore likelihood fit

In the above "cubes" refer the the 3 dimensional nature of the data (space, time and energy).

Data Quality Cuts

The standard data-quality cuts are applied in the analysis presented in this thesis. When filtering data using `gtselect` the event class (`evclass`) 128 is chosen and the corresponding instrument response functions (IRFs), `P8R2_SOURCE_V6`, is used. The event class refers to the probability of the registered event being a photon. This event class is the recommended event class for point source analysis. The event type (`evtype`) used in this analysis is 3. This refers to how the photon is measured, i.e. whether the photon converted in the front or back of the LAT. `evtype` 3 refers to both front-converting and back-converting events. A cut on the zenith angle (`zmax`) of 90 degrees is applied. This reduces background contamination due to events which originate in Earth's limb. Good time intervals (GTIs) are selecting by `gtmktime` using the filter `(DATA_QUAL>0)&&(LAT_CONFIG==1)`. `(DATA_QUAL>0)` excludes times in which the quality of the data taken has been affected (for example instrument/spacecraft failure). `(LAT_CONFIG==1)` refers to times in which the telescope is in data taking mode.

Analysis Description

A basic overview of the analysis steps is given in this section:

Counts Cubes

Once data quality cuts have been applied to the data, the data is then binned in energy into a counts cube file. A counts cube file contains information of the events passing quality cuts, binned in both space and in energy.

Live-Time File

The live-time file contains a list of the GTIs passing the time quality cuts.

Exposure Cube

The exposure cube file combines information on the pointing of the spacecraft with knowledge of the instrument response functions to determine the energy dependent exposure across the field of view.

Source Model

A model of the FoV is required for *Fermi*-LAT analysis. In this analysis the model includes all known 3FGL sources with 15 degrees of the source of interest, a model of the isotropic diffuse gamma-ray emission (`iso_P8R2_SOURCE_V6_v06.txt`) and a model of the Galactic diffuse gamma-ray emission (`gll_iem_v06.fits`). The 3FGL spectral and spatial parameters of all known sources are used when constructing a source model.

Source Map

A source map file is obtained. This is a map of the expected counts within the FoV. The source maps are obtained by taking the individual source models defined in the source models and obtaining a predicted number of counts, correcting for exposure time and IRFs. The source map is used in the likelihood analysis stage and may be adjusted during the likelihood optimization.

Likelihood Analysis

Model Optimization

Fermi-LAT analysis applies a binned-likelihood analysis. This is done by comparing the observed counts to the counts predicted by the source model. The log-likelihood equation is given as:

$$\log \mathcal{L}(S) = \sum_i N_i \log \lambda_i(S) - N_{pred}(S), \tag{4.14}$$

where $S = S(E_i, p_i)$ is the source model, and is a function of energy (E) and position (p) in the FoV, N_i is the observed counts in the i-th energy-spatial bin, $\lambda_i(S)$ is the expected number of counts in the i-th bin given the model and $N_{pred}(S)$ is the total number of predicted counts given the model. $\lambda_i(S)$ is the Poissonian mean of the distribution which describes N_i and is obtained by folding the model S with the IRFs.

The test statistic (TS) is calculated using a likelihood ratio test, between the optimized model ($\mathcal{L}_{max}$) and a model excluding the source ($\mathcal{L}_0$) :

$$TS = -2 \log \left(\frac{\mathcal{L}_0}{\mathcal{L}_{max}} \right). \tag{4.15}$$

Note Wilks theorem (Wilks, 1938) suggest that the likelihood ratio is $\sim \chi^2$ distributed, with the degree of freedom given by the difference in dimensionality of $\mathcal{L}_0$ and $\mathcal{L}_{max}$. The TS is a

measure of the source significance such that $\sqrt{TS} \cong \sigma$.

During the optimization stage, sources greater than 2° from the location of interest have their model parameters frozen to their 3FGL values. Sources within 2° of the location of interest are allowed to vary[4] and the isotropic and Galactic diffuse components' normalizations are allowed to vary. Sources with a high TS or a high variability index (TS_{var}) may be allowed to vary. This is done on a source-by-source basis upon evaluating the optimized likelihood fit. To evaluate the fit, one can look at the residual and TS maps. The residual map is a map of the counts map minus the best-fit model. The TS maps is obtained by artificially inserting a point source at each location of in the FoV and calculating the TS for an unaccounted for source.

Spectral Flux Points

The optimized model returns the best fit energy spectrum and the covariance matrix. Using these a confidence interval on the fit can be obtained. Spectral flux points can be obtained by freezing the model's spectral shape parameters and reapplying the fit over the desired energy bin to obtain the flux normalization. This produces model dependent spectral points.

Integral Flux Points

The integral flux is obtained by applying a spectral fit over the desired energy range and integrating the model. In order to obtain a light curve, time cuts corresponding to the temporal intervals of interest are applied during the data selection stage, generating live-time, exposure and source maps corresponding to these time cuts. A fit is then applied to the time-cut-adjusted data from which the integral flux can be determined. This must be done for each time bin. Note: `fermipy` simplifies this process by calculating the source maps as the total source map weighted by the relative exposure. This simplification breaks down for particularly short time bins and observations with peculiar observing conditions (e.g. pointed observations).

In this thesis *Fermi*-LAT analysis performed for OJ 287 (see Chapter 7 to obtain the time-averaged SEDs and to obtain light curves. In Chapter 6 *Fermi*-LAT analysis will be performed on candidate VHE blazars in order to obtain the time-averaged SED and integral flux. These shall be used extrapolate the high-energy flux into the VHE regime.

[4]Typically only the normalization is allowed to vary. However the spectral shape parameters (for example, spectral index) may be allowed to vary if the model fails to obtain an adequate fit.

4.4 Swift-XRT

4.4.1 *Swift*-XRT Analysis

In this section the *Swift*-XRT analysis chain will be discussed. In this thesis data taken by the *Swift*-XRT was processed and cleaned using the `xrtpipeline` v0.13.4 which is provided as part of the `HEAsoft` software package v6.22.1. Spectral fitting was performed using the `PyXSpec` which is the python implementation of `XSpec` v12.9.1p. The `xrtpipeline` is the standard analysis pipeline written and developed by the *Swift* collaboration. Full details of the `xrtpipeline` can be found in Capalbi et al. (2005). Only general topics of the analysis will be discussed in the following sections.

Data Quality Selection

Several data quality cuts are applied to the raw data. These quality cuts are summarized in Table 4.1. The data obtained by *Swift*-XRT is processed by the `xrtpipeline`. This pipeline cleans the data, selecting events which meet the user defined criteria (for example event grade). The pipeline also calibrates the images and, using the telemetry data, obtains GTIs for analysis. The output products of the pipeline relevant to this analysis include the cleaned events files from which higher-level analysis products can be obtained and the exposure images.

Cut Name	Value Used	Description
obsmode	pointing	Observing mode. This refers to data taken which pointing to the target, slewing to the target or while setting after slewing.
exprpcgrade	0-12	Event grades used for photon counting observations.
exprwtgrade	0-2	Event grades used for window timing observations.
SUN_ANGLE	$\geq$ 45 degrees	The angle between the centre of the Sun and the pointing direction.
MOON_ANGLE	$\geq$ 30 degrees	The angle between the centre of the Moon and the pointing direction.
ANG_DIST	$\geq$ 0.08 degrees	The angle between the source of interest and the pointing direction.
ELV	$\geq$ 45 degrees	The angle between the Earth's limb and the pointing direction.
BR_EARTH	$\geq$ 120 degrees	The angle between day-night twilight line and the pointing direction.

Table 4.1: Summary of data quality cuts applied by `xrtpipeline`.

Extracting Results

Source-Background Estimation

To estimate the source and background contributions, an On and an Off region are defined. The On region is a circular region of radius 20 pixels ($\sim$ 47 arcseconds) located at the source location. This 20-pixel radius corresponds to the 90% containment of the PSF for a 1.5 keV photon. For both PC and WT analysis an annular region is selected centred on the source location. For PC mode the outer and inner radii of the region are selected to have equal areas to the On region. For WT mode the outer and inner radii of the region are set to 120 and 80 pixels respectively. This ensures that there is always at least 40 pixels within the off region. On and Off counts spectra are then obtained from these regions using `xselect`.

Exposure Correction

Exposure maps are needed to correct the observed image for the relative exposure differences across the field of view (vignetting effects) and to account for disabled channels in the CCD image. Ancillary Response Files (ARFs) also need to be generated for each observation. The ARF contains the instrument response matrix which has been corrected for vignetting corrections and PSF corrections potentially due to "missing" data (for example, due to faulty channels or data excluded due to a pile-up correction). ARFs are generated for the spectral analysis of each observations using the `xrtmkarf` command. The most recent response matrix files (RMF) were used (`swxwt0to2s6_20131212v015.rmf`).

Pile-Up

For PC mode, and to a lesser extent WT mode, observations, photon pile-up can occur when two or more photons arrive at the same CCD location, within a signal readout window. This affects the charge distribution measured around that pixel within the integration window. This has two effects on the data. Firstly, the number of detected counts is reduced due to the overlapping events being measured as one. This has the effect of reducing the observed flux. Secondly the event registered has a larger charge due to the overlapping or two or more events. This results a single event having a higher estimated energy and missing the detection of the lower energy events, hence artificially hardening the energy spectrum.

In order to correct for pile-up, knowledge of the point spread function (PSF) is needed. The *Swift*-XRT PSF has been measured by Moretti et al. (2005) after launch, using two relatively low-flux sources so that pile-up effects are negligible. Moretti et al. (2005) found that the PSF is best modeled by a King function of form:

$$PSF(r) = N\left(1 + \left(\frac{r}{r_c}\right)^{-\beta}\right), \tag{4.16}$$

where r_c is referred to as the core radius, β is referred to as the slope and N is a normalization factor. For data unaffected by pile-up one would expect its PSF to be well fitted by a King function with $r_c = 5.8$ and $\beta = 1.55$. As pile-up will affect the inner most pixels, we can estimate the effect of pile-up by fitting a King function to the outer regions of the PSF with parameters r_C and β frozen. The best-fit model can then be extrapolated to smaller radii to find where the data and model diverge. Figure 4.10 shows the PSF of an observation of TeV blazar H 1426+428. The best-fit PSF model (shown in black) is obtained by fitting Equation 4.16 to the observed counts (red points) between 15 and 50 arcseconds using the *ximage* package. For this fit, it is evident that the model and the data begin to diverge at around 5-6 arcseconds. To correct for pile-up, one simply excludes the affected regions of the image (in the above case the inner most 6 arcseconds of the source) from the analysis and, using the *xrtmkarf* package, generates a new ancillary response file (ARF) with this exclusion region taken into account. The generated ARF will correct for the lost counts due to the excluded region.[5]

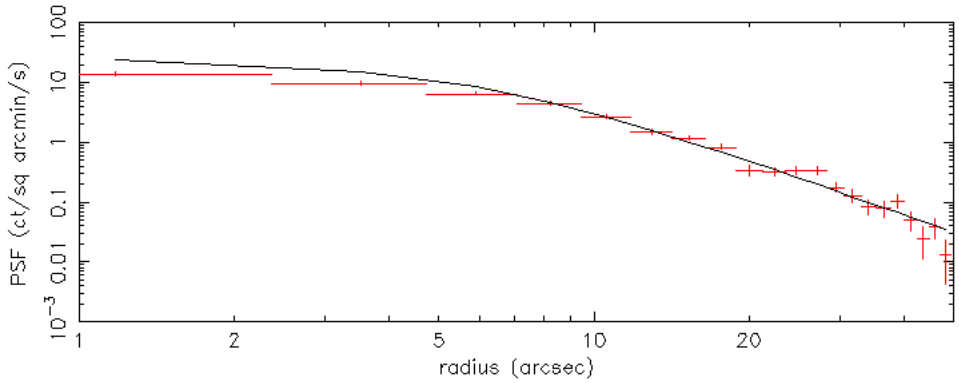

Figure 4.10: Point Spread Function (PSF) of TeV blazar H 1426+428 as measured by *Swift*-XRT (observation ID: sw00030375016, observation count rate: 0.82 cts/s). The red points show the measured counts rates per squared arcminute per second, the black line is the best-fit King function (obtained using the *ximage* package).

Spectral Analysis

The source spectrum can be obtained by a simple On-Off subtraction, correcting for any differences in the relative exposures. The On and Off photon files are grouped together along

[5] See http://www.swift.ac.uk/analysis/xrt/pileup.php for a tutorial on pile-up correction.

with the ARF and RMF files using the `grppha`. During this stage bad energy channels[6] are removed and the data is binned such that each energy bin has at least 20 counts. This ensures the validity of the χ^2-fit applied by `PyXSpec` (for reasons discussed in Section 5.2). The source model fitted by `PyXSpec` is an absorbed model such that:

$$\frac{d\phi}{dE} = \left(\frac{d\phi}{dE}\right)_{intrinsic} e^{-n_H \sigma(E)}, \tag{4.17}$$

where $\left(\frac{d\phi}{dE}\right)_{intrinsic}$ is the intrinsic source spectrum, n_H is the hydrogen column density in the direction of the source and $\sigma(E)$ is the photo-electric cross section. In this analysis n_H is taken as the weighted mean obtained by the LAB survey (Kalberla et al., 2005).

Integral Flux Analysis

In this thesis the integral flux is obtained on a run-wise basis. Hence the quoted integral flux is obtained by integrating Equation 4.17 over the energy range of interest. It is worth noting that as the sources analyzed in this thesis are extragalactic the effects of extinction due to local absorption by gas within the Galaxy is non-negligible. This is particularly the case for energies lower than $\sim$ 2 keV where any derived results will be dependent on the confidence of the estimate of n_H and hence will have a higher systematic uncertainty. It is therefore common practice to quote the x-ray flux in the 2 – 10 keV energy range. The `cflux` source model option may be used to obtain the reabsorbed integral flux at lower energy ranges and is the method used in this thesis.

4.5 Summary

In this chapter I have discussed the analysis methods used in this thesis. This allows for the analysis of multiwavelength data taken from X-ray to VHE wavelengths to be presented. In this thesis, the primary instrument used is VERITAS. In Section 4.2.1 details of the VERITAS analysis chain were discussed in detail. As was highlighted in Section 4.2.6, this thesis makes use of advanced gamma/hadron seperation techniques known as BDTs. All VERITAS analysis presented in this thesis was performed using these BDT gamma/hadron seperation cuts. As part of this thesis improvements to this analysis chain were made by the implementation of a Poisson binned-likelihood analysis, which is discussed in Chapter A.

[6] Channels outside of the safe analysis range.

Chapter 5

Implementation of a Binned-Likelihood Analysis Method

5.1 Overview

In counting experiments, such as VERITAS, it is common practice to bin one's spectral data into energy bins. This has the result of reducing the time required for analysis, by instead considering the bin-wise properties of the data. It is also common practice to apply a χ^2-minimization to binned data to obtain a best-fit model for the source. This method assumes that the errors in each bin are in fact described by Gaussian statistics. However, for counting experiments, the counts in each bin are described by Poisson statistics. For high-statistics bins (i.e. well sampled, >10 counts in each bin), the data can be assumed to be Gaussian as the Central Limit Theorem (see, for example, James, 2006, Chapter 3) suggests that a well sampled distribution tends to a Gaussian. In the case of low statistics, the Gaussian assumption no longer holds and the Poissonian nature of the bins needs to be considered. In practice this involves forward-folding a source model with the instrument response functions in order to obtain a model prediction for the mean number of counts observed by the instrument. This mean will be the mean of the Poisson distribution from which the observed counts are drawn. Using this, a binned-likelihood analysis can be performed to obtain the best-fit source model.

In this Chapter the implementation of a binned-likelihood analysis into the Event Display analysis software is discussed. In Section 5.2 the key principle of maximum likelihood analysis and its application to binned data, specifically data taken by a VERITAS-like instrument, is discussed. This method was developed by Piron et al. (2001) to analyze data taken by the CAT experiment. In Section 5.3 the implementation and application of the maximum likelihood method to VERITAS data are discussed. In Section 5.4 the performance of this analysis is measured. Section 5.5 looks at results obtained by this method, focusing on validation of the method on well-known sources and previous results. Finally in Section 5.6 further applications of this method are discussed.

5.2 Binned-Likelihood Analysis

In this section the key concepts of the binned-likelihood analysis implemented are discussed. In simple terms the analysis can be described using the following steps:

1. A model for the source emission is defined (for example a power law).
2. For each data run, the instrument response functions (effective areas and response matrix) are obtained.
3. For each data run, the On and Off counts, and the exposure normalization α are obtained.
4. The model predicted excess counts are obtained by forward folding the instrument response functions and the source model.
5. The maximum likelihood estimator (MLE) of the mean off counts is obtained assuming the model predicted excess counts obtained in the previous step.
6. The likelihood of the On and Off counts coming from distributions described by the means obtained in the previous two steps is obtained.
7. The maximum likelihood estimators of the model parameters are obtained by numerically maximizing the likelihood of the previous step with respect to the model parameters.

This is an iterative process in which steps 4-6 are repeated until the maximum likelihood estimators are obtained.

5.2.1 Maximum Likelihood Methods

The likelihood function is defined as:

$$\mathcal{L}(\theta|x) = \mathcal{P}(X = x|\theta), \tag{5.1}$$

where θ is the parameter of interest, x is a random variable with probability mass/density function $\mathcal{P}(X)$ which is parameterized by the parameter or set of parameters θ.[1] Here $\mathcal{P}(X = x|\theta)$ refers to the probability of observing x given the parameter θ. Likewise $\mathcal{L}(\theta|x)$ can be

[1] In this section vector of parameters/data shall be represented by **bold** values, for example $\boldsymbol{\Theta} = \{\theta_i\}$.

considered the likelihood of θ given the observed data x. The likelihood equation can be expanded to contain the joint likelihood of observing multiple events such that:

$$\mathcal{L}(\theta|\mathbf{x}) = \prod_{i}^{n} \mathcal{P}(X = x_i|\theta), \tag{5.2}$$

where $\mathbf{x}$ is the set of n observations $\{x_1, ..., x_n\}$.

The maximum likelihood estimator (MLE) is defined the value $\hat{\theta}$ which maximizes the likelihood equation:

$$\left.\frac{d\mathcal{L}(\theta|\mathbf{x})}{d\theta}\right|_{\hat{\theta}} = 0 \tag{5.3}$$

As a result $\hat{\theta}$ represents the best-fit value for θ given the observed data $\mathbf{x}$.

5.2.2 Application of Maximum Likelihood Methods to IACT Data

As discussed in Section 4.2.7 VERITAS defines On and Off regions from which counts are measured. Using Equation 4.6, the number of On and Off counts (N_{ON} and N_{OFF}, respectively) are used to obtain the number of excess counts (N_{Excess}) which is an estimate of the number of events from the source (N_{Source}). Taking the errors to follow Poisson statistics, in the case that N_{ON} and N_{OFF} are large ($\gtrsim 5$), we can apply simple Gaussian propagation of errors to estimate the error on N_{Excess} to be:

$$\Delta N_{Excess} = \sqrt{N_{ON} + \alpha^2 N_{Off}} \tag{5.4}$$

This allows for the testing and fitting of models, for example the energy spectrum, by minimizing the χ^2-statistic:

$$\chi^2_\nu = \sum_{i}^{\#\text{ Energy Bins}} \frac{(N_{Excess,i} - S_i^{Pred})^2}{(\Delta N_{Excess,i})^2}, \tag{5.5}$$

where S_i^{Pred} is the model-predicted excess counts in the i^{th} energy bin and ν is the number degrees of freedom which is given by the number of energy bins minus the number of free parameters of the model.

In the case where N_{ON} and N_{OFF} are small ($\lesssim 5$), the errors cannot be approximated as Gaussian, hence Equation 5.4 is no longer valid and χ^2-fitting techniques are not appropriate. To correctly take into account the errors, Piron et al. (2001) apply a binned-likelihood method to give a proper treatment of the Poissonian nature of N_{ON} and N_{OFF}. This method, originally developed for the CAT experiment (Barrau et al., 1998), has been implemented into

the Event Display analysis package, for the purpose of the analysis presented in this thesis. A description of this method will be given in this section.

Consider the number of events observed k to be a Poisson random number obtained from a distribution of mean λ. The probability mass function is given by:

$$\mathcal{P}(k) = \frac{e^{-\lambda}\lambda^k}{k!}. \tag{5.6}$$

For a given model, $\lambda = \lambda(\mathbf{\Theta})$, where $\mathbf{\Theta}$ is a set of parameters, thus likelihood function is given as:

$$\mathcal{L}(\mathbf{\Theta}|\mathbf{K}) = \prod_i \mathcal{P}(k_i|\mathbf{\Theta}). \tag{5.7}$$

By maximizing $\mathcal{L}$ with respect to $\mathbf{\Theta}$ one can obtain the Maximum Likelihood Estimator (MLE) $\hat{\mathbf{\Theta}}$. Given that we are observing a set of On and Off counts, the likelihood equation can be written as:

$$\mathcal{L}(\mathbf{\Theta}|\mathbf{N_{ON}}, \mathbf{N_{OFF}}) = \prod_i \mathcal{P}(N_{ON,i}|\mathbf{\Theta})\mathcal{P}(N_{OFF,i}|\mathbf{\Theta}). \tag{5.8}$$

Where the On and Off counts are Poissonian distributed with means $\overline{N_{ON,i}}$ and $\overline{N_{OFF,i}}$ respectively. The average number of On counts can be estimated as a function of the model predicted excess counts and the mean Off counts:

$$\overline{N_{ON,i}} = S_i^{Pred} + \alpha_i \overline{N_{OFF,i}}. \tag{5.9}$$

As the VERITAS IRFs are binned in energy and defined for specific observing conditions (e.g. zenith and azimuth angle, NSB, HV configuration, etc), it is convenient to bin the observed counts into intervals Δ_{i_e,i_ω} where i_e corresponds to the reconstructed energy ($\tilde{E}$) interval $[\tilde{E}_{i_e}^{min}, \tilde{E}_{i_e}^{max}]$ and i_ω corresponds to the specific observing conditions, with the set of observational parameters represented by $\mathbf{\Omega}$. In practice this is implemented as an observation-wise energy binning.[2] Using this binning the model predicted excess can be obtained by forward folding the source model, $\left(\frac{d\phi}{dE}\right)^{Pred}$, with the instrument response functions:

$$S_{i_e,i_\omega}^{Pred} = T_{ON} \int_{\tilde{E}_{i_e}^{min}}^{\tilde{E}_{i_e}^{max}} d\tilde{E} \int_0^\infty dE \left(\frac{d\phi}{dE}\right)^{Pred} A_{eff}(\mathbf{\Omega}, E)\gamma(\mathbf{\Omega}, E \to \tilde{E}), \tag{5.10}$$

[2]Observation-wise binning of IRFs is standard practice for Event Display. In doing this the IRFs are time-averaged across the different observing conditions of the run. As the observations are typically taking under stable conditions (for example slowly varying telescope pointing) the effect on the data is small and within the expected systematic errors. For rapidly varying observations, the data could be finely binned into chunks with comparable observation conditions (for example $\Delta IRF/IRF = \delta$, where ΔIRF is the observed spread in values of an arbitrary IRF and δ is the desired fractional spread in the bin grouping).

where T_{ON} is the livetime, $\tilde{E}$ is the reconstructed energy, E is the true (Monte Carlo), A_{eff} is the effective area and γ is the probability of reconstructing a gamma ray of true energy E to have a reconstructed energy $\tilde{E}$. Rewriting Equation 5.8, the practical form of the likelihood equation can be obtained:

$$\mathcal{L}(\mathbf{\Theta}|\mathbf{N_{ON}}, \mathbf{N_{OFF}}) = \prod_{i_e,i_\omega} \mathcal{P}(N_{ON_{i_e,i_\omega}}|\mathbf{\Theta})\mathcal{P}(N_{OFF_{i_e,i_\omega}}|\mathbf{\Theta}). \tag{5.11}$$

To simplify calculations, the log-likelihood equation is often used:

$$l = \log(\mathcal{L}), \tag{5.12}$$

where $\log(X) = \log_e(X)$. Given that the log function is a monatomic function, the value which maximizes $\mathcal{L}$ will also maximize l.

Equation 5.12 can be rewritten in terms of the observables $N_{ON_{i_e,i_\omega}}$ and $N_{OFF_{i_e,i_\omega}}$, the model predicted excess counts $S^{Pred}_{i_e,i_\omega}$ and the unknown mean off counts $\overline{N_{OFF_{i_e,i_\omega}}}$.

$$\begin{aligned} l(\Theta) = \sum_{i_e,i_\omega} \Big[& N_{ON_{i_e,i_\omega}} \log\left(S^{Pred}_{i_e,i_\omega} + \alpha_{i_e,i_\omega}\overline{N_{OFF_{i_e,i_\omega}}}\right) \\ & + N_{OFF_{i_e,i_\omega}} \log(\overline{N_{OFF_{i_e,i_\omega}}}) - (\alpha_{i_e,i_\omega}+1)\,\overline{N_{OFF_{i_e,i_\omega}}} - S^{Pred}_{i_e,i_\omega}\Big], \end{aligned} \tag{5.13}$$

where I have used the Poission distributions defined in Equation 5.6, with the mean On counts given by Equation 5.9 and the mean Off counts $\overline{N_{OFF_{i_e,i_\omega}}}$. Hence for a given source model we only have one unknown, $\overline{N_{OFF_{i_e,i_\omega}}}$. The MLE of $\overline{N_{OFF_{i_e,i_\omega}}}$ can be obtained by maximizing the log-likelihood function with respect to $\overline{N_{OFF_{i_e,i_\omega}}}$. Hence setting $dl/d\overline{N_{OFF_{i_e,i_\omega}}} = 0$ the MLE can be obtained:

$$\widehat{\overline{N_{OFF_{i_e,i_\omega}}}} = \frac{1}{2\alpha_{i_e,i_\omega}(\alpha_{i_e,i_\omega}+1)}\left[b_{i_e,i_\omega} + \sqrt{b^2_{i_e,i_\omega} + 4\alpha_{i_e,i_\omega}(\alpha_{i_e,i_\omega}+1)S^{Pred}_{i_e,i_\omega}}\right], \tag{5.14}$$

where

$$b_{i_e,i_\omega} = \alpha_{i_e,i_\omega}(N_{ON_{i_e,i_\omega}} + N_{OFF_{i_e,i_\omega}}) - (\alpha_{i_e,i_\omega}+1)S^{Pred}_{i_e,i_\omega}. \tag{5.15}$$

This allows for the prediction of the average number of Off counts which is dependent on the observed number of On and Off counts, and the model predicted counts, i.e. $\widehat{\overline{N_{OFF_{i_e,i_\omega}}}} = \widehat{\overline{N_{OFF_{i_e,i_\omega}}}}(N_{ON_{i_e,i_\omega}}, N_{OFF_{i_e,i_\omega}}, S^{Pred}_{i_e,i_\omega})$. Taking the solution of Equation 5.14, Equation can be writ-

ten as:

$$
\begin{aligned}
l(\Theta) = \sum_{i_e,i_\omega} \Bigg[& N_{ON_{i_e,i_\omega}} log\left(S^{Pred}_{i_e,i_\omega} + \alpha_{i_e,i_\omega}\widehat{\overline{N_{OFF_{i_e,i_\omega}}}}\right) \\
& + N_{OFF_{i_e,i_\omega}} \log(\widehat{\overline{N_{OFF_{i_e,i_\omega}}}}) - (\alpha_{i_e,i_\omega}+1)\,\widehat{\overline{N_{OFF_{i_e,i_\omega}}}} - S^{Pred}_{i_e,i_\omega}\Bigg].
\end{aligned}
\tag{5.16}
$$

Hence by numerically maximizing Equation 5.16 with respect to the source model parameters the MLE $\hat{\Theta}$ can be obtained.

Note in practice it is often convenient to sum the run-wise counts in each energy bin:

$$
\begin{aligned}
N_{ON_{i_e}} &= \sum_{i_\omega} N_{ON_{i_e,i_\omega}}, \\
N_{OFF_{i_e}} &= \sum_{i_\omega} N_{OFF_{i_e,i_\omega}}, \\
\widehat{\overline{N_{OFF_{i_e}}}} &= \sum_{i_\omega} \widehat{\overline{N_{OFF_{i_e,i_\omega}}}}, \\
S^{Pred}_{i_e} &= \sum_{i_\omega} S^{Pred}_{i_e,i_\omega}.
\end{aligned}
\tag{5.17}
$$

Hence Equation 5.16 becomes:

$$
\begin{aligned}
l(\Theta) = \sum_{i_e} \Bigg[& N_{ON_{i_e}} log\left(S^{Pred}_{i_e} + \overline{\alpha_{i_e}}\widehat{\overline{N_{OFF_{i_e}}}}\right) \\
& + N_{OFF_{i_e}} \log(\widehat{\overline{N_{OFF_{i_e}}}}) - (\overline{\alpha_{i_e}}+1)\,\widehat{\overline{N_{OFF_{i_e}}}} - S^{Pred}_{i_e}\Bigg],
\end{aligned}
\tag{5.18}
$$

where $\overline{\alpha_{i_e}}$ is the exposure-weighted mean α. By summing the counts in each energy bin, the contribution to each run is still handled on a run-wise bases. This instead reduces the number of degrees of freedom from $nRuns \times nBins - nFreeParameters$ to $nBins - nFreeParameters$. Which is similar to the degrees of freedom argument for a standard χ^2-fit. This can also reduce the effect of outliers on the likelihood fit.[3]

5.2.3 Likelihood-Ratio Test

Unlike χ^2-fitting, a pure likelihood fit doesn't give any insight into the goodness of a fit. Indeed, for any given model, the procedure described above will find the MLE for that model, given the observed data. In order to quantify whether or one model is a better fit than another,

[3] Likelihood fits were obtained with and without run-wise binning and found to be well within statistical errors. It was found that by binning the data as such the computation time was decreased and the fitting procedure became more stable, with only a negligible effect on the fit results.

one may use the likelihood ratio:

$$\lambda = \frac{\mathcal{L}}{\mathcal{L}_0}, \tag{5.19}$$

where $\mathcal{L}$ is the likelihood obtained by the null hypothesis and $\mathcal{L}_0$ is the likelihood obtained by the alternative hypothesis. Wilk's theorem (Wilks, 1938) suggests that for two nested models, the likelihood-ratio test can be used to obtain an equivalent χ^2 statistic:

$$-2\log(\lambda) \sim \chi^2_\nu, \tag{5.20}$$

where ν is the number of degrees of freedom given by the difference in degrees of freedom between the two models. This allows one to test, for example, if an energy spectrum is better fit by a power-law or log-parabola model.

For a standalone model, one may also obtain an estimate of the goodness of fit. This is obtained by considering an "ideal model", that is a model which perfectly describes the observed data, such that:

$$\begin{aligned} \overline{N_{ON_{i_e,i_\omega}}} &= N_{ON_{i_e,i_\omega}}, \\ \overline{N_{OFF_{i_e,i_\omega}}} &= N_{OFF_{i_e,i_\omega}}, \\ S^{Pred}_{i_e,i_\omega} &= N_{ON_{i_e,i_\omega}} - \alpha_{i_e,i_\omega} N_{OFF_{i_e,i_\omega}}. \end{aligned} \tag{5.21}$$

While the true form of this model is unknown, every bin is required to have a fixed value. Hence the ideal model has zero degrees of freedom. The log-likelihood of this model can be obtained by substituting Equation 5.21 into Equation 5.16:

$$\log \mathcal{L}' = \sum_{i_e,i_\omega} \left[N_{ON_{i_e,i_\omega}} \log\left(N_{ON_{i_e,i_\omega}}\right) + N_{OFF_{i_e,i_\omega}} \log(N_{OFF_{i_e,i_\omega}}) - \left(N_{ON_{i_e,i_\omega}} + N_{OFF_{i_e,i_\omega}}\right)\right], \tag{5.22}$$

or using the convention defined by Equation 5.17:

$$\log \mathcal{L}' = \sum_{i_e} \left[N_{ON_{i_e}} \log\left(N_{ON_{i_e}}\right) + N_{OFF_{i_e}} \log(N_{OFF_{i_e}}) - \left(N_{ON_{i_e}} + N_{OFF_{i_e}}\right)\right]. \tag{5.23}$$

Applying the likelihood-ratio test in which the null hypothesis is the obtained best-fit model and the alternative hypothesis is the ideal model, one can obtain an equivalent χ^2-statistic. In doing so one is essentially testing how much of an improvement the ideal model is over the best-fit model, where if the best-fit model accurately describes the data then the

likelihood-ratio test will be χ^2-distributed with $\nu = nBins - nFreeParameters$, hence providing a goodness-of-fit statistic.

5.3 Implementation

5.3.1 Implementation

Instrument Response Functions

In order to perform the a likelihood fit, Equation 5.10 requires the Effective Area $A_{Eff}(\mathbf{\Omega}.E)$ and the response matrix $\gamma(\mathbf{\Omega}, E \rightarrow \tilde{E})$. The effective areas are obtained by analyzing Monte Carlo simulations of showers of known energies (as described in Section 4.2.8), and are a measure of the probability a shower being detected by the instrument. The response matrix is obtained by passing simulated gamma rays of true energy E, through the analysis chain and recording the reconstructed energy $\tilde{E}$. The 2-dimensional distribution of E as a function of $\tilde{E}$), is shown in Figure 5.1. The energy resolution of VERITAS is approximately a Gaussian in log space, this is evident by the symmetric shape of the response matrix about the diagonal (the line $x = y$). Typical values of the energy resolution are 20% at 1 TeV, that is the reconstruction of gamma ray with a true photon energy of 1 TeV will be described by a log-normal distribution of mean $\sim$ 1 TeV and standard deviation 0.2 .

At low and high energies, the reconstruction process becomes unreliable due to the lack of simulated gamma-ray showers which pass cuts. To quantify this, the reconstruction bias is estimated by obtained a Gaussian fit of $\tilde{E}$ as a function of E:

$$bias(E) = \left| \frac{\mu_{\tilde{E}} - E}{E} \right|, \tag{5.24}$$

where E is the true energy and $\mu_{\tilde{E}}$ is the mean of the best fit Gaussian. At lower energies this is dominated by the shower being dimmer and therefore less likely triggering the array. At higher energies the bias in the reconstruction process is due to the poor statistics at higher energies (note the simulated gamma rays are drawn from a power-law distribution of index $\Gamma = 2.5$) and larger showers being truncated by the camera's edge. During the likelihood fit, a cut on energy bias is applied to Equation 5.10. This has the effect of restricting the analysis to a reconstructed energy range in which the reconstruction of events is accurately described by the response matrix.

The mean effective area and mean response matrix is obtained by time-averaging the response functions over the duration of an individual observation. This accounts for changes

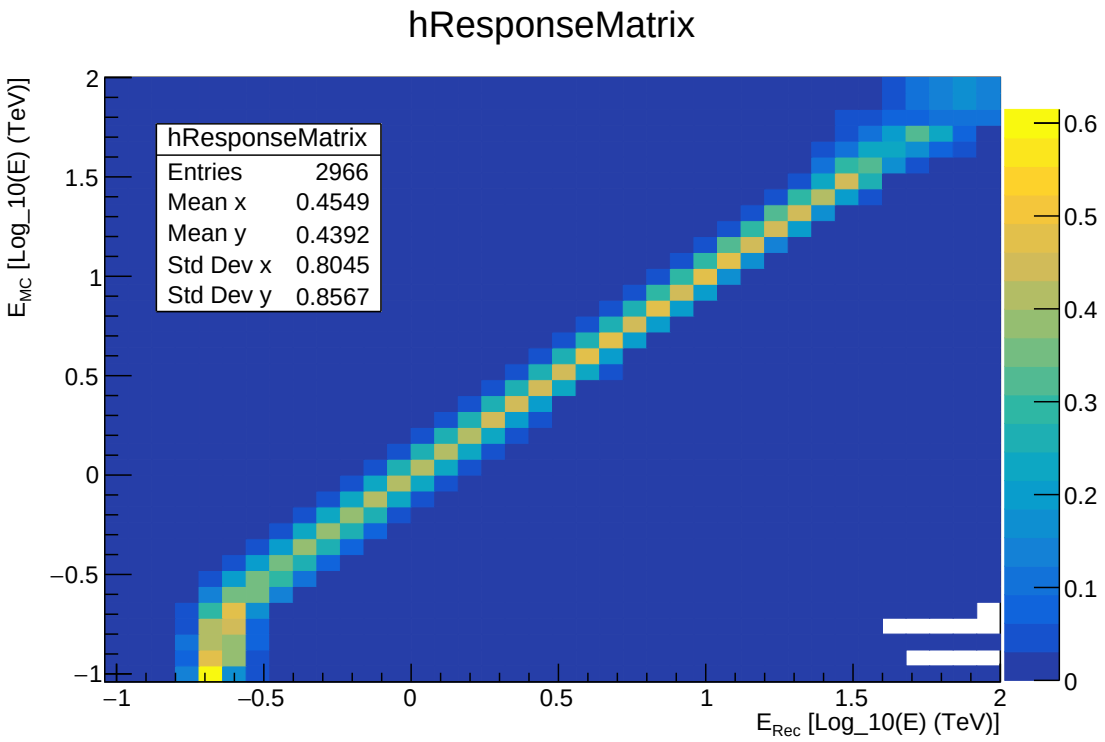

Figure 5.1: Example of a VERITAS response matrix, time-averaged over a run of typically 30 minutes, used in a binned-likelihood fit. The color scale corresponds to the probability of reconstructing an event with true energy E_{MC} to have a reconstructed energy E_{Rec}.

in the observational conditions, for example the zenith and azimuthal pointing angles.

Profile Likelihood

The profile likelihood is obtained by freezing all but one of the model parameters and obtaining the likelihood at each point of a scan over that parameter. It is convenient to plot the profile likelihood as the $-2\Delta\log(\mathcal{L}) = -2\left(\log\mathcal{L} - \log\mathcal{L}_{max}\right)$, where $\mathcal{L}_{max}$ is the maximum log-likelihood. It is evident from Wilk's Theorem that the profile likelihood will be approximately χ^2-distributed with one degree of freedom. Using this information, the profile likelihood acts as a powerful tool for examining the parameter space. For example, invoking Wilk's theorem, one can obtain upper limits on parameters by finding value of that parameter for which $-2\Delta\log(\mathcal{L}) = C$ where C is the critical value for a $\chi^2_{1,1-\delta}$ distribution with significance level δ. Bayesian based upper limits can be obtained using Bayes' theorem (see Loredo, 1992, and references therein for a discussion of Bayes' theorem and its applications in astrophysics):

$$\mathcal{P}(\theta|x) = \frac{\mathcal{P}(\theta)\mathcal{P}(x|\theta)}{\mathcal{P}(x)}, \tag{5.25}$$

Where $\mathcal{P}(\theta|x)$ is the posterior probability density of observing θ given the data x, $\mathcal{P}(\theta)$ is the prior probability density of θ, $\mathcal{P}(x|\theta)$ is the probability of observing x given θ and $\mathcal{P}(x)$ is the probability of observing x and can be considered a normalization constant. Equation 5.25 becomes:

$$\mathcal{P}(\theta|x) \propto \mathcal{P}(\theta)\mathcal{L}(\theta|x), \tag{5.26}$$

where $\mathcal{L}(\theta|x)$ is the likelihood of observing θ given x and is related to $\mathcal{P}(x|\theta)$ by Equation 5.1. The prior probability density is the probability of observing θ given all other possible hypotheses. In the case of an upper limit on the flux normalization, it is only possible to observe non-negative flux normalization hence the prior probability distribution could take the form:

$$\mathcal{P}(\theta) = \mathcal{P}(N_0) = \begin{cases} 1, & \text{if } N_0 \geq 0 \\ 0, & \text{otherwise} \end{cases} \tag{5.27}$$

Hence an upper limit can be calculated by finding the value of θ_{UL} for which:

$$\frac{\int_{-\infty}^{\theta_{UL}} \mathcal{P}(\theta)\mathcal{L}(\theta|x)d\theta}{\int_{-\infty}^{\infty} \mathcal{P}(\theta)\mathcal{L}(\theta|x)d\theta} = 1 - \delta. \tag{5.28}$$

5.3.2 Intrinsic Spectral Analysis

Attenuation of VHE photons by the extragalactic background light (EBL), results in the modification of the spectrum observed from extragalactic source. This can be characterized as:

$$\left(\frac{d\phi}{dE}\right)_{observed} = \left(\frac{d\phi}{dE}\right)_{intrinsic} e^{-\tau(E)}, \tag{5.29}$$

where $\left(\frac{d\phi}{dE}\right)_{observed}$ is the observed energy spectrum, $\left(\frac{d\phi}{dE}\right)_{intrinsic}$ is the intrinsic energy spectrum and $\tau(E)$ is the optical depth of the EBL. Using equations 5.10 and 5.29, one can obtain an expression for the model predicted excess counts for given EBL model:

$$S_{i_e,i_\omega}^{Pred} = T_{ON} \int_{\tilde{E}_{i_e}^{min}}^{\tilde{E}_{i_e}^{max}} d\tilde{E} \int_0^\infty dE \left(\frac{d\phi}{dE}\right)^{Pred} e^{-\tau(E)} A_{eff}(\mathbf{\Omega}, E)\gamma(\mathbf{\Omega}, E \to \tilde{E}). \tag{5.30}$$

For a known EBL model, one can apply a maximum likelihood fit to the intrinsic spectrum of a source. It is also possible to apply a scaled EBL model approach such as those implemented by Abramowski et al. (2013) (H.E.S.S.), Moralejo et al. (2017) (MAGIC) and Ackermann et al. (2012b) (*Fermi*-LAT). In this case one would fit a EBL model with a scaling

factor, $\tilde{\tau} = \beta_{scale}\tau$, where $\beta_{scale} = 0$ suggests no EBL absorption and $\beta_{scale} = 1$ suggests this EBL model accurately describes the attenuation. Applying a scaled EBL method allows for the testing of theoretical EBL models such as Franceschini et al. (2008), Finke et al. (2010), Domínguez et al. (2011) and Dwek & Krennrich (2013). This is a likelihood-based EBL analysis and is presented in Chapter 8.

5.3.3 Confidence Intervals

Taking into account the covariance terms obtained from a best fit, one can obtain the 1-σ confidence interval on the best fit. In general, we have a covariance matrix Σ which is a $M \times M$ matrix where M is the number of fitting parameters. Element σ_{ij} corresponds to the covariance between fitting parameters i and j. In the case of a simple power-law model with fitting parameters N_0 and Γ we have:

$$\Sigma = \begin{pmatrix} \sigma_{N_0 N_0} & \sigma_{N_0 \Gamma} \\ \sigma_{\Gamma N_0} & \sigma_{\Gamma\Gamma} \end{pmatrix}. \tag{5.31}$$

The error on the best fit model, F, can then be calculated as:

$$(err\,(F))^2 = \Delta\Sigma\Delta^T, \tag{5.32}$$

where Δ is a $1 \times M$ matrix of the partial derivatives. This can be written as:

$$err\,(F) = \sqrt{\sum_i^M \sum_j^M \left(\frac{\partial F}{\partial x_i}\frac{\partial F}{\partial x_j}\sigma_{ij}\right)}. \tag{5.33}$$

In the case of a power law:

$$F(E) = N_0 \left(\frac{E}{E_0}\right)^{-\Gamma}, \tag{5.34}$$

where E_0 is the normalisation energy, the partial derivatives are given by:

$$\frac{\partial F}{\partial N_0} = \left(\frac{E}{E_0}\right)^{-\Gamma}, \tag{5.35}$$

$$\frac{\partial F}{\partial \Gamma} = -N_0 \left(\frac{E}{E_0}\right)^{-\Gamma} \log\left(\frac{E}{E_0}\right). \tag{5.36}$$

Hence the error on the best-fit-power-law model is given as:

$$err\,(F) = F\left[\frac{\sigma_{N_0N_0}}{N_0^2} + \log^2\left(\frac{E}{E_0}\right)\sigma_{\Gamma\Gamma} - \frac{2}{N_0}\log\left(\frac{E}{E_0}\right)\sigma_{N_0\Gamma}\right]^{\frac{1}{2}}. \tag{5.37}$$

The decorrelation energy, the energy at which the correlation between the two fitting parameters is minimized, can be obtained by taking the derivative of Equation 5.37 with respect to the energy (E):

$$\frac{d}{dE}\left(\frac{err(F)}{F}\right)^2_{E=E_D} = 0, \tag{5.38}$$

$$\Rightarrow E_D = E_0 e^{\left(\frac{\sigma_{N_0\Gamma}}{N_0\sigma_{\Gamma\Gamma}}\right)}. \tag{5.39}$$

The 1-σ confidence interval is therefore defined as the region $F \pm err(F)$, where the fractional error $(err(F)/F)$ has a minimum at the decorrelation energy E_D.

5.4 Performance

5.4.1 Performance of Likelihood Fit

To compare the performance of the likelihood fitting procedure to standard analysis methods, a set of simulated energy spectra were created. The energy spectra were created using the following procedure:

1. Effective areas, response matrices and observed Off counts were taken from real observations.

2. Using Equation 5.10, excess counts were obtained by forward folding a known spectral model with the effective areas and response matrices.

3. The mean predicted On counts were obtained using Equation 4.6 in which the excess was obtained from Step 2 and the Off counts were taken from the data.

4. On count were drawn from a random Poisson distribution with mean equal to the mean predicted On counts obtained in Step 3.

A likelihood fit was then applied to each energy spectrum, with failed fits being discarded. When applying the likelihood fit, three different criteria for when to stop including data were tested:

1. Stop after the last observed On count.

2. Stop after the last observed Off count.

3. Apply the fit over a predefined range of 0.2-30 TeV.

Three power-law energy spectra were simulated, each with a flux normalization of $N_0 = 3 \times 10^{-11}$ cm^{-2}s^{-1}TeV^{-1} at the normalization energy $E_0 = 1.0$ TeV. This ensures a moderate detection within 30 minutes of observations (the averaged duration of the real data used). The spectral indices where chosen to represent three different spectral types, Soft ($\Gamma = 3.5$), Moderate ($\Gamma = 2.5$) and Hard ($\Gamma = 2.0$). The Moderate spectrum approximately corresponds to a 1 Crab source. To estimate the bias on the best-fit parameters, the pull distributions[4] are obtained. One would expect that for an unbiased estimator, with accurate error estimation, that the pull distributions would be well described by a Gaussian of mean 0 and standard deviation 1. A total of 9,500 simulations were performed for each spectral type. Simulations for which the fitting procedure fails are excluded from the final dataset and make up $< 1\%$ of the total simulated datasets. The results of these simulations are shown in Table 5.1.

Table 5.1 indicates that the errors are accurately estimated. There is a marginal indication in a biasing towards softer spectral indices and dimmer flux normalizations, however this can be accounted for in the asymmetric shape of the pull distributions. The asymmetric shape is due to the true errors not being symmetric as is assumed in obtaining the pull distributions. This is particularly the case for the normalization distributions.

Assuming that each simulation is equally affected by the apparent biasing due to asymmetric errors, then we can compare the different stopping conditions for each spectral type. Taking the smallest offset to represent a baseline bias, then one can compare the excess bias. For soft models, choosing the last On or the last Off count provide consistent results, however when the default range is chosen the bias is roughly twice the baseline bias. For harder models the bias on the spectral index increases when the last Off count is used. This is due to higher energy data observed in the On region, being rejected from the fitting procedure which would otherwise increase the likelihood of a harder model. Taking the last On count as the final energy bin provides the least-biased estimation of the data's true parameters.

[4]This is a distribution commonly used in particle physics which is defined as $\left(\frac{\text{Best fit}-\text{True}}{\text{Error on best fit}}\right)$. If the errors on the best fit are Gaussian then one would expect the pull distribution to be normally distributed with $\mathcal{N}(\mu = 0, \sigma = 1)$. Deviation from this would suggest a bias ($\mu \neq 0$) or that the errors aren't Gaussian ($\sigma \neq 1$).

Simulated Spectral Type	Soft		Moderate		Hard	
	Γ	N_0	Γ	N_0	Γ	N_0
Stop Condition (last On)						
μ (Pull)	0.04 ± 0.01	0.13 ± 0.01	0.01 ± 0.01	0.15 ± 0.01	0.03 ± 0.01	0.16 ± 0.01
σ (Pull)	1.00 ± 0.01	1.00 ± 0.01	0.98 ± 0.01	1.01 ± 0.01	0.963 ± 0.01	0.98 ± 0.01
Stop Condition (last Off)						
μ (Pull)	0.04 ± 0.01	0.11 ± 0.01	0.04 ± 0.01	0.15 ± 0.01	0.08 ± 0.01	0.17 ± 0.01
σ (Pull)	1.01 ± 0.01	0.98 ± 0.01	0.98 ± 0.01	0.95 ± 0.01	0.95 ± 0.01	0.94 ± 0.01
Stop Condition (predefined)						
μ (Pull)	0.06 ± 0.01	0.14 ± 0.01	0.01 ± 0.01	0.16 ± 0.01	0.01 ± 0.01	0.15 ± 0.01
σ (Pull)	1.00 ± 0.01	1.00 ± 0.01	0.99 ± 0.01	0.99 ± 0.01	0.97 ± 0.01	0.99 ± 0.01

Table 5.1: Summary of bias simulation results.

5.4.2 Performance of Equivalent χ^2-Statistic

In this section the use of the likelihood ratio test is demonstrated. Firstly, the ability of the likelihood ratio as a goodness of fit statistic is demonstrated. Secondly the ability of the test as a discriminator between different models is demonstrated by obtaining the likelihood ratio test of a simulated log-parabola model, fit by a power-law model for different degrees of spectral curvature.

Goodness of Fit

To verify that Equation 5.23 provides the correct normalization of the likelihood ratio test, that is the resultant likelihood ratio test is χ^2-distributed with degrees of freedom equal to the number of bins minus the number of free parameters, the χ^2-values obtained from the "Soft" spectrum simulations were examined (see Section 5.4.1). When choosing the last On count as the final energy bin to include in the fit, one observes a distribution of degrees of freedom due to random fluctuations of the data.[5] This allows for the χ^2-values for different degrees of freedom to be examined. Figure 5.2 shows the distribution of χ^2-values obtained for 3 - 6 degrees of freedom. Good agreement is found between the distribution of χ^2-values and the expected χ^2-distributions (plotted in red), which have been scaled by the total number of counts.

[5]This is simply due to the Poissionian nature of the data. Individual observations will have low probability of observing a count in their final bin. In combining these observations one therefore will randomly observe a different final energy bin with each simulated dataset.

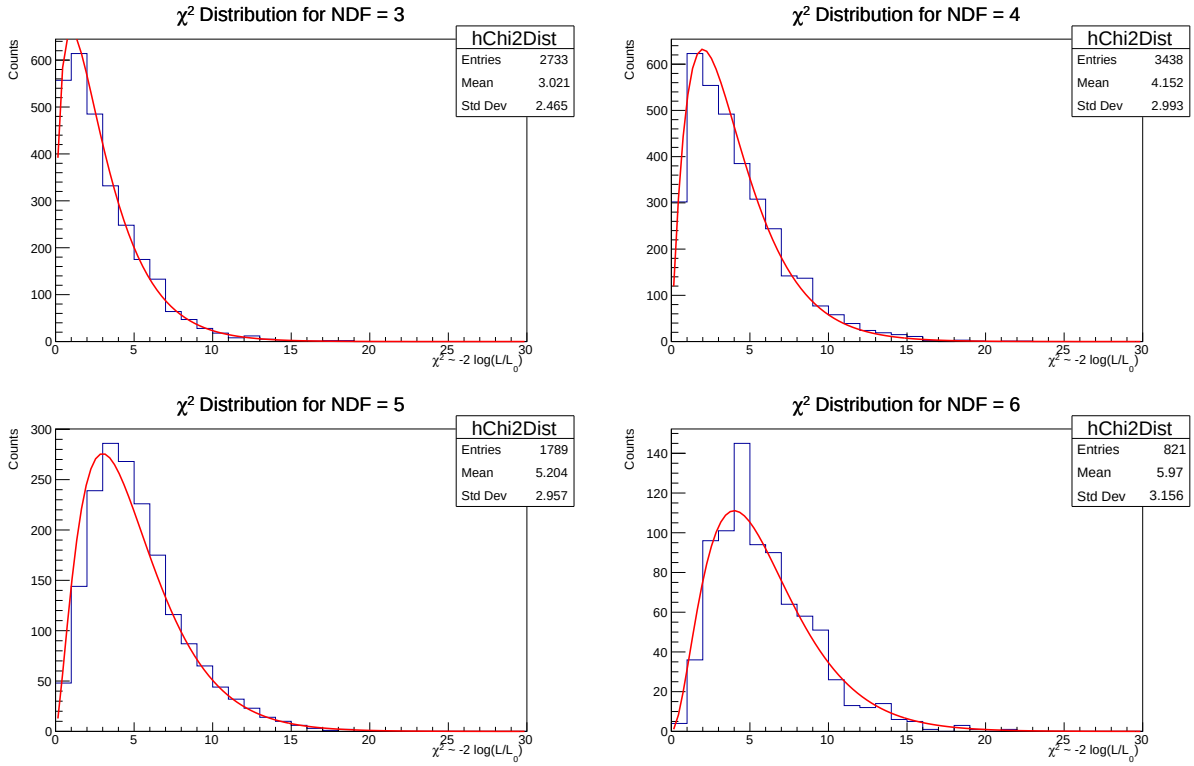

Figure 5.2: χ^2-distributions obtained from simulated "Soft" spectra. The different panels correspond to different degrees of freedom observed, where each distribution is obtained for a subset of simulations which have the same final energy bin. The χ^2 distribution scaled by the number of total number of counts is overlaid as a red line.

Model Rejection

To test the ability of the likelihood ratio test as a model discriminator, three different spectra were simulation using the methods described in 5.4.1. In each case a log-parabola model of the form:

$$\frac{dN}{dE} = N_0 \left(\frac{E}{E_0}\right)^{-\alpha + -\beta \log\left(\frac{E}{E_0}\right)} \tag{5.40}$$

was simulated with model parameters varied to produce different degrees of spectral curvature. A summary of the spectral parameters simulated is given in Table 5.2.

Figures 5.3 - 5.5 show the obtained distributions of χ^2-values for a power-law fit and log parabola fit for each simulated spectral type. As the curvature becomes more pronounced (β increases) the likelihood fit is more efficient at selecting a curved model. This is evident from the likelihood ratio test distributions. The likelihood ratio test is χ^2-distributed with one degree of freedom (the difference in degrees of freedom between the two models). For the weak curvature case (Figure 5.5) the observed data is indistinguishable from a power law

Simulated Spectral Type	N_0 ($\mathrm{cm}^{-2}\mathrm{s}^{-1}\mathrm{TeV}^{-1}$)	α	β
Strong Curvature	3×10^{-11}	2.5	0.5
Moderate Curvature	3×10^{-11}	2.5	0.1
Weak Curvature	3×10^{-11}	2.5	0.01

Table 5.2: Summary of the different models used to test the likelihood-ratio test's ability to discriminate between different models.

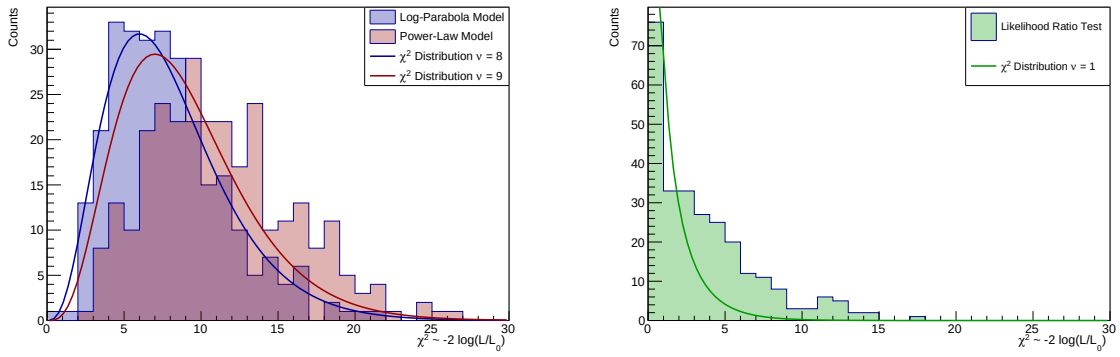

Figure 5.3: The left panel shows the distribution of χ^2-values obtained for a log-parabola fit (blue) and a power-law fit (red) for the simulated "Strong Curvature" spectrum described in Table 5.2. The right panel shows the distribution of values obtained by a likelihood ratio test for testing whether the log-parabola model offers a significant improvement over the power-law model.

model, with the log-parabola model offering no significant improvement over the power-law model. This indicated by the likelihood ratio test being well described by a $\chi^2_{\nu=1}$-distribution. When the curvature is more pronounced (Figure 5.3) the power-law model is a poor fit to the data, while the log-parabola model offers a significant improvement over the power-law model. This is also evident from the likelihood ratio test which is no longer adequately described by a $\chi^2_{\nu=1}$-distribution.

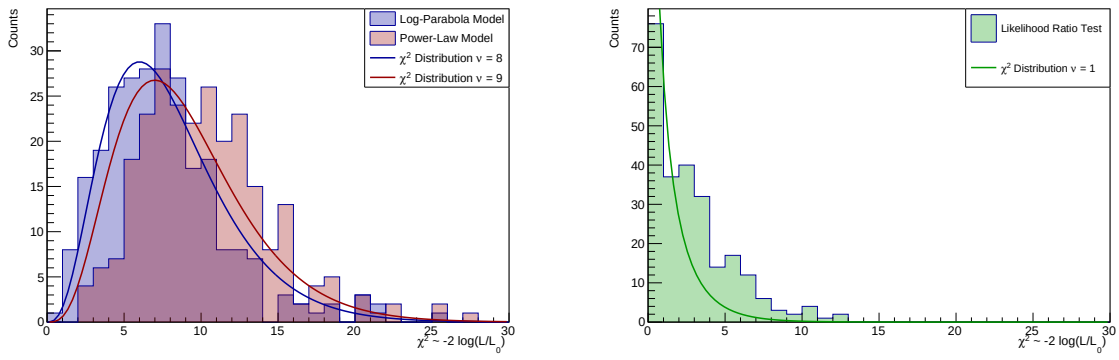

Figure 5.4: The left panel shows the distribution of χ^2-values obtained for a log-parabola fit (blue) and a power-law fit (red) for the simulated "Moderate Curvature" spectrum described in Table 5.2. The right panel shows the distribution of values obtained by a likelihood ratio test for testing whether the log-parabola model offers a significant improvement over the power-law model.

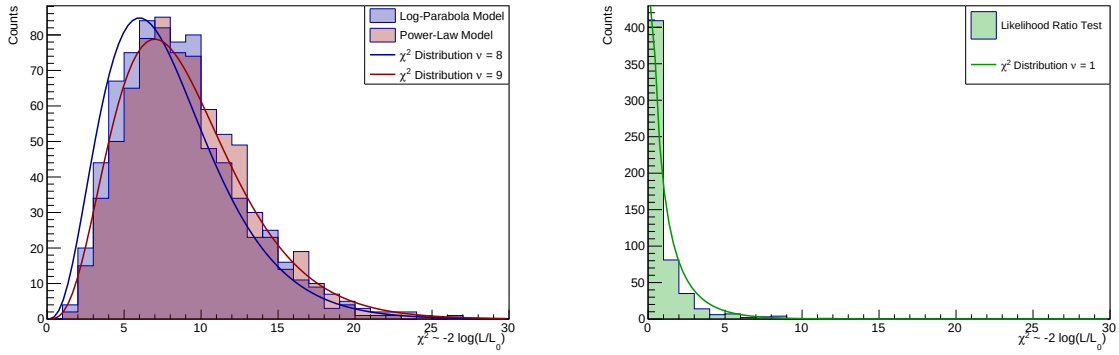

Figure 5.5: The left panel shows the distribution of χ^2-values obtained for a log-parabola fit (blue) and a power-law fit (red) for the simulated "Weak Curvature" spectrum described in Table 5.2. The right panel shows the distribution of values obtained by a likelihood ratio test for testing whether the log-parabola model offers a significant improvement over the power-law model.

5.5 Results

5.5.1 Crab Nebula Analysis

A sample of 95 runs taken between 2012 and 2017 at an elevation >70 degrees was analyzed using a standard χ^2-fit and the binned-likelihood analysis. The energy spectrum was obtained between 180 GeV - 80 TeV (note 80 TeV is defined as the upper bin edge of the bin with the highest energy On count) and is shown in Figure 5.6. The energy spectrum is best-fit by a log-parabola model of the form (note errors are purely statistical):

$$\frac{dN}{dE} = (2.95 \pm 0.05) \times 10^{-11} \left(\frac{E}{1\ \text{TeV}}\right)^{\left(-(2.62\pm0.02)-(0.10\pm0.01)\log\left(\frac{E}{1\ \text{TeV}}\right)\right)} \text{cm}^{-2}\text{s}^{-1}\text{TeV}^{-1}, \quad (5.41)$$

with $\chi^2/NDF = 18.2/10$. The χ^2-probability of this fit is low (0.05) and would warrant further investigation, however a full analysis of the Crab, particularly at higher energies where camera saturation effects high-energy events, is out of the scope of this thesis.

Note a power-law model was also fit to the data, however a likelihood ratio test indicated a >3σ preference for the log-parabola model. The best-fit model and 1-σ confidence level are plotted as a red line and red shaded region, respectively, in Figure 5.6. Spectral points are plotted as black squares in Figure 5.6 and are obtained by reapplying the likelihood fit across each energy bin, with only the flux normalization parameter allowed to vary. Two different methods are used to obtain upper limits. 95% confidence level "Frequentist" upper limits are shown as red arrows and are obtained by finding the flux normalization for which the $\Delta \log \mathcal{L} = -2.706$, this corresponds to the critical value for a χ^2-distribution with one degree of freedom. This corresponds to the 95% p-value for a χ^2 distribution with one degree of freedom. 95% confidence level "Bayesian" upper limits are plotted as green arrows and are obtained using Equation 5.28. It is interesting to note that the upper limit plotted at 16 TeV has an excess with a significance of $\sim 5.8\sigma$. This point is plotted as a upper limit due to the point's fit failing. The fit has failed due to the irregular shape of the profile likelihood (plotted in Figure 5.7). The irregular shape is due to the specific flux level and that zero Off counts are observed in this energy bin. In this case Equation 5.15 becomes:

$$b_{i_e,i_z} = \alpha_{i_e,i_\omega}(N_{ON_{i_e,i_\omega}}) - (\alpha_{i_e,i_\omega} + 1)S^{Pred}_{i_e,i_\omega}. \quad (5.42)$$

In the case when $\alpha_{i_e,i_\omega}(N_{ON_{i_e,i_\omega}}) < (\alpha_{i_e,i_\omega} + 1)S^{Pred}_{i_e,i_\omega}$, and by Equation 5.14, $\widehat{\overline{N_{OFF_{i_e,i_\omega}}}} = 0$. Thus

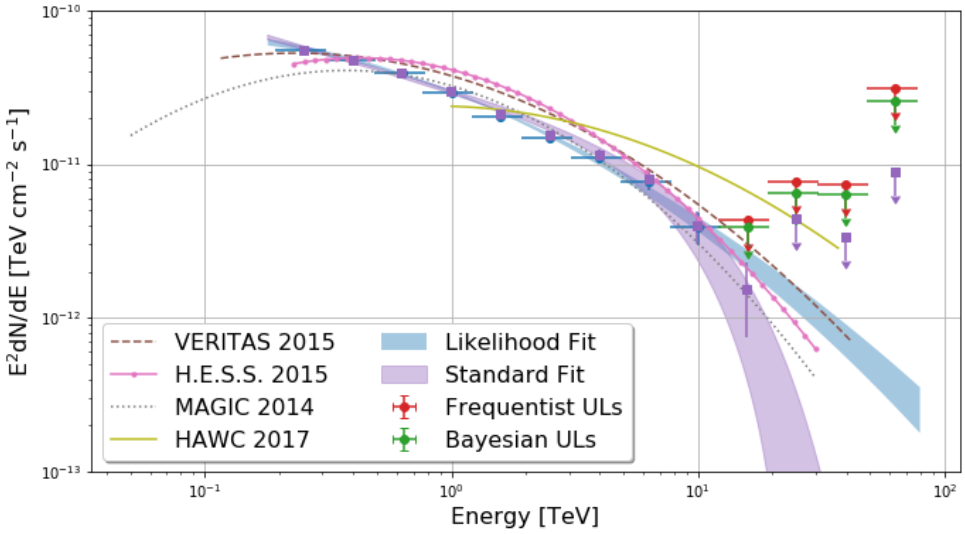

Figure 5.6: Differential energy spectrum of the Crab Nebula. The 1-σ confidence interval on the best-fit log-parabola obtained using the binned-likelihood analysis is plotted as a blue shaded region. The spectral points obtained from the likelihood fit are plotted as blue circles. The 1-σ confidence interval on the best-fit log-parabola obtained using a standard χ^2 analysis is plotted as a purple shaded region. The spectral points derived from the standard analysis are plotted as purple squares. Note in this fit only energy bins with > 5 On counts and $> 2\sigma$ excess significance are included in the χ^2 fit, bins failing to meet this criteria are plotted as 95% confidence level upper limits (Rolke et al., 2005). 95% confidence level upper limits are plotted for the likelihood energy bins if either the bin-wise fit fails or the TS of the energy bin is < 9 ($\sim 3\sigma$). For comparison the Crab energy spectra as measured by other instruments are plotted. MAGIC (dotted gray line, Aleksić et al., 2015), VERITAS (dashed brown line, Meagher, 2015), H.E.S.S. (magenta line with points, Holler et al., 2015), HAWC (solid yellow line Abeysekara et al., 2017)

the log-likelihood equation (Equation 5.16) is:

$$l(\Theta) = \sum_{i_e,i_\omega} \left[N_{ON_{i_e,i_\omega}} log\left(S^{Pred}_{i_e,i_\omega}\right) - S^{Pred}_{i_e,i_\omega} \right]. \tag{5.43}$$

This describes the shape of the Figure 5.7. As $\log \mathcal{L}$ is not smooth near $\alpha_{i_e,i_\omega}(N_{ON_{i_e,i_\omega}}) < (\alpha_{i_e,i_\omega} + 1)S^{Pred}_{i_e,i_\omega}$, the estimated distance to the minimum (EDM) changes rapidly depending on the direction one approaches from. This is interpreted as a function error within Minuit. Taking the errors on this point to be $\Delta \log \mathcal{L} = -0.5$ the differential flux is determined to be $(1.24^{+0.22}_{-0.36}) \times 10^{-14}\text{cm}^{-2}\text{s}^{-1}\text{TeV}^{-1}$, however due to the irregular shape of the profile likelihood, a Bayesian-based confidence interval may be more relevant.

The data is also fit using the standard χ^2-analysis method. The 1-σ confidence interval of

the best-fit log-parabola model and differential flux points are plotted as a blue shaded region and blue circles in Figure 5.6. Energy bins with < 5 On counts or with $< 2\ \sigma$ excess are excluded from the fit and are plotted as 95% confidence level upper limits (blue arrows in Figure 5.6). There is excellent agreement between the two fitting procedures up until the last spectral point at 16 TeV. The upper limits above 16 TeV are in agreement with the best-fit binned-likelihood model. The standard χ^2 analysis method obtains upper limits using the method described by Rolke et al. (2005). In this method, an upper limit on the excess counts is obtained by assuming the observed On counts come from a Poisson distribution of mean $N_{Source} + \alpha N_{Off}$. The MLE of N_{Source} is found and the upper limit on N_{Source} found by finding the value such that $-2\Delta \log(\mathcal{L}) = C$ where C is the critical value for a $\chi^2_{1,1-\delta}$ distribution with significance level δ. The method used here differs slightly from the Rolke et al. (2005) method due to the inclusion of the IRFs in the forward folding processes.

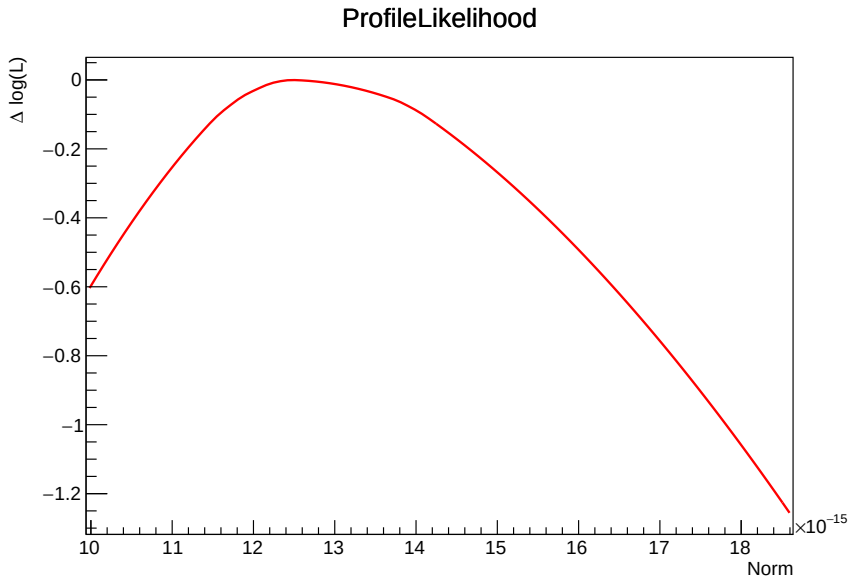

Figure 5.7: Irregular profile likelihood of the spectral point at 16 TeV. The form of the profile likelihood is described by Equation 5.43.

In addition to getting the differential energy spectrum from the total dataset, a binned-likelihood fit and standard χ^2-fit was applied to each of the 95 Crab runs. In both cases a power-law model was fit to the total data set and each individual run. For the χ^2-fit, the fit was performed only including significant energy bins and including all energy bins, with a significant energy bin defined as an energy bin with > 5 On counts and $> 2\sigma$ excess significance. A summary of the best-fit parameter distributions is given in Table 5.3. Figures 5.8 - 5.11 show the distributions of the best-fit parameters, the best-fits obtained from the binned-likelihood method are shown in blue and the χ^2-method are shown in green. The

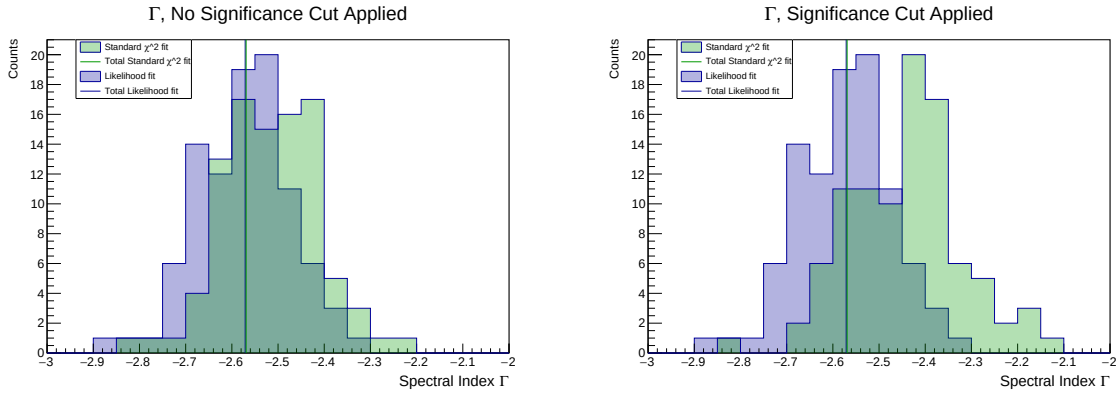

Figure 5.8: Distribution of best-fit power-law spectral indices (Γ) obtained using a binned-likelihood fit (blue) and standard χ^2 fit. The left panel shows the distribution of parameters when no significance cut is applied to the χ^2 fit. The right panel shows the distribution of parameters when a significance cut is applied to the χ^2 fit.

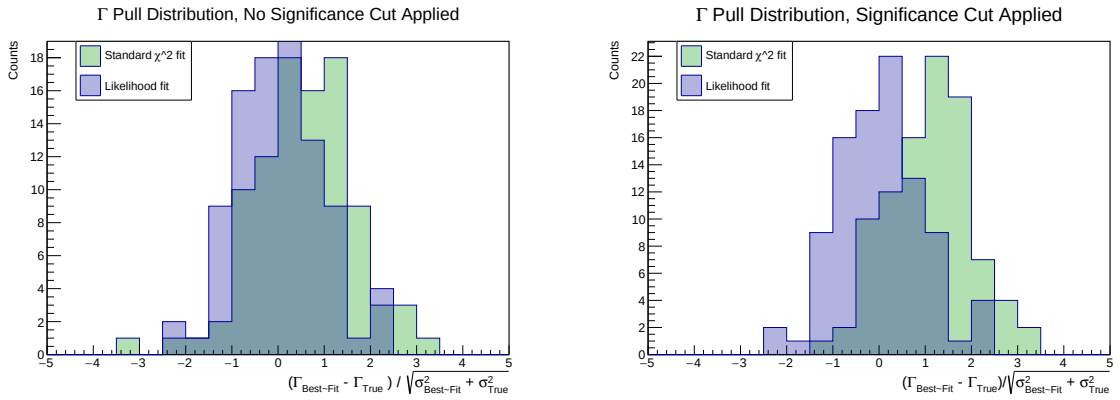

Figure 5.9: Pull distribution of best-fit power-law spectral indices (Γ) obtained using a binned-likelihood fit (blue) and standard χ^2 fit. The left panel shows the pull distribution when no significance cut is applied to the χ^2 fit. The right panel shows the pull distribution when a significance cut is applied to the χ^2 fit.

best-fit and 1-σ error on the best-fit parameters obtained from the total dataset are plotted as solid and dashed lines respectively.

Figures 5.8 and 5.9 show the distribution of spectral indices obtained from the fits without and with a significance cut applied to the bin significance. The results of a Gaussian fit to the pull distributions are summarized in Table 5.3. The binned-likelihood fit shows the smallest bias, with the mean of the best fit Gaussian being consistent with zero. By excluding insignificant data, in the χ^2 fit, the fit is biased towards harder spectral indices. This is due to the fact that observed data come from some distribution and by excluding insignificant data, only positive fluctuations of that distribution are allowed. Likewise this effect is seen in Figures 5.10 and 5.11 which show the distribution of normalizations obtained from the fits

Fit Type	μ	σ
Binned Likelihood		
Γ	-0.10 ± 0.10	0.92 ± 0.08
N_0	0.15 ± 0.20	1.58 ± 0.25
χ^2 (No Significance Cut)		
Γ	0.35 ± 0.13	1.09 ± 0.14
N_0	0.26 ± 0.15	1.23 ± 0.14
χ^2 (Significance Cut)		
Γ	0.78 ± 0.10	0.88 ± 0.07
N_0	0.89 ± 0.14	1.11 ± 0.14

Table 5.3: Best-fit Gaussian parameters (μ - mean , σ - standard deviation) of the pull distributions for the different fitting procedures.

without and with a significance cut applied. When insignificant energy bins are excluded, brighter spectral models are preferred. Note the standard deviations of pull distributions for the normalization are systematically larger than one would expect if the errors were correctly accounted for. As the atmosphere itself is a component of the detection apparatus, results are therefore affected by atmospheric effects, for example aerosols (see, Hahn et al., 2014, for a discussion on the effect of aerosols on Cherenkov transparency for IACT data). The estimated systematic uncertainty due to atmospheric variation is $\sim 15\%$. Taking into account a 15% uncertainty in the flux normalization when calculating the pull distributions accounts for the discrepancy between the observed standard deviation and the expected.

Figure 5.12 shows the distribution of χ^2-values obtained from the binned-likelihood method using Equation 5.20. In fitting the run-wise data, the final two energy points were excluded from the analysis. This is due to the final two energy bins in the time-averaged dataset (Figure 5.6) having zero and one On counts, respectively. This suggests only one run is contributing to the higher number of degrees of freedom. Hence, the number of energy bins is 11, with 2 free fitting parameters, giving the expected number of degrees of freedom as 9. A χ^2-distribution with 9 degrees of freedom is plotted as a red line in Figure 5.12. The distribution is in good agreement with the $\chi^2_{\nu=9}$-distribution.

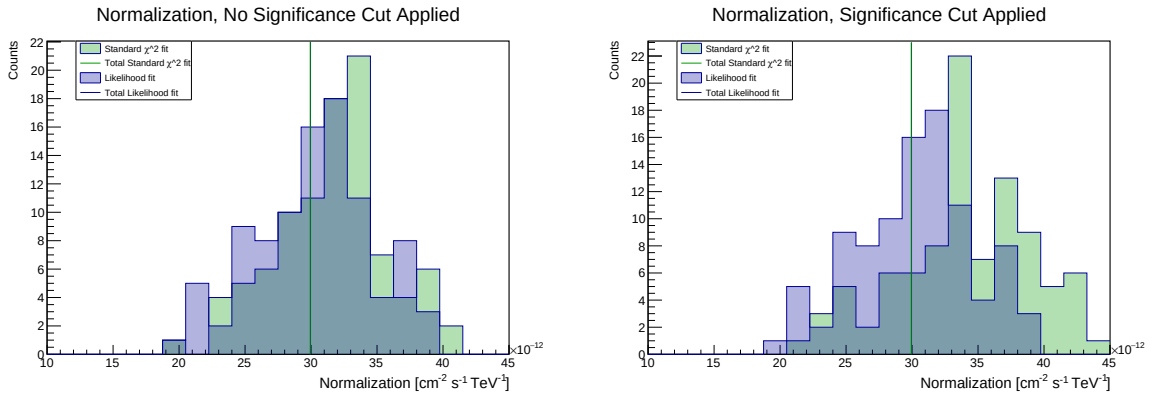

Figure 5.10: Distribution of best-fit power-law normalization (N_0) obtained using a binned-likelihood fit (blue) and standard χ^2 fit. The left panel shows the distribution of parameters when no significance cut is applied to the χ^2 fit. The right panel shows the distribution of parameters when a significance cut is applied to the χ^2 fit.

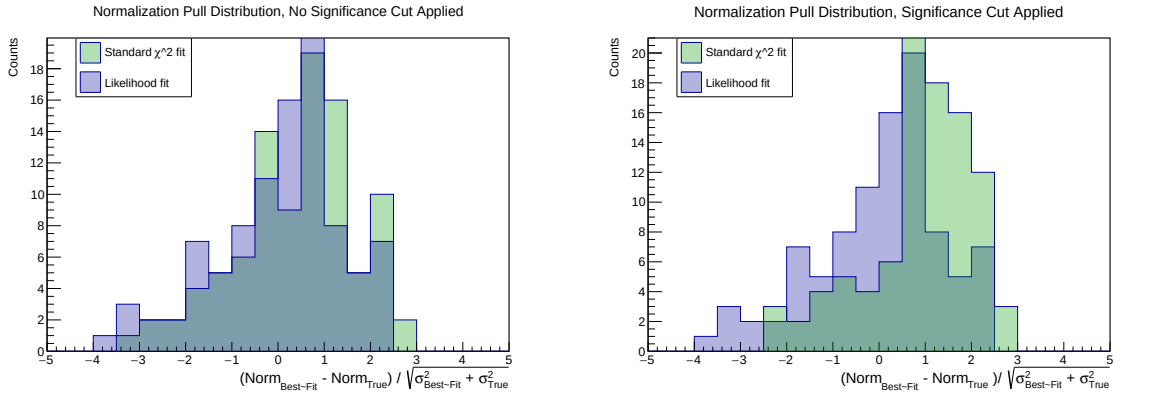

Figure 5.11: Pull distribution of best-fit power-law normalization (N_0) obtained using a binned-likelihood fit (blue) and standard χ^2 fit. The left panel shows the pull distribution when no significance cut is applied to the χ^2 fit. The right panel shows the pull distribution when a significance cut is applied to the χ^2 fit.

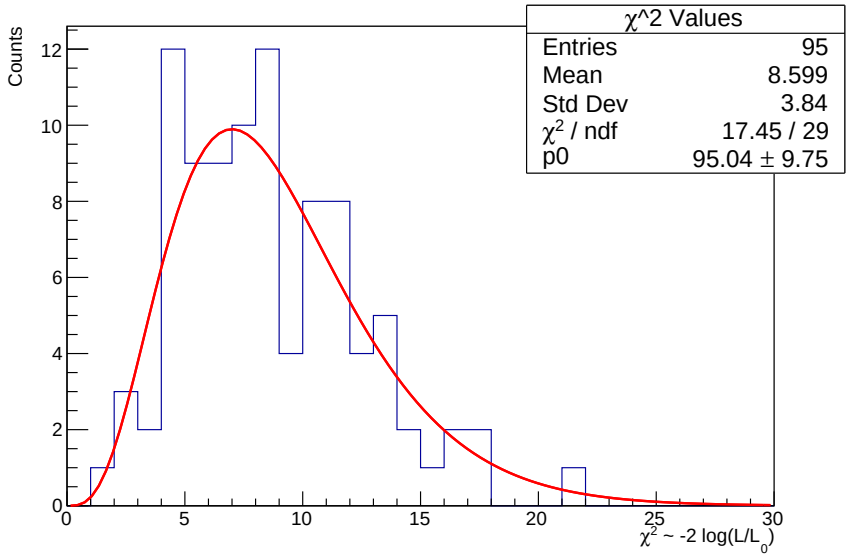

Figure 5.12: Distribution of χ^2-values obtained from a binned-likelihood fit of a power-law model to 95 Crab Nebula observations. A χ^2-distribution with 9 degrees of freedom (plotted as a red line) is fitted to the distribution of χ^2-values, with a scale factor allowed to vary.

5.5.2 BL Lac 2016 Flare

BL Lacertae (BL Lac) is an IBL located at a redshift of z = 0.069. Historically, BL Lac is a well-studied and important source. Lending its name to the source class, BL Lac is the original prototype BL Lac Object, making it one of the most studied objects in the extragalactic sky. BL Lac was originally detected at VHE by the MAGIC collaboration during an observational campaign between 2005 and 2006 with a time-averaged flux of $\sim$ 3% Crab (Albert et al., 2007). Since its detection long term monitoring of the source has revealed intense VHE flaring with rapid variability time scales. In 2011 VERITAS observed the decay of an exceptionally bright VHE flare with a peak flux of $\sim$ 125% Crab and a variability timescale of 13 ± 4 minutes (Arlen et al., 2013).

Due to its variability, BL Lac is regularly monitored by VERITAS. On 5th October 2016, VERITAS observed the rise and fall of a bright ($\sim$ 125% Crab) flare. The observations of this flare, reported in Abeysekara et al. (2018a), result in a strong 70σ detection within 153 minutes of observations. The brightness of this source and its known redshift, makes this dataset an excellent test dataset for verifying the binned-likelihood method.

Figure 5.13 shows the differential energy spectrum obtained from observations of BL Lac on 5th October 2016. The secondary analysis for the results reported in Abeysekara et al. (2018a) was obtained by myself using an earlier version of the Event Display analysis

package (`v480-b`). This data was reanalysed with a newer version of Event Display (`v480-f pre-release`) in which binned-likelihood analysis has been implemented. The energy spectrum is best fit by a log-parabola model of the form:

$$\frac{dN}{dE} = 2.57^{+0.19}_{-0.17} \times 10^{-10} \left(\frac{E}{0.4\ \mathrm{TeV}}\right)^{\left(-(3.72\pm0.11)-0.67^{+0.21}_{-0.23}\log\left(\frac{E}{0.4\ \mathrm{TeV}}\right)\right)} \mathrm{cm}^{-2}\mathrm{s}^{-1}\mathrm{TeV}^{-1}, \tag{5.44}$$

with $\chi^2/NDF = 0.6/2$. A power-law model was also fit to the data resulting in a best-fit power-law index of $\Gamma = 3.64 \pm 0.08$, and $\chi^2/NDF = 13.8/3$. The likelihood ratio test can be applied as:

$$\chi^2_{\nu=1} = \chi^2_{PWL} - \chi^2_{LP}, \tag{5.45}$$

where $\chi^2_{PWL/LP}$ is the χ^2-value for the power-law/log-parabola model. This results in $\chi^2 = 13.2$, hence the power-law model is rejected with $> 99.9\%$ certainty.

A fit to the intrinsic differential energy spectrum is applied by assuming a Franceschini et al. (2008) EBL model (see Figure 5.14), by invoking Equation 5.29 during the fitting procedure. The intrinsic spectrum is best-fit by a log-parabola of the form:

$$\frac{dN}{dE} = 3.29^{+0.24}_{-0.22} \times 10^{-10} \left(\frac{E}{0.4\ \mathrm{TeV}}\right)^{\left(-(3.36^{+0.10}_{-0.11})-0.55^{+0.20}_{-0.22}\log\left(\frac{E}{0.4\ \mathrm{TeV}}\right)\right)} \mathrm{cm}^{-2}\mathrm{s}^{-1}\mathrm{TeV}^{-1}, \tag{5.46}$$

with $\chi^2/NDF = 0.64/2$.

As shown in Figure 5.13, the results of the binned-likelihood fits are in excellent agreement with the results reported by Abeysekara et al. (2018a). The χ^2/NDF values obtained for the likelihood fit to the intrinsic and observed spectra suggest that the model is over fitting the data $\chi^2/NDF < 1$. As the power-law fit provides an insufficient fit and the log-parabola model is the next degree of complexity over a power-law model, this would suggest not that the model is over fitting the data, rather that the errors on the data are over estimated. This would explain the low χ^2/NDF values obtained. This appears to be specific to the BL Lac dataset, rather than a relic of the analysis method as the χ^2 values obtained by fits to the Crab dataset (see Figure 5.12) is in excellent agreement with the expected χ^2 distribution.

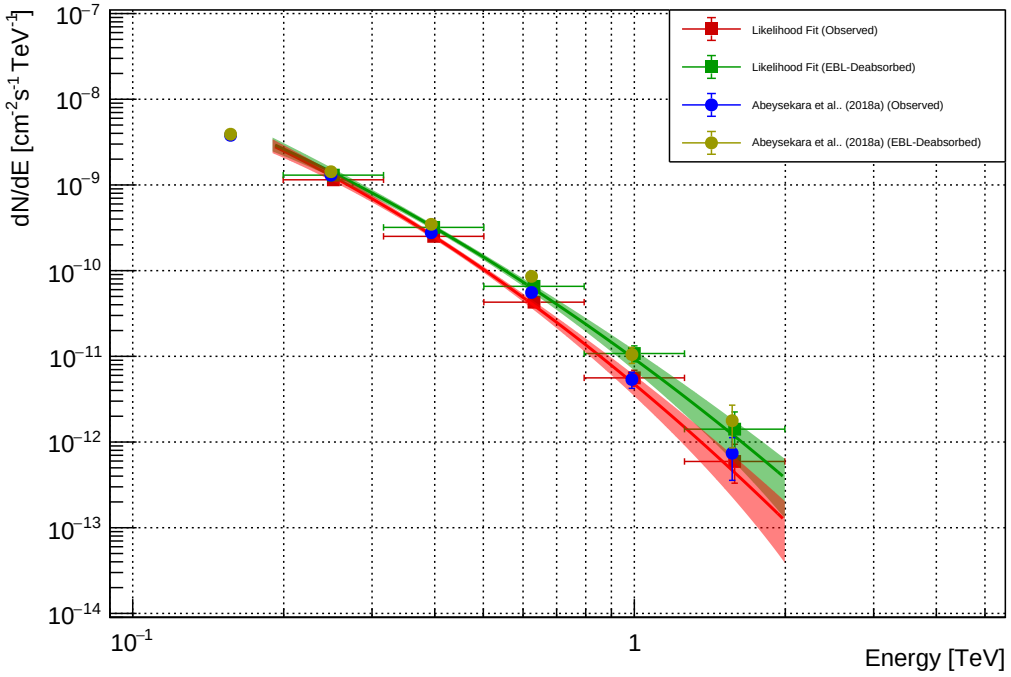

Figure 5.13: Energy spectrum of BL Lac obtained on the 5th October 2016. The blue and brown circles show the energy spectrum as recorded by Abeysekara et al. (2018a) before and after attenuation due to a Franceschini et al. (2008) EBL model respectively. The red points are the energy spectral points obtained by a binned likelihood analysis with the red line and red shaded region represent the best-fit log parabola and the 1 σ confidence interval obtained from a binned-likelihood fit respectively. The green points show the energy spectral points obtained by convolving a Franceschini et al. (2008) EBL model with the binned-likelihood analysis. The green line and green shaded region represent the best fit log-parabola and 1-σ confidence interval obtained from a binned-likelihood analysis.

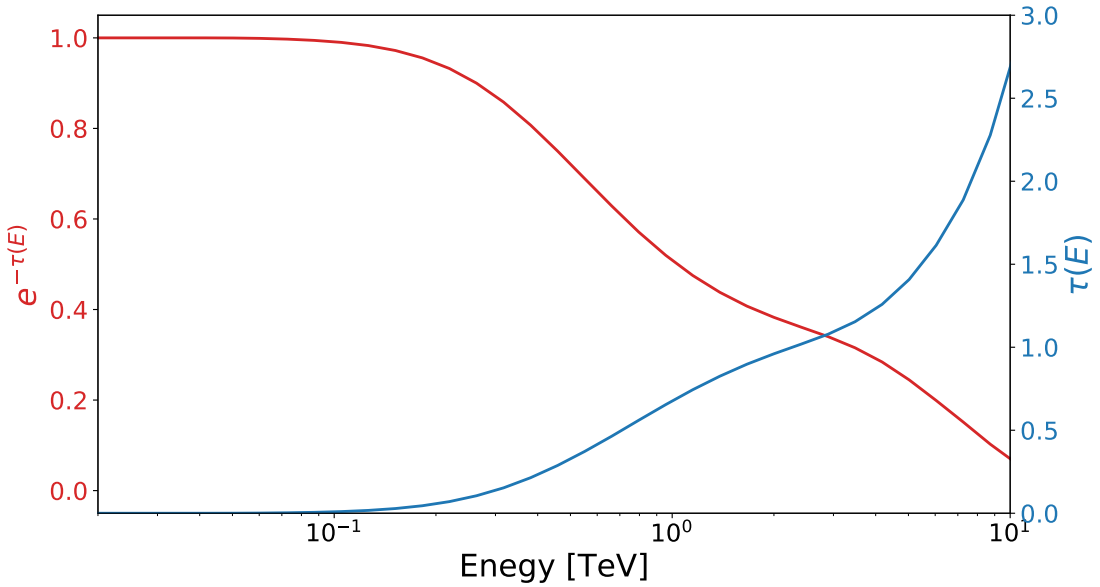

Figure 5.14: Plot of EBL opacity ($\tau(E)$, shown in blue) and EBL attenuation factor ($e^{-\tau(E)}$, shown in red) for a Franceschini et al. (2008) EBL model assuming for a redshift of 0.069.

5.6 Discussion

Likelihood analysis provides a powerful and versatile tool for analysing and interpreting astronomical data. While only spectral fitting has been discussed here, likelihood techniques have applications in a number of different regimes, allowing for temporal to morphological studies to be conducted. In this section some of the possible applications are discussed.

5.6.1 Flux Analysis

The binned-likelihood analysis can be extended to obtain the integral flux of an observation. This can be done by simply applying a fit to the integral flux rather than the flux normalization. One can therefore obtain values such as a variability index to test the stability of the source's flux level over an observing campaign, whilst taking into account the effect of the IRFs on individual events in the calculation, unlike a standard χ^2 variability test. Robust variability tests are essential for any future catalog of VHE emitters. This is used in the analysis of OJ 287 (see Chapter 7) and discussed further in Appendices A.1 and A.2.

5.6.2 Source Morphology

The binned-likelihood analysis can be naturally adapted to allow for modeling of the source morphology. Equation 5.10 can be adapted to produce the model predicted excess counts at a point within the FoV. This is done by considering the VERITAS point spread function and energy dependent radial acceptance:

$$S^{Pred}_{i_e,i_z}(\vec{r}) = T_{ON} \int_{\tilde{E}^{min}_{i_e}}^{\tilde{E}^{max}_{i_e}} R(\tilde{E}, \mathbf{\Omega}, \vec{r}) P(\tilde{E}, \mathbf{\Omega}, \vec{r}, \vec{r_0}) d\tilde{E} \int_0^\infty dE \left(\frac{d\phi}{dE}\right)^{Pred} A_{eff}(\mathbf{\Omega}, E) \gamma(\mathbf{\Omega}, E \rightarrow \tilde{E}), \tag{5.47}$$

where $\vec{r}$ is the location of interest within the FoV, $\vec{r_0}$ it the location of the source, $P(\tilde{E}, \mathbf{\Omega}, \vec{r}, \vec{r_0})$ is the point spread function and $R(\tilde{E}, \mathbf{\Omega}, \vec{r})$ is the energy dependent radial acceptance at location $\vec{r}$. In order to obtain $R(\tilde{E}, \mathbf{\Omega}, \vec{r})$ one needs to understand how the radial acceptance of the camera changes with energy. To do this one needs detailed observations of dark FoVs and observations of highly extended source with known energy profile. While the time to take such observations is expensive, it could possibly be done by taking so-called "raster scans" of a known VHE source such as the Crab Nebula (see, for example, Bird et al., 2015). A raster scan works by adjusting the telescope's pointing software so that it believes that it is pointing at the target, while it is in fact offset by a known amount. By applying a change to only the pointing software, no changes need to be made to existing analysis software. A raster scan can therefore smear a known point source to appear as an extended source.

5.6.3 Multi-Instrument Fitting

Two or more likelihood equations can be "combined" to get a joint-likelihood. This can allow one to obtain the joint-likelihood fit of a source, obtained by two or more instruments. For example, one could apply a joint-likelihood fit to VERITAS and *Fermi*-LAT data:

$$\mathcal{L}(\mathbf{\Theta}|\mathbf{N}) = \mathcal{L}_{\mathbf{VERITAS}}(\mathbf{\Theta}|\mathbf{N}) \mathcal{L}_{\mathbf{Fermi-LAT}}(\mathbf{\Theta}|\mathbf{N}), \tag{5.48}$$

where $\mathcal{L}_{VERITAS/Fermi-LAT}(\mathbf{\Theta}|\mathbf{N})$ is the likelihood of observing model parameters Θ given data N by VERITAS/*Fermi*-LAT. The log-likelihood equation can be simply written as:

$$\log \mathcal{L}(\mathbf{\Theta}|\mathbf{N}) = \log \mathcal{L}_{\mathbf{VERITAS}}(\mathbf{\Theta}|\mathbf{N}) + \log \mathcal{L}_{\mathbf{Fermi-LAT}}(\mathbf{\Theta}|\mathbf{N}), \tag{5.49}$$

hence a joint-likelihood fit can be obtained by simply summing the log-likelihood of the respective instruments. A joint-likelihood fit allows a model to be tested across a far

larger energy range and allows the analysis to be extended, by incorporating the strengths of different instruments (for example energy resolution, FoV, sensitivity, etc). This method is being implemented by a number of different collaborations (see, for example 3ML, Vianello et al., 2015) to allow joint-fitting of sources using two or more instruments. Future CTA data will be processable using software such as CTools (Knödlseder et al., 2016) which shall allow for joint-likelihood fitting of CTA data with other experiments such as *Fermi*-LAT.

Chapter 6

Upper Limits on the Very-High-Energy Gamma-Ray Flux of Six Candidate TeV Blazars

6.1 Overview

In this section the observations and analysis of several TeV blazar candidates are discussed. In the absence of detections, the upper limits on the VHE flux of these sources are presented. As discussed in Section 1.2, there are 75 AGN which have been discovered at VHE energies. Of the 75 sources, the majority of these objects belong to the BL Lac class of objects, with HBL being the dominant subclass detected at VHE energies. For a summary of the latest results for the major IACTs see Benbow (2017, (VERITAS)), Taylor et al. (2017, (H.E.S.S.)) and Sitarek et al. (2017, (MAGIC)).

Despite the number of sources detected at VHE energies, the true distribution of the different source classes, their SEDs and temporal properties, are not well understood. This is because many detections of VHE emission occur during periods of enhanced brightness. To fully study the properties of TeV blazars, one needs to consider an unbiased sample of objects as to not bias towards extreme events. Flaring events in particular may point to atypical events, somewhat unrelated to low-state VHE emission that has been observed from some sources.

In order to provide an unbiased study of sources, deep and regular observations are required. These types of observation campaigns are very time intensive for IACTs, and generally targeted observations of particularly promising TeV blazar candidates are more favorable (see, for example, Archambault et al., 2016; Aleksic et al., 2011; Abramowski et al., 2014). Indeed, truly unbiased surveys of the VHE sky are only viable to survey instruments such as HAWC (see, 2HWC catalog, Abeysekara et al., 2017), which have poorer resolution and sensitivities than their IACT counter parts.

Despite the time requirements, regular unbiased monitoring campaigns on individual

sources allow for the study of the temporal evolution of targeted sources. This method has been adopted by the FACT collaboration to study a number of bright sources (see, for example, Dorner et al., 2015).

In the absence of a detected VHE signal, it is common to place upper limits on the flux from sources. Upper limits provide important constraints on the broadband spectral properties of the source, and allow constraints to be placed on the high-energy emission processes. Upper limits may also be of interest for future experiments (such as CTA), by providing an limit on the flux level, and therefore the detectability of a source.

The work presented in this chapter is part of a scaled down blazar discovery program currently being performed by VERITAS. This scaled down program has three main components. The first component corresponds to deep observations on a select few promising VHE blazar candidates which have historically shown a moderate excess significance ($> 3\sigma$), such as the six sources reported here. The second component is survey based, in that it aims to obtain observations at all promising VHE blazar candidates as identified by surveys such as hard and bright 2FHL sources[1], and the 2WHSP survey[2] (see Section 6.2). An example of a recent AGN detected from this program would be RGB J2056+ 496 (Mukherjee et al., 2016). The final component corresponds to a target of opportunity follow up program. In this program, multiwavelength data from various sources is regularly monitored for enhanced activity that might suggest enhanced TeV activity. An example of a recent detection from this program would be OJ 287 which will be discussed further in Chapter 7. Upper limits will be calculated for sources not yet detected and presented in an up coming publication, of which I will be a co-author. This publication will include ~700 and ~400 hours of previously unpublished SHV and RHV data, respectively. This builds upon the work previously presented by the VERITAS Collaboration (Archambault et al., 2016). Archambault et al. (2016) present upper limits on 114 blazars based on observations taken by VERITAS between 2007 and 2012, resulting in a total live time of ~570 hours. In addition to calculating upper limits, Archambault et al. (2016) also perform a stack significance analysis of the blazars, which shows a $\sim 4\sigma$, suggesting a population of blazars below the sensitivity of the analysis. Archambault et al. (2016) also note that the majority of this significance is due to nearby ($z < 0.6$) HBLs, a feature also reported by Aleksic et al. (2011).

In this chapter upper limits on the VHE flux from six candidate TeV blazars are discussed. In Section 6.2 the resources used in selecting the targets are discussed, and a summary of their

[1]Candidate sources are selected based on their spectral index ($\Gamma_{2FHL} < 2.0$ or $\Gamma_{2FHL} < 2.8$) and how that relates to the sources brightness (using the test statistic (TS) as a proxy, $TS_{2FHL} > 25$ or $TS_{2FHL} > 28$)

[2]Promising VHE detection candidates are blazars with a TeV figure of merrit > 1. This is discussed in Section 6.2

multiwavelength properties is presented. In Section 6.3 the results of VERITAS observations are presented and 99% confidence level (CL) upper limits are calculated. A dedicated *Fermi*-LAT analysis is also presented and compared to the VERITAS results. In Section 6.4 the results are discussed in the context of future observational campaigns.

6.2 Selection Criteria

When selecting VHE detection candidates one must consider the multiwavelength properties of each source. In particular one must consider how specific multiwavelength properties maybe be indications of VHE activity from a source. To do this one generally relies on large population studies and how certain properties show a potential correlation to known VHE emitters. In this study a number of catalogs and surveys have been used to aid in the selection of detection candidates. A summary of the main sources is as follows:

- **The Einstein Slew Survey Sample of BL Lacertae Objects** (Perlman et al., 1996). A lot of early VHE observation campaigns focused on observations of nearby HBLs identified by the Einstein Slew Survey. Selecting bright objects in this survey essentially makes use of the assumption that HBLs are well described by SSC models. Under this simple assumption objects that are nearby, hard and bright in x-rays, should also be bright in VHE.

- **2WHSP** (Chang et al., 2017). The 2WHSP catalog identifies targets as potential VHE emitters based on the properties of their synchrotron peak. Again exploiting a simple SSC assumption, Chang et al. (2017) consider the intensity of the synchrotron peak ($\nu_{peak} F_{\nu_{peak}}$) of known HBLs and compares it to brightness of the dimmest blazar already detected in the TeV band. In doing so they arrive at a TeV "figure of merit" (FoM), where a FoM of 1 suggests that the HBL should be detectable at VHE energies by current generation IACTs. Many known VHE emitters are identified to have high FoM values, for example 1ES 1959+650, a nearby-bright HBL (z = 0.048, ~0.64 Crab)[3], has a FoM of 19.9. Hence potential candidates are identified as objects with a high TeV FoM.

- **The Second and Third *Fermi*-LAT Point Source Catalogs** (2FGL, 3FGL Nolan et al., 2012; Acero et al., 2015). The space-based *Fermi* gamma-ray telescope, provides excellent coverage of the HE gamma-ray sky. Deep exposures obtained by the LAT have allowed for extensive searches for point source HE-emitters. Cataloged in

[3] http://tevcat.uchicago.edu/?mode=1;id=79

2FGL and more recently 3FGL are detailed measurements of the spectral and flux properties of all detected HE emitting point sources within the surveys. Promising VHE candidates can be selected based on their extrapolated VHE properties, in particular the hardness and brightness of the source, reflected by the spectral index and integrated flux. A promising VHE candidate would be a bright source whose spectral index is also hard, suggesting that the flux level extrapolated into the VHE regime may be at a detectable level by current generation IACTs.

- **The Second and Third Catalog of Hard *Fermi*-LAT Sources** (2FHL, 3FHL Ackermann et al., 2016; Ajello et al., 2017). Similar to 2/3FGL, 2/3FHL provide a detailed study of the higher energy range accessible to *Fermi*-LAT. 3FHL undertakes a search for hard spectrum sources by analyzing *Fermi*-LAT data between 10 GeV and 2 TeV. The spectral details provided by the harder source catalogs are closer in energy range to the VHE regime, hence provide a more accurate extrapolation into the VHE regime.

- **VERITAS Archival Data**. VERITAS has observed a vast number of fields of view during its lifetime. Reanalysis of archival data, using advanced and more sensitive analysis techniques (see, for example, Krause et al., 2017; Christiansen et al., 2017), has revealed moderated excesses ($> 3\sigma$) within the archival dataset. In the cases of most of the observations presented here, while the multiwavelength sources mentioned above provided some of the initial motivation for observations, reanalysis of archival data has been the main justification for their inclusion in this work. In particular, observations taken during the 2016-2017 and 2017-2018 observational seasons were taken as part of a VERITAS deep observation campaign on promising VHE candidates, a proposal of which I was a co-P.I.

After considering the above multiwavelength sources, 6 detection candidates where chosen for targeted deep follow up observations with VERITAS. These targets are summarized in Table 6.1 and are discussed in the following sections.

AGN	z	FoM	ν_{peak}	Γ_{3FGL}	Γ_{3FHL}	ϕ_{3FHL} [$\times 10^{-10}$ cm^{-2}s^{-1}]	ϕ_{3FHL} (% Crab)
B2 0912+29	N/A	2.51	15.8	1.88 ± 0.04	2.39 ± 0.18	2.15 ± 0.28	1.43
1ES 1028+511	0.36	2.51	17.0	1.71 ± 0.07	1.94 ± 0.15	1.54 ± 0.22	3.90
1ES 1118+424	0.124	1.00	16.2	1.62 ± 0.06	2.07 ± 0.11	3.17 ± 0.32	5.51
3C 273[a]	0.158	N/A	N/A	2.66 ± 0.02	3.48 ± 0.74	0.49 ± 0.15	0.01
RGB J1243+364	> 0.485	3.16	16.2	1.77 ± 0.04	2.21 ± 0.13	3.23 ± 0.33	3.70
1ES 1255+244[b]	0.14	0.63	16.9	N/A	N/A	N/A	N/A

[a] 3C 273 is not included in 2WHSP.

[b] 1ES 1255+244 has not been detected by *Fermi*-LAT.

Table 6.1: Summary of VHE discovery targets. Column 1 shows the name of the source. Column 2 shows the redshift of the source. Column 3 shows the TeV FoM obtained by the 2WHSP survey. Column 4 shows the log of frequency of the synchrotron peak of the SED. Columns 5 and 6 show the spectral index obtained in the 3FGL and 3FHL catalogs. Column 7 and 8 shows the 3FHL and 3FHL flux extrapolated into the VHE regime (E > 200 GeV).

6.2.1 B2 0912+29

B2 0912+29 (RA: 09h 15′ 52.4016″, Dec: +29° 33′ 24.043″, J2000, Ma et al., 1998) is a HBL of uncertain redshift. In the Sloan Digital Sky Survey (SSDS) data release 7 (Adelman-McCarthy & et al., 2009), the redshift of the source is estimated to be $z = 1.585$ based on a photometric template-fitting approach, while a more recent SSDS release (release 13, SDSS Collaboration et al., 2016)) estimate the redshift to be $z = 1.2396 \pm 0.0002$. Furthermore Hwang et al. (2012) estimate the redshift to be $z = 1.521 \pm 0.001$, while Trichas et al. (2012) estimate the redshift to be $z = 1.0654$

Despite the potentially high redshift of B2 0912+29, it was initially selected as a detection candidate as it was one of the hardest and brightest objects in the 2FGL catalog. The 2WHSP TeV FoM value of 2.51 also suggests that, based on the brightness of the synchrotron peak, this source should be detectable at VHE energies. While observations between *Swift* and VERITAS in the 2013-2014 observational season, failed to yield a significant detection, reanalysis of B2 0912+29 has shown a moderate excess at the expected source location. The results of early VERITAS observations of B2 0912+29 have been reported by Archambault et al. (2016). They report on 11.7 hours of observation resulting in a 3.49σ excess. The 99% confidence level upper limit on the flux was determined to be 3.6% Crab. While the quoted excess significance is a pre-trials significance, the moderate excess has prompted further VERITAS observations. Here I report on 29.8 hours of observations taken between MJD 55570 (9th January 2011) and 58173 (24th February 2018). This corresponds to 18.1 hours of unpublished data.

6.2.2 1ES 1028+511

1ES 1028+511 (RA: 10h 31′ 18.52517″, Dec: +50° 53′ 35.8193″, J2000, Petrov, 2013) is a moderately distant (z = 0.360, Adelman-McCarthy & et al., 2009) HBL. Costamante & Ghisellini (2002) initially predicted this source to have a detectable VHE emission ($\phi(E > 300$ GeV$) = 4.2 \times 10^{-12}$cm^{-2}s^{-1}, 30% Crab) based on the radio to x-ray SED. Indeed, the x-ray brightness of this source places it as one of the brightest objects in surveys of BL Lacs such as the ROXY survey (Cavazzuti et al., 2007) and the Sedentary survey of extreme HBLs (Giommi et al., 2005).

More recently, the source has been identified as a promising candidate for VHE emission based on its *Fermi*-LAT properties. It is particularly hard in the 3FHL catalog, with a spectral index of 1.94, resulting in an extrapolated VHE flux of 3.9% Crab. 1ES 1028+511 has been identified in the 2WHSP catalog as a promising target, with a TeV FoM of 2.51. Furthermore,

its 2WHSP $\log_{10}\left(\nu_{peak}[Hz]\right)$ = 17.0 suggests that the source belongs to the extreme HBL subclass, a rare subclass which typically show hard VHE spectra.

Given the promising properties of this source, it has been subject to a lot of VHE interest. The MAGIC Collaboration (Aleksic et al., 2011), observed 1ES 1028+511 for 3.71 hours, resulting in a 1.20σ excess. Aleksic et al. (2011) determine the 99.7% CL upper limit on the integral flux above 140 GeV to be 3.3% Crab. Similarly, VERITAS have previously reported upper limits from 24.1 hours of observations (Archambault et al., 2016), where a 1.16σ excess resulted in a 99% CL upper limit on the integral flux above 182 GeV of 2% Crab.

Reanalysis of archival data has revealed a moderated excess at the source location. Here I report on 39.3 hours of observations taken between MJD 54828 (28th December 2008) and 58185 (8th March 2018). This corresponds to 15.2 hours of unpublished data.

6.2.3 1ES 1118+424

1ES 1118+424 (RA: 11h 20′ 48.06232″, Dec: +42° 12′ 12.4616″, J2000, Petrov, 2013) is a relatively nearby (z = 0.124, Mao, 2011) HBL. 1ES 1118+424 was initially targeted and observed by VERITAS during the 2009-2010 observing season as it was a nearby Einstein Slew survey blazar (Perlman et al., 1996), which showed a promising predicted VHE flux (Stecker et al., 1996). 1ES 1118+424 has been detected in the 1FGL, 2FGL and 3FGL *Fermi*-LAT source catalogs and also in the 1FHL, 2FHL and 3FHL hard source catalogs, showing that the source is both bright and hard in the HE band. Indeed, 1ES 1118+242 shows a promising VHE extrapolated flux of 5.51% Crab. More recently 1ES 1118+424 has been identified as a promising candidate for detection at VHE by the 2WHSP survey, with a TeV FoM of 1.

Using data taken by *Fermi*-LAT Brown (2014) claims the detection of VHE emission based on the detection of three >100 GeV photons with a high probability (>99%) of originating from 1ES 1118+424. Brown (2014) analyzed 5.3 years of *Fermi*-LAT data in the 100-300 GeV energy range, fitting the data with a power-law model resulting in a TS = 41.9 or $\sim 6.5\sigma$. The time-averaged flux was determined to be $F(E > 100\ \text{GeV}) = (2.47 \pm 1.26) \times 10^{-11}\ \text{cm}^{-2}\ \text{s}^{-1}$ (~4% Crab). The best-fit energy spectrum between 100-300 GeV was determined to be (Brown, 2014):

$$\frac{dN}{dE} = (0.9 \pm 5.2) \times 10^{-13} \left(\frac{E}{3795.5\ \text{MeV}}\right)^{-1.71 \pm 1.56} \text{photons cm}^{-2}\ \text{s}^{-1}\ \text{MeV}^{-1}.$$

It is worth noting that in the spectrum quoted above, the pivot energy of 3795.5 MeV is

an order of magnitude outside of the analysis regime. This results in the large errors on the flux normalization.

This claim of VHE emission was "confirmed" by Armstrong et al. (2015), who apply a cluster analysis to 6.25 years of *Fermi*-LAT events with energies $E > 100$ GeV. The cluster analysis showed marginal evidence of a cluster of VHE events around 1ES 1118+424 with a (model dependent) significance of 2.35σ. This prompted a full follow-up unbinned-likelihood analysis of events between 100-300 GeV, resulting in a TS of 34.34 or 5.86σ. The integral flux was determined to be $\phi\,(100 - 300\ \mathrm{GeV}) = (2.18 \pm 1.13) \times 10^{-11}\ \mathrm{cm}^{-2}\ \mathrm{s}^{-1}$ and the differential spectral index obtained from a fit between 0.1-100 GeV was determined to be $\Gamma = 1.55 \pm 0.05$.

This claim of VHE emission prompted renewed interest in 1ES 1118+424, with a co-ordinated ToO campaign between VERITAS and *Swift* being initiated, which resulted in a non-detection of the source. Based on 17 hours of observations, Archambault et al. (2016) determine a 99% CLs upper limit on the flux above 150 GeV of 2.8% Crab. Archambault et al. (2016) calculated the excess significance to be 0.39σ. A more recent reanalysis of this source using advanced analysis techniques showed a moderate excess at the source location, prompting further exposure on the source. Here I report on 32.4 hours of good quality observations taken between MJD 55206 (10th January 2010) and 58213 (5th April 2018). This corresponds to 15.4 hours of unpublished data.

6.2.4 3C 273

3C 273 (RA: 12h 29′ 06.69512″, Dec: +02° 03′ 08.6628, J2000, van Leeuwen, 2007), is well-studied[4] blazar located at a redshift of z = 0.158 (Tang et al., 2012). Its close proximity and brightness makes 3C 273 an excellent laboratory to study the emission processes in relativistic jets. Multiwavelength studies of this source have led to the discovery of discernible knots which have been resolved from radio to X-ray energies (see, for example, Jester et al., 2006; Uchiyama et al., 2006).

Despite the well-studied nature of 3C 273, the origin of the hard X-ray emission is still debated (see, Georganopoulos et al., 2006). Two popular explanations for the X-ray emission are that the emission is due to inverse-Compton scattering of the synchrotron-emitting elections off the CMB (IC-CMB) or due to synchrotron emission from a second population of electrons, different from the population responsible for the raido-optical synchrotron emis-

[4] 3C 273 is a source with a rich history. 3C 273 was one of the first radio quasars to be asociated with an optical counterpart. Spectral measurements of 3C 273 allowed for the identification of the observed emission lines to be the Balmer-series emission lines and $\mathrm{Mg}_{II}\lambda 2798$, observed at a redshift which suggested it was of extragalactic origin. See Peterson (1997) for a discussion of the historical significance of 3C 273.

sion. These two emission models result in different predictions for TeV emission. The second synchrotron model requires multi-TeV elections which could produce a TeV component in the SED due to inverse-Compton scatter of CMB photons. The IC-CMB model requires a cut-off in the electron energy distribution below TeV energies, hence the SED is expected to also cut-off below TeV energies. Using observations by *Fermi*-LAT, Meyer & Georganopoulos (2014) place an upper limit on any steady-state emission from 3C 237 in the high-energy regime and find it to be inconsistent with the IC-CMB model. A VERITAS detection of steady-state emission would rule out the IC-CMB. A detection or strong upper limit allows for testing of the second synchrotron model and for limits to be placed on the magnetic field and Doppler factor, as the IC-CMB component's flux level scales by B/δ (Georganopoulos et al., 2006).

3C 273 has been detected in the 1FGL, 2FGL and 3FGL *Fermi*-LAT point source catalogs and the 3FHL catalog. While the VHE extrapolated flux for this source isn't particularly promising, VHE emission is predicted by the second synchrotron model. This, combined with a moderate excess in a recent reanalysis of archival data with new techniques, has warranted further observations to be taken on 3C 273. Here I report on 124.98 hours of good quality observations taken between MJD 54592 (6th May 2008) and 58228 (20th April 2018).

6.2.5 RGB J1243+364

RGB J1243+364 (RA: 12h 43′ 12.73628″, Dec: +36° 27′ 43.9999, J2000, Petrov, 2011) is a HBL of unknown redshift. Analyzing SDSS spectra of RGB J1243+364, Plotkin et al. (2010) put a lower limit on the redshift of $z \geq 0.485$ based on Mg_{II} absorption. RGB J1243+364 shows a moderately hard 3FHL spectrum with an index of $\Gamma \sim 2$, giving a favorable VHE extrapolation of 3.7% Crab above 200 GeV. In addition to this the high TeV FoM of 3.16, makes this source a very promising VHE candidate.

VERITAS have previously observed this source, as reported by Aliu et al. (2012), for a total of 11.5 hours, resulting in a non-detection and a 99% confidence level upper limit on the integral flux > 150 GeV (3.1% Crab). Reanalysis of archival data with improved analysis techniques has revealed a moderate excess at the expected source location, thus prompting further VERITAS observations. Here I report on 25.8 hours of good quality observations taken between MJD 55189 (24th December 2009) and 58214 (6th April 2018). This corresponds to 14.3 hours of unpublished data.

6.2.6 1ES 1255+244

1ES 1255+244 (RA: 12h 57′ 31.931″, Dec: +24° 12′ 40.16, J2000, Cutri et al., 2003) was initially targeted by VERITAS as it was identified as a nearby (z = 0.14, Adelman-McCarthy & et al., 2009) HBL in the Einstein Slew Survey (Perlman et al., 1996). Archival observations of 1ES 1255+244 have shown a moderate excess at the source's location. Archambault et al. (2016) observed a 2.24σ excess, with a 99% confidence-level upper limit on the flux above 166 GeV of 2.5% Crab. Further reanalysis of this source with more advanced techniques has also shown a moderate excess at the source location.

Interestingly 1ES 1255+244 has not been detected in any of the *Fermi*-LAT catalogs. In addition, the TeV FoM obtained by the 2WHSP catalog is 0.63, suggesting that the source is not a strong detection candidate for current generation IACTs. Given the location of the synchrotron peak ($\log_{10}\left(\nu_{peak}[Hz]\right)$ = 16.9) and the moderate excess observed by VERITAS, this could be evidence that the source belongs to the extreme-HBL subclass. Dim objects belonging to this subclass are particularly difficult to detect with *Fermi*-LAT as the inverse-Compton peak is in the TeV regime. These sources typically have hard VHE energy spectra making them ideal sources of VHE photons, hence making them of great interest to photon propagation studies and studies of cosmological field studies such as the EBL and the inter-galactic magnetic field (IGMF). Here I report on 38.46 hours of good quality observations taken between MJD 54531 (6th March 2008) and 58214 (6th April 2018).

6.3 Results

6.3.1 VERITAS Analysis and Results

VERITAS analysis was performed on all good quality data, taken from each epoch (V4-V6) and both SHV and RHV high voltage configurations were used. A set of BDT cuts, optimized and verified a priori on soft spectrum sources ($\Gamma \sim 3.5$), was used, with all events triggering at least 2 telescopes and passing quality cuts considered. As likelihood-capable instrument response functions were not available at the time of analysis, standard analysis procedures, as discussed in Section 4.2.1, were used. In analyzing the flux, a spectral index of $\Gamma = 3.5$ was assumed in the effective area folding (see Section 4.2.8) and integral flux calculation.

The results of the VERITAS analysis of the detection candidates are summarized in Table 6.2. Column 5 of Table 6.2, reports the excess significance observed from all detected events. As none of the sources show an excess significance > 5σ, no detection is claimed for any of these sources. 99% CL upper limits are determined using the methodology of Rolke et al.

(2005), that is the spectral index is frozen at $\Gamma = 3.5$ and the upper limit on the number of excess events is obtained by analyzing the likelihood profile. This is implemented into the VERITAS analysis chain using the `TRolke` ROOT Cern class. The number of excess counts is converted to an upper limit on the flux normalization by correcting for exposure (lifetime and effective areas), before an assumed spectral model is used to obtain an upper limit on the integral flux using Equation 4.12. In calculating the upper limit, the energy threshold E_{Thresh} is chosen to act as a global energy threshold providing a safe analysis threshold for all observational epochs, therefore the upper limit is reported on only events above this common energy threshold. Details of the obtained upper limits are shown in Table 6.3

AGN	Live Time (Hours)	N_{On}	N_{Off}	Excess Significance (σ)	Additional Time Required ($t_{5\sigma}$) (Hours)
B2 0912+29	29.84	1416	7872	2.62	78.84
1ES 1028+511	39.26	1466	7938	3.57	37.75
1ES 1118+424	32.39	1466	7819	4.08	16.25
3C 273	124.98	4897	28022	3.04	213.11
RGB J1243+364	25.84	1078	5756	3.47	27.81
1ES 1255+244	38.46	1581	8564	3.69	32.15

Table 6.2: Summary of VERITAS analysis. Column 2 shows the live time (total deadtime-corrected exposure). Columns 3 and 4 show the number of On and Off counts observed with a normalization between the On and Off exposure of $\alpha = 0.167$. Column 5 shows the excess significance calculated using Equation 17 of Li & Ma (1983). Column 6 shows the additional time required to reach a 5σ detection, assuming a simple $\sigma/\sqrt{Hour}$ extrapolation.

AGN	$E_{Threshold}$ (GeV)	$N_{Excess} > E_{Threshold}$	$N_{Excess,UL}$	$\phi_{UL}(E > E_{Threshold})$ $\times 10^{-12}(\mathrm{cm}^{-2}\mathrm{s}^{-1})$	$\phi_{UL}(E > E_{Threshold})$ (% Crab)
B2 0912+29	150	46 ± 33.9	126.2	3.70	1.02
1ES 1028+511	250	106 ± 33.8	184.7	2.75	1.63
1ES 1118+424	150	82 ± 34.3	161.7	4.16	1.15
3C 273	250	181 ± 46.9	290.6	1.04	0.61
RGB J1243+364	200	49 ± 24.7	106.9	2.55	1.08
1ES 1255+244	200	76 ± 31.9	150.3	2.73	1.16

Table 6.3: Summary of the upper limits on the VHE flux. Column 2 shows the energy threshold of the analysis ($E_{Threshold}$). Column 3 shows the number of excess events above the analysis threshold. Column 4 shows the 99% confidence level upper limit on the number of excess events above the analysis threshold. Column 5 shows the 99% confidence level upper limit on the integral flux. Column 6 shows the same as Column 5 except in units of percentage of the Crab nebula flux.

6.3.2 *Fermi*-LAT Analysis

A dedicated analysis of *Fermi*-LAT data, taken between the start of the mission (2008-08-04) and 2018-04-20, was performed, this corresponding to 9.7 years of data. Events with energies between 100 MeV and 300 GeV were analyzed using standard data selection and quality criteria discussed in Section 4.3. Each source was analyzed using an EBL absorbed log-parabola model (`EblAtten::LogParabola`), in which a Franceschini et al. (2008) EBL model was assumed. For souces without a firm redshift measurement, the lower limit on the redshift was used. This corresponds to z = 1.0654 for B2 0912+29 and z = 0.485 for RGB J1243+364. The FoV of each source was analyzed for unaccounted sources by obtaining a TS map assuming a point-source model fit by a power-law model with spectral index frozen to $\Gamma = 2$. Additional point sources were added to the model when a point source with a $\sqrt{TS} > 5$ was found, however none were found significantly close to the sources of interest as to affect the fit results. Details of the best-fit *Fermi*-LAT results are summarized in Table 6.4.

AGN	Test Statistic (TS)	ϕ(100 MeV − 300 GeV) $\times 10^{-9}$(cm^{-2}s^{-1})	α	β
B2 0912+29	2474.1	10.71 ± 1.04	1.71 ± 0.05	0.05 ± 0.02
1ES 1028+511	1196.7	3.95 ± 0.55	1.59 ± 0.07	0.03 ± 0.02
1ES 1118+424	1781.6	3.83 ± 0.59	1.44 ± 0.09	0.03 ± 0.02
3C 273	25978.5	(3.13 ± 0.03) × 10^2	2.86 ± 0.02	0.10 ± 0.01
RGB J1243+364	3426.8	9.18 ± 0.83	1.56 ± 0.05	0.05 ± 0.01
1ES 1255+244	14.65	0.40[a]	2.00	N/A

[a] 95% CL upper limit assuming a power law model with $\Gamma = 2$.

Table 6.4: Summary of *Fermi*-LAT results. Column 2 shows the TS statistic for the optimized model. Column 3 shows the integral flux between 100 MeV and 300 GeV. Columns 4 and 5 show the best fit α and β parameters for a log-parabola model. In the case of 1ES 1255+244, Column 4 shows the assumes power law spectral index.

6.3.3 Source Specific Results

B2 0912+29

A 2.62σ excess was observed from B2 0912+29. The significance sky map and significance distribution are obtained and shown in Figure 6.1. No evidence of any unaccounted-for sources, or bright sections of the sky, is observed, and the significance distribution is well described by a Gaussian distribution with mean -0.038 and RMS of 1.034. The 99% CL upper limit above 150 GeV is determined to be 3.70×10^{-12} cm^{-2}s^{-1} or 1.02% Crab. Figure 6.2 shows the *Fermi*-LAT spectrum obtained between 100 MeV and 300 GeV, with the upper limit on the flux normalization at 1 TeV, obtained from the VERITAS analysis shown.

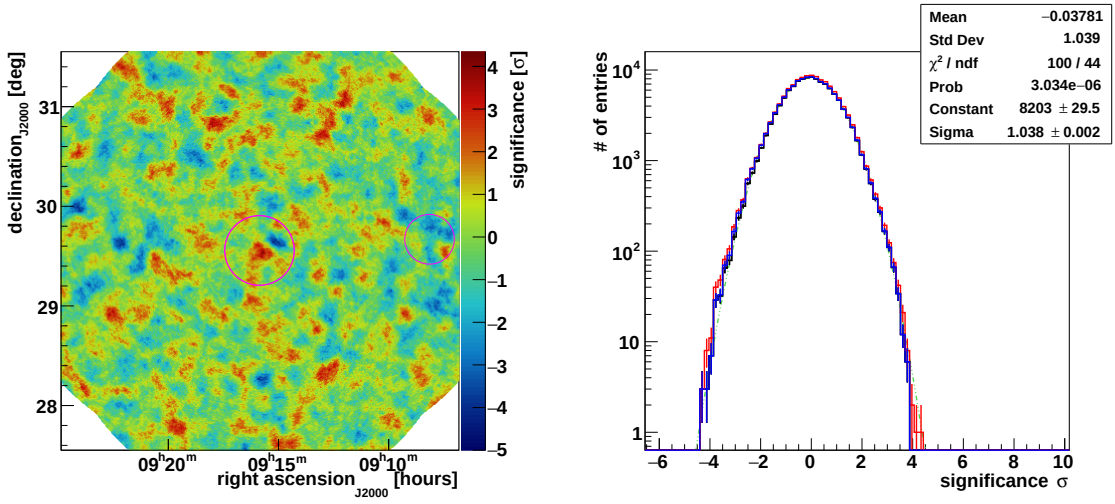

Figure 6.1: Left): Significance sky map centered on B2 0912+29. Regions shown as a red circle correspond to regions excluded from the background estimation and analysis. Right) Distribution of the significance of each point in the sky map shown on the left. The red line corresponds to the total sky map, blue corresponds to data excluding the On region and the black line corresponds to data excluding the On region and any other excluded regions. The green dot-dashed line is a Gaussian with mean of 0 and RMS of 1.

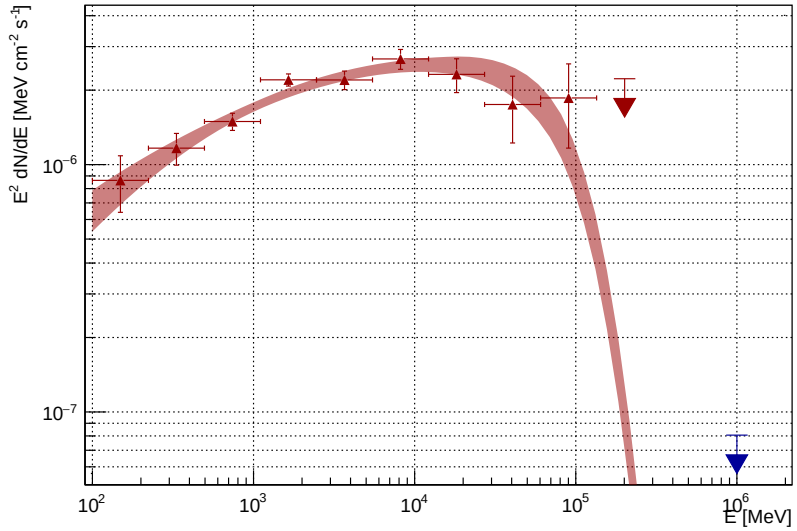

Figure 6.2: *Fermi*-LAT - VERITAS SED of B2 0912+29. The shaded red region corresponds to the 1-σ confidence interval on the best-fit *Fermi*-LAT spectrum obtained. The red points are the obtained differential flux points, where 95% CL upper limits are plotted for a TS< 9. The blue arrow is the observed VERITAS 99% upper limit at 1 TeV.

1ES 1028+511

A 3.57σ excess was observed from 1ES 1028+511. The significance sky map and significance distribution are obtained and shown in Figure 6.3. The significance distribution is well described by a Gaussian distribution with mean -0.002 and RMS of 1.041. There appears to be a hot spot located around ~0.5° to the north-west of the source, which extends the significance distribution to ~5σ. This location also happens to be one of the Off regions used in the background subtraction, which somewhat reduces the significance at the location of 1ES 1028+511. This location does not correspond to any known TeV source, hence there is no justification to exclude this region from the analysis. The 99% CL upper limit above 250 GeV is determined to be 2.75×10^{-12} cm^{-2}s^{-1} (1.63% Crab). Figure 6.4 shows the *Fermi*-LAT spectrum obtained between 100 MeV and 300 GeV, with the upper limit on the flux normalization at 1 TeV, obtained from the VERITAS analysis shown.

The extrapolated flux obtained from the *Fermi*-LAT fit between 100 MeV - 300 GeV is $\phi_{HE,Ext} = 1.13 \times 10^{-11}$ cm^{-2}s^{-1} or 1.60×10^{-12} cm^{-2}s^{-1} given a redshift of z = 0.36. This gives the ratio of $\phi_{UL}/\phi_{HE,Ext} = 1.72$, indicating that the upper limit derived here does not constrain the VHE flux further than the model-dependent constraints derived from the *Fermi*-LAT extrapolated spectrum.

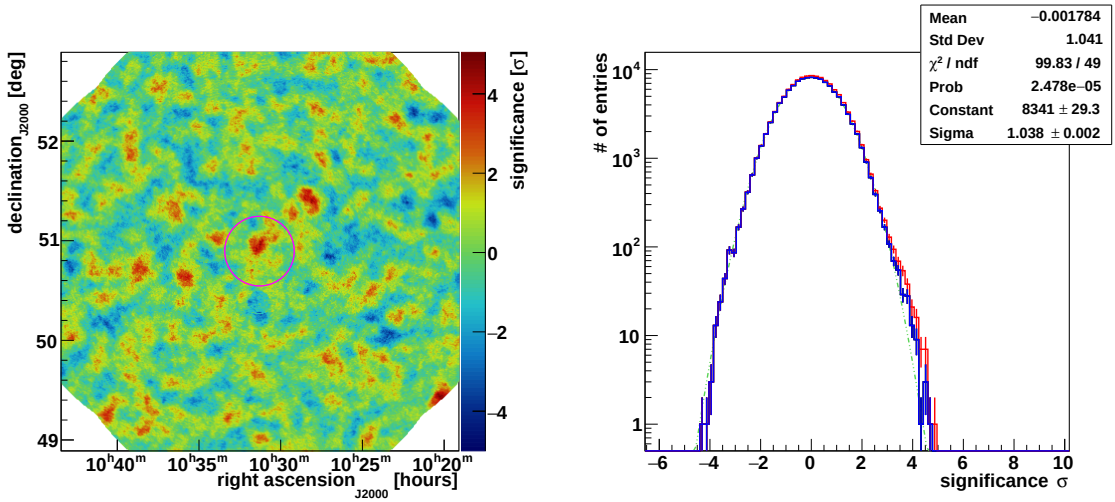

Figure 6.3: Left): Significance sky map centered on 1ES 1028+511. Regions shown as a red circle correspond to regions excluded from the background estimation and analysis. Right) Distribution of the significance of each point in the sky map shown on the left. The red line corresponds to the total sky map, blue corresponds to data excluding the On region and the black line corresponds to data excluding the On region and any other excluded regions. The green dot-dashed line is a Gaussian with mean of 0 and RMS of 1.

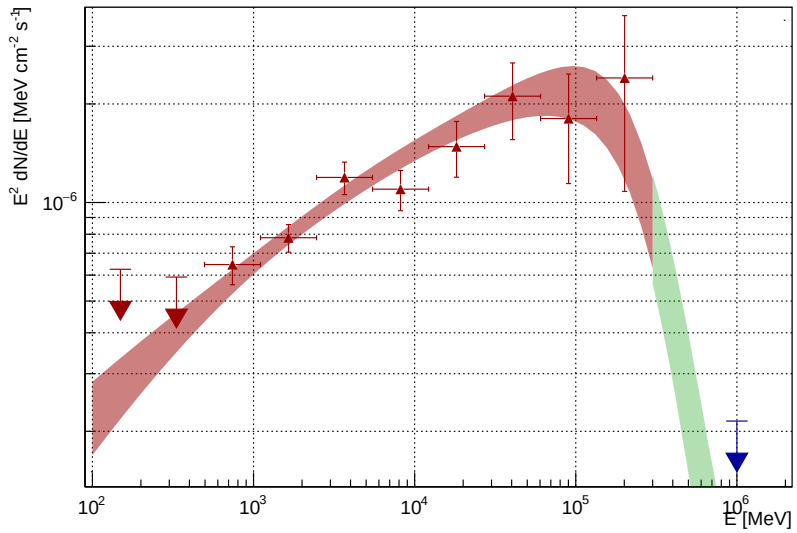

Figure 6.4: *Fermi*-LAT - VERITAS SED of 1ES 1028+511. The shaded red region corresponds to the 1-σ confidence interval on the best-fit *Fermi*-LAT spectrum obtained. The red points are the obtained differential flux points, where 95% CL upper limits are plotted for a TS< 9. The green shaded region shows the Fermi-LAT spectrum extrapolated into the VHE regime, assuming a Franceschini et al. (2008) EBL model. The blue arrow is the observed VERITAS 99% upper limit at 1 TeV.

1ES 1118+424

A 4.08σ excess was observed at the location of 1ES 1118+424. The significance sky map and significance distribution are obtained and shown in Figure 6.5. No evidence of any unaccounted-for sources, or bright sections of the sky, is observed, and the significance distribution is well described by a Gaussian distribution with mean -0.014 and RMS of 0.995. The significance distribution, including the On region (shown as a red line in the right panel of Figure 6.5) extends beyond 5σ. The interpretation of this will be discussed in Section 6.4. The 99% CL upper limit above 150 GeV is determined to be 4.16×10^{-12} cm^{-2}s^{-1} (1.15% Crab). Figure 6.6 shows the *Fermi*-LAT spectrum obtained between 100 MeV and 300 GeV, with the upper limit on the flux normalization at 1 TeV, obtained from the VERITAS analysis shown.

The extrapolated flux obtained from the *Fermi*-LAT fit between 100 MeV - 300 GeV is $\phi_{HE,Ext} = 4.37 \times 10^{-11}$ cm^{-2}s^{-1} or 2.69×10^{-11} cm^{-2}s^{-1} given a redshift of z = 0.124. This gives the ratio of $\phi_{UL}/\phi_{HE,Ext} = 0.15$, indicating that the upper limit derived here places tighter constraints on the VHE flux than those obtained by *Fermi*-LAT. This suggests a turn over in the HE-VHE spectrum which EBL attenuation alone cannot account for.

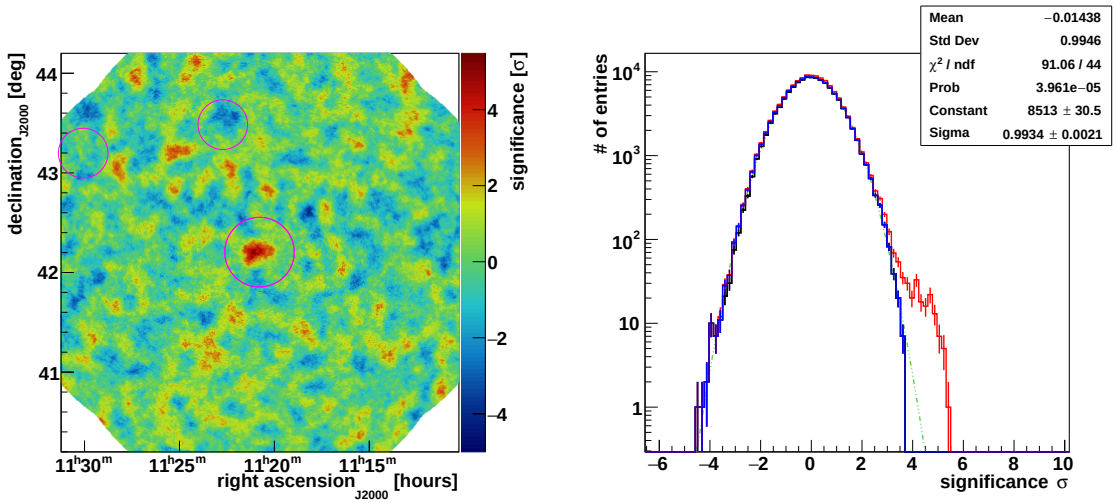

Figure 6.5: Left): Significance sky map centered on 1ES 1118+424. Regions shown as a red circle correspond to regions excluded from the background estimation and analysis. Right) Distribution of the significance of each point in the sky map shown on the left. The red line corresponds to the total sky map, blue corresponds to data excluding the On region and the black line corresponds to data excluding the On region and any other excluded regions. The green dot-dashed line is a Gaussian with mean of 0 and RMS of 1.

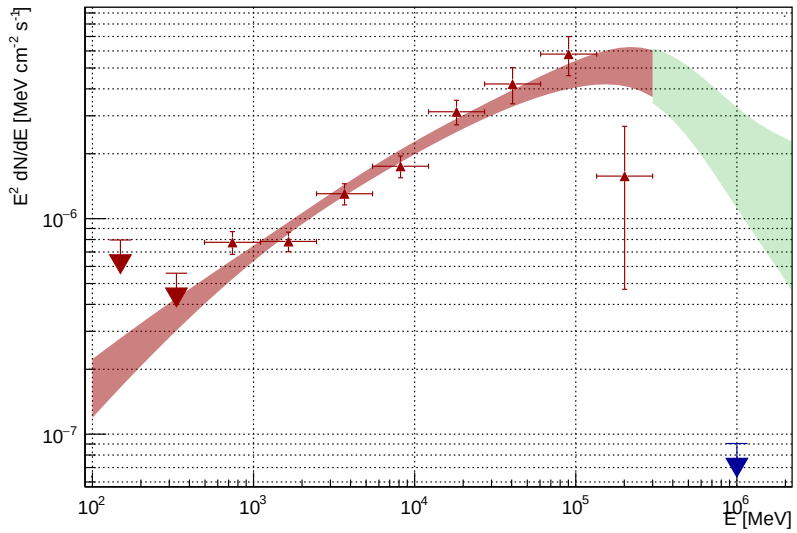

Figure 6.6: *Fermi*-LAT - VERITAS SED of 1ES 1118+424. The shaded red region corresponds to the 1-σ confidence interval on the best-fit *Fermi*-LAT spectrum obtained. The red points are the obtained differential flux points, where 95% CL upper limits are plotted for a TS< 9. The green shaded region shows the Fermi-LAT spectrum extrapolated into the VHE regime, assuming a Franceschini et al. (2008) EBL model. The blue arrow is the observed VERITAS 99% upper limit at 1 TeV.

3C 273

A 3.04σ excess was observed from 3C 273. The significance sky map and significance distribution are obtained and shown in Figure 6.7. No evidence of any unaccounted-for sources, or bright sections of the sky, is observed, and the significance distribution is well described by a Gaussian distribution with mean -0.037 and RMS of 1.032. The 99% CL upper limit above 150 GeV is determined to be 1.04×10^{-12} cm^{-2}s^{-1} (0.06% Crab). Figure 6.8 shows the *Fermi*-LAT spectrum obtained between 100 MeV and 300 GeV, with the upper limit on the flux normalization at 1 TeV obtained from the VERITAS analysis shown.

Curiously, archival VERITAS observations of this source have yielded a moderate excess around the source location. Figure 6.9 shows a plot of the cumulative significance of this source vs $\sqrt{Hours}$ (plotted assuming 10% dead time on all observations). A peak significance of 4.75σ occurs after ~55 hours of observations. While this may be an indication of long-term variability of the source, but it also roughly coincides with the upgrade of the VERITAS camera's PMTs (start of V6 observations). It is noteworthy that the energy threshold chosen for deriving upper limits of 250 GeV approximately corresponds to the pre-camera upgrade energy threshold and that the significance calculated solely from events above 250 GeV, from the total dataset, is $> 4\sigma$. This may indicate one of three things. Firstly, that this is purely a statistical fluctuation. Secondly, that the source shows long-term variability. Or thirdly, that the true spectrum of the source is harder than first assumed. In the latter case, the analysis cuts used in this analysis have not been optimized for a very weak (< 1% Crab), moderate spectrum source ($\Gamma \sim 2-3$). The softer set of cuts work by essentially allowing in more lower energy events at the cost of also letting in more background events. For a softer source this isn't an issue as most of the contribution to the source's flux is coming from lower energies, therefore the signal isn't as badly affected as a harder source. The combination of observations of a weak source with a moderate spectrum with different energy thresholds could explain what is shown in Figure 6.9 and the $> 4\sigma$ excess above 250 GeV.

Further optimization and study of this blazar will be presented in a future publication.

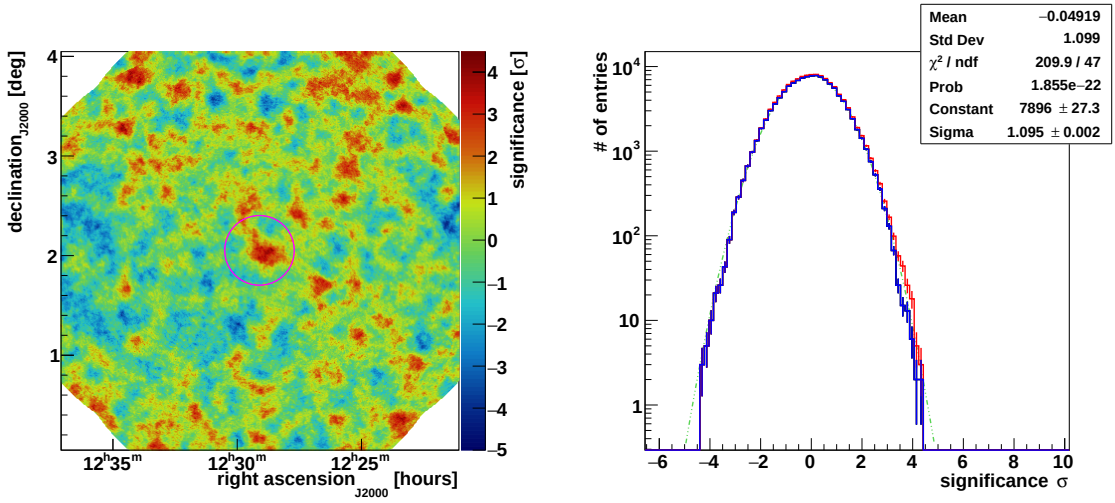

Figure 6.7: Left): Significance sky map centered on 3C 273. Regions shown as a red circle correspond to regions excluded from the background estimation and analysis. Right) Distribution of the significance of each point in the sky map shown on the left. The red line corresponds to the total sky map, blue corresponds to data excluding the On region and the black line corresponds to data excluding the On region and any other excluded regions. The green dot-dashed line is a Gaussian with mean of 0 and RMS of 1.

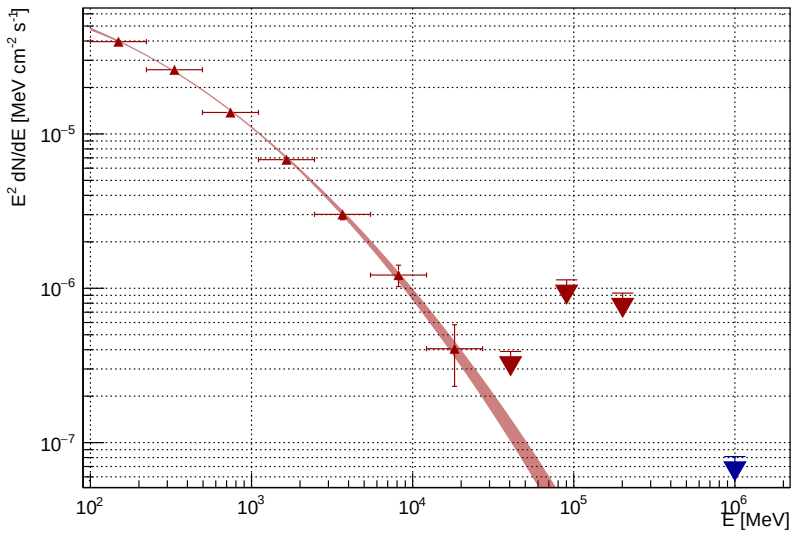

Figure 6.8: *Fermi*-LAT - VERITAS SED of 3C 273. The shaded red region corresponds to the 1-σ confidence interval on the best-fit *Fermi*-LAT spectrum obtained. The red points are the obtained differential flux points, where 95% CL upper limits are plotted for a TS< 9. The blue arrow is the observed VERITAS 99% upper limit at 1 TeV.

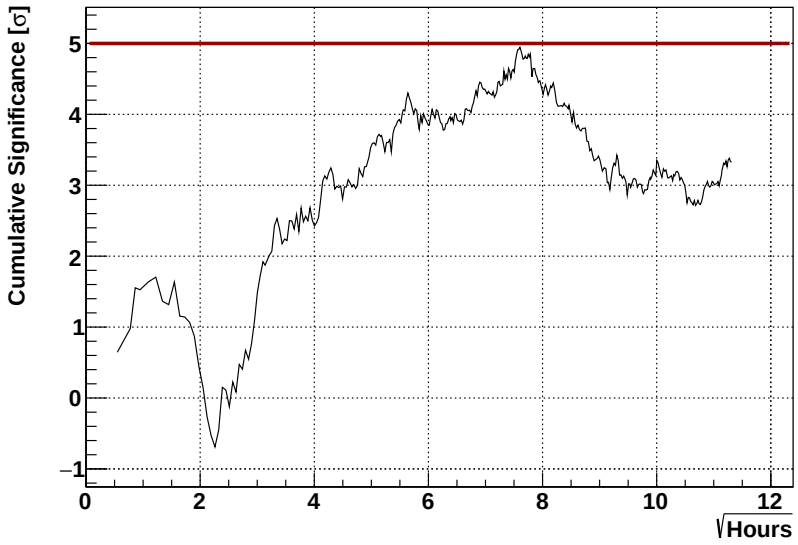

Figure 6.9: Cumulative significance vs $\sqrt{Hours}$ for 3C 273. The red line corresponds to a pre-trials excess of 5σ.

RGB J1243+364

A 3.47σ excess was observed from RGB J1243+364. The significance sky map and significance distribution are obtained and shown in Figure 6.10. No evidence of any unaccounted-for sources, or bright sections of the sky, is observed, and the significance distribution is well described by a Gaussian distribution with mean -0.056 and RMS of 1.033. The 99% CL upper limit above 150 GeV is determined to be 2.55×10^{-12} cm^{-2}s^{-1} (1.08% Crab). Figure 6.11 shows the *Fermi*-LAT spectrum obtained between 100 MeV and 300 GeV, with the upper limit on the flux normalization at 1 TeV, obtained from the VERITAS analysis shown.

Assuming a redshift of z=0.485, the VHE extrapolated integral flux is determined to be 2.62×10^{-12} cm^{-2}s^{-1} This gives the ratio of $\phi_{UL}/\phi_{HE,Ext} = 0.97$, suggesting the upper limits presented here place tighter constraints on the VHE emission.

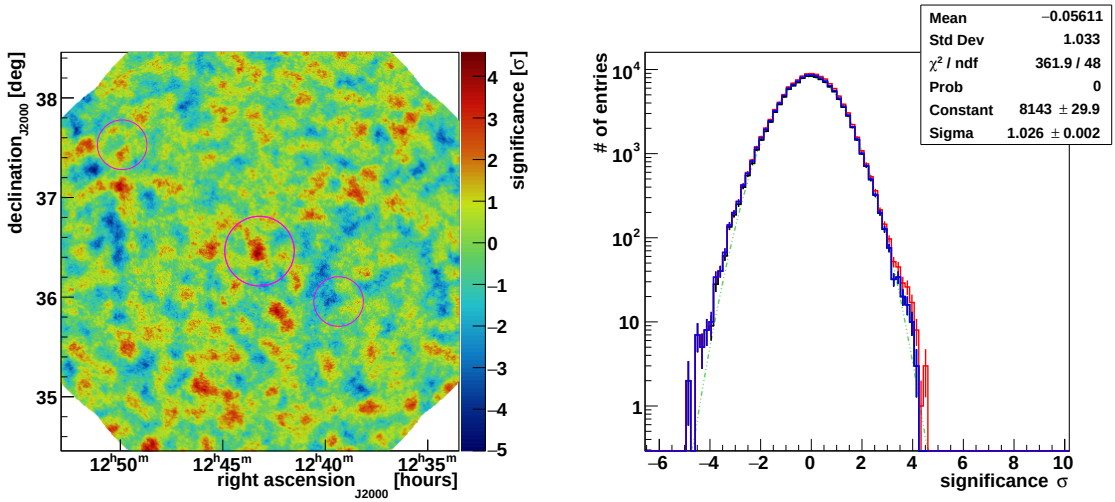

Figure 6.10: Left): Significance sky map centered on RGB J1243+364. Regions shown as a red circle correspond to regions excluded from the background estimation and analysis. Right) Distribution of the significance of each point in the sky map shown on the left. The red line corresponds to the total sky map, blue corresponds to data excluding the On region and the black line corresponds to data excluding the On region and any other excluded regions. The green dot-dashed line is a Gaussian with mean of 0 and RMS of 1.

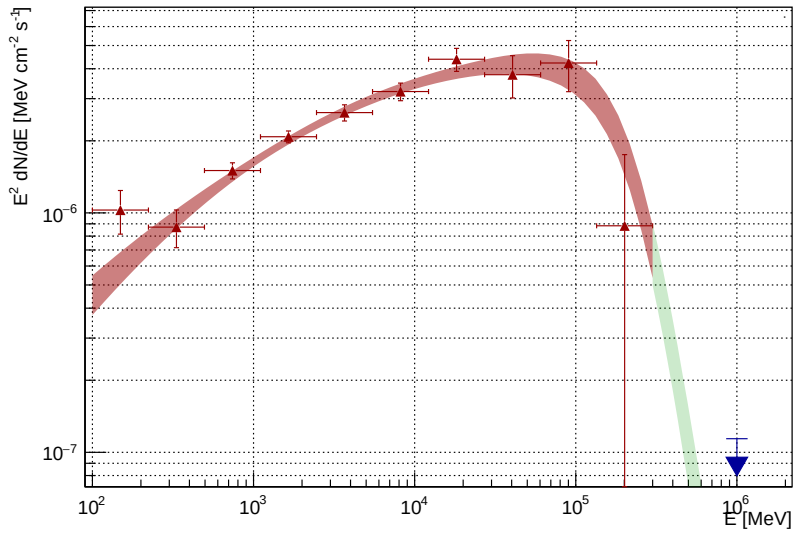

Figure 6.11: *Fermi*-LAT - VERITAS SED of RGB J1243+364. The shaded red region corresponds to the 1-σ confidence interval on the best-fit *Fermi*-LAT spectrum obtained. The red points are the obtained differential flux points, where 95% CL upper limits are plotted for a TS< 9. The green shaded region shows the Fermi-LAT spectrum extrapolated into the VHE regime, assuming a Franceschini et al. (2008) EBL model. The blue arrow is the observed VERITAS 99% upper limit at 1 TeV.

1ES 1255+244

A 3.69σ excess was observed from 1ES 1255+244. The significance sky map and significance distribution are obtained and shown in Figure 6.12. No evidence of any unaccounted-for sources, or bright sections of the sky, is observed, and the significance distribution is well described by a Gaussian distribution with mean -0.21 and RMS of 1.006. The 99% CL upper limit above 150 GeV is determined to be 2.73×10^{-12} cm^{-2}s^{-1} (1.16% Crab).

As this source has not been detected by *Fermi*-LAT in any of the point source catalogs, a power law model is fit to the data. The analysis results in a TS of 14.65 which corresponds to a significance of $\sim 3.83\sigma$. An upper limit on the integral flux is obtained by analyzing the profile likelihood with the spectral index frozen to $\Gamma = 2.0$. This is shown in Figure 6.13. The 95% CL upper limit on the integral flux is determined to be $\phi(100\ \text{MeV} - 300\ \text{GeV}) < 4.04 \times 10^{-10}\text{cm}^{-2}\text{s}^{-1}$.

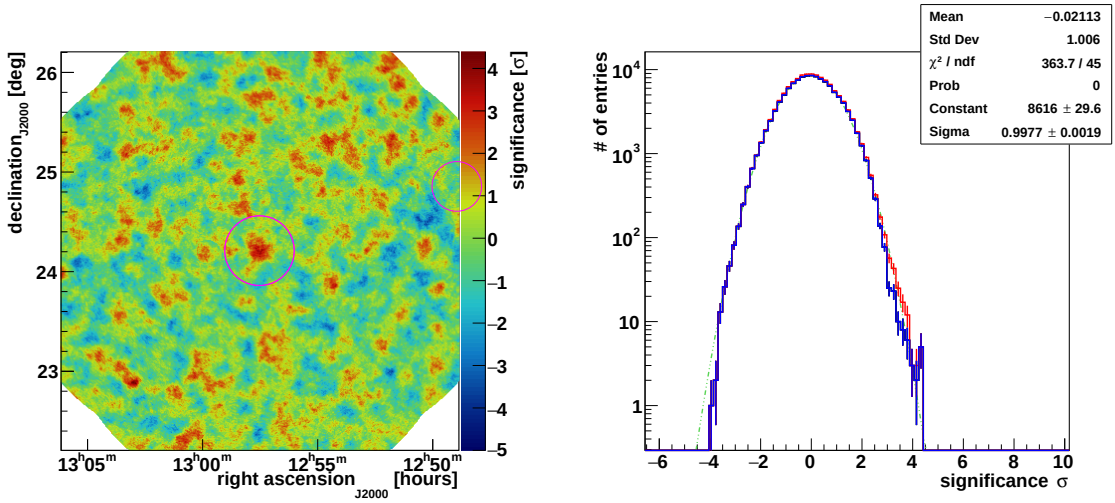

Figure 6.12: Left): Significance sky map centered on 1ES 1255+244. Regions shown as a red circle correspond to regions excluded from the background estimation and analysis. Right) Distribution of the significance of each point in the sky map shown on the left. The red line corresponds to the total sky map, blue corresponds to data excluding the On region and the black line corresponds to data excluding the On region and any other excluded regions. The green dot-dashed line is a Gaussian with mean of 0 and RMS of 1.

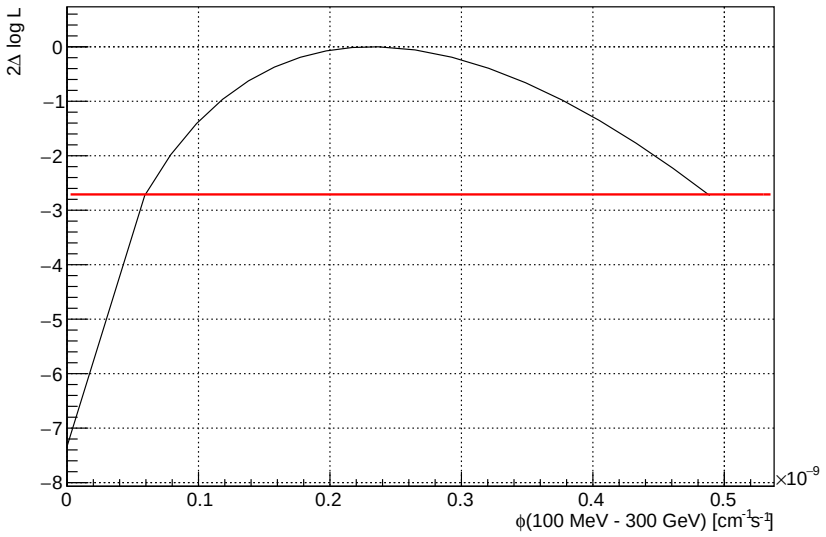

Figure 6.13: Profile likelihood scan of the integral flux for 1ES 1255+244. The red line corresponds to -2.71 or 95% containment of a χ^2-distribution with one degree of freedom.

6.4 Discussions

I have presented 99% CL upper limits on the integral flux for 6 promising candidate TeV blazars. Assuming a constant signal from these sources, one can obtain a simplistic $\sigma/\sqrt{hour}$ extrapolation to obtain an estimate of the time require to detect such a source. The additional VERITAS exposure required is shown in Column 7 of Table 6.2. It is worth noting that the figures reported here do not account for the approximate 10-15% deadtime that one could expect from VERITAS observations, therefore the true number of hours is somewhat larger. Based on this this extrapolation, detection of objects such as B2 0912+29 and 3C 273 may not be feasible by current generation IACTs as they will require dedicated long exposures. This excludes detections during periods of exceptions multiwavelength activity, during which the simplistic extrapolation is no longer valid.

1ES 1118+424's significance distribution extends beyond 5σ. Before claiming a detection, one must take a number of factors into account. Firstly, VERITAS requires that any detection be confirmed by two independent analyses. At the time of writing the secondary analysis is still on-going, however the secondary analysis does show an equally promising result, with an excess significance of $\sim 3.7\sigma$ and a significance distribution extending beyond 5σ. In both the analysis posted here and the secondary analysis, the peak significance is located slightly offset from the catalog position ($< 0.1°$). While one might simply asumme that this emission is co-spatial with the source as it is in the approximate location of the source, moving one's predefined location of interest after observing one's data incurs what is known as a trials penality. In addition to this, looking at number of different sources also introduces a trials penality.

A trials penality acts to decrease the significance of a result, based on the number of different data choices which were applied to obtain that result. The effect of statistical trials on a result can be estimated by considering the result to follow a Binomial process. That is to say one of two things occur, either one observes a significant excess or one does not. The probability of observing k significant results, given N trials is simpy the Binomial probability:

$$P(k) = \binom{N}{k} P_{obs}^{k}(1 - P_{obs})^{N-k}, \tag{6.1}$$

where P_{obs} is the observed pre-trials probability and

$$\binom{N}{k} = \frac{N!}{k!(N-k)!}. \tag{6.2}$$

The probability of observing at least one significant excess ($k \geq 1$) can be simply calculated as

$$P(k \geq 1) = 1 - P(k = 0) = 1 - (1 - P_{obs})^N, \tag{6.3}$$

where $P(k \geq 1)$ can be considered the post-trials probability. Going back to 1ES 1118+424, assume the pre-trials siginificance is given by the upper edge of the significance distribtion, 5.5σ, given that we have observed 6 sources this results in a post-trials significance of $\sim 5.2\sigma$. While this is still a positive, one must also account for the source not being at the centre of the sky map. The sky map is divided up into bins of size 1×10^{-4} squared degrees. Considering the radius of the On region is 0.35°, this corresponds to 3848 trials. Hence the observed 5.5σ would have a post-trials significance of 3.8σ. If this is the true location of the VHE emission, it would require a pre-trials significance of 6.4σ before a detection could be claimed.

The above estimation assumes that each trial is independent, however given the correlated nature of the observed events, this is not the case. A proper estimation of the trials factor would require the simulation of sky maps, which incorporates the correlation of bins due to the instrument's PSF. While this source is indeed very promising, it falls short of what is required by the VERITAS Collaboration for a detection to be claimed.

The most promising target for future VERITAS observations is 1ES 1118+424, requiring an additional 16.25 hours of observations. Assuming a conservative 15% deadtime this suggests $\sim$ 20 hours of additional observations. Given that data set consists of observations taken across all epochs, this number could be decreased further as the current configuration of VERITAS is more sensitive than V4 and V5. Further observations of 1ES 1118+424 will be proposed. Should these observations result in a detection, a dedicated publication will be prepared which incorporates all available multiwavelength data.

In summary, upper limits on the integral flux of six promising VHE candidates have been presented. These are part of the larger VERITAS blazar discovery program, the results of which shall be presented as a blazar upper limits paper similar to that of Archambault et al. (2016).

Chapter 7

Detection of Very-High-Energy Gamma-Ray Emission from OJ 287

7.1 Introduction

OJ 287 (R.A.: 08h 54′48.8749″, Dec: +20h 06′30.641″(J2000), Johnston et al., 1995) is a peculiar blazar located at a redshift of z = 0.306 (Nilsson et al., 2010) with a somewhat unclear classification. TeVCat[1] classifies OJ 287 as a BL Lac object with a "class unclear" while 3FHL (Ajello et al., 2017) reports the synchrotron peak (in νF_ν representation) to be located at $\log_{10}(\nu\ [\mathrm{Hz}]) = 13.62$, suggesting OJ 287 belongs to the LBL subclass of blazars. OJ 287 is detected in all of the *Fermi*-LAT point-source catalogs (1FGL, 2FGL and 3FGL, Abdo et al., 2010; Nolan et al., 2012; Acero et al., 2015, respectively), with the 3FGL time-averaged energy spectrum being best-fit by a log-parabola model, with the IC-peak of the SED peaking in the MeV to sub-GeV energy range and the time-averaged flux (1 GeV - 100 GeV) of $(5.9 \pm 0.2) \times 10^{-9}$ph cm^{-2} s^{-1} (Acero et al., 2015). Assuming a power law extrapolation from the HE to VHE regime, the VHE-extrapolated flux is ∼0.4% Crab. This suggests that VHE detection would require a deep observational campaign, not feasible with current generation IACTs. The 3FGL variability index of 1059.565 suggests that the source is highly variable, with a $TS_{var,3FGL} > 72.44$ suggesting, at the 99% confidence level, that the emission is inconsistent with a constant-flux model. This variability may also be present at higher energies as shown by its inclusion in the 1FHL (Ackermann et al., 2013) and 3FHL (Ajello et al., 2017) hard-source catalogs, but not the 2FHL (Ackermann et al., 2016) catalog, potentially indicating long-term variability in the highest energies observable by *Fermi*-LAT. However, the hard-source catalogs have different energy ranges and different exposure, hence making a direct comparison speculative.

OJ 287 is a remarkably well-studied object, with optical observations dating back to 1890 (Sillanpaa et al., 1988). Long-term optical observations of OJ 287 show a peculiar ∼12-year quasi-periodic structure in the light curve. Sillanpaa et al. (1988) accredit this periodicity to

[1] http://tevcat.uchicago.edu/?mode=1;id=286

the presence of a binary super-massive black hole (SMBH) system at the core of the AGN, with an orbital period of ~9 years and suggest that variations in the light curves may be due to tidally induced mass flows from the accretion disks onto the black holes. Reanalyzing archival observations of the 1900 and 1910 outburst, Hudec et al. (2013) show that the light curves of OJ 287 are not truly periodic and suggest that the timing between outbursts is consistent with a precessing orbit.

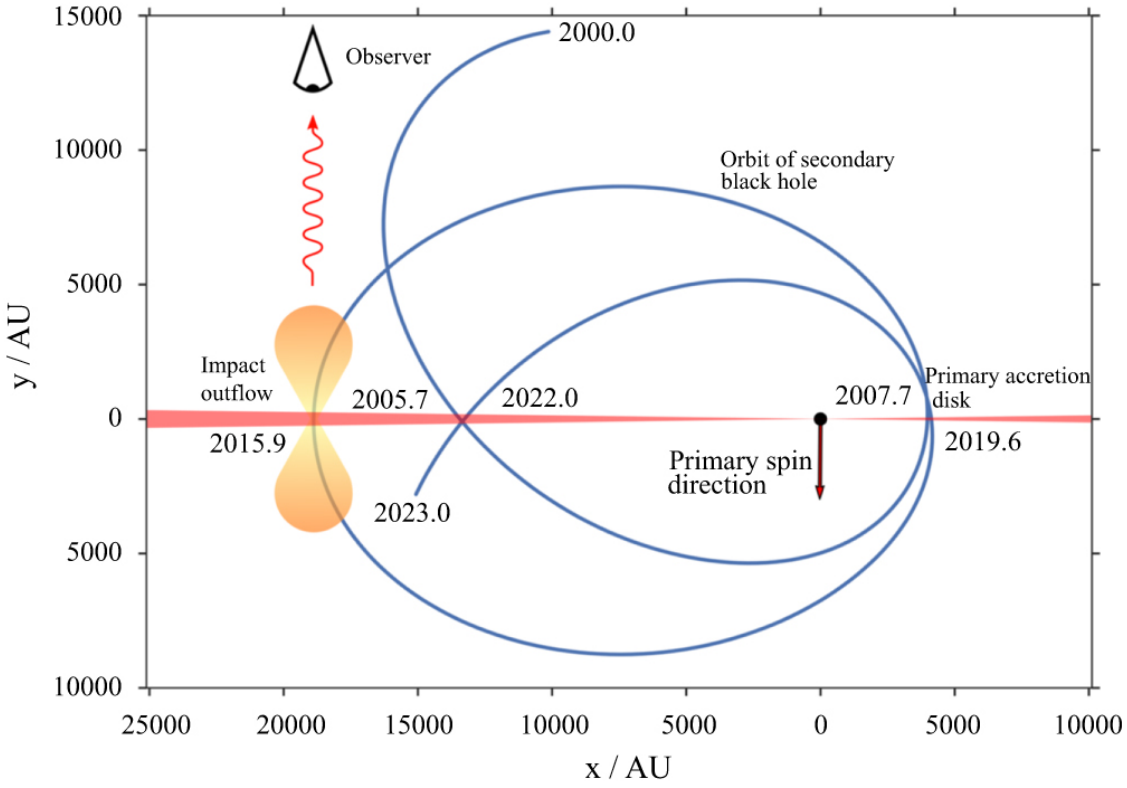

Figure 7.1: Orbital path of the secondary black hole about the primary black hole. Image credit Figure 2 of Valtonen et al. (2016).

In the precessing binary SMBH model, two types of optical outbursts are expected. The first type of outburst occurs due to the secondary black hole impacting the accretion disk of primary black hole, causing a hot cloud of gas to be shocked and pulled from the accretion disk (Lehto & Valtonen, 1996). This, initially optically thick, cloud expands to become optically thin, causing the optical emission to increase with variability time scales on the order of light travel times through the cloud. This appears as the emergence of an optical flare. The flux then decreases due to the decreasing energy density of the cloud (the energy density of the cloud decreases due to the expansion of the cloud, resulting in the flux decreasing with time as $t^{-3/2}$ (Hudec et al., 2013)). As the radiation produced in this process is Bremsstrahlung radiation, the light is expected to be unpolarized (Hudec et al., 2013), hence this outburst

should show a decrease in the overall degree of polarization.

The second form of optical outburst is due to increased accretion rates as the secondary black hole approaches close to the primary black hole (Hudec et al., 2013). The tidal transfer of matter toward the black hole results in an increased accretion rate, with some of the matter being transferred into the jet, and therefore enhancing the brightness of the jet. As the jet radiation is expected to be due to synchrotron radiation, this outburst results in a characteristic increase in the degree of polarization.

The precessing binary SMBH model has been developed into a model which has accurately predicted optical outbursts with its accuracy increasing with each observed outburst (see, for example, Valtonen, 2007; Valtonen et al., 2009, 2011, 2016). In this model the masses of the primary and secondary SMBHs are $1.8 \times 10^{10} M_{\odot}$ and $1.3 \times 10^{8} M_{\odot}$, respectively and the precession rate is 37.5° - 39.1° (Valtonen et al., 2011). Figure 7.1 shows a representation of the orbital path of the secondary black hole with the expected disk crossings highlighted. Valtonen et al. (2011) predicted an optical flare to occur in December 2015. This optical flare was observed to peak on December 5th 2015 by Valtonen et al. (2016) as part of a multiwavelength monitoring campaign, involving a large number of optical observatories and, UV and X-ray observations taken by *Swift*. During the campaign the R-band light-curve trend agreed well with the assumed optical outburst model, and optical emission in excess of the outburst model was found to be in good agreement with small scale variations in the optical polarization measurements. This suggests that the excess optical emission is polarized and of jet-origin. Valtonen et al. (2016) also observed modest X-ray flaring during this campaign, however the variability time-scales are consistent with the variations observed in the optical polarization and show a flux level comparable to X-ray flares observed in a previous campaign by Edelson et al. (2015). This also suggests that the X-ray emission is mostly synchrotron radiation of jet origin.

Very Long Baseline Array (VLBA) observations of OJ 287 reveal complexed jet features. Analyzing data from 1994-2002 Tateyama & Kingham (2004) observe a rotation in the position angle of the unresolved jet by $\sim 30°$ over the space of 8 years. Tateyama & Kingham (2004) find that a precessing jet with a helical structure can explain the position and viewing angles observed, however these cannot account for those observed in 2002. Tateyama & Kingham (2004) suggest that a precessing ballistic jet best explains the structure observed in radio maps, suggesting a precession period of ~12 years, consistent with the time scales expected from the binary SMBH model (see, for example, Valtonen & Pihajoki, 2013). Agudo et al. (2012) analyze ~15 years of 7-mm VLBA observation between 1995 and 2011, observing a sharp swing in the position angle of $> 100°$, with fluctuation in the position angle of $\sim 40°$ over time scales of ~3 years. While not ruling out the effect of a binary-black-hole

system or jet precession on longer time scales and on the jet at large scales (such as those proposed by Tateyama & Kingham (2004)), Agudo et al. (2012) suggest that the time scale of the erratic wobbling of the inner-most jet components is inconsistent with the time scales expected from such modulations. Agudo et al. (2012) purpose that the erratic and non-periodic changes in the position angle are possibly due to an asymmetric fluctuations in the injection of plasma at the origin of the jet.

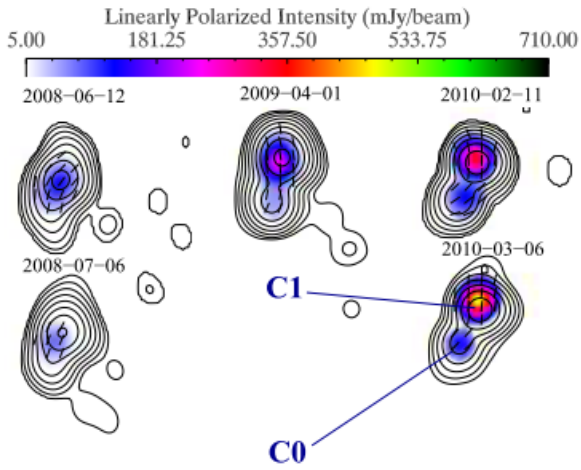

Figure 7.2: Radio map of OJ 287 showing different jet features. Adapted from Figure 1 of Agudo et al. (2011).

HE gamma-ray flaring activity has also been observed from OJ 287. Agudo et al. (2011) observe a HE flare from OJ 287 during 2009 using observations taken by *Fermi*-LAT. Agudo et al. (2011) compare the LAT data to contemporaneous mm and optical-polarization data. They find strong correlation between HE flaring and the 7-mm polarization of a quasi-stationary jet feature (C1, see Figure 7.2) located >14 pc from the innermost quasi-stationary jet region (C0), suggesting that the events are co-spatial. Applying a DCF analysis, Agudo et al. (2011) observe a HE-lead time lag of ∼80 days, significant at the 99.7% confidence level. Based on the distance from the core (>14 pc) the HE emission could be due to SSC or IC scattering of infrared photons from a hot dusty torus. Agudo et al. (2011) suggest this could arise due to a blob traversing through a stationary shock within the jet (for example C1). Kushwaha et al. (2013) model the brightest of the 2009 flares by taking contemporaneous optical, *Swift*-XRT and *Fermi*-LAT data. Kushwaha et al. (2013) find a combination of both SSC and EC models are required to explain the broadband SED, suggesting the emission region is surrounded by a warm infrared emitting region of $T \sim 250$K. This is consistent with a spherical region illuminated by an accretion disk, located ∼9 pc from the central engine.

Neronov & Vovk (2011) search for HE flaring on short time scales from OJ 287 be-

tween 2008 and 2010. By considering photon counts during *Fermi* orbits, Neronov & Vovk (2011) determine the minimum observed variability time scale to be on the order of a single *Fermi* orbit ($T_{var} \lessapprox 3 - 10$ hours). In the context of a binary SMBH model, this time scale is inconsistent with the light-crossing time for the more massive primary black hole, hence suggesting that the emission is coming from the secondary black hole.[2] Neronov & Vovk (2011) postulate that although the primary black hole's jet is expected to be the dominent emitter at HE, due to larger accretion rates, the secondary black hole could momentarily be brighter due to a change in the viewing angle with respect to the observer. A change in viewing angle results in a change in the Doppler factor, as the emission will be Doppler boosted by a factor of δ^4 this could potentially result in the jet of the secondary black hole temporarily being the dominant HE emitter. It is worth noting that Neronov & Vovk (2011) determine the lower limit on the variability time scale based on a series of three orbits in which the first and last orbit have significant flux measurements with an elevated photon flux, but no photons are observed during the second orbit. Neronov & Vovk (2011) determine the probability of observing 0 photons during the second orbit, assuming the flux to be constant between the first and second orbit, to be 7×10^{-4}. While it is not explicitly stated how the probability is calculated, it is crucial to include the full instrument response functions into the probability calculation when dealing with such low counts taken on short time scales. For this reason, one might consider the more conservative estimate of $T_{var} \sim 10$ hours which is obtained from fitting an exponential rise and decay profile to the light curve. This more conservative estimate does not change the overall interpretation as the variability time scale of ~10 hours is also inconsistent with the primary black hole. Neronov & Vovk (2011) also consider that the emission is occurring close to the central engine of the jet, however Agudo et al. (2011) observe mm-flaring of a downstream stationary jet feature temporally consistent with the HE emission during this flaring period, suggesting the emission is co-spatial.

OJ 287 has previously been observed by VERITAS. During the anticipated optically active phase of 2007-2008, Archambault et al. (2016) observed OJ 287 from 4th December 2007 - 1st January 2008). Archambault et al. (2016) combine this data with data taken during 2010-2011 season, resulting in a non-detection, and set a 99% CL upper limit on the integral flux (E > 182 GeV) of 2.6% Crab. The MAGIC Collaboration (Seta et al., 2009) observed OJ 287 as part of a multiwavelength campaign in 2007. They report on data taken during two

[2] Neronov & Vovk (2011) assume that the size of the jet will scale with the gravitational radius of the black hole, therefore approximating the size of the jet based on the light crossing time for the black hole. This also assumes that the emission region occupies the entire radius of the jet, therefore the light crossing time cannot be less than that of the black hole. This is somewhat inconsistent with acceleration processes such as magnetic reconnection which would produce "mini-jets". Furthermore knots have been observed from OJ 287 which may arise due to regions of the jet being compressed.

different periods 10th April - 13th April 2007 and 7th November - 9th November 2007, both of which resulted in non-detections. Seta et al. (2009) determine 95% CL upper limits on the integral flux of (E > 145 GeV) 3.3% and (E > 150) 1.7% Crab for the periods, respectively.

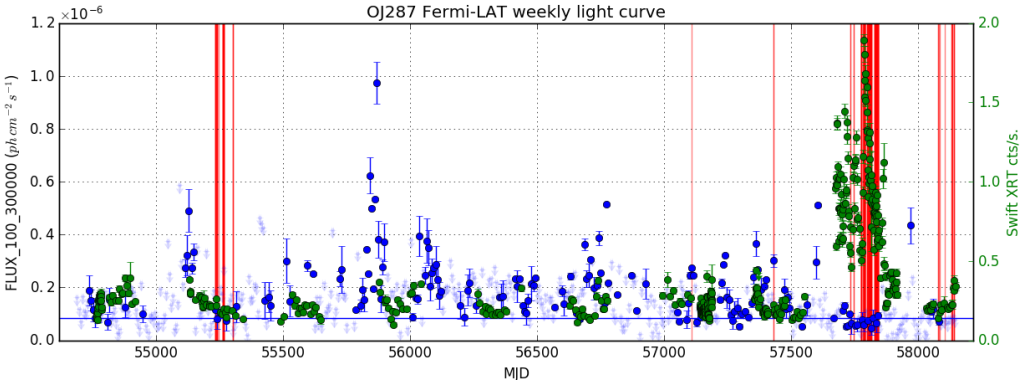

Figure 7.3: Long term light curve for OJ 287. The blue points show the weekly-binned *Fermi*-LAT flux in the 100 MeV to 300 GeV range. The blue horizontal vertical line shows the 3FGL time-averaged flux. The green points show the *Swift*-XRT count rates. The red vertical lines indicate VERITAS observations.

During the 2016-2017 observing season, OJ 287 was observed to undergo a period of enhanced X-ray activity by *Swift*-XRT (see, for example, Grupe et al., 2016; Verrecchia et al., 2016). Based on elevated *Swift*-XRT count rates reported by Stroh & Falcone (2013)[3], VERITAS took a number of snapshots on OJ 287 between 9th December 2016 and January 2017. This revealed a moderate excess ($\sim 2\sigma$) in gamma-ray events. In response to historic XRT count rates (see Figure 7.3) observed from the 1st of February 2017, VERITAS initiated ToO observations of OJ 287. The observed gamma-ray excess prompted further VERITAS observations and follow up observations were trigger with *Swift*-XRT. These observations resulted in a $> 5\sigma$ detection of OJ 287 by VERITAS and the release of an Astronomer's Telegram (Mukherjee et al., 2017). Further observations were taken between 16th February 2017 and 30th March 2017 as part of a multiwavelength follow up campaign involving both VERITAS and *Swift*.

In the context of the binary SMBH model, the next disk crossing isn't expected until 2019. This is shown in Figure 7.1. The binary SMBH model suggests that the secondary black hole should be behind the accretion disk of the primary black hole (with respect to an Earth-based observer). This would suggest that the enhanced activity observed during this period is originating from the jet of the primary black hole.

In this chapter the results of the joint-multiwavelength campaign around the VERITAS

[3] https://www.swift.psu.edu/monitoring/

detection of OJ 287 are discussed. In Section 7.2 the multiwavelength observations, *Swift*-XRT, *Fermi*-LAT and VERITAS, are discussed. In particular VERITAS observations are discussed in Section 7.2.1. Expanding on preliminary results presented at the 35th International Cosmic Ray Conference (O'Brien et al., 2017), the VERITAS analysis uses a binned-likelihood analysis, as presented in Chapter A (Binned Likelihood Analysis Section), to correctly handle the low statistics data. In Section 7.3.1 the temporal properties are discussed. A search for correlation and possible time lag between the different *Swift* energy bands is performed using a DCF analysis in Section 7.3.2. In Section 7.3.3 a search for correlation between VERITAS and *Swift*-XRT is performed by applying a likelihood-based correlation analysis. In Section 7.3.4 the broadband spectral properties are discussed. Finally, in Section 7.4 the results are discussed and future observations and studies are discussed.

7.2 Observations

In this section the observations taken by VERITAS, *Fermi*-LAT and *Swift*-XRT are discussed. These observations were taken as part of a joint monitoring campaign between VERITAS and *Swift* . I define three periods which observations shall be grouped into:

- **Period 1:** MJD 57731 - 57777
- **Period 2:** MJD 57785 - 57817
- **Period 3:** MJD 57827 - 57843

The periods discussed above approximately correspond to periods of approximately constant gamma-ray signal as will be shown in Section 7.2.1.

7.2.1 VERITAS

VERITAS observed OJ 287 for a total exposure of 58 hours (50 hours deadtime corrected) between 57731 and 57843 MJD (9th December 2016 - 31st April 2017). The data were analyzed using standard analysis techniques as described in Section 4.2.1. A set of boosted decision tree gamma/hadron cuts (BDTs) optimized and verified a proiri on soft spectra sources ($\Gamma \sim 3.5$), were used. The observations resulted in a total of 3179 On events and 15906 Off events, with an on/off normalization of $\alpha = 1/6$. This gives an excess significance of 9.2σ.

The sky map centered on the radio location of OJ 287 is shown in the left hand plot of Figure 7.4. OJ 287 is clearly visible at the center of the FoV. The significance distribution of

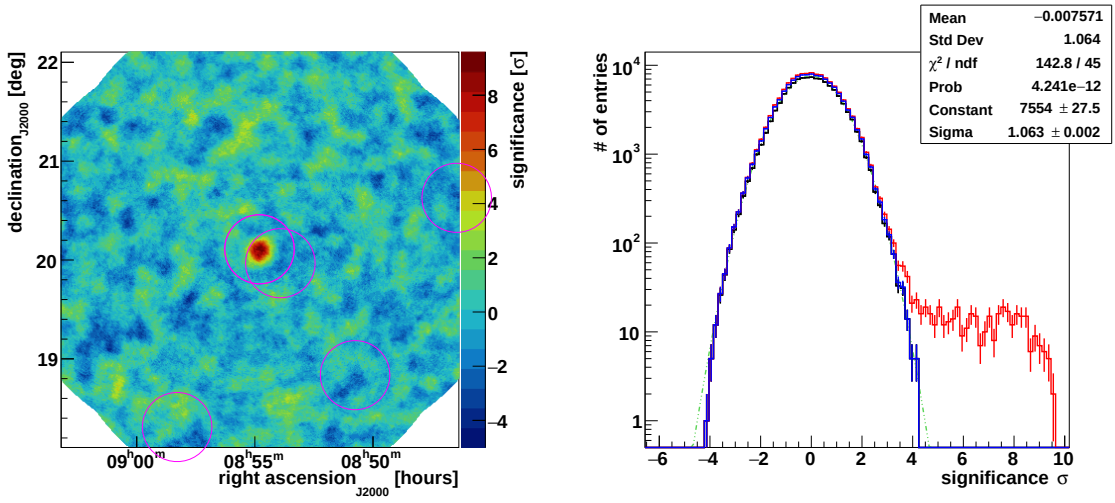

Figure 7.4: (Left): Significance sky map centered on OJ 287. Regions shown as a red circle correspond to regions excluded from the background estimation and analysis. (Right) Distribution of the significance of each point in the sky map shown on the left. The red line corresponds to the total sky map, blue corresponds to data excluding the On region and the black line corresponds to data excluding the On region and any other excluded regions. The green dot-dashed line is a Gaussian with mean of 0 and RMS of 1.

the sky map is shown on the right hand plot of Figure 7.4. The On-region-excluded significance distribution, shown in blue, is well described by a Gaussian of mean -0.008 and RMS of 1.064, hence indicating that there are no unaccounted for hot or cold spots within the FoV that may affect the analysis. The cumulative significance as a function of $\sqrt{Hour}$ is shown in Figure 7.5. The shaded regions in Figure 7.5 correspond to the boundaries of the defined analysis periods. Periods 2 and 3 show approximately constant gamma-ray signal. Period 1, which is poorly sampled, shows statistical variability in the signal. It is worth noting that the Period 2 - Period 3 boundary corresponds to a break in VERITAS observations due to increased moon brightness. This, coupled with the gamma-ray signal, results in the selection of these three analysis periods. A $\sigma/\sqrt{Hour}$ plot provides an measure of the gamma-ray rate. While in general the gamma-ray rate is dependent on the observation conditions, and therefore not directly related to the gamma-ray flux, in this case all observations were taken under similar conditions. Small variations in the gamma-ray rate are likely either statistical or due to varying zenith angle rather than longer term instrumental or environmental effects. Hence the gamma-ray rate provides an accurate estimate of the relative gamma-ray flux. A summary of results of each period is given in Table 7.1.

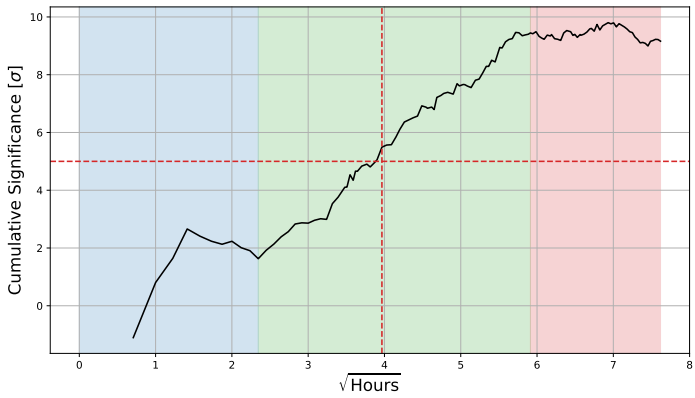

Figure 7.5: Cumulative significance as a function of $\sqrt{Hour}$ for OJ 287. The horizontal dashed line corresponds to a 5σ detection. The vertical dashed line corresponds to the date of the ATel release. The different shaded regions correspond to data taken in the different periods.

Period	Live Time (Hours)	N_{On}	N_{Off}	Excess Significance (σ)	ϕ(E > 110 GeV) ($\times 10^{-11}$[cm^{-2} s^{-1}])	ϕ(E > 110 GeV) ([% Crab])	Spectral Index (Γ)
Period 1	5.0	293	1583	1.6	< 2.03	< 3.52	3.96
Period 2	25.3	1788	8300	9.6	(1.96 ± 0.27)	(3.41 ± 0.47)	(4.01 ± 0.35)
Period 3	20.0	1098	6023	2.7	(0.67 ± 0.24)	(1.16 ± 0.41)	3.96
Total	50.0	3179	15906	9.2	(1.23 ± 0.16)	(2.14 ± 0.27)	(3.96 ± 0.30)

Table 7.1: Summary of detection analysis of VERITAS observations. Column 2 shows the live time (total deadtime corrected exposure). Columns 3 and 4 show the number of On and Off counts observed. Column 5 shows the excess significance calculated using Equation 17 of Li & Ma (1983). Columns 6 and 7 show the integral flux above 110 GeV in units of cm^{-2}s^{-1} and percentage Crab flux, respectively. Column 8 shows the spectral index assumed in the integral flux calculation. When no error is reported the integral flux is frozen to the quoted value in the fitting procedure.

The spectral analysis was performed in the 110 GeV - 900 GeV range. As discussed in Section 5.4.1 no bias is expected from using a predefined energy range. The data were binned into energy bins separated by 0.15 in log space. The total time-averaged energy spectrum was obtained by a binned-likelihood analysis, allowing for the inclusion of low statistics data, and is best-fit by a power-law of the form:

$$\frac{dN}{dE} = (3.46 \pm 0.44) \times 10^{-11} \left(\frac{E}{0.2 \text{ TeV}}\right)^{-3.96 \pm 0.30} [\text{ cm}^{-2}\text{s}^{-1}\text{TeV}^{-1}].$$

The data is adequately fit by the power-law model with a $\chi^2/NDF = 1.41/4 = 0.35$. A log-parabola model is also fit to the data; however, the best-fit is found to be consistent with the power-law fit ($\beta \approx 0$) and doesn't offer a significant improvement over the power-law model ($\mathcal{L}_{lp} \approx \mathcal{L}_{pwl}$). The decorrelation energy (E_D), the energy at which the correlation between the N_0 and Γ is at a minimum is $E_D = 230$ GeV. This corresponds to a flux normalization of $N_0 = (1.99 \pm 0.24) \times 10^{-11}$ cm^{-2}s^{-1}TeV^{-1} at E_D. The integral flux is determined to be ϕ(E > 110 GeV) = $(1.23 \pm 0.16) \times 10^{-11}$ cm^{-2}s^{-1} or (2.14 ± 0.27) % Crab. Figure 7.6 shows the counts spectra and residual plots for the fit. The model-predicted On counts are obtained by combining the model-predicted Off and Excess counts ($\overline{N_{ON}} = S^{Pred} + \alpha\widehat{\overline{N_{OFF}}}$). In applying the fit, the first energy bin (~100 GeV) is excluded as it is below the nominal energy threshold and has a large reconstruction bias. It is worth noting that the spectral fit is consistent up to the last On count (~8 TeV), with the significances of the energy bins suggesting the On counts arise due to background fluctuations rather than an unaccounted-for spectral feature.

The total-time averaged VHE SED (plotted as E^2dN/dE) is shown in Figure 7.7. Spectral points are obtained by reapplying the spectral fit over each energy bin, with the normalization energy set to the (log-spaced) bin center. 95% confidence level (CL) upper limits are obtained for energy bins with a $TS < 4$ ($\lesssim 2\sigma$). The upper limits are calculated by freezing the spectral index to the best-fit value and obtaining the profile likelihood. As discussed in Section 5.3.1, the 95% upper limit is the value N_{UL}, for which $-2\Delta \log \mathcal{L}(N_{UL}) = -2.708$.

The energy spectrum for Period 2 is best-fit by a power-law ($\chi^2/NDF = 1.95/4 = 0.49$) of the form:

$$\frac{dN}{dE} = (4.88 \pm 0.67) \times 10^{-11} \left(\frac{E}{0.2 \text{ TeV}}\right)^{-4.01 \pm 0.35} [\text{ cm}^{-2}\text{s}^{-1}\text{TeV}^{-1}].$$

This corresponds to an integral flux ϕ(E > 110 GeV) = $(1.96 \pm 0.27) \times 10^{-11}$ cm^{-2}s^{-1} or (3.41 ± 0.47) % Crab.

As the Period 3 observations only result in a 2.7σ excess, the integral flux is obtained by freezing the spectral index to that of the total best-fit spectral index ($\Gamma = 3.96$). The flux

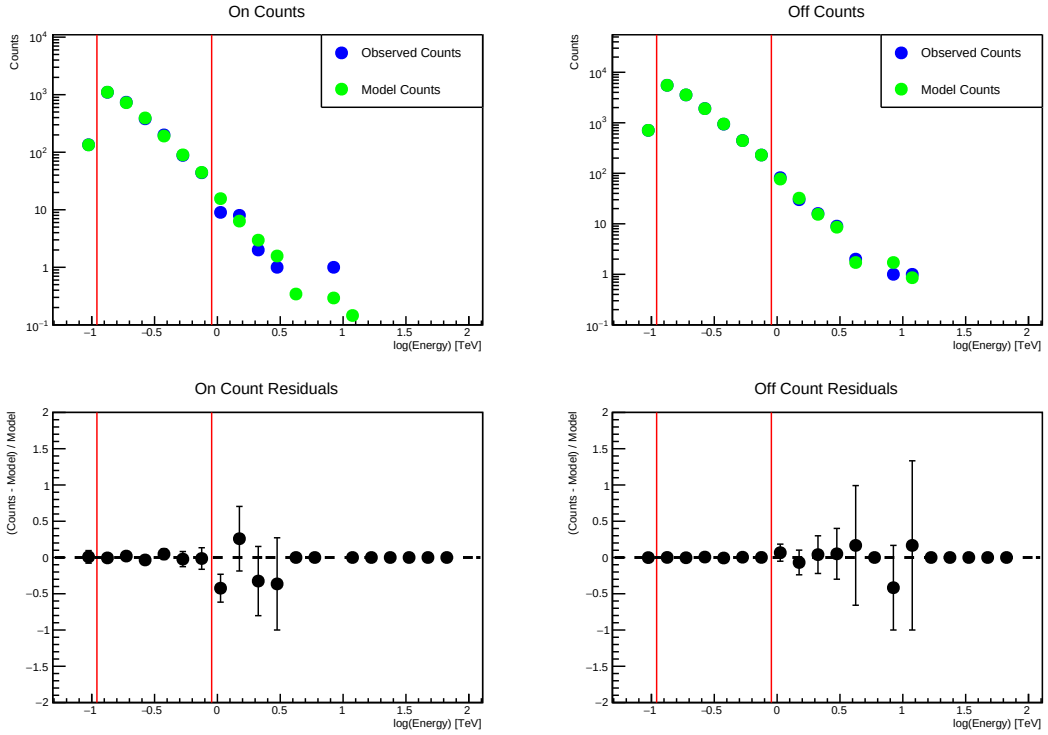

Figure 7.6: Top row: On (left) and Off (right) counts spectra for the total dataset. The observed counts are shown in blue with the model predicted counts shown in green. The red lines signify the energy range used for the spectral analysis. Bottom row: residuals ((observed - model) / model) for the On (left) and Off (right) counts.

normalization $N_{0,P3}$ is then obtained by applying a likelihood fit to the Period 3 data. The best-fit flux normalization is $N_{0,P3} = (1.68 \pm 0.60) \times 10^{-11}$ cm^{-2}s^{-1}TeV^{-1}. This corresponds to an integral flux ϕ(E > 110 GeV) = $(0.67 \pm 0.24) \times 10^{-11}$ cm^{-2}s^{-1} or (1.16 ± 0.41) % Crab.

The overall shape of the energy spectrum is consistent in the total dataset and during Period 2. The brightness of the source however, decreases by a factor of ∼3 between Periods 2 and 3. The significance of the decrease in the integral flux can be determined as $(\phi_{Period\ 2} - \phi_{Period\ 3})/\sqrt{\Delta\phi^2_{Period\ 2} + \Delta\phi^2_{Period\ 3}}$ where $\phi_{Period\ i}$ and $\Delta\phi_{Period\ i}$ are the integral flux and error on the integral flux for Period i. The significance of the decrease is determined to be 3.6σ.

The daily-binned light curve is obtained by applying a binned-likelihood fit to temporally binned data, with the spectral index frozen to that of the best-fit spectrum. The integral flux is obtained by integrating the best-fit model over the defined energy range. 95% CL upper limits are calculated in a similar manner to those of the spectral points. The VERITAS light curve is shown in the Panel (a) of Figure 7.11. To test for variability, the variability index (TS_{var}) is obtained (see Appendix A.1 for a discussion on the application of a TS_{var} to VERITAS data). The data is binned into daily time bins, resulting in 32 integral flux

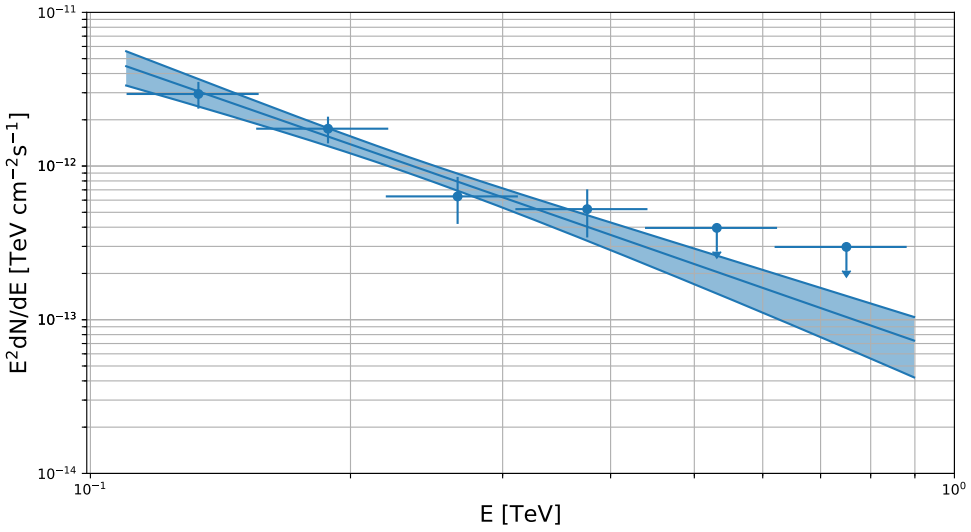

Figure 7.7: Total-time averaged VHE spectral energy density of OJ 287. The shaded region corresponds to the 1σ confidence interval on the best-fit power-law model. 95% CL upper limits are shown for energy bins with a $TS < 4$ ($\lesssim 2\sigma$).

points and $TS_{var} = 30.14$. This corresponds to a $\chi^2/NDF = 30.14/31 = 0.97$, which has a probability of $p = 0.51$. This suggests that the data is consistent with a constant-flux model. This indicates that any variability present is below the sensitivity of VERITAS. This shows that while the source doesn't show strong variability on daily timescales (as shown by the TS_{var}), there is a decreasing trend between Periods 2 and 3.

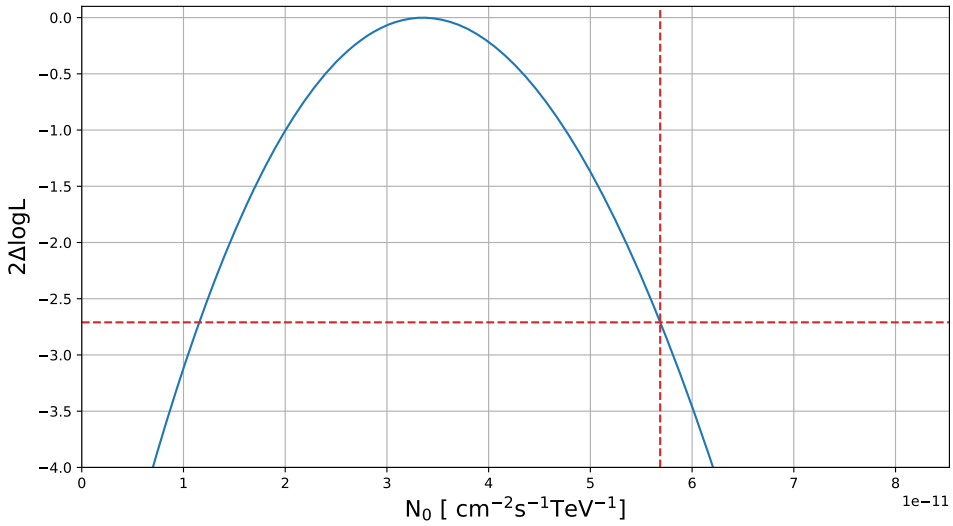

Figure 7.8: Profile likelihood for the flux normalization for Period 1. This is obtained by freezing the spectral index to $\Gamma = 3.96$ and scanning over N_0. The dashed vertical line shows the value of N_0 for which $-2\Delta \log \mathcal{L} = -2.708$, which is illustrated by the dashed horizontal line.

7.2.2 *Fermi*-LAT

Data from *Fermi*-LAT were analyzed between the dates 57731-57843 MJD using standard selection and quality criteria as discussed in Section 4.3. The energy spectrum was fit with a power-law of the form:

$$\frac{dN}{dE} = N_0 \left(\frac{E}{E_0} \right)^{-\Gamma} \quad [\text{ cm}^{-2}\text{s}^{-1}\text{MeV}^{-1}],$$

where the pivot energy, E_0, is set to 1000 MeV. A summary of the period-wise results is given in Table 7.2. A log-parabola model was also applied to the data, however the improvement to the fit was found to be statistically insignificant ($\sim 1\sigma$ improvement), hence the power-law model is favored in all cases. The results reported in Table 7.2 show that the spectral fits are self-consistent during all tested periods, suggesting that the scale of any spectral variability during this period is below the sensitivity of *Fermi*-LAT.

The time-averaged HE SED is obtained by dividing the data into 5 energy bins equi-spaced in log-space between 0.1-300 GeV. E_0 is set to the central energy in each energy bin and a fit is applied over the energy range of the bin, with the spectral index frozen to 2.0. The best-fit time-averaged HE SED is shown in Figure 7.9, flux points are shown for energy bins

with a $TS > 9$, otherwise 95% CL upper limits are calculated. The spectral indices for all periods are marginally harder than the 3FGL index of 2.12. This is consistent with a shift in the peak energy of the IC peak and will be discussed further in Section 7.3.

The 5-day binned light curve is obtained by freezing the spectral index to 2.0 and reapplying the fit to each time bin. This is shown in Panel (b) of Figure 7.11. 95% CL upper limits are shown for time bins with a $TS < 9$. The time-averaged 3FGL integral flux is extrapolated into the 0.1-300 GeV energy range, assuming a power-law model holds over this range. This is given in Table 7.2.

Period	Test Statistic (TS)	$\Phi(0.1-300$ GeV) ($\times 10^{-8}$ [cm^{-2}s^{-1}])	N_0 ($\times 10^{-12}$ [cm^{-2}s^{-1}MeV^{-1}])	Γ
Period 1	132.5	(4.56 ± 1.12)	(5.03 ± 0.89)	(1.92 ± 0.13)
Period 2	104.7	(6.26 ± 1.62)	(5.99 ± 1.04)	(2.03 ± 0.14)
Period 3	93.8	(6.55 ± 2.19)	(7.63 ± 1.68)	(1.88 ± 0.17)
Total	474.9	(5.88 ± 0.81)	(6.54 ± 0.60)	(1.91 ± 0.07)
3FGL	3193.4	(7.86 ± 0.28)[a]	N/A	$(2.12 \pm 0.03), (0.064 \pm 0.015)$[b]

[a] 3FGL fit is applied between 1 GeV and 100 GeV, this results in a flux of $(5.90 \pm 0.21) \times 10^{-9}$ cm^{-2}s^{-1}. The quoted flux assumes the best-fit 3FGL power law (of $\Gamma = 2.18$) is valid over the analysis range of 0.1 - 300 GeV.

[b] The 3FGL spectrum is best-fit by a log-parabola model. The quoted values are the best-fit α and β parameters, respectively.

Table 7.2: Summary of the *Fermi*-LAT results. Column 1 shows the period of analysis, with Total refering to data taken between 57731 and 57843 (MJD). Column 2 shows the TS of the best-fit model. Column 3 shows the integral flux between 0.1-300 GeV assuming a power-law model. Column 4 shows the best-fit flux normalization (N_0) at a normalization energy (E_0) of 1000 MeV. Column 5 shows the best-fit spectral parameters, which in the case of Periods 1-3 and the total dataset is the power-law index and for the 3FGL fit is the log-parabola model parameters.

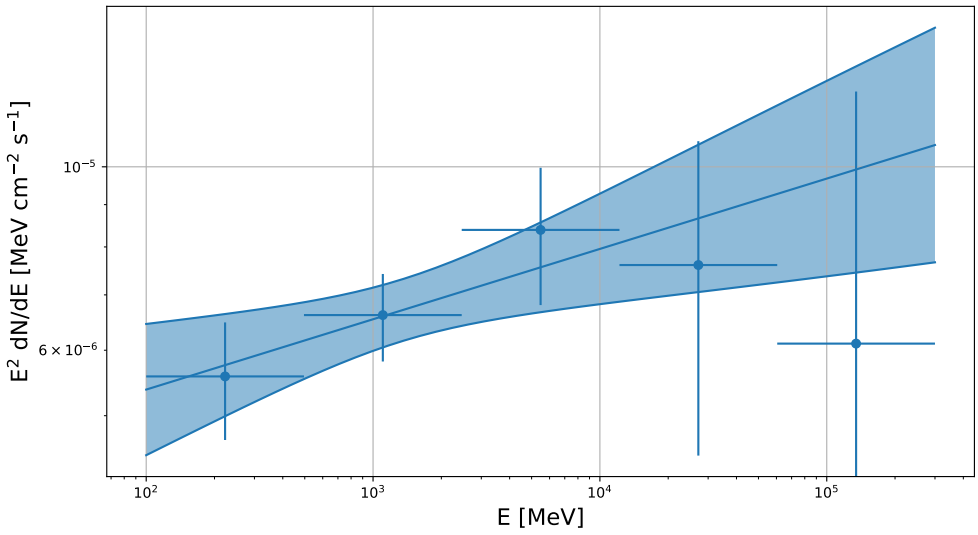

Figure 7.9: Total time-averaged spectral energy distribution of OJ 287 between 100 MeV and 300 GeV as observed by *Fermi*-LAT. The shaded region corresponds to the 1σ confidence interval on the best-fit power law. All energy bins are show a $TS > 9$ corresponding to $> 3\sigma$.

7.2.3 *Swift*-XRT

Swift-XRT data taken between 57723 and 57858 MJD (1st December 2016 - 15th April 2017) were reduced using the `xrtpipeline` using the standard procedures discussed in Section 4.4. As all of the observations considered here were taken in the window timing (WT) observing mode and the count rates were nominally less than 2 cts s^{-1}, pile-up effects are negligible, therefore no pile-up correction is required. Spectral analysis was performed by applying a power-law model and a log-parabola model modified by applying a neutral hydrogen (n_H) absorption factor (as described by Equation 4.17) to the data. The significance of the improvement of the log-parabola model was determined using a F-Test (see, for example, Chapter 11 of Bevington et al., 1993). A log-parabola was considered to be a significant improvement over a power-law model for a F-Test probability of $P_{F-Test} < 0.05$. In the fitting procedure n_H was set to the distance-weighted mean value obtained by the LAB survey of $n_H = 2.49 \times 10^{-20}$ cm^{-2} (Kalberla et al., 2005). The observation-wise results are shown in Table B.1 of Appendix B.1.

The integral flux between 0.3 - 10 keV was determined using the `cflux` spectral component[4] and is shown in Panel (c) of 7.11. This method calculates the intrinsic integral flux by

[4] see https://heasarc.gsfc.nasa.gov/xanadu/xspec/manual/node270.html

deabsorbing the spectrum for an assumed n_H. This allows for an estimate of the intrinsic flux of the source across the entire energy range of *Swift*-XRT. The integral flux is also obtained in three energy bands, "Soft" (0.3-1.0 keV), "Moderate" (1.0-3.0 keV) and "Hard" (3.0-10.0 keV). The multi-band X-ray light curve is shown in Panel (d) of Figure 7.11.

Figure 7.10 shows the best-fit spectral index plotted vs time. A constant fit model was applied to the data and was best-fit by a mean spectral index of $\Gamma = 2.44 \pm 0.01$. However, this model is a poor fit, as shown by the χ^2/NDF of 219.25/63. This poor fit quality indicates spectral variability during the observation campaign.

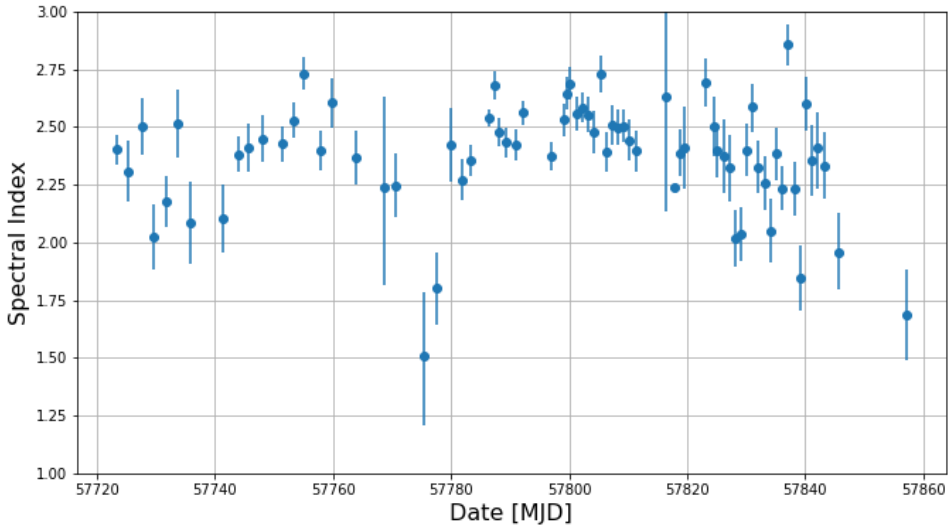

Figure 7.10: Observation-wise XRT spectral index, obtained from a fit to data between 0.3 and 10 keV, plotted as a function of time.

7.3 Discussions

7.3.1 Light-Curve Analysis

In addition to XRT observations, simultaneous observations were taken by *Swift*-UVOT as part of the follow-up campaign. While the results of the UVOT observations are included in this work, the analysis was performed by a VERITAS collaborator Dr. Karlen Shahinyan. Details of this analysis shall be presented in a future publication. The tools which Karlen has used to produce the UVOT results are publicly available on his GitHub.[5] The UVOT light

[5] https://github.com/KarlenS/swift-uvot-analysis-tools

curves are shown in Panels (e) and (f) of Figure 7.11.

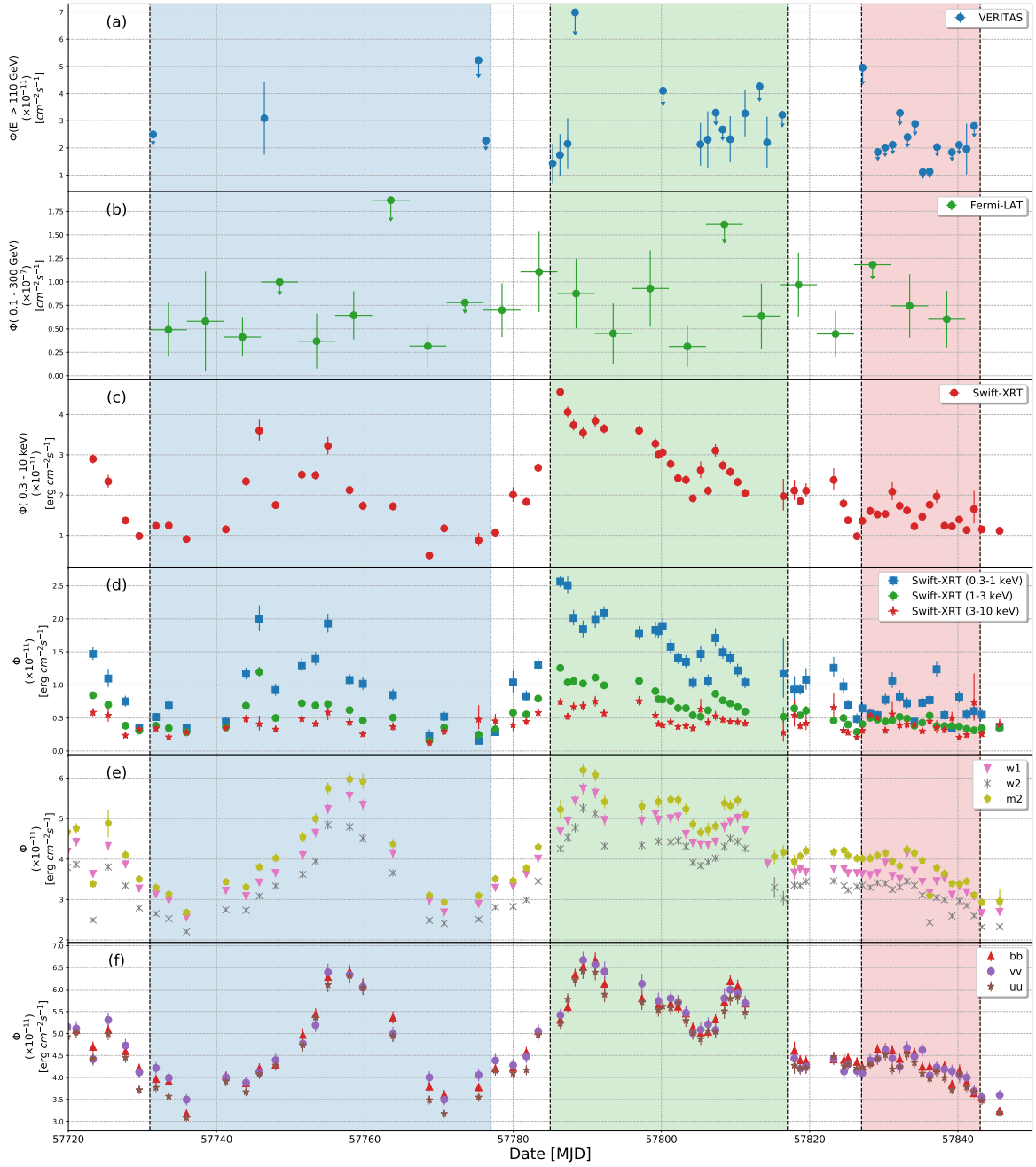

Figure 7.11: Multiwavelength light curve of OJ 287. Panel (a) VERITAS daily-binned integral flux above 150 GeV. Panel (b) *Fermi*-LAT five-day binned integral flux between 0.1-300 GeV. Panel (c) *Swift*-XRT daily-binned integral flux between 0.3-10 keV. Panel (d) *Swift*-XRT soft, moderate and hard X-ray flux, as defined in Section 7.2.3. Panel (e) *Swift*-UVOT daily-binned integral flux in the *w1*, *w2* and *m2* energy bands. Panel (f) *Swift*-UVOT daily-binned integral flux in the *bb* , *vv* , *uu* energy bands. The shaded regions correspond to the different analysis periods.

The multiwavelength light curves are shown in Figure 7.11. The general trend from UVOT-XRT is in good agreement and shows consistent variability patterns, however around ~ 57745 MJD there is an apparent flare in the XRT observations which is observed in each of the XRT energy bands (Panels (c) and (d) of Figure 7.11). This represents the second brightest X-ray flaring event during the entire campaign. There is no evidence of increased flux in the UVOT energy bands around this time. Conversely the flare which peaks at ~ 57755 MJD in the UVOT bands is not evident in either of the moderate or hard X-ray light curves. The soft X-ray flux shows an increase in flux at the onset of this event, however the decay timescale is different to those displayed in the UVOT bands. Similarly, the largest flare observed in X-ray energies, peaking on 57786 MJD, appears to peak while the UVOT flux is still increasing and decays more rapidly than the UVOT flux. This may be evidence of an X-ray led time lag between the two energy bands or due to different populations of elections resulting in different emission features. This shall be discussed further in Section 7.3.2.

The minimum variability time scale (Δt_{min}) is defined as the minimum time required for the flux to double. A search is applied to the X-ray energy bands to find Δt_{min}[6] with the results summarized in Table 7.3. A constraint on the size of the emission region can be obtained from Δt_{min} such that:

$$R \leq \frac{\delta c \Delta t_{min}}{1+z}, \tag{7.1}$$

where R is the size of the emission region, δ is the Doppler factor and z is the redshift of the source. Assuming the mean value of the doppler factor obtained by Jorstad et al. (2005) of $\delta = 18.9 \pm 6.4$, the size of the emission region is estimated and is shown in Column 8 of Table 7.3. The minimum emission size is determined from the soft band observations and is determined to be 3.70×10^{16} cm. This is approximately two times smaller than the constraints obtained from the moderate and hard X-ray fluxes. As the variability observed in the UVOT data is of a lower amplitude, with the flux increases on longer time scales, the Δt_{min} observed from the UVOT data corresponds to ~15 days. This corresponds to an emission size of $R = 5.62 \times 10^{17}$ cm, on order of magnitude larger than the constraint obtained from the soft X-ray light curve.

[6] A requirement on the significance of the flux change of 3σ was applied.

XRT Data Set	Δt_{min} ([Days])	t_{Start} ([MJD])	t_{Stop} ([MJD])	ϕ_{Start} ($\times 10^{-12}$ [erg cm^{-2}s^{-1}])	ϕ_{Stop} ($\times 10^{-12}$ [erg cm^{-2}s^{-1}])	Significance (σ)	R ([cm])
Total (0.3-10 keV)	2.00	57768.7	57770.7	(5.00 ± 0.85)	(11.72 ± 0.88)	5.5	7.50×10^{16}
Soft (0.3-1 keV)	0.99	57839.2	57840.2	(3.46 ± 0.59)	(8.14 ± 0.91)	4.3	3.70×10^{16}
Moderate (1-3 keV)	2.00	57768.7	57770.7	(1.52 ± 0.30)	(3.57 ± 0.30)	4.8	7.50×10^{16}
Hard (3-10 keV)	1.80	57826.4	57828.4	(2.05 ± 0.48)	(5.38 ± 0.92)	3.2	6.73×10^{16}

Table 7.3: Minimum variability time scale for X-ray observations. Column 1 shows the XRT dataset being tested. Column 2 shows the minimum variability time scale. Column 3 shows the MJD of the first observation. Column 4 shows the MJD of the last observation. Column 5 shows the integral flux of the first observation. Column 6 shows the integral flux of the last observation. Column 7 shows the significance of the flux increase, calculated as $(\phi_{Stop} - \phi_{Start})/\sqrt{\Delta\phi^2_{Stop} + \Delta\phi^2_{Start}}$, where $\Delta\phi$ is the error on ϕ. Column 8 shows the minimum size of the emission region, calculated using Equation 7.1.

The variability index of the VHE data of 30.14 is consistent with a constant flux model. While this doesn't rule out variably from OJ 287, it does suggest that the scale of any variability is smaller than the sensitivity of VERITAS for such a source. Due to the sampling of the dataset and the dimness of OJ 287 at VHE, studying the correlation of VHE to XRT data cannot be done using a DCF analysis. This is because a DCF analysis assumes that the error on one's data is Gaussian. A likelihood method has been developed to test for such correlation between XRT and VHE data and is discussed in Section 7.3.3.

The *Fermi*-LAT flux is on average lower than the time-averaged 3FGL flux (shown as a shaded region in Panel (b) of Figure 7.11) during the entire period, with no exceptional activity visible. It is worth noting that OJ 287 is more consistently detected on five-day time scales during the campaign than in previous observations[7].

7.3.2 Discrete Correlation Function Analysis

The discrete correlation function (DCF, Edelson & Krolik, 1988; Alexander, 2013), is a discrete implementation of the cross correlation function. DCF allows for one to test the correlation between two discretely sampled time series, such as blazar light curves, and to search for a time lag between the two series. The DCF of two dataset $\vec{a}$ and $\vec{b}$ is given by:

$$UDCF_{ij} = \frac{(a_i-\bar{a})(b_i-\bar{b})}{\sqrt{(\sigma_a^2-e_a^2)(\sigma_b^2-e_b^2)}}, \tag{7.2}$$

$$DCF(\tau) = \frac{1}{M}\sum UDCF_{ij}, \tag{7.3}$$

where τ is the time-lag, $\bar{f}$ is the mean value of $\vec{f}$, σ_f is the standard deviation of $\vec{f}$, e_f is the observed error associated with dataset $\vec{f}$, $UDCF_{ij}$ is the unbinned discrete correlation between the time-lag pair $\Delta t_{ij} = t_j - t_i$, hence $DCF(\tau)$ is the mean discrete correlation for M time-lag pairs such that $\tau - \Delta\tau/2 \leq \Delta t_{ij} < \tau + \Delta\tau/2$. The error on the DCF can be calculated as (Edelson & Krolik, 1988):

$$\sigma_{DCF}(\tau) = \frac{1}{M-1}\left(\sum\left[UDCF_{ij} - DCF(\tau)\right]^2\right)^{\frac{1}{2}}. \tag{7.4}$$

A DCF analysis is performed on each of the *Swift*-XRT flux bands (soft, moderate, Hard) and the *Swift*-UVOT observations to search for correlation between the different bands. To quantify the significance of peak in the DCF, one must obtain the probability distribution of the DCF of two uncorrelated time series with similar temporal properties and amplitudes as

[7] see https://fermi.gsfc.nasa.gov/ssc/data/access/lat/msl_lc/source/OJ_287 for long-term *Fermi*-LAT light curves of OJ 287.

the observed time series. To do this, random light curves are generated using the method described by Emmanoulopoulos et al. (2013) (herinafter E13). The method described by E13 generates light curves with identical power spectrum distribution (PSD), by invoking a similar treatment as Timmer, J and König (1995), and flux probability distribution function (PDF) as the observed light curves. The method is applied as follows:

1. The PSD (S) and PDF (PDF_{obs}) of the observed dataset, with n observations, is obtained using the method in Appendix A2 of E13. In these methods the PSD is estimated using a likelihood analysis, while the PDF is estimated from the observed data.

2. The random Fourier components of the time series are generated as (adapted from Equation 9 of Timmer, J and König, 1995):

$$\mathcal{F}(\omega) = \sqrt{\frac{1}{2}S(\omega)}\mathcal{N}(0,1) + i\sqrt{\frac{1}{2}S(\omega)}\mathcal{N}(0,1), \tag{7.5}$$

   where ω is the Fourier frequency and $\mathcal{N}(0,1)$ is a normally-distributed random variable.

3. A random time series (x_{norm}) is obtained by taking the inverse-Fourier transform of Equation 7.5.

4. A set of n random numbers is drawn from PDF_{obs}. Let this be $x_{sim,i}$.

5. The discrete Fourier transform (DFT) of x_{norm} and $x_{sim,i}$ are obtained and their amplitude ($\mathcal{A}_{norm/sim_i}$) and phase ($\psi_{norm/sim,i}$) are obtained:

$$\mathcal{A} = \frac{1}{n}\sqrt{Re[DFT]^2 + Im[DFT]^2} \tag{7.6}$$

$$\psi = \tan^{-1}\left(\frac{Im[DFT]}{Re[DFT]}\right) \tag{7.7}$$

6. An adjusted DFT is obtained by combining the amplitude of x_{norm}, $\mathcal{A}_{norm}$, and the phase of $x_{sim,i}$, $\psi_{sim,i}$. The inverse DFT is taken to obtain the combined time series $x_{adj,sim}$.

7. A new time series ($x_{sim,i+1}$) is created by ranking the values of $x_{sim,i}$ based on the order of $x_{adj,sim}$. That is, the highest value in $x_{adj,sim}$ is replaced by the highest value in $x_{sim,i}$, the second highest value in $x_{adj,sim}$ is replaced by the second highest value in $x_{sim,i}$ and so on.

8. Steps 5 - 7 are repeated, setting $x_{sim,i} = x_{sim,i+1}$ for each new iteration until convergence is achieved (i.e. $x_{sim,\lambda} = x_{sim,\lambda+1}$, where convergence has occurred after λ iterations).

The time series $x_{sim,\lambda}$ will have identical PSD and PDF as x_{obs}.

Using the method discussed above, 100,000 random light curves are generated for each *Swift* flux band. The DCFs for 100,000 pairs of random light curves are obtained. The binned, normalized distributions of $DCF(\tau)$ therefore act as a probability distribution of the DCF for the pair of observations. When generating light curves, it is crucial to use the same temporal sampling as the observed datasets. To achieve this the observed light curve is re-sampled at a regular rate equal to $1/\Delta t_{min}$, where Δt_{min} is minimum time between two observations. The light curve is resampled by interpolating between the observed data points to achieve the desired sampling. The final random light curve is then resampled at the observed sampling.

The DCF analysis is applied to each UVOT and XRT energy band, which each combination of observations explored. The results of each analysis is given in Appendix B.2, with an example set of results of the Soft XRT shown in Figure 7.12. The correlation between the Soft XRT and UVOT data shows a 2-3σ correlation slightly offset from zero. For example in Figure 7.12 the peak in the DCF for *bb* and soft X-rays (top left panel) occurs at a time lag of -1 days, suggesting that the soft-XRT flux is leading the *bb* flux by 1 days. To ensure this is not due to a binning effect the time-lag bins were shifted by 0.5 days. Under this new binning the peak occurred at 0.5 days, which is consistent with no time lag between the energy bands. For UVOT observations, when comparing with other UVOT bands, there the peak DCF value occurs for a τ consistent with zero, suggesting no time lag. It is worth noting that both the Soft and Moderate X-ray flux shows a 2-3σ correlation to each of the UVOT-energy bands, however the Hard X-ray flux doesn't show any significant correlation to the UVOT flux. This, when combined with the flaring activity observed in UVOT and soft X-rays which does not occur in the Hard X-ray flux, may indicate that the X-ray emission may be a composite of the X-ray flux from two or more different regions, with the Harder component of the X-ray flux coming from a different region to the UVOT and softer X-ray flux.

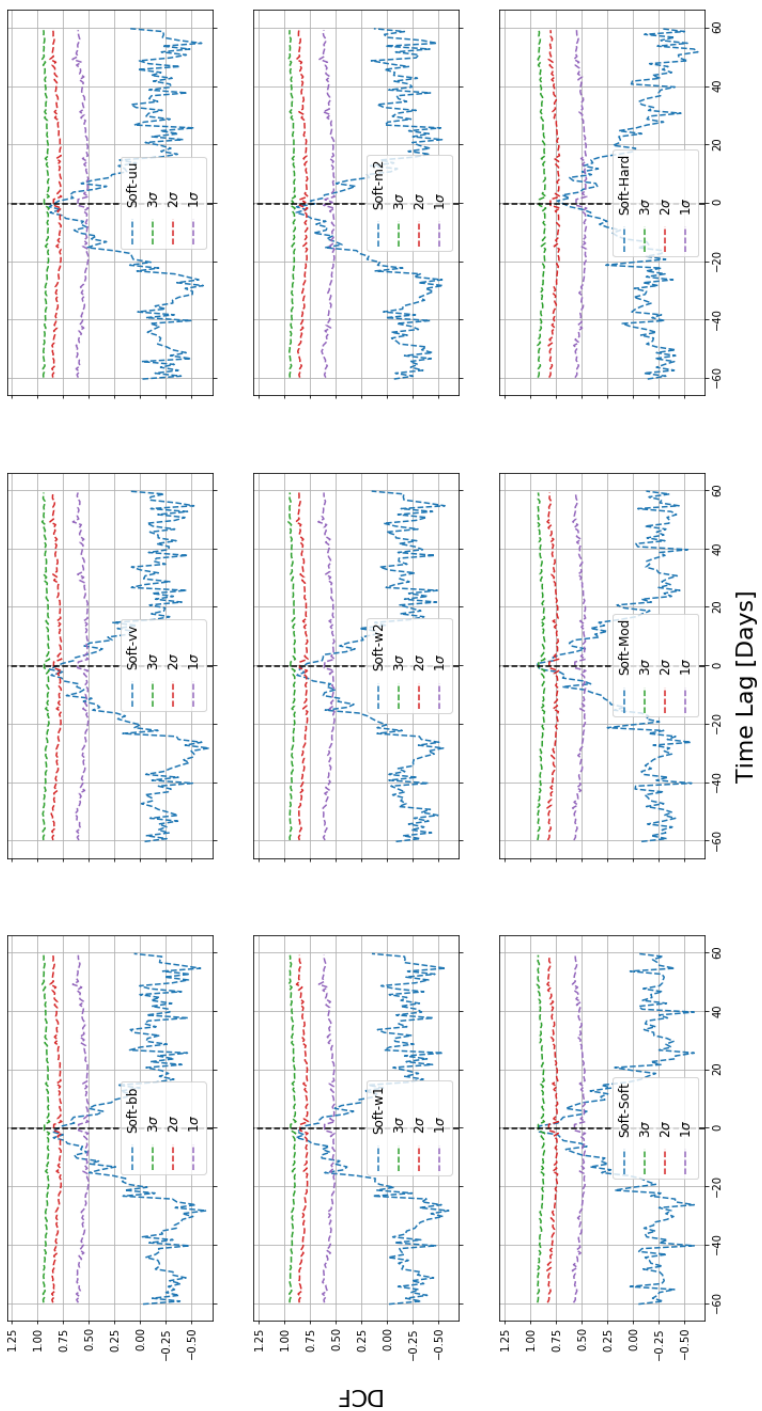

Figure 7.12: Discrete correlation function analysis for Soft-XRT observations. The blue points show the experimentally measured DCF values. The dashed purple, red and blue lines correspond to 1-, 2- and 3-σ confidence intervals obtained using the method described in Section 7.3.2. A negative time lag suggests a Soft-XRT-lead, while a positive time lag suggests the Soft-XRT data is trailing the tested energy band. The top two rows show the correlation between Soft-XRT and UVOT, which the bottom row shows the correlation between Soft-XRT and other XRT bands. Note the time bin at $\tau = 0$ is removed.

7.3.3 VHE - XRT Flux Correlation Analysis

To test for a correlation between VHE and XRT observations, a likelihood-based flux-flux correlation analysis, as described in Appendix A.2, is applied to the VHE and XRT data. This method correctly handles the non-significant VHE data, as simply excluding non-significant data results in a bias towards positive fluctuations of an experimentally measuremed true distribution of fluxes. The flux-flux correlation test assumes a simple linear correlation between VHE and XRT data (i.e. $\phi_{VHE} = m \times \phi_{XRT} + c$), with the null hypothesis being a constant relation (i.e. $\phi_{VHE} = c$). This allows for the significance of such a correlation to be estimated a using a likelihood-ratio test (as described in Appendix A.2).

A fit is applied to the VERITAS data and each XRT energy band (soft, moderate, hard, total). In doing so, data taken within ±0.5 days of each other are considered simultaneous for the fitting procedure. The results of these fits are shown in Table 7.4. A flux-flux plot of the VHE vs total X-ray flux is shown in Figure 7.13, with the dashed lines corresponding to the best-fit constant-flux model (red) and correlated-flux model (green). While upper limits are shown in Figure 7.13, these observations are included in the fitting procedure.

XRT Data Set	Slope (m) ([ergs−1])	Constant (c) ($\times 10^{-12}$ [cm^{-2}s^{-1}])	log $\mathcal{L}$	$-2 \log \frac{\mathcal{L}}{\mathcal{L}_0}$	Prob
Constant Flux	0	(13.42 ± 1.74)	42686.998[a]	N/A	N/A
Total (0.3-10 keV)	(0.47 ± 0.18)	(3.85 ± 4.03)	42690.236	6.47	0.011
Soft (0.3-1 keV)	(0.66 ± 0.28)	(6.21 ± 3.42)	42689.787	5.58	0.018
Moderate (1-3 keV)	(1.79 ± 0.70)	(3.19 ± 4.28)	42690.188	6.38	0.012
Hard (3-10 keV)	(1.28 ± 1.20)	(7.52 ± 5.75)	42687.507	1.02	0.313

[a] This corresponds to the likelihood of the Null hypothesis (log $\mathcal{L}_0$)

Table 7.4: Summary of the search for flux-flux correlation betwen VHE and XRT data. Column 1 shows the XRT dataset being tested. Column 2 shows the best-fit slope. Column 3 shows the best-fit constant. Column 4 shows the log-likelihood of the best-fit model. Column 5 shows the likelihood-ratio test results. This assumes log $\mathcal{L}_0$ to be the log-likelihood of the constant-flux model. This is χ^2-distributed with one degree of freedom. Column 6 shows the probability of the test model being observed assuming the constant-flux model is the true model.

The flux-flux correlation test shows that a correlated-flux model is significant at the $\sim 98\%$ confidence level for all energy ranges with the exception being the hard X-ray range. This is surprising as the obtained VHE TS_{var} of 30.14 (with 31 degrees of freedom) suggests that emission is consistent with a constant-flux model. The difference between the two tests can be reconciled by considering that the two tests utilize different data sets. While the TS_{var} calculation considers all observations, the correlation test only considers VHE data with con-

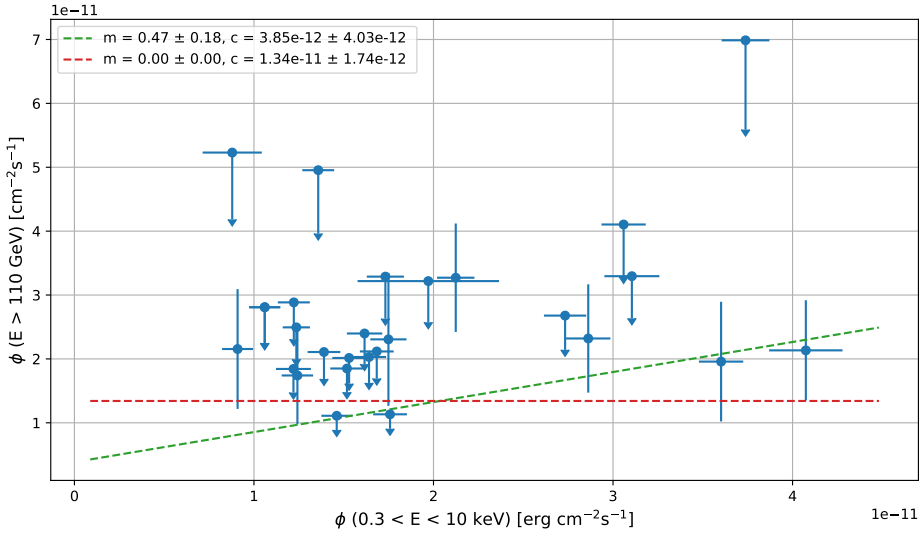

Figure 7.13: Flux-Flux correlation between *Swift*-XRT (0.3-10 keV, x-axis) and VERITAS (E > 150 GeV, y-axis), for data binned into daily time bins. 95% CL Upper limits are plotted for VERITAS data with a TS<4, corresponding to $\sim 2\sigma$. The dashed red line shows the best-fit constant flux model. The dashed green line shows the best-fit correlated flux model. While upper limits are plotted for some points, all data points are included in the fitting procedure (as discussed in Appendix A.2).

temporaneous X-ray observations (taken within one day of the VERITAS observation). For VHE observations with contemporaneous X-ray observations the TS_{var} is determined to be 38.06 for 26 degrees of freedom. This results in a χ^2-probability of 0.06. As the correlated model is less complicated than the alternative hypothesis of the TS_{var}, a smaller improvement to the model will be more significant than a similar improvement to the more complicated model. While the null hypothesis is common between the two tests (constant-flux model), the two models are not strictly nested, therefore Wilks' Theorem doesn't hold when applying a likelihood-ratio test between the two models. This is reflected in the fact that each test considers a different "analysis question".

Considering the probabilities given in Table 7.4, the VHE flux is more strongly correlated to the soft and moderate energy bands than the hard band. This suggests that the VHE flux is more likely originating from the same emission process responsible for the soft and moderate X-ray flux. This could also be due to poorer statistics in the hard X-ray band. In this case the variability of the hard X-rays would be below the sensitivity of *Swift*.

7.3.4 Spectral Energy Distribution

The time-averaged SED is obtained for Period 2. This is shown in Figure 7.14. The *Swift*-XRT observations during Period 2 are combined using the guidelines available described on the *Swift* FAQ webpage.[8] These methods involve combining the photon files and exposure files to correctly account for the exposure in a time-averaged fit. Once combined, standard signal and background analysis is performed as described in Section 4.4 and the best-fit energy spectrum is obtained using `PyXSpec`. The time-averaged spectrum is best-fit by a power-law model with a spectral index $\Gamma = 2.53 \pm +0.01$ and integral flux $\phi(0.3 - 10\ \mathrm{keV}) = \left(3.28^{+0.03}_{-0.02}\right) \times 10^{-11}$ erg cm^{-2}s^{-1}. The time-averaged X-ray SED is shown in Figure 7.14. The yellow data points correspond to the observed data while the purple data points correspond to the deabsorbed SED (deabsorbed assuming $n_H = 2.49 \times 10^{-20}$ cm^{-2}).

The time-averaged Period 2 SED for *Fermi*-LAT and VERITAS are also shown in Figure 7.14 in green and blue, respectively. While statistics-limited at the highest *Fermi*-LAT energy range, the *Fermi*-LAT and VERITAS SED are in good agreement, suggesting a turnover in the SED close to 100 GeV. For comparison, 3FGL SED is overlaid as a red line. The 3FGL SED peaks in the MeV to sub-GeV range, orders of magnitude below that of the Period 2 SED. This suggests a shift in the IC-peak during the campaign. The shifting in the IC-peak also explains the increased detection rate by *Fermi*-LAT accompanied by decreased integral flux, as more photons are being detected in the GeV range where *Fermi*-LAT has a greater sensitivity. This combined with an inversion of the X-ray SED (with respect to archival data) suggests a broadband shift in the overall SED.

Britzen et al. (2018) suggest that the long-term multiwavelength behavior of OJ 287 can be credited to geometric effects of a precessing jet with a precession timescale of ~22 years. Geometric effects of a precessing jet would result in changes in the jet-viewing angle and hence the Doppler factor. This would result in dramatic changes in the SED. This has been shown for changes in the X-ray SED of Mrk 501 (Villata & Raiteri, 1999). It was suggested (via a private communication with the authors) that the model proposed by Britzen et al. (2018) would reach a maximum Doppler factor during 2017, potentially suggesting that the VHE emission is solely due to a change in Doppler factor. However, this doesn't entirely account for VLBI observations taken by Svetlana Jorstad and Alan Marscher (via private communication), which show the emission of a new subluminal knot, temporally coincident with the observed VHE emission. Furthermore previous observations of multiwavelength flares do not report X-ray variability on the scale of those reported here (see, for example, Valtonen et al., 2016).

[8] https://swift.gsfc.nasa.gov/help/swiftfaq.html#_xrt-combine

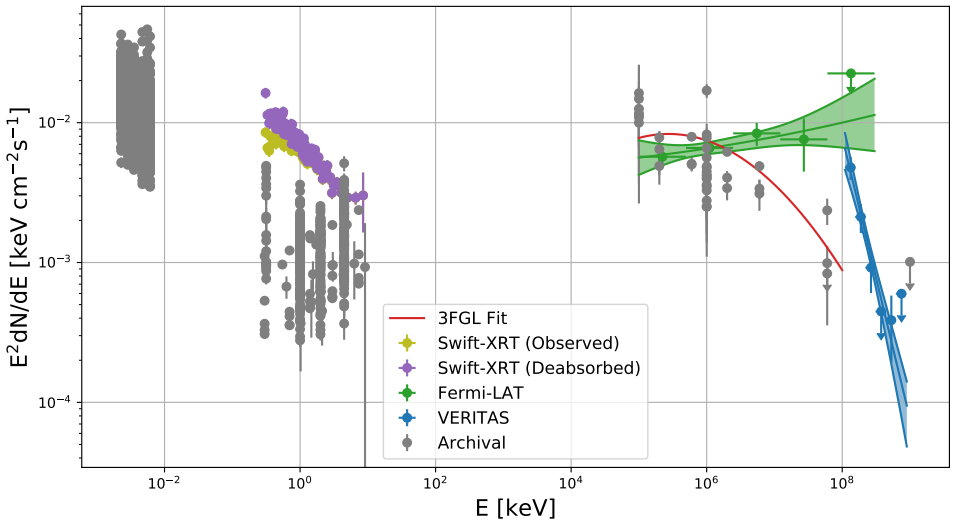

Figure 7.14: Time-averaged Period 2 SED for OJ 287. The grey data is archival data obtained from https://tools.asdc.asi.it/SED/

Kushwaha et al. (2018) attempt to model the SED of OJ 287 during this period, by assuming the emission originates from two spectral components, with the first spectral component resulting from a sub-parsec region of the jet and the second component at the parsec scale being responsible for the VHE emission. It should be pointed out that in an attempt to model the evolution of the SED Kushwaha et al. (2018) use the incorrect VHE spectrum, using the total-time averaged rather that the spectrum for Period 2. The modelled SED for MJD 57786, corresponding to approximately the start of Period 2, is in poor agreement with the observed data, particularly at UV and VHE energies. The SED is below the incorrectly selected VERITAS time-averaged SED, which is dimmer than the correct SED for Period 2, hence it would be in further disagreement.

The modeling of the SED of OJ 287, at the time of writing, is being finalized by collaborator Dr Olivier Hervet (UCSC) and will be presented in a future publication, however I will briefly discuss the main concepts of the model. The evolution of the SED shall be modelled used the model described by Hervet et al. (2015). This model assumes the emission originates from a "blob in jet" system, which is supported by the emission of a new radio knot at the time of the VHE detection. In this model, the relative components of jet and local environment which would interact with the blob are also accounted for. In the case of HBLs, these contributions are generally neglected. However, if OJ 287 is a LBL/IBL, one might expect a rather dusty region. The broadband SED is therefore described by a blob of relativistically

travelling electrons in a jet, in which the jet's SSC component will significantly contribute to the SED. The blob emission will be SSC and EC emission where the EC emission is due to a different component:

- The blob is within a wider jet which is emitting synchrotron emission. As the Doppler factor of the blob is larger than the jet, the blob will upscatter the jet synchrotron photons.
- The blob is assumed to be within the BLR. For this reason, there will be an EC component due to disk radiation reprocessed by the BLR. The disk radiation is well constrained by the UVOT observations.

This model can successfully explain the observed variability features, for example the relative strength of the correlations. The correlation between XRT soft/moderate with the UVOT and VHE datasets arises due to the blob's synchrotron component dominating the SED at these energies, while the hard XRT band is dominated by the jet's IC component, possibly explaining the lack of strong correlation. The transition between Period 1 and Period 2 can be explained as a change in the magnetic field strength of the blob by a factor of 2, with all other parameters remaining constant. This provides a physically motivated evolution of the SED between periods.

7.4 Summary

In this section the results of an exceptional period of enhanced multiwavelength activity from OJ 287 have been presented. These observations have resulted in the first detection of VHE gamma-ray emission from OJ 287. This has allowed the VHE energy spectrum of the source to be obtained. The VHE energy spectrum for Period 2, the period of exceptional VHE activity, was found to show a consistent spectral shape with the total time-averaged VHE spectrum. The VHE flux, when binned into daily time bins, was found to be consistent with a constant-flux model. However, when binned into coarser bins, a general decreasing trend is observed over the course of the campaign. This suggests a general decline in the VHE flux over the campaign, with daily variations in the flux below the sensitivity of VERITAS. Additionally, correlation between the VHE and X-ray integral flux was found to provided a significant improvement over the constant flux model at the 98% confidence level, with the VHE flux showing a stronger correlation to the soft and moderate X-ray flux than the hard X-ray flux.

X-ray and UVOT observations taken by *Swift* show a 2-3σ correlation for all tested energy bands apart from the hard X-ray energy band. While there is marginal evidence for an X-ray led time lag of 1-2 days, the time lag is found to be consistent with zero when binning effects are considered. The lack of a strong correlation between the hard X-ray flux and the UVOT flux, coupled with different variability structures observed in different energy bands, suggest that the observed emission is arising from number of different emission regions. The X-ray light curves allow for the minimum variability time scale to be obtained and for constraints on the size of the emission region to be obtained. The constraints obtained from soft and hard X-ray observations are 3.70×10^{16} cm and 6.73×10^{16} cm, respectively. This may be further evidence of multiple emission regions. The idea of multiple emission regions shall be discussed further in a future publication detailing the full broadband SED modelling of OJ 287 during this observation campaign.

OJ 287 is a moderately distant blazar ($z = 0.306$). The energy spectrum of OJ 287 can be used to place constraints on the shape and density of the EBL. The high statistics obtained during the campaign allow for the energy spectrum to be probed up to $\sim$ 900 GeV. This corresponds to an EBL opacity of $\tau_{EBL} > 3$ (Franceschini et al., 2008). The energy spectra detailed here shall be combined with observations of other blazars and used in an EBL constraint effort in an upcoming publication by the VERITAS Collaboration. In addition, a likelihood-based EBL constraint method is presented in Chapter 8 in which a joint-likelihood fit shall be used to obtain a fit to the EBL density, assuming a theoretical model.

In summary, this flaring event represents the most extreme X-ray event observed from OJ 287, a source of tremendous interest to the astronomical community. The deep observational campaign performed by VERITAS and *Swift* results in an exceptional dataset with UV to VHE coverage on a near daily basis. This exceptional dataset has also been used to test new variability and correlation tools for VHE instruments, allowing for the study to be extended to low-statistics data.

Chapter 8

Constraints on the Extra-Galactic Background Light using Very-High-Energy Observations of TeV Blazars

8.1 Overview

In this section the Extragalactic Background Light (EBL) is discussed. In Section 8.1.1 an overview of the EBL is provided with its cosmological importance and its effect on VHE observations of distant sources discussed. In Section 8.1.2 an overview of the different methods that have been applied to modeling the EBL are discussed. In Section 8.1.3 state-of-the-art constraints on the EBL intensity, placed by VHE observations of blazars are discussed. In Section 8.2 the method used in this analysis is discussed. In Section 8.3 the sources used in this analysis are discussed. In Section 8.4 the results of a likelihood analysis, obtained assuming different EBL models, is presented, with upper limits and discussions of the results discussed in Section 8.5.

8.1.1 Extragalactic Background Light

The Extragalactic Background Light (EBL) is the second-most-intense form of background light, with the first being the Cosmic Microwave Background (CMB), and contains the redshifted optical radiation emitted across all epochs. A portion of the optical emission will be absorbed by dust and reemitted at IR wavelengths. This results in SED of the EBL being characterized by a double peak structure, with the lower wavelength peak ($\sim$ 1 μm) being due to light emitted by stars and the longer wavelength peak ($\sim$ 100 μm) being due to the light reemitted by dust. See Figure 8.1 for a plot of the SED models of the EBL.

As the EBL contains a record of the optical light emitted during the history of the universe, it is of great cosmological significance, as the evolution of the background optical light is correlated to the star formation rates. Indeed, the EBL may contain the imprint of the yet

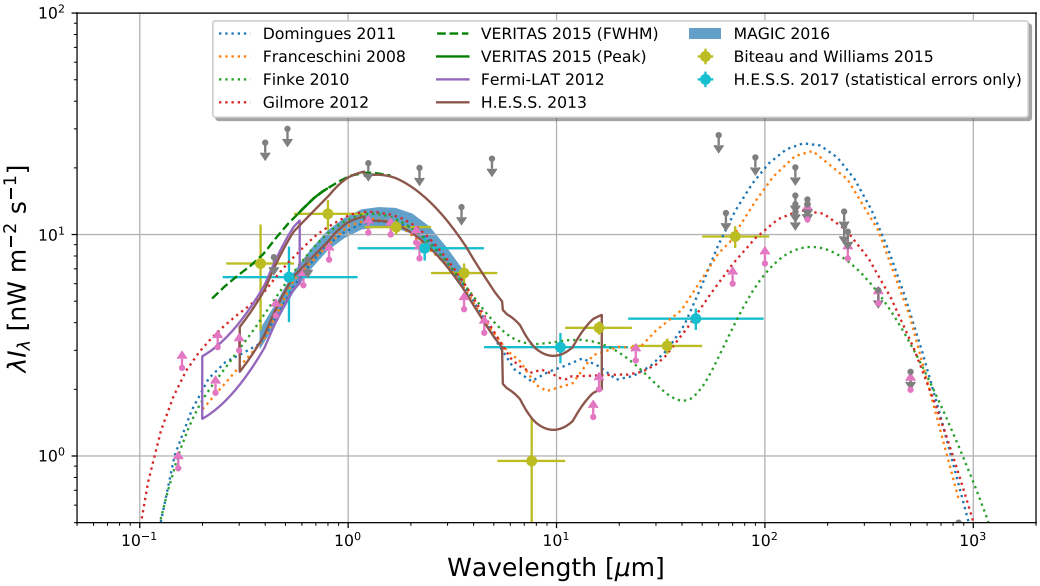

Figure 8.1: Comparison of EBL models, measurements and constraints. VERITAS 20015 (FWHM) and (Peak) refer to the constraints made by Abeysekara et al. (2015), where FWHM and Peak refer to the full width half max and peak of $\sigma_{\gamma\gamma}$. Fermi-LAT 2012 refer to the results obtained by Ackermann et al. (2012b). H.E.S.S. 2013 refers to the results obtained by Abramowski et al. (2013). H.E.S.S. 2017 refers to the results obtained by Abdalla et al. (2017). Biteau and Williams 2015 refers to the results by Biteau & Williams (2015). MAGIC 2016 refer to the results obtained by Ahnen et al. (2016). The upper and lower limits, gray and pink arrows respectively, correspond to the limits obtained from direct measurements, as compiled by Biteau & Williams (2015), relying heavily on the work of Dwek & Krennrich (2013). See text for a description of the different EBL measurements.

unresolved first population of stars (Population III stars). Furthermore as the EBL contains an imprint of stellar evolution, it may be used to derive estimates on properties such as X-ray and Radio background light, supernovae rates and neutrino background (for a review see, Dwek & Krennrich, 2013; Costamante, 2013).

Despite its importance the true shape and intensity of the EBL is not well constrained. This is due to the intrinsic difficulties in measuring such a faint photon field. Direct EBL measurements are hindered by the presence of zodiacal light. Strict lower limits on the intensity of the EBL can be obtained by integrating the light from resolved galaxies obtained from deep-field surveys. However, these limits are subject to the sensitivity of the surveying instrument's limiting magnitude and estimates of the SEDs of resolved sources. For a review of direct measurement methods and results see Hauser & Dwek (2001); Dwek & Krennrich (2013).

Indirect measurements of the EBL can be done using observations of distant sources of VHE emission, for example blazars. VHE photons traversing the universe will undergo an energy and distance dependent attenuation due to pair production via photon-photon interaction of the VHE photons with lower-energy photons ($\gamma_{VHE} + \gamma_{EBL} = e^+ + e^-$, Gould & Schréder, 1967). The energy threshold hold for such an interaction will be:

$$\epsilon_{thresh} = \frac{2\left(m_e c^2\right)^2}{E\,(1-\mu)}, \tag{8.1}$$

where ϵ_{thresh} is the threshold energy for an EBL photon interacting with VHE photon of Energy E and $\mu = \cos\theta$ where θ is the angle of interaction.

The cross section of this interaction is given by (Heitler, 1954; Franceschini et al., 2008):

$$\sigma_{\gamma\gamma}(E,\epsilon,\theta) = \frac{3\sigma_T}{16}(1-\beta^2)\times\left[2\beta(\beta^2-2)+(3-\beta^4)\ln\left(\frac{1+\beta}{1-\beta}\right)\right], \tag{8.2}$$

where σ_T is the Thompson cross-section and β is given by:

$$\beta = \left(1-\frac{2m_e^2c^4}{E\epsilon(1-\mu)}\right)^{1/2} = \sqrt{1-\frac{\epsilon_{thresh}}{\epsilon}}, \tag{8.3}$$

The maximum probability of interaction occurs at $\mu = 0$, where the energy threshold is at a minimum (Mazin & Raue, 2007; Franceschini et al., 2008):

$$\lambda^{max}(\mu\mathrm{m}) \approx 1.24E(\mathrm{TeV}), \tag{8.4}$$

where λ^{max} is the wavelength at which the cross-section is at a maximum for a photon of energy E. This is shown in Figure 8.2.

The optical depth of a gamma ray emitted at a redshift z will be (Dwek & Krennrich, 2013):

$$\tau(E,z) = \int_0^z dz' \frac{dl}{dz'}\int_{-1}^{1} d\mu \frac{1-\mu}{2}\int_{\epsilon'_{thresh}}^{\infty} d\epsilon n_\epsilon(\epsilon,z')(1+z')^3\sigma_{\gamma\gamma}(\beta',z'), \tag{8.5}$$

where l is the proper distance such that:

$$\frac{dl}{dz} = c\left|\frac{dt}{dz}\right| = \frac{c}{H_0(1+z)[\Omega_m(1+z)^3+\Omega_\Lambda]^{1/2}}, \tag{8.6}$$

assuming a flat ($\Omega_k = 0$) and matter dominated ($\Omega_R \ll 1$) ΛCDM universe, with Hubble constant H_0 and dimensionless density parameters Ω_R, Ω_m, Ω_k, and Ω_Λ for the radiation,

matter, curvature and the cosmological constant Λ. $n_\epsilon = dn/d\epsilon$ is the specific co-moving number density of the EBL. The $(1+z)^3$ corresponds to the conversion from specific to proper number density. In the above the energy threshold ϵ'_{thresh} is modified by a factor of $(1+z)$ such that:

$$\epsilon'_{thresh} = \frac{2(m_e c^2)^2}{E(1-\mu)(1+z)}, \tag{8.7}$$

with β' appropriately becoming $\beta' = \left(1 - \frac{\epsilon'_{thresh}}{\epsilon}\right)^{1/2}$. This is due to the interacting gamma ray being emitted at a higher redshift than when the interaction occurs.

This opacity factor results in an energy and redshift modification of the VHE energy spectrum as observed by an observer at $z = 0$:

$$\left(\frac{dN}{dE}\right)_{obs} = \left(\frac{dN}{dE}\right)_{int} e^{-\tau(E,z)}, \tag{8.8}$$

where $\left(\frac{dN}{dE}\right)_{obs}$ and $\left(\frac{dN}{dE}\right)_{int}$ are the observed and intrinsic energy spectrum. This results in the observed energy spectra of distance VHE emitters containing the imprint of EBL attenuation. Further more this also suggests a distance after which the VHE emission is totally attenuated and no VHE emission is visible from Earth. This is known as the "gamma-ray horizon". Using methods discussed below, constraints and measurements of the EBL can be made using VHE observations of distant sources.

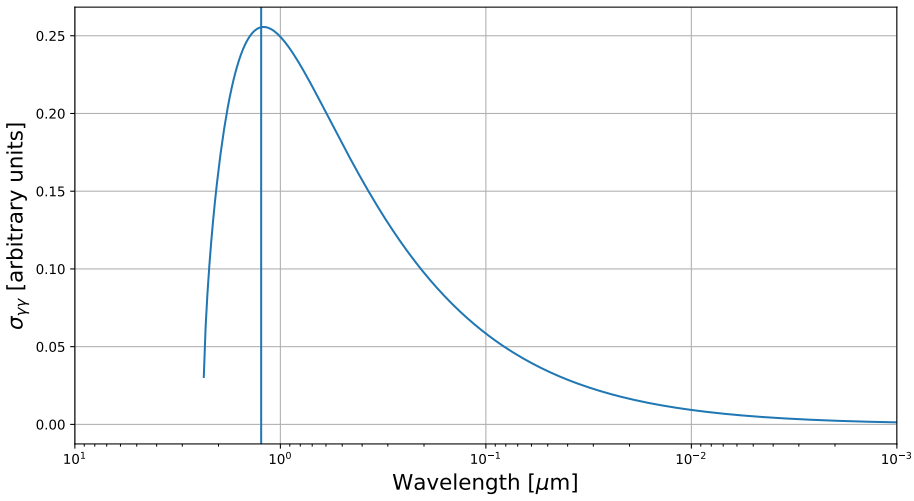

Figure 8.2: Cross section for a gamma ray with energy 1 TeV and $\mu = 0$. The cross-section is given by Equation 8.2 and peaks at 1.24 μm, as given by Equation 8.4.

8.1.2 Extragalactic Background Light Models

Figure 8.1 shows a comparison of the different EBL models discussed here, as well as limits obtained from VHE observations, as discussed in Section 8.1.3, and upper and lower constraints obtained from direct measurements and integrated galaxy counts as compiled by Biteau & Williams (2015), building on the work of Dwek & Krennrich (2013). For a review of the different EBL constraint methods, direct measurements of the EBL and a discussion of the different EBL modeling methods, see Hauser & Dwek (2001); Dwek & Krennrich (2013); Costamante (2013).

In general, modelling of the EBL has taken one of the following methods:

- Backwards Evolution Models
- Forward Evolution Models
- Semi-Analytical Models

Backwards Evolution Models, such as Franceschini et al. (2008); Domínguez et al. (2011), construct libraries of the local SED of galaxies and extrapolate their evolution backwards in time. These libraries represent the different types of galactic morphologies observed (i.e. spirals, ellipticals, irregulars) as well as any activity observed from galaxies such as galaxy mergers, AGNs and starburst galaxies. The evolution of the luminosity function (number of galaxies per luminosity interval) is then inferred either from deep field surveys, for example those obtained by the Herschel and Spitzer missions, or modelled using some form of redshift evolution (for example $(1 + z)^{\gamma}$, Dwek & Krennrich, 2013).

Forward Evolution Models, such as Finke et al. (2010), use the redshift-dependent cosmic star-formation rates (CSFR), in order to model the EBL intensity. This method is hampered (see, for example, Dwek & Krennrich, 2013) by the difficulty in measuring the CSFR, in particular at high redshifts due to UV-extinction, uncertainty in the initial mass function of galaxies, uncertainty in the duration of starburst activity as a function of redshift, the determination of galactic SEDs and the fraction of starlight absorbed and remitted by dust.

Semi-Analytical Models, such as Gilmore et al. (2012), model the formation and evolution of galaxies assuming a ΛCDM universe. Using parameters derived from the 5-year Wilkinson Microwave Anisotropy Probe (WMAP5), semi-analytical models model the formation, growth and evolution of galaxies, and the associated physical processes such as star formation, supernovae rates, galaxy mergers, etc., to obtain a model of the EBL. These complex models rely on the modelling of a large number of physical processes in deriving galactic properties, from which EBL estimates and evolution can be obtained.

In this thesis I use the models obtained by Franceschini et al. (2008); Finke et al. (2010); Domínguez et al. (2011) and Gilmore et al. (2012). While disagreeing at larger wavelengths ($\lambda \gg 10\mu$m), these models are generally in good agreement in the $\sim 0.1-\sim 10\mu$m range, the range this analysis is sensitive to.

Note: while a more recent release of the Franceschini et al. (2008) EBL model has been released (see, Franceschini & Rodighiero, 2017), the updated model does not affect the results of Franceschini et al. (2008) in the wavelength range relevant to this analysis.

8.1.3 Constraints on the Extragalactic Background Light from VHE observations

While not discussed here, similar methods to those described in this section have also been performed using HE observations of blazars (see, Ackermann et al., 2012b).

Constraints on the EBL from VHE observations have generally adopted either a model-dependent of model-independent approach. In model-dependent methods, a known theoretical model of the EBL is used. A normalization β_{scale} is then applied to the model such that $\beta_{scale} = \tau_{test}/\tau_{theory}$. In this form, $\beta_{scale} = 0$ suggests no EBL, while $\beta_{scale} = 1$ suggests the test model is equal to the theoretical model. A fit is then applied to the observed VHE data such that:

$$\left(\frac{dN}{dE}\right)_{obs} = \left(\frac{dN}{dE}\right)_{int} e^{-\beta_{scale}\tau_{theory}(E,z)}. \tag{8.9}$$

A scan of β_{scale} is then applied with the best-fit intrinsic parameters treated as nuisance parameters. The treatment of the allowed values of the spectral parameters vary from analysis to analysis, but then generally either require the spectral parameters to conform to theoretical bounds, to be in agreement with extrapolated values from lower energies (for example requiring the VHE spectrum to be not harder than the gamma-ray spectrum below ~ 20 GeV, where EBL attenuation is negligible) or make no assumption on the intrinsic spectral parameters. Using this profile scan of β_{scale}, either a best-fit value of β_{scale} can be obtained or upper limits can be derived. In this method, it is common to compare one's results to a no-EBL hypothesis ($\beta_{scale} = 0$) in order to quantify the significance of the best-fit spectral model with and without EBL attenuation. This is often used to quantify the significance of an EBL "detection".

The H.E.S.S. Collaboration (Abramowski et al., 2013) claim the first measurement of the EBL using VHE gamma rays. Assuming a Franceschini et al. (2008) EBL model, Abramowski et al. (2013) analyse 17 spectra from 7 VHE blazars detected by H.E.S.S. Abramowski et al. (2013) obtain a best-ft value $\beta_{scale} = 1.27^{+0.18}_{-0.15}$, and find no redshift dependence on β_{scale} suggesting the Franceschini et al. (2008) EBL model accurately describes the redshift evolution

of the EBL. However, the strength of this claim, as pointed out by the authors, is also questionable due to the small sample size of blazars used. Comparing to the no-EBL hypothesis, this corresponds to an 8.8σ "measurement" of an EBL imprint in VHE spectra. It is also worth noting that, while all tested blazars give individually give a consistent value for β_{scale}, the overall result is dominated by one blazar, PKS 2155-304.

During February 2014, 1ES 1011+496, a HBL located at a redshift of (z = 0.212), was observed to be in an exceptional high VHE state by VERITAS and MAGIC, during which the integral flux peak at $\sim$ 75% Crab (Mirzoyan, 2014). Based on observations during this period and assuming a Domínguez et al. (2011) EBL model, the MAGIC Collaboration (Ahnen et al., 2016) placed constraints on the EBL density scale to be $\beta_{scale} = 1.07(-0.20, +0.24)_{stat+sys}$. This method applies the assumption that the energy spectrum of 1ES 1011+496 must not be harder than the theoretical upper limit of $\Gamma = 1.5$.

During April and May 2015 PKS 1441+25, a distant FSRQ (z = 0.939), underwent a period of exceptional multiwavelength activity, during which VHE emission was detected by VERITAS and MAGIC (see, for example, Pacciani, 2015; Mukherjee, 2015; Mirzoyan, 2015), The VERITAS collaboration (Abeysekara et al., 2015) used these observations of a distant blazar to place constraints on the EBL. Assuming a Gilmore et al. (2012) EBL Model and applying a similar χ^2 penalty to the agreement between the HE and VHE spectra as Biteau & Williams (2015) (see below), Abeysekara et al. (2015) obtain an 95% confidence-level upper limit of $\beta_{scale} = 1.5$. This upper limit places tight constraints on the EBL density in the near-UV to near-IR range, suggesting that galaxy surveys have resolved most of the sources of the EBL at these wavelengths. While Abeysekara et al. (2015) quote their limit for only a Gilmore et al. (2012) EBL model, they find, when testing Franceschini et al. (2008) and Domínguez et al. (2011) EBL models, that this result is almost independent of EBL model, with each tested EBL model providing a consistent upper limit.

The MAGIC Collaboration (see, Moralejo et al., 2017; Prandini et al., 2017; Mazin et al., 2017) analyse 32 energy spectra from 12 VHE blazars, and apply a fit to β_{scale} assuming Franceschini et al. (2008), Domínguez et al. (2011) and Gilmore et al. (2012) EBL models. Their best-fit values of β_{scale} are in good agreement with the models, with best-fit value of $1.0^{+0.11}_{-0.12}$, $0.95^{+0.11}_{-0.12}$ and $0.98^{+0.11}_{-0.12}$ for Franceschini et al. (2008), Domínguez et al. (2011) and Gilmore et al. (2012) EBL models respectively.

In a model-independent method, generic EBL shapes are considered. This generally takes the form of one or two methods. In the first method, a large number of generic EBL models is generated. These generic EBL models are then used to deabsorb VHE spectra, with EBL models being rejected if the resultant intrinsic spectra are unphysical. This allows one to generate a confidence band of allowed EBL shapes or to obtain strong upper limits on the

EBL density. Using this method Mazin & Raue (2007) generate over 8 million generic EBL models. Mazin & Raue (2007) constrain the EBL between $\sim$ 1μm and $\sim$ 80μm. These constraints are within a factor of 2 to 3 of absolute lower limits obtained from source counts, suggesting that either source counts accurately account for the majority of the EBL intensity or that assumptions about the underlying emission processes of blazars are invalid (Mazin & Raue, 2007).

The second method generally employed by model-independent methods involves a direct fit to the EBL intensity as a function of wavelength. This involves some parameterization of the EBL shape and redshift evolution. Biteau & Williams (2015) apply a model independent fit to the EBL using ~20 years worth of VHE observations. Biteau & Williams (2015) parameterize the EBL shape as a set of overlapping Gaussian functions of wavelength with fixed average and width (set to the centre and width of each wavelength bin) and the normalization free.

The redshift evolution of the EBL density, for model-independent models, is assumed to be locally decoupled (see, for example, Madau & Phinney, 1996; Raue & Mazin, 2008; Biteau & Williams, 2015) such that:

$$d\epsilon \frac{dN}{d\epsilon}(E, z) = d\epsilon_0 \frac{dN}{d\epsilon_0}(E, 0) \times \mathrm{evol}(z), \tag{8.10}$$

where evol(z) parameterizes the redshift evolution of the EBL and is applied by modifying the cosmological dependence term such that,

$$\mathrm{evol}(z) = (1 + z)^{3 - f_{evol}}, \tag{8.11}$$

where f_{evol} is introduced to estimate the evolution effect of emitting sources. For an isolated photon field undergoing cosmological expansion $f_{evol} = 0$.

Analysing over 100 VHE spectra, Biteau & Williams (2015) impose a χ^2-penalty to their test statistic requiring that the VHE spectra not be harder than contemporaneously obtained HE spectra such that (Biteau & Williams, 2015):

$$\chi^2_{HE-VHE} = \Theta(\Gamma_{HE} - \Gamma_{VHE}) \left(\frac{\Gamma_{HE} - \Gamma_{VHE}}{\sigma_{\Gamma_{HE}}} \right)^2, \tag{8.12}$$

Where Γ_{HE} and Γ_{VHE} are the spectral indices of the HE and VHE spectra respectively, $\sigma_{\Gamma_{HE}}$ is the error on Γ_{HE} and Θ is a Heaviside function:

$$\Theta(x) = \begin{cases} 1, & \text{if } x \geq 0 \\ 0, & \text{otherwise} \end{cases}. \tag{8.13}$$

A similar χ^2 penalty, χ^2_{EBL}, is applied requiring the EBL values to be within upper and lower constraints, giving the hence the full χ^2 test statistic as:

$$\chi^2 = \chi^2_{EBL} + \sum_{\gamma ray\ spectra} \left(\chi^2_{\gamma ray\ points} + \chi^2_{HE-VHE} \right), \tag{8.14}$$

where $\chi^2_{\gamma ray\ points}$ is the χ^2 goodness of fit of the intrinsic spectra to the data points. The best-fit EBL obtained by Biteau & Williams (2015) results in a 11σ improvement to the spectral points, with respect to a no-EBL hypothesis.

Using a similar dataset to Abramowski et al. (2013), Abdalla et al. (2017) apply a direct fit to the EBL density. The EBL density is binned in energy and parameterized such that:

$$\epsilon_0 \frac{dN}{d\epsilon_0} = \sum_i w_i(\epsilon_0)\rho_i, \tag{8.15}$$

where ρ_i is the EBL density in the i^{th} wavelength bin and w_i is a bin-wise weighting factor such that:

$$w_i(\epsilon_0) = \begin{cases} 1, & \text{if } \epsilon_0 \in [\epsilon_i, \epsilon_{i+1}] \\ 0, & \text{otherwise} \end{cases}. \tag{8.16}$$

The set of parameters $\{\rho_i\}$ are included into a fit to the intrinsic spectra such that:

$$\left(\frac{dN}{dE}\right)_{obs} = \left(\frac{dN}{dE}\right)_{int} e^{-\tau(E,z,\{\rho_i\})}. \tag{8.17}$$

Abdalla et al. (2017) make no assumptions on the underlying shape of the EBL or on the intrinsic spectra of the blazars used, other than they be smooth and convex. The best-fit to the EBL density obtained by Abdalla et al. (2017) is preferred over the no-EBL hypothesis at the 9.5σ level, and is in good general agreement with the results obtained by Biteau & Williams (2015).

8.2 Analysis Method

In this section the methods used to obtain to fit to an EBL model are discussed. In this analysis the methods described by Abramowski et al. (2013) are used. In this a profile likelihood

scan as a function of EBL opacity normalization β_{scan} is obtained. The profile likelihood of each spectrum is combined to obtain the joint-likelihood profile. In obtaining the profile likelihoods, the intrinsic spectra are treated as nuisance parameters, that is to say for each value of β_{scan} a fit is applied to the intrinsic spectra. The best-fit parameters themselves are ignored with the only requirement being that the results are physical ($\Gamma > 1.5$), however this was found to have a minimal effect on the results (in particular non-power-law models) in the $0 \leq \beta_{scale} \lessapprox 1.5$ range. In deriving upper limits, see Section 8.5, only power-law models were considered. The log-likelihood for each value of β_{scale} was obtained, allowing the profile likelihood to be written as:

$$\log \mathcal{L}(\beta_{scale}) = \log \mathcal{L}(\beta_{scale}, \hat{\mathbf{\Theta}}), \tag{8.18}$$

where $\hat{\mathbf{\Theta}}$ is the maximum likelihood estimator (MLE) of the spectral parameters $\mathbf{\Theta}$.

For each EBL model and EBL opacity normalization, the intrinsic energy spectrum was obtained assuming the following models:

- Power Law (PWL): $N_0 \left(\frac{dN}{dE}\right)^{-\Gamma}$.
- Power Law with Exponential Cutoff (EPWL): $N_0 \left(\frac{dN}{dE}\right)^{-\Gamma} e^{\left(-\frac{E}{E_C}\right)}$.
- Log Parabola (LP): $N_0 \left(\frac{dN}{dE}\right)^{-\alpha-\beta\log\left(\frac{E}{E_0}\right)}$.
- Log Parabola with Exponential Cutoff (ELP): $N_0 \left(\frac{dN}{dE}\right)^{-\alpha-\beta\log\left(\frac{E}{E_0}\right)} e^{\left(-\frac{E}{E_C}\right)}$.

The physical motivation for these models is that the intrinsic spectrum of inverse-Compton emission, in which the scattering occurs in the Thomson regime, is expected to be a power law. Therefore a first order approximation of this would be a power-law model (see Section 2.5). If the inverse-Compton scatter occurs in the Klein-Nishina regime then the spectrum will be characterized by a cutoff. A log parabola, and a log parabola with exponential cutoff, could also characterize intrinsic source effects resulting in a deviation from a power-law model.

Deviation from a simple power-law model allows for effects such curvature and exponential cutoffs in the intrinsic energy spectra to be considered in the spectral fit. Constraints on the log-parabola models are applied such that $\beta \geq 0$. This ensures that the resulting intrinsic energy spectra become convex with increasing energy. Further constraints on the spectral index (power law Γ, log parabola α) are discussed and applied in Section 8.5.

When selecting which model is used for a given source, the profile likelihood for each model is examined. While normally one might only choose a more complex model over a

simpler model if it offers a significant improvement over the simpler model, in this analysis the most likely model is considered regardless. In the event of two models having a similar peak value, but the width of the peaks differs, the model with the wider peak is chosen. This usually arises due to the degeneracy of the models as a more complicated model encapsulates the simpler model. The width of the peak likelihood generally extends to lower values of β_{scan} due to the presence of curvature in the spectra. A power-law model will tend to attribute this curvature to EBL effects, and hence the likelihood will peak in over smaller range at higher values of β_{scan}. A more curved model such as a log parabola will attempt to fit the curved model assuming that all the observed curvature is an intrinsic effect. This results in a higher likelihood value at lower values of β_{scan} when compared to the non-curved power-law model. For this reason, the model which has a profile likelihood which encompasses the profile likelihood of other models is preferentially chosen as not to confuse intrinsic and extrinsic curvature.

8.3 Source Selection

In this section the sources used to study the EBL are discussed. A summary of the sources and their properties of interest to this analysis can be found in Table 8.1. One should point out that while all the likelihood-based spectral and EBL analysis was performed by the author, for the sources 1ES 1011+496 and MS 1221.8+2452 the data quality selection and data processing were performed by a collaborator Dr. Patrick Moriarty (NUIG), as part of the VERITAS EBL working group (see Pueschel, 2017).

1ES 2344+514 (VER J2347+517, R.A.: (23h 47′4″) ± $(2'')_{stat}$, Dec.: +51° 42′49′± $(16'')_{stat}$ (J2000 Allen et al., 2017)) is a nearby HBL (z = 0.044, Perlman et al., 1996). 1ES 2344+514 was discovered to emit VHE gamma-ray emission by the Whipple Collaboration (Catanese et al., 1998). In this thesis I consider the dataset I compiled, analyzed and previously presented in Allen et al. (2017). As shown in Figure 8.3, Allen et al. (2017) divide the dataset into two, based on the reanalysis of the 2007-2008 dataset and the presented 2008-2015 dataset. I refer to these datasets as the "Old" and "New" data sets respectively. In this analysis I exclude all RHV observations taken from the analysis. The RHV observations correspond to ∼25% of the data presented in Allen et al. (2017).

1ES 1959+650 (R.A.: 19h 59′59.8521″, Dec.: +65° 08′54.652″(J2000, Beasley et al., 2002)) is a nearby HBL (z = 0.048 Sanchez et al., 2013). 1ES 1959+650 was originally detected at VHE by the Utah Seven Telescope Array (Nishiyama, 1999). The data used here corresponds to 3- and 4-telescope standard HV data taken between MJD 54414 and 57553 (10

Source	Live Time (Hours)	Redshift (z)	E_{max} (TeV)	τ_{max}
1ES 2344+514 (Old)	17.2	0.044	10.0	1.64
1ES 2344+514 (New)	18.4	0.044	15.0	2.97
1ES 1959+650 (Low)	16.9	0.048	13.0	2.59
1ES 1959+650 (High)	9.0	0.048	13.0	2.59
BL Lac	2.6	0.069	3.2	1.12
RGB J0710+591	112.1	0.125	10.0	5.35
H 1426+428	74.9	0.129	7.2	3.82
1ES 1011+496 (High)	6.7	0.212	5.2	5.23
MS 1221.8+2452	2.1	0.218	1.8	3.19
OJ 287	50.0	0.306	0.9	3.31

Table 8.1: Summary of the sources used in this analysis. Column 2 shows the total live time (total deadtime corrected exposure). Columns 3 shows the redshift of the source. Column 4 shows the maximum energy, defined as the upper edge of the final energy bin (choses as one bin after the final bin with a $TS > 4$), probed in this analysis. Columns 5 shows the maximum EBL opacity probed by the source assuming a Franceschini et al. (2008) EBL model.

November 2007 and 14 June 2016). The nightly-binned light curve of 1ES 1959+650 above 0.35 TeV is shown in Figure 8.4. 1ES 1959+650 has a nominal flux level of $\sim$ 12% Crab, however during the 2015-2016 and 2016-2017 observing seasons 1ES 1959+650 exhibited a number of exceptional TeV flaring events (see, for example, Santander, M. and others, 2017; Ciprini et al., 2015; Mukherjee, 2015; Biland, 2016; Buson et al., 2016). In this analysis the data is divided up into "Low" and "High" state datasets, with the definition of the low state data defined by data whose distribution $(\phi_i - \bar{\phi})/\sigma_{\phi,i}$, where ϕ_i is the flux of the i-th measurement, $\sigma_{\phi,i}$ is the error in the i-th measurement and $\bar{\phi}$ is sample mean, is approximately Gaussian with mean 0 and rms $\approx$ 1.2.[1] The definition of these states will be discussed further in an upcoming VERITAS EBL publication.

BL Lacertae: As discussed in Section 5.5.2, BL Lacertae (BL Lac) is an IBL located at a redshift of $z = 0.069$. The data used in this analysis corresponds to the flaring state observed on MJD 57666 (5 October 2016) as presented by Abeysekara et al. (2018a).

RGB J0710+591: (VER J0710+591, R.A.: 07h 10′26.4″ $\pm$ $(2.4')_{stat}$, Dec.: +59° 09′00″ $\pm$ $(36)_{stat}$ (J2000, Acciari et al., 2010)) is an extreme HBL located at a redshift of $z = 0.125$

[1] In general if a dataset is described by Gaussian statistics, one would expect $(\phi_i - \bar{\phi})/\sigma_{\phi,i}$ to be distributed as $\mathcal{N}(0, 1)$. This is often referred to as a "pull" distribution. In the case of VERITAS data there is an additional systematic error of about 20% on flux estimates arising due to, for example, atmospheric variations. Hence the pull distribution is will be approximately Gaussian with a rms of ~1.2. This value was also found experimentally by considering time bins obtained via a Bayesian block analysis. Outlier blocks were removed until a fit to a Gaussian distribution provided an adequate fit to the observed distribution. This will be discussed further in an future EBL publication.

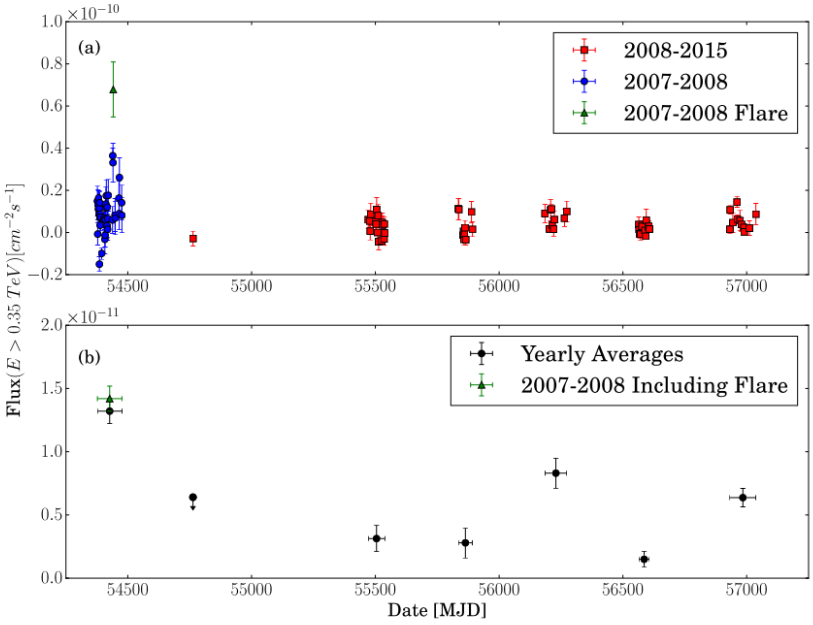

Figure 8.3: Panel (a): Nightly-binned light curve of 1ES 2344+514. The blue circles correspond to date taken between 2007-2008. The red circles correspond to data taken between 2009-2015. The green triangle corresponds to a flare observed during the 2007-2008 observing season which was observed under sub-optimal observing conditions and is hence removed for this analysis. Panel (b): Yearly-binned light curve for 1ES 2344+514. The green triangle corresponds to the 2007-2008 season including the flaring observation. (From Allen et al., 2017).

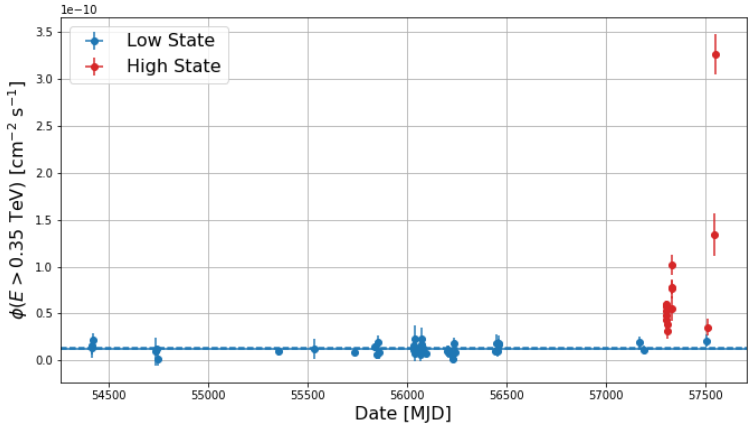

Figure 8.4: Light curve of 1ES 1959+650. The blue points correspond to "low"-state data. The blue line corresponds to the time-averaged Low-state flux of $\sim$ 12% Crab. The red points correspond to the "High'-state data.

(Giommi et al., 1991). RGB J0710+591 was originally detected at VHE by VERITAS during the 2008-2009 observing season, having a time-averaged integral flux of ~ 3% Crab. The data used here corresponds to SHV data passing standard quality cuts taken between MJD 54834 and 57456 (3 January 2009 and 9 March 2016).

H 1426+428: (R.A.: 14h 28′32.6″, Dec.:+42° 40′21″(J2000, Gaia Collaboration, 2018)) is a HBL located at a redshift of z = 0.129 (Ahn et al., 2012). H 1426+428 was originally detected by the Whipple Collaboration based on a multi-season monitoring program (Horan et al., 2002). In this work, VERITAS data between MJD 54907 and 57536 (17 March 2009 and 28 May 2016) is considered.

1ES 1011+496: (R.A.:10h 15′04.1″, Dec.: +49° 26′01″(J2000, Petrov & Taylor, 2011)) is a HBL located at a redshift of z = 0.212 (Albert et al., 2007). 1ES 1011+496 was originally detected by the MAGIC Collaboration in 2007 (Albert et al., 2007). Data taken between MJD 56693 and 56723 (5 February 2014 and 7 March 2014), were taken during a the period of enhanced VHE activity and are referred to as the "High-state" dataset and are considered in this work. This dataset corresponds to the time range considered in Ahnen et al. (2016) with the addition of the initial observations, taken on MJD 56693 by VERITAS, which triggered the MAGIC observation campaign.

MS 1221.8+1452: (R.A.:12h 24′24.2″, Dec.: +24° 36′23.5″(J2000, Gaia Collaboration, 2018)) is a HBL located at a redshift of z = 0.218 (Paiano et al., 2017). MS 1221.8+1452 was detected by the MAGIC collaboration (Cortina, 2013) in 2013 with an integral flux of ~ 4% Crab. MS 1221.8+1452 has since been regularly monitored by VERITAS and on the nights of MJD 56686 and 56687 (29 January 2014 and 30 January 2014), MS 1221.8+1452 was observed to be in an exceptionally high flaring state. Data taken on these nights are reported here.

OJ 287: As reported in Chapter 7, OJ 287 underwent and exceptional period of enhanced X-ray and VHE activity during the 2016-2017 observing season. Here I included data taken during all periods reported in Chapter 7.

8.4 Results

8.4.1 Energy Spectra

For a comparison, the intrinsic energy spectrum of each source was obtained assuming a Franceschini et al. (2008) EBL model, with $\beta_{scale} = 1$. The intrinsic spectrum was obtained using both a power-law and log-parabola model. The results of the intrinsic spectra analysis are reported in Table 8.2 with the intrinsic and observed spectrum of each source shown in

Appendix C.2.

Source	E_0	Power Law			Log Parabola			
		N_0	Γ	χ^2/NDF	N_0	α	β	χ^2/NDF
	(TeV)	($cm^{-2}s^{-1}TeV^{-1}$)			($cm^{-2}s^{-1}TeV^{-1}$)			
1ES2344+514 (Old)	1.0	$(5.99 \pm 0.40) \times 10^{-12}$	2.12 ± 0.08	9.42/9	$(6.99 \pm 0.64) \times 10^{-12}$	2.00 ± 0.11	0.25 ± 0.12	3.94/8
1ES2344+514 (New)	1.0	$(2.03 \pm 0.21) \times 10^{-12}$	2.26 ± 0.12	8.84/10	$(2.10 \pm 0.29) \times 10^{-12}$	2.26 ± 0.13	0.05 ± 0.13	8.71/9
H1426+428	0.7	$(3.59 \pm 0.31) \times 10^{-12}$	2.04 ± 0.10	20.77/9	$(4.44 \pm 0.5) \times 10^{-12}$	2.12 ± 0.14	0.39 ± 0.18	13.29/8
RGBJ0710+591	1.5	$(9.22 \pm 1.15) \times 10^{-13}$	2.07 ± 0.11	5.13/9	$(9.23 \pm 1.16) \times 10^{-13}$	2.07 ± 0.12	0.00 ± 0.43	5.13/8
OJ287	0.2	$(6.03 \pm 0.80) \times 10^{-11}$	2.97 ± 0.40	2.17/4	$(6.03 \pm 0.80) \times 10^{-11}$	2.97 ± 0.40	0.00 ± 0.52	2.17/3
BLLac	0.3	$(9.45 \pm 0.30) \times 10^{-10}$	3.20 ± 0.05	25.18/6	$(1.11 \pm 0.05) \times 10^{-09}$	3.21 ± 0.06	0.43 ± 0.10	1.74/5
1ES1959+650 (Low)	2.0	$(8.91 \pm 1.10) \times 10^{-13}$	2.72 ± 0.11	7.59/6	$(9.19 \pm 1.05) \times 10^{-13}$	2.83 ± 0.15	0.11 ± 0.12	7.04/5
1ES1959+650 (High)	2.0	$(4.92 \pm 0.27) \times 10^{-12}$	2.48 ± 0.04	20.16/6	$(4.89 \pm 0.29) \times 10^{-12}$	2.80 ± 0.11	0.20 ± 0.06	7.71/5
MS1221.8+2452	0.2	$(8.27 \pm 0.58) \times 10^{-10}$	2.36 ± 0.15	5.66/6	$(8.27 \pm 0.58) \times 10^{-10}$	2.36 ± 0.15	0.00 ± 0.21	5.66/5
1ES1011+496 (High)	0.4	$(3.52 \pm 0.14) \times 10^{-10}$	2.30 ± 0.07	6.68/8	$(3.52 \pm 0.14) \times 10^{-10}$	2.30 ± 0.07	0.00 ± 0.08	6.68/7

Table 8.2: Summary of the best-fit intrinsic spectra of the source used in this analysis. Column 2 shows the normalization energy (E_0) used in the fit. Columns 3-5 show the results of the best-fit power-law model. Columns 6-9 shows the results of the best-fit log-parabola model. The best-fit spectra are obtained assuming a Franceschini et al. (2008) EBL model.

8.4.2 Estimation of the EBL Opacity Normalization

Figures 8.5 - 8.8 show the results obtained using the methods described above. In the figures, the individual results obtained for each source are shown with the model used in the analysis denoted in the legend. The joint-likelihood fit results are shown as a black line, with the blue vertical line denoting the maximum-likelihood estimate (MLE) for β_{scale} and the shaded grey region denoting the 1σ confidence interval on the MLE. The results of these fits are summarize in Table 8.3.

The significance of the improvement to the fit, with respect to the no-EBL hypothesis ($\beta_{scale} = 0$) is shown in Column 4 of Table 8.3. The maximum significance occurs for a Franceschini et al. (2008) model with $\beta_{scale} = 0.85(+0.26 - 0.31)$. This corresponds to an significance of $\sigma = 2.01$ with respect to $\beta_{scale} = 0$. This low significance suggests that the imprint of the EBL is not well measured. Indeed, this is reflected in the large errors on the MLE values. The obtained errors show that the lower bound on the 1σ confidence interval have consistently a larger magnitude error than the upper. This is to be expected as in choosing the analysis model, care was given to choose curved models so as to not over attribute intrinsic curvature as EBL curvature. As the models are degenerate models (exponential-cutoffs cannot be considered nested models), employing a curved model over a non-curved model (for example log-parabola over a power-law model) will naturally encompass the non-curved model (for a log-parabola $\beta \to 0$), and therefore the curved model will have a similar shape to the non-curved model.

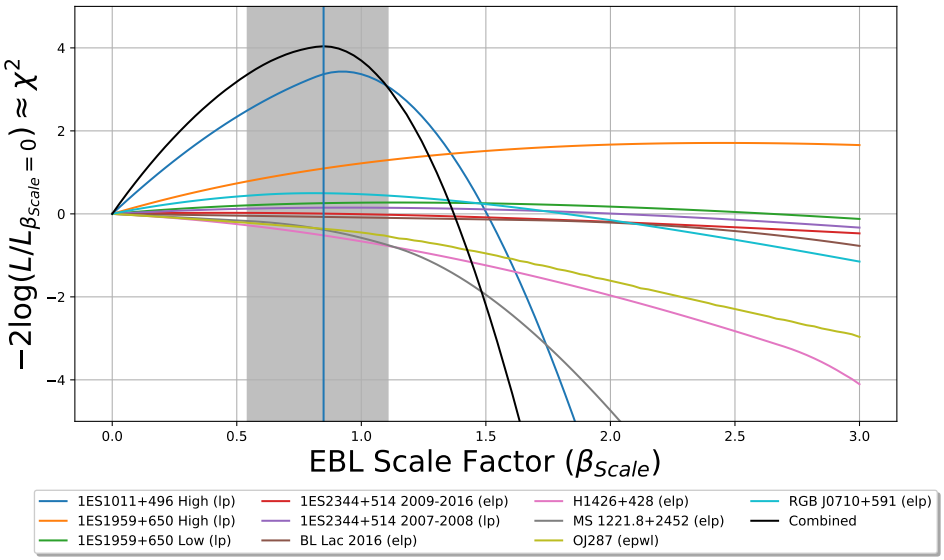

Figure 8.5: Results for a scaled EBL model assuming a Franceschini et al. (2008) model.

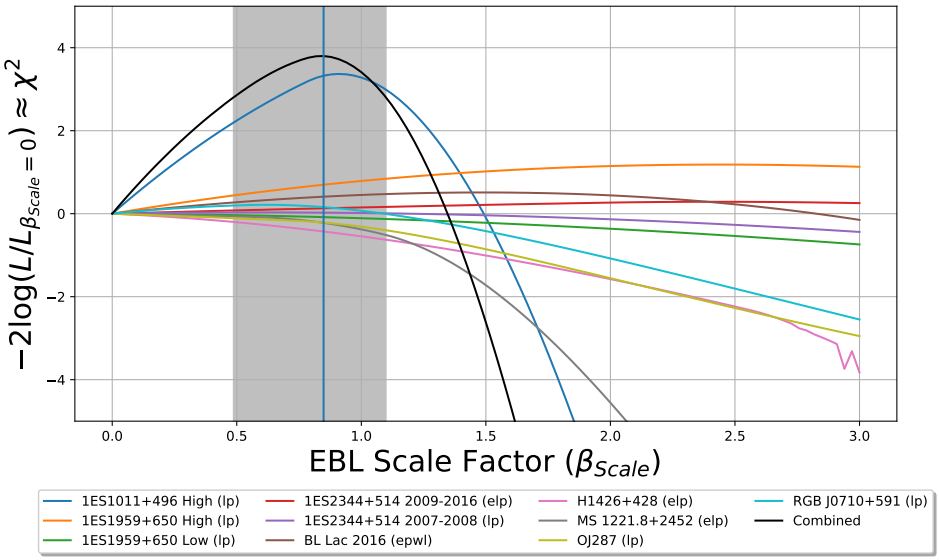

Figure 8.6: Results for a scaled EBL model assuming a Finke et al. (2010) model.

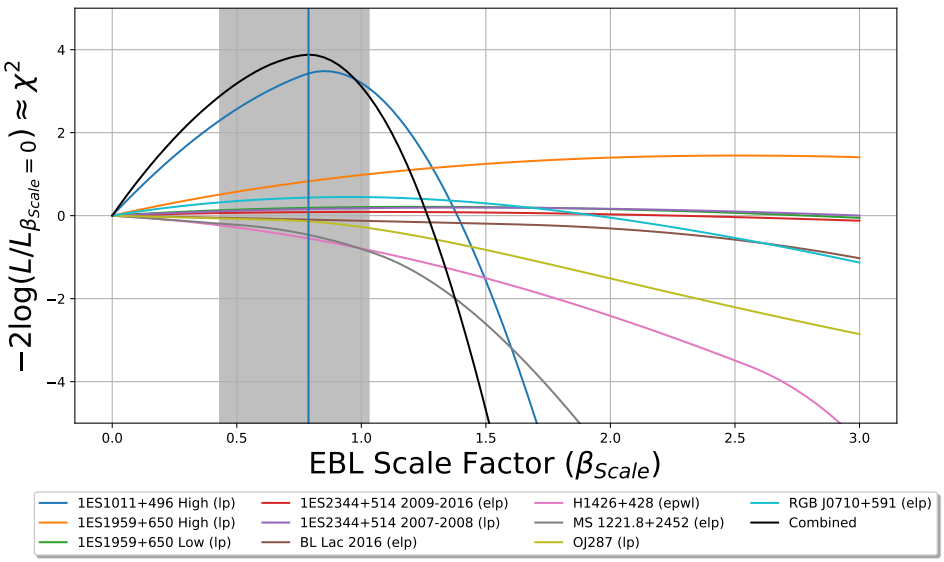

Figure 8.7: Results for a scaled EBL model assuming a Domínguez et al. (2011) model.

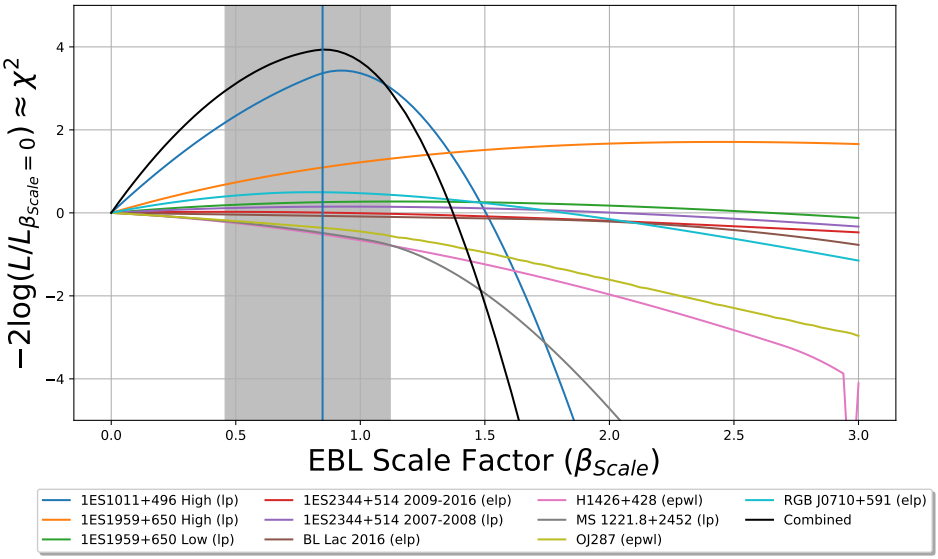

Figure 8.8: Results for a scaled EBL model assuming a Gilmore et al. (2012) model.

EBL Model	β_{scale}	$-2\log\left(\frac{\mathcal{L}}{\mathcal{L}(\beta_{scale}=0)}\right) \sim \chi^2_{\nu=1}$	σ
Fran08[a]	$0.85^{+0.26}_{-0.31}$	4.04	2.01
Finke10[b]	$0.85^{+0.25}_{-0.36}$	3.80	1.95
Dom11[c]	$0.79^{+0.24}_{-0.36}$	3.88	1.97
Gil12[d]	$0.85^{+0.27}_{-0.39}$	3.94	1.98

[a] Franceschini et al. (2008).
[b] Finke et al. (2010).
[c] Domínguez et al. (2011).
[d] Gilmore et al. (2012).

Table 8.3: Best-fit β_{scale} values for each EBL model tested. Column 3 shows the χ^2 obtained using the likelihood ratio test to compare with the no-EBL hypothesis. Column 4 shows the significance of the improvement provided by assuming an EBL mode with corresponding β_{scale}, compared to the no-EBL hypothesis.

8.5 Discussions

The best-fit values of β_{scale} are in agreement with the theoretical models ($\beta_{scale} = 1$). As the improvement of the best-fit β_{scale} is insignificant when compared to the no-EBL hypothesis ($\beta_{scale} = 0$), it would not be appropriate to claim this result as a measurement of the EBL imprint. Additionally, it is clear that the peak in the profile likelihood is largely dominated by 1ES 1011+469. As this is the case, one cannot rule out this results being simply due to a local effect on the spectrum of 1ES 1011+469. It would therefore be more appropriate to use the VHE observations reported here to place upper limits on β_{scale}.

Frequentist upper limits can be obtained by examining the joint-profile likelihood of the data, with respect to β_{scale}. Following the method described by Rolke et al. (2005), upper limits can be obtained for β_{scale} be treating the spectra fit parameters as nuisance parameters and optimizing the joint-likelihood equation with respect to β_{scale}. Wilks' Theorem suggests that the likelihood ratio is χ^2-distributed. Using this a frequentist upper limit can be obtained as follows:

$$-2\log\left(\frac{\mathcal{L}(\beta_{scale,UL})}{\mathcal{L}(\hat{\beta}_{scale})}\right) = C, \tag{8.19}$$

where $\hat{\beta}_{scale}$ is the MLE of β_{scale} and C is the critical value for a χ^2 distribution with one degree of freedom. For example, in the case of a 95% confidence level upper limit, $C = 2.708$.

Bayesian upper limits can be determined by considering Bayes' Theorem:

$$P(\beta_{scale}|Data) = \frac{P(\beta_{scale})\mathcal{L}(Data|\beta_{scale})}{P(Data)}, \tag{8.20}$$

where $P(\beta_{scale})$ is the prior probability distribution of β_{scale}, $P(Data)$ is the prior probability distribution of the data and $\mathcal{L}(Data|\beta_{scale})$ is the likelihood of observing the data given β_{scale}. The upper limit $\beta_{scale,UL}$ is defined as the value such that:

$$\frac{100 - CL}{100}\int_{-\infty}^{\infty} P(\beta_{scale})\mathcal{L}(Data|\beta_{scale})d\beta_{scale} = \int_{-\infty}^{\beta_{scale,UL}} P(\beta_{scale})\mathcal{L}(Data|\beta_{scale})d\beta_{scale}, \tag{8.21}$$

where CL is the confidence level on the upper limits (for example 95%). When considering the prior probability distribution of β_{scale} a logical prior would be that the resultant energy spectrum for an assumed β_{scale} be physical.

This assumption leads to a conservative prior that:

$$P(\beta_{scale}) \approx P(\Gamma) = \begin{cases} 1, & \text{if } \Gamma \geq 1.5 \\ 0, & \text{otherwise} \end{cases}, \tag{8.22}$$

where Γ or, in the case of a log-parabola α, is the spectral index of the model. This prior requires that the spectral index not be harder than the theoretical, or observational, upper limit on the hardness.

Feldman & Cousins (1998) argue that the real strength of a Bayesian analysis resides in the definition of the prior, suggesting that a conservative prior naturally results in overcoveraged of the parameter estimation. More over Feldman & Cousins (1998) suggest that all knowledge of previous experimental results should be incorporated into the prior probability distribution. Taking this into account, one can use the *Fermi*-LAT energy spectrum of the source to provide a stronger limit on the hardness of the VHE energy spectra. In the event of sources which show a steady VHE state during the period of observations analysed here, the time-averaged 3FGL spectral index is used as the upper limit on the spectral hardness. For flaring periods, the *Fermi*-LAT spectral index is obtained from a fit to data taken contemporaneously to the flare.

One should also consider the experimental error in the prior probability distribution. This takes into account that a spectral fit can produce a spectral index which is harder than the upper limit, but within experimental error of the upper limits. Hence the prior probability distribution takes the form:

$$P(\beta_{scale}) \approx P(\Gamma) = 1 - F((\Gamma - \Gamma_{lim})/\sigma_{\Gamma}, \sigma = 1), \tag{8.23}$$

where Γ_{lim} is the limit on the spectral index, σ_{Γ} is the experimental error on Γ and $F(x, \sigma)$ takes the form:

$$F(x, \sigma) = H(x) erf\left(\frac{x}{\sigma\sqrt{2}}\right), \tag{8.24}$$

where erf is the error function and $H(x)$ is a Heaviside function:

$$H(x) = \begin{cases} 1, & \text{if } x \geq 0 \\ 0, & \text{otherwise} \end{cases}. \tag{8.25}$$

Hence one can see that the prior probability distribution is the survival probability of a half-normal distribution. This reflects that one expects the experimental errors to be Gaussian and penalizes the measurements which are above the upper limit hardness based on the experi-

mental error. Figure 8.9 shows the prior probability distributions for different experimental errors, assuming $\Gamma_{lim} = 1.5$. One can see that larger experimental error expands the width of the prior probability distribution, hence "allowing" larger deviation from the Γ_{lim}.

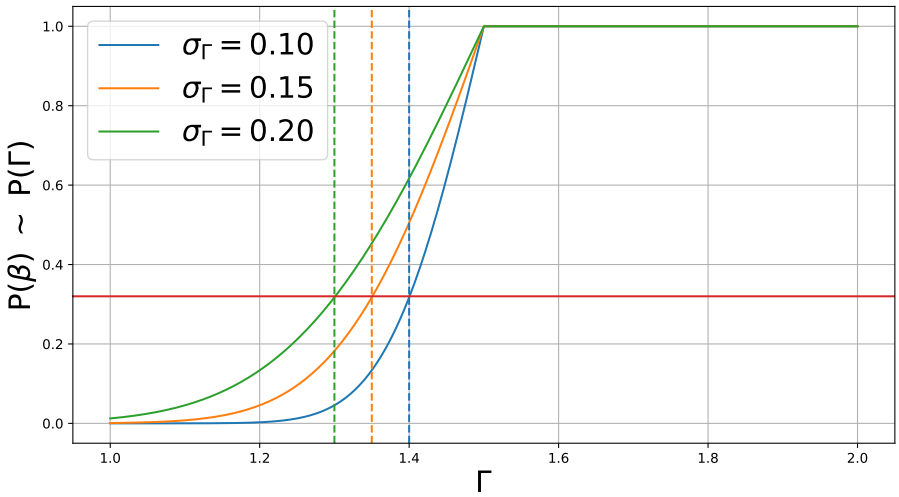

Figure 8.9: Prior probability distribution of $P(\beta_{scale}) \sim P(\Gamma)$ as given by Equation 8.23. Γ_{lim} is set to 1.5. The horizontal line corresponds to 1σ containment of the distribution. This corresponds to $\Gamma_{lim} + \sigma_\Gamma$ and is portrayed as the different coloured vertical lines.

In the case of the frequentist upper limits, the prior discussed above could also be applied in the upper limit calculation such that:

$$\tilde{\mathcal{L}}(\beta_{scale}) = P(\beta_{scale})\mathcal{L}(\beta_{scale}). \tag{8.26}$$

In the above equation, the inclusion of $P(\beta_{scale})$ restricts the observed distribution of the physical domain. Restricting to the physical domain is common practice and is similar to the "bound-likelihood" method employed by Rolke et al. (2005). Rolke et al. (2005) use a bound-likelihood analysis to limit observed counts to the physical domain (i.e. $nCounts \geq 0$) when determining the profile likelihood. The upper limits are then determined using Wilks' Theorem. Rolke et al. (2005) argue that this is a valid method as since it would make the upper limit value larger the method "cannot make the coverage worse". Similarly, in this case one can argue that applying such a prior is valid as it restricts the upper limit to the physical domain.

Bayesian and Frequentist upper limits are obtained for each tested EBL model in a conservative manner. To ensure the EBL opacity is not under estimated, each source is fitted with an intrinsic power-law model. This suggests that all observed curvature is due to EBL

attenuation, rather than source intrinsic effects. The upper limits obtained from this analysis are shown in Figure 8.10, with the individual results of the upper limit analysis is summarized in Table 8.4. The profile likelihood and posterior probability distributions used to obtain the Frequentist- and Bayesian-based upper limits for a Franceschini et al. (2008) EBL model are shown in Figures 8.11 and 8.12 respectively. The results for individual models are given in Appendix C.1. Figure 8.10 shows the most constraining limit for each model plot as a solid line. In all cases the most constraining upper limits were the Bayesian limits which incorporated a prior probability distribution in which Γ_{lim} was obtained from HE observations. It is worth noting that when no prior is assumed, the profile likelihood peaks at values around $\beta_{scale} = 1.5$, in contrast to the fit analysis presented earlier, which peak $\beta_{scale} \approx 0.8 \pm 2$. This is not surprising as one expects that when a pure power-law model is fit to the data, this analysis will attempt to accredit all spectral curvature as extrinsic to the source (i.e. due to the EBL). Observing a peak in the profile likelihood at $\beta_{scale} \sim 1.5$ which, as reflected by the effect of the prior probably distributions effect on the results, results in non-physical spectra, highlights the importance of assuming some intrinsic curvature.

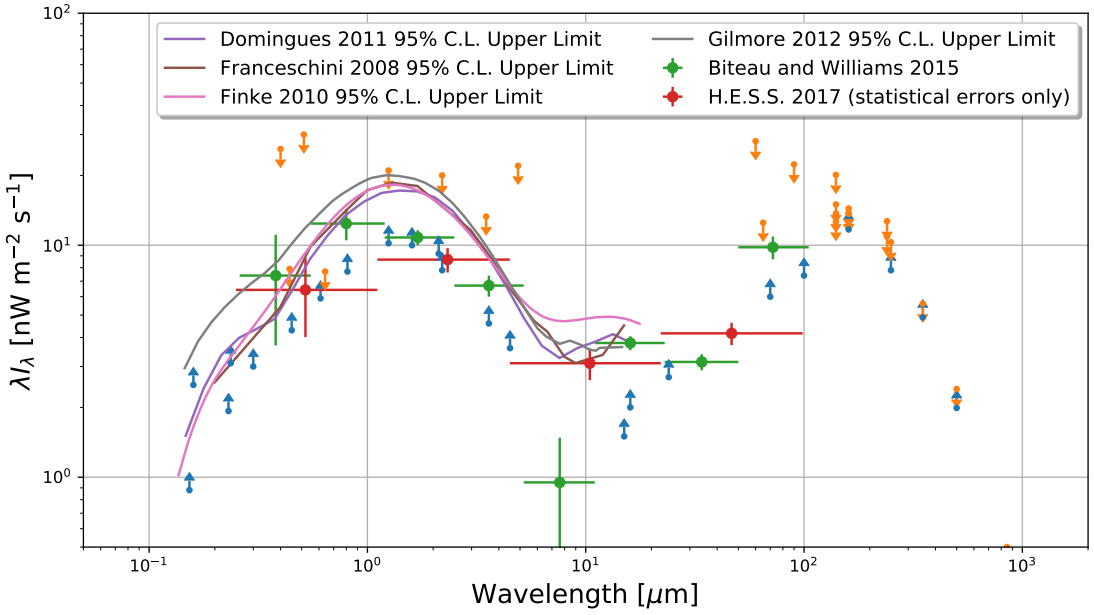

Figure 8.10: Upper limits on the EBL opacity normalization. For a definition of the different upper and lower limits see Section 8.1.2.

EBL Model	Frequentist			Bayesian		
	No Prior	$\Gamma > 1.5$	$\Gamma > \Gamma_{Fermi}$	No Prior	$\Gamma > 1.5$	$\Gamma > \Gamma_{Fermi}$
Fran08[a]	2.05	1.76	1.68	1.87	1.67	1.58
Finke10[b]	2.16	1.62	1.54	1.97	1.55	1.47
Dom11[c]	1.88	1.68	1.60	1.71	1.59	1.50
Gil12[d]	2.05	1.76	1.68	1.87	1.67	1.58

[a] Franceschini et al. (2008).
[b] Finke et al. (2010).
[c] Domínguez et al. (2011).
[d] Gilmore et al. (2012).

Table 8.4: 95% confidence level upper limits on the EBL opacity scale (β_{scale}).

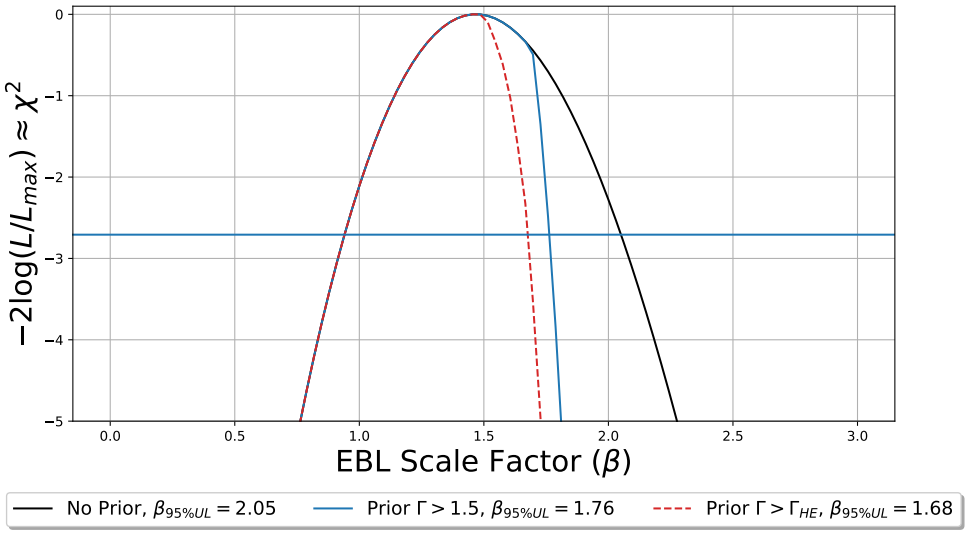

Figure 8.11: 95% confidence level upper limits obtained using a Frequentist approach. The results shown here assume a Franceschini et al. (2008) EBL model. The black line shows the posterior probability distribution with not prior assumptions. The blue line shows the posterior probability distribution assuming an upper limit on the blazar hardness of $\Gamma_{lim} = 1.5$. The dashed red line shows the posterior probability distribution assuming an upper limit on the blazar hardness of $\Gamma_{lim} = \Gamma_{HE}$.

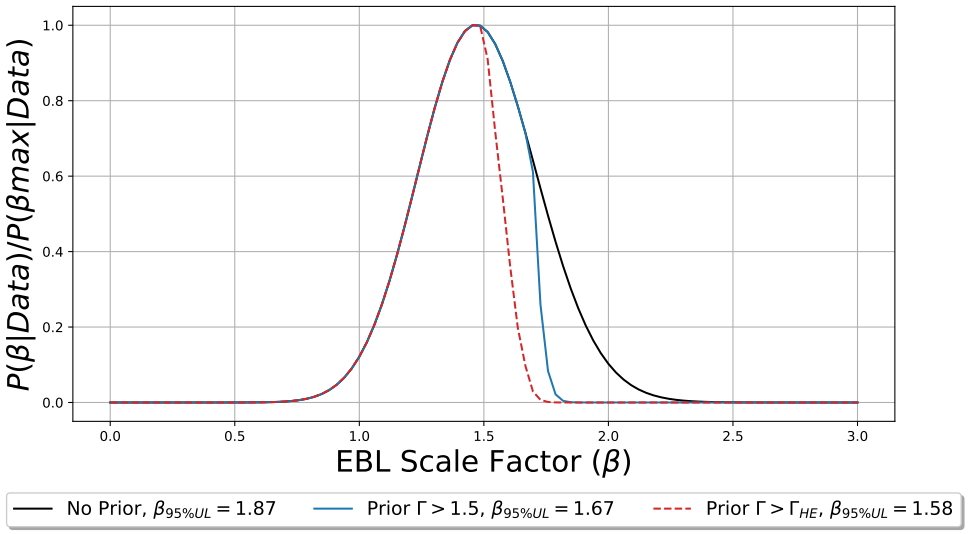

Figure 8.12: 95% confidence level upper limits obtained using a Bayesian approach. The results shown here assume a Franceschini et al. (2008) EBL model. The black line shows the posterior probability distribution with not prior assumptions. The blue line shows the posterior probability distribution assuming an upper limit on the blazar hardness of $\Gamma_{lim} = 1.5$. The dashed red line shows the posterior probability distribution assuming an upper limit on the blazar hardness of $\Gamma_{lim} = \Gamma_{HE}$.

8.6 Summary

The analysis discussed in this thesis, corresponds to the first likelihood-based EBL analysis using VERITAS data. The motivation for this work is two part, firstly to build the machinery necessary for a full likelihood-based analysis and secondly to test this analysis using a subset of the larger VERITAS EBL dataset. As discussed in Pueschel (2017), the VERITAS EBL effort is focusing on a model independent approach to measuring the EBL shape and intensity, by following the method of Mazin & Raue (2007) to generate generic EBL models. The analysis presented here focuses mostly on the harder sources within the EBL dataset due to availability of reduced data and the availability of instrument response function simulations for soft spectra sources. The required instrument response functions shall be simulated and provided in an upcoming release of the Event Display analysis package which shall allow for binned-likelihood analysis. Nonetheless, the analysis reported here, while not providing a firm measurement of the EBL's imprint on VHE spectra, does set competitive limits on the intensity of the EBL in the $\sim 0.1 - 10\mu$m range, providing consistent results to those obtained by, for example, Biteau & Williams (2015) and Abdalla et al. (2017).

Future analysis will extend the dataset to include the entire VERITAS EBL dataset (~1500 hours, compared to the ~300 hours presented here), providing a complementary analysis to that currently being performed (see, Pueschel, 2017).

Chapter 9

Conclusions and Final Remarks

9.1 Summary

In this thesis I have studied a number of VHE blazars and candidate VHE blazars using observations taken by VERITAS. These observations have led to the detection of VHE emission from OJ 287. To maximize the scientific output of the observations, I have implemented a binned-likelihood analysis into the VERITAS analysis package Event Display. This has allowed for the probing of the highest energy spectral bins of OJ 287 and for the temporal variability properties to be investigated, despite the low significance of the data. Combining the observations of OJ 287 with long-term monitoring observations of other known VHE blazars, I have placed constraints on the opacity of the EBL.

In this section I provide some concluding remarks on the work presented in this thesis. In particular, I discuss future prospects and studies related to the work presented here.

9.2 The Search for New VHE Blazars

In this thesis, I have aimed to expand the catalog of known VHE Blazars, as for VHE population studies to be performed, a larger population is needed. In doing so, I compiled a list of promising VHE blazar candidates based on their multiwavelength properties and archival VHE data. Having compiled this list, further VERITAS observations of these sources were taken. As none of these sources led to a firm detection (5σ, post-trials significance), upper limits on the integral flux of the sources in the VHE regime were determined.

Of the observed targets 1ES 1118+424 is the most promising. The excess significance of 1ES 1118+424 is 4.2σ at the catalog position, with a max significance of $\sim 5.5\sigma$ within the On region, slightly offset from the catalog position of the source. Based on this result, further observations of 1ES 1118+424 with VERITAS will be proposed. If this source is detected, a publication will be prepared. While it is difficult to speculate on the scope of such a paper until a result is clear, one could foresee the publication including long-term multiwavelength data taken contemporaneously by *Swift*-XRT and *Fermi*-LAT. Indeed, in the

event of the detection of a new VHE blazar, there are existing agreements between VERITAS and *Swift* to coordinate multiwavelength observations. Alternatively, should the source not warrant an individual publication, it shall be included in a VERITAS catalog paper.

These observations have been taken as part of the VERITAS blazar discovery program. In addition to the sources discussed here, the blazar discovery program has ∼1000 hours of unpublished data on candidate VHE blazars. A publication, of which I shall be a corresponding author, is currently being prepared, in which upper limits on the flux level of the non-detected sources shall be presented. If, at the time of publication the sources remain undetected, then these sources will be included in this publication.

9.3 OJ 287

The period of enhanced activity presented in this thesis represents the historic peak X-ray flux in the long-term light curve. The atypical nature of this flare allowed for the detection of VHE emission from OJ 287. The low-state VHE spectrum of the source (as estimated by the extrapolated 3FGL spectrum, see Figure 9.1) is below the sensitivity of current generation IACTs. Detection of such a low-state would require dedicated observations by CTA, which shall be over-subscribed. This suggests that the observations reported here might be the only VHE detection of OJ 287 for some time. CTA's sensitivity might allow for the detection of flaring activity from OJ 287 on time scales smaller than observed here. To catch these flares, either CTA will need to regularly monitor OJ 287, or CTA observations will need to be triggered by other multiwavelength sources. The detection, and communication, of enhanced multiwavelength activity is therefore crucial to any future VHE observation campaign on OJ 287.

The variability and correlation tools developed in the analysis of OJ 287 have been shown to be powerful tools, that allow one to utilize low-significance data. These tools have been incorporated into the VERITAS analysis chain and will allow future studies to be performed. In particular, these tools can be used to combine observations taken using different instruments, allowing one to optimize the science results one can obtain.

As shown in Figure 7.1, the next predicted optical outburst is expected to occur around 2019.6 (August 2019). Observations of OJ 287 during the expected outburst might not be possible due to the close proximity of OJ 287 to the Sun at the time of crossing. The crossing of the primary accretion disk by the secondary black hole is expected to displace a large amount of gas (Valtonen et al., 2016). This displaced gas may "feed" the two black holes, resulting in a prolonged period of enhanced multiwavelength activity. VERITAS will regu-

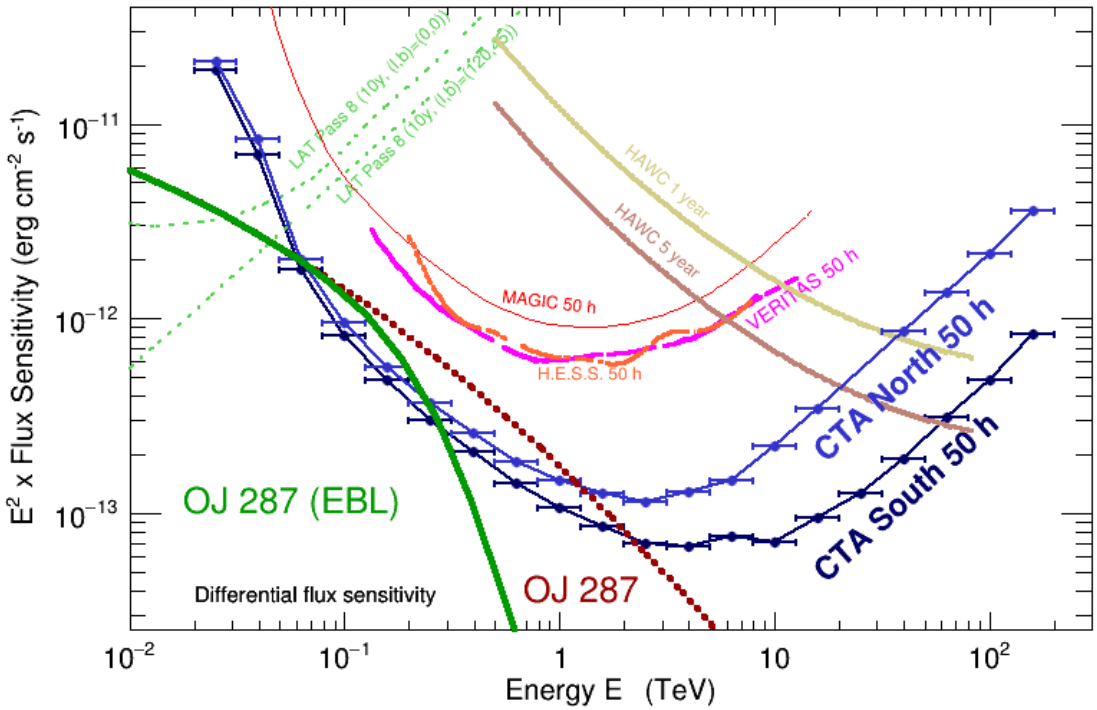

Figure 9.1: Differential flux sensitivity of current and future gamma-ray instruments. Note: the sensitivity curve for H.E.S.S. corresponds to the H.E.S.S.-1 (4-telescope) array. The extrapolated 3FGL spectrum of OJ 287 is shown assuming no EBL (dotted brown line) and assuming a Franceschini et al. (2008) EBL model (solid green line).

larly monitor OJ 287 during the months after the expected crossing. In the event of enhanced VHE flux, the wider astronomical community will be notified via pre-existing agreements and established media such as The Astronomers Telegram.[1]

The results presented in this thesis shall form the basis of an upcoming publication. In addition to the results shown here, this publication will present multiwavelength analysis of the source, from radio to VHE energies, with detailed modeling of the broadband SED of OJ 287 during this exceptional state done by a VERITAS collaborator Dr. Olivier Hervet.

9.4 Extragalactic Background Light

The EBL constraints presented here represent the first likelihood-based EBL analysis performed with VERITAS data. While the analysis does not result in a firm detection, the derived upper limits on the EBL intensity are competitive with results obtained by Abeysekara et al. (2015) using observations of the distant FSRQ PKS 1441+25 (z = 0.939).

[1] http://www.astronomerstelegram.org/

The dataset used here corresponds to a subset of the VERITAS EBL dataset, with this analysis representing a *proof of concept* study. I plan to expand this analysis to include the total EBL dataset of ~1500 hours of data, including sources with redshifts out to z = 0.6035 (PKS 1424+240). As discussed in Section 5.6 it is possible to apply a joint fit to multiwavelength data, using a binned-likelihood fit. This would allow for a joint fit between VERITAS and *Fermi*-LAT data, adding a further requirement of a smooth transition between the regions of the energy spectrum effected and unaffected by EBL attenuation. A future publication, utilizing this analysis, shall consider such a multi-instrument fit.

9.5 Publication Plans

The work presented in this thesis will lead to at least three publications. I have presented preliminary VERITAS analysis of OJ 287 at the 2017 International Cosmic Ray Conference (ICRC) (O'Brien et al., 2017). The updated results and multiwavelength analysis presented here, and SED modeling, shall be presented in a publication which is currently being prepared.

As part of the blazar discovery program, a publication detailing upper limits on the integral flux of a number of candidate VHE blazars is being prepared. This paper shall take a similar approach to a previous VERITAS blazar upper limits paper (Archambault et al., 2016), and I shall be a corresponding author. Individual sources from this program which result in a detection (for example 1ES 1118+424) or which are of great interest to the astronomical community (for example 3C 273), may be presented as standalone publications. I would pay a lead role in these publications and would expect to be a corresponding author.

The EBL constraints presented in this thesis are largely a proof of concept study. This analysis will be extended to the entire EBL dataset (~1500 hours). It is not yet clear whether this will form a standalone publication or if it shall provide a secondary/complementary analysis to the overall VERITAS EBL paper. Nonetheless I anticipate this will at least be presented at a conference and be incorporated into a larger EBL paper.

As part of the VERITAS EBL effort, I have analyzed data for the sources presented in Chapter 8 (with the exception of 1ES 1011+496 and MS 1221.8+2452). Of these sources, 1ES 2344+514 has already been the subject of a publication of which I am a corresponding author (Allen et al., 2017). H 1426+428 will be the subject of an up-coming publication, a publication I've played a significant role in by providing VERITAS and *Swift*-XRT analysis. I have also provided the secondary analysis for the 2016 BL Lac flare paper (Abeysekara et al., 2018a).

I have provided *Swift*-XRT analysis for a VERITAS publciation on the extreme HBL 1ES 0033+595. At the time of writing, the scope of this publication is unclear as to whether it will be a standalone publication or be included into a large VERITAS extreme HBL paper.

9.6 Future Prospect with CTA

One of the key science goals of CTA to perform a deep (~0.3% Crab) survey of the extragalactic sky (Acharya et al., 2017). This unbiased survey will surely lead to the discovery many new blazars, possibly with higher redshifts than those currently detected by current generation AGN. It it noteworthy that, typically, ToO observations of distant AGN are less common due to the EBL-attenuated extrapolated flux being lower than the sensitivity of current generation IACTs. Furthermore, discovery programs generally focus on candidate sources with a favorable VHE extrapolation, this naturally promotes a preference for nearby objects. Given the unbiased nature of the CTA extragalactic survey, an unbiased sample of candidates will be observed. This will provide a larger sample of VHE blazars, allowing for more detailed measurements of the EBL to be made using VHE observations. In addition to this, the redshift-blind survey may allow for a detailed study of the redshift evolution of the EBL, a study which is currently limited by the low statistics and low source numbers currently available to current generation VHE observatories. The CTA extragalactic survey may detect a baseline emission from sources which have previously only been detected at VHE during flaring epochs, allowing the for the study of the evolution of such sources.

Based on the upper limits obtained in this thesis, some of these objects may be detectable within this survey. However, it is worth noting that most of the objects included here are not included within the proposed FoV of the survey. 3C 273 shall be included in the proposed FoV, however the upper limit on the flux was determined to be 0.6% Crab above 250 GeV. This suggests that, in the absence of flaring activity coincident with observations, 3C 273 might not be detectable within the survey. Rather a targeted observational campaign might be required. This is however neglecting the fact the CTA will have a lower energy threshold than VERITAS, the analysis cuts used by Acharya et al. (2017) are optimized for a Crab-like source and that the VHE spectral properties of 3C 273 are still not well constrained. None the less, future CTA observations will provide new discoveries and stride towards obtaining an unbiased sample of TeV blazars.

In addition to the extragalactic survey, CTA's improved sensitivity will allow for more detailed spectral measurements of TeV sources, extending out to higher energies. It is possible that these observations may lead to the discovery of exotic, non-standard model, physics.

The discovery of distant AGN emitting at VHE, the EBL-desabsorbed spectra of which show an up-tick or are harder than the limits current models predict, would suggest that either our knowledge of the emission processes of blazars are not valid, or that there are unknown physical processes affecting the propagation of VHE photons throughout the Universe.

Lorentz Invariance Violation (LIV) is a proposed mechanism that arises out of many attempts to unify General Relativity and Quantum Mechanics. Simply put, LIV would be expected to arise due to quantum effects on the space-time structure at sufficiently short scales. The natural assumption for this scale would be the Planck Scale. LIV would introduce an energy dependence in the vacuum speed of light (see, for example, Nogués et al., 2017; Abdo et al., 2009) and a modification of the energy threshold of a photon-photon interaction (Gaté et al., 2017).

Other processes such as the coupling of photons with axion-like particles in the presence of magnetic fields (for a review see, Hooper & Serpico, 2007; Arias et al., 2012) would reduce the opacity of the universe to gamma-ray photons. This coupling would also result in spectral irregularities which could result in deviations from a smooth VHE energy spectrum, and would be evident in the residuals in the data-model fit (as demonstrated by Gaté et al., 2017).

Studies performed by Daniel et al. (2015); Gaté et al. (2017) show the capabilities of CTA in performing such searches of non-Standard Model physics. The combination of the improved sensitivity of CTA with the larger blazar sample size provided by the extragalactic survey will allow for detailed searches for such processes to be performed. An increase in the number of VHE blazars, with detailed spectral measurements, will no doubt be a key result of CTA. This larger sample size will reduce the effect of individual source dominance on EBL studies which affects current generation studies, for example 1ES 1011+496 in this work and Ahnen et al. (2016), and PKS 2155-304 in Abramowski et al. (2013) and Abdalla et al. (2017).

While CTA alone will lead to countless new discoveries, new results will also arise from the combination of CTA observations with other wavelengths and even different messengers (such as neutrinos). The importance of multiwavelength observations requires complementary instruments to be in operation. CTA will provide orders of magnitude improvements in sensitivity in the 10s of GeV to 100s of TeV energy range. An important feature of CTA that must be considered is that it is not a surveying instrument. The limited field of view of CTA means that only a very small portion of the sky will be monitored at any given time. While CTA's self-triggering mechanisms will be crucial in catching rapid flaring of VHE blazars, due to CTA being oversubscribed the number of blazars regularly monitored by CTA will be small. CTA will rely on multiwavelength triggers to follow up on enhanced activity. Current

generation survey instruments such as *Fermi*-LAT have been instrumental in the detection of exceptional TeV flaring of blazars. *Fermi* however is a relatively old instrument with no proposed successor. While *Fermi*'s mission lifetime may be extended, one cannot rule out the mission ending due to aging components. HAWC has the potential to act as a complementary survey instrument to CTA. However, HAWC's sensitivity limits its triggers to sources flaring at the ~1 Crab level.

Missions proposed at other wavelengths may produce some very interesting results. In the MeV range there are a number of proposed space-based instruments (for example AMEGO ~300 keV - > 10 GeV)[2]. These proposed instruments will explore a largely unstudied region of the electromagnetic spectrum, providing crucial information in a region of SEDs in which models can largely disagree. MeV bright blazars are also predicted by a number of models. VHE gamma rays may be produced in or near opaque regions. This would induce $\gamma\gamma$ interactions, resulting in an electromagnetic cascade, producing MeV emission.

In summary, CTA will play a central role in future studies of blazars. However, CTA alone will not be enough to study blazar emission, current and future instruments will act as a complementary instrument to CTA and aid the development of emission models of TeV blazars. The increased sensitivity of CTA over a broad energy range will allow for detailed spectral measurements and the discovery of many new VHE sources. This will allow for many exciting studies to be performed.

[2] https://asd.gsfc.nasa.gov/amego/index.html

Appendices

Appendix A

Applications of Binned-Likelihood Analysis

A.1 Variability Index for VHE Data

Variability is a property exhibited by a wide variety of astrophysical objects. In the context of blazars, varaibiltiy has been exhibited on time scales from minutes to years with the variability timescale being crucial in the understanding of the emission process. In the TeV regime, the lack of variability may suggest that there is a low-level steady-state from which the VHE emission is originating, which has variability amplitudes below the sensitivity of current generation instruments. Alternatively multiple, low-level flares could reproduce this effect. Variability in excess of this steady-state may be caused by flares from which the temporal profile of the flare allows for constaints to be put on the emission region.

One of the most basic methods to test for variability is to apply a χ^2-test to a constant-flux model. In this method one essentially assumes that the light curve can be fit by a constant flux roughly equal to the time-averaged flux. One obtains the χ^2-value that the data is fit by this model and compares it to a predefined critical value which has been chosen to give a predefined degree of confidince.

When one moves to the VHE (and HE) regimes, the flux of the sources are low, resulting in a low number of events to be analyzed. This results in the data being described by Poisson statistics. As a χ^2-test requires that the errors on the data be Gaussian, the χ^2-test is no longer valid. One possible solution would be to exclude any data that is outside of the Gaussian regime. This however biases the data by only allowing positive fluctuations of the data be included. To correctly incorporate the Poissonian statistics, a binned-likelihood analysis can be applied to the data. The application of a likelihood-based χ^2-test has been developed and is known as the variability index (TS_{var}).

TS_{var} (as defined in Nolan et al., 2012) is given by:

$$TS_{var} = 2\left[\log \mathcal{L}\left(\{F_i\}\right) - \log \mathcal{L}\left(F_{Const}\right)\right] = 2\sum_i \left[\log \mathcal{L}_i\left(F_i\right) - \log \mathcal{L}_i\left(F_{Const}\right)\right], \qquad \text{(A.1)}$$

where $\{F_i\}$ is the set of best-fit flux for each i-th time bin assuming a constant spectral shape, F_{Const} is the sample-averaged flux obtained by applying a joint-likelihood fit to the total binned dataset. We can see from Equation A.1, that one is applying Wilks' theorem to compare two nested models. Simply put, the null hypothesis is that the entire dataset, when binned into the defined time bins, is adequately described by the mean flux (i.e. the flux is constant) and the alternative hypothesis is that the mean flux doesn't adequately describe the dataset. Hence by Wilks' theorem (Wilks, 1938), TS_{var} is χ^2-distributed and enables variability to be tested in a similar maner to a χ^2-test.

I have incorporated the TS_{var} as part of the binned-likelihood fitting procedures implemented into the Event Display analysis package. The algorithm works as follows:

1. Data is binned into user defined time bins.
2. A joint-likelihood fit is applied to the temporally binned data to obtain the mean fit parameters to the data.
3. The likelihood of each time bin being fit by the mean fit parameters ($\log \mathcal{L}_{0,i}$) is obtained.
4. A likelihood fit is applied to each time bin ($\log \mathcal{L}_i$) with the spectral shape parameters frozen to the mean fit parameters and the normalization allowed to vary.
5. TS_{var} is calculated as:

$$TS_{var} = -2 \sum_i (\log \mathcal{L}_{0,i} - \log \mathcal{L}_i) \tag{A.2}$$

6. A test for variability can is applied by using Wilks' theorem, to obtain an equivalent χ^2-statistic. The number of degrees of freedom is given by the number of time bins minus the number of free parameters.

Note: it is important to include Step 2 in the fitting procedure. If one was to simply take a non-temporally binned fit as the mean-fit parameters, such as one obtianed in a total time-averaged fit, Wilks' theorm no longer holds for the Equation A.2. This is due to the likelihood equation no longer being correctly normalised for the analysis question (normalization is equivilient to $\sum_i \log \mathcal{L}_{0,i}$), as $\mathcal{L}_{0,i}$ does not repersent an optimized likelihood equation for the obsevered dataset. The introduction of the time bins results in a non-temporally binned fit differing slightly from a temporally binned fit. This has the affect of introducing a bias in the resulting χ^2-distribution, as the likelihood normalization repesents a sub-optimal–and potentially worse– model.

Figure A.1 shows the TS_{var}-distriubtion for a Monte Carlo simulation of a Crab-like spectrum. To mimic real observations the instrument response functions and observed Off counts from the OJ 287 dataset were used. This corresponds to 129 observations, taken over 32 days. Simulated observations were generated by obtaining the model-predicted Excess counts spectra for a Crab-like spectrum for each run. Random On-counts spectra were obtain by drawing random Poisson numbers from the combined Excess and Off spectra. A best fit was applied to 500 simulated spectra and the TS_{var} was obtained for daily binned observations. The distribution is well described by a χ^2 distribution with $\nu = 31$.

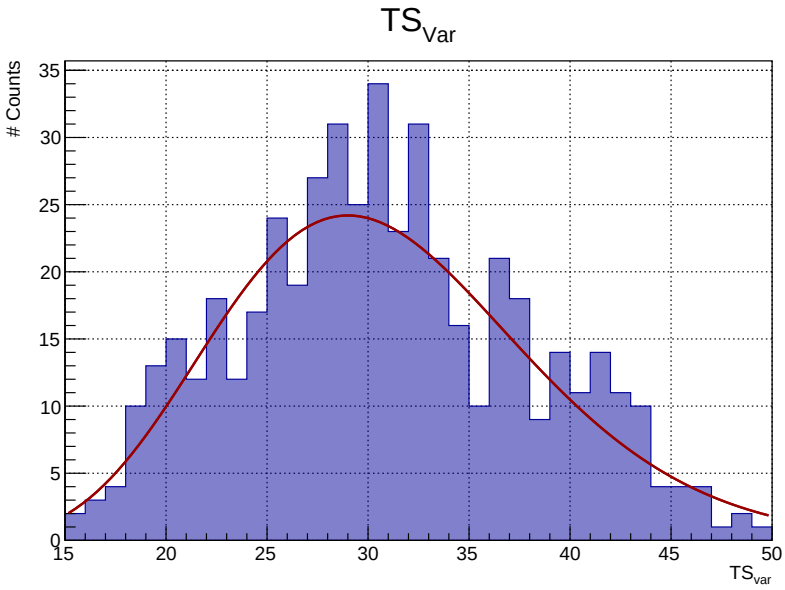

Figure A.1: Distribution of 500 simulated TS_{var} obtained for a Crab-like spectrum. The data is binned into 32 time bins when obtaining the TS_{var}. The red line shows a scaled χ^2-distribution with 31 degrees of freedom.

TS_{var} offers a novel extension of likelihood analysis into the time domain to test further hypotheses. By setting $\mathcal{L}\left(\vec{\Theta}\right) = \mathcal{L}\left(\vec{\Theta}, t\right)$, one can apply the principles discussed here to any temporal model which can provide an estimate of the model's flux (for example an exponetially decaying flare profile, $\phi(t) = \phi_0 e^{-t/\tau}$). This concept is discussed further in Appendix A.2.

A.2 Likelihood Based Correlation Analysis

Correlation between very-high-energy (VHE) and X-ray fluxes arises naturally assuming a synchrotron self-Compton model. This is due to the fact that the low-energy photons from the synchrotron process are the seed photons for the higher-energy inverse-Compton process. Variations in the synchrotron process naturally result in variations in the inverse-Compton process.[1]

For bright sources with deep VHE exposure, significant detections can be made allowing for correlation studies between the VHE and X-ray band. For weaker sources however, the data is described by Poisson statistics and hence common fitting procedures breakdown. A χ^2-fit cannot be applied to data described by Poisson statistics, as the χ^2-fit requires that the errors on each measurement be described by Gaussian statistics. In order to deal with low-statistic VHE data, one must correctly account for the Poissonian nature of one's data. This involves folding a theoretical model with the instrument response functions to get a model prediction for the mean observed counts.

Correlation between VHE data and data from different bands can be investigated by naturally extending the likelihood equation into the temporal domain, such that $\mathcal{L}\left(\vec{\theta}\right) = \mathcal{L}\left(\vec{\theta}, t\right)$. To do this, one requires a model that can predict the excess counts to be observed as a function of time. It is common for weaker sources to assume the spectral shape of the source doesn't change dramatically during the course of a set of observations. This allows one to fix the spectral shape parameters during a fitting procedure, resulting in only one free parameter, the normalization N_0. With N_0 being the only free fit parameter, it becomes directly correlated to the integral flux of the source. Therefore if one can predict the integral flux of a source one can simply obtain a testable model for the observed counts. This could be interpreted as assuming some form of temporal profile, binning the data into reasonable time bins and using the flux model to obtain a prediction of the binned data's spectrum. A fit to the optimal model parameters could therefore be obtained. In the following section an algorithm to test for a Flux-Flux correlation between VHE and X-ray data is discussed.

A.2.1 Algorithm

The fitting procedure determines the likelihood of the data being described by a general trend between VHE and X-ray data.

[1] One would expect the inverse Compton (IC) and synchrotron (sync) fluxes to be related as $\phi_{IC} \propto \phi^2_{sync}$ in an SSC model and $\phi_{IC} \propto \phi_{sync}$ in an EC model, assuming a change in the electron density. See Ghisellini & Maraschi (1996) for a discussion of the different variability relations.

1. Bin the VHE data into observational bins of comparable cadence to the X-ray observations (for example 1 day).

2. Apply a likelihood fit to the energy spectrum of the total VHE dataset. Let the best fit parameters be $\vec{\theta}$.

3. Create a model which links the VHE and X-ray data such that

$$f(\phi_{\text{X-ray}}) = \phi_{\text{VHE}}, \tag{A.3}$$

   where ϕ is the integral flux. For example take a linear model $f(x) = m \times x + c$.

4. For each i^{th} data bin with a VHE observation and an X-ray observation:

   Using Equation A.3 obtain a prediction of the VHE flux.

   Using this prediction obtained the spectral normalization assuming the same spectral shape parameters of $\vec{\theta}$ (e.g. spectral index), let this be $\tilde{\theta}$.

   Obtain $\log \mathcal{L}_i\left(\tilde{\theta}_i\right)$.

5. Sum over each time bin to obtain the joint-likelihood:

$$\log \mathcal{L}\left(\tilde{\theta}\right) = \sum_i \log \mathcal{L}_i\left(\tilde{\theta}_i\right) \tag{A.4}$$

6. Generate a model of no-correlation between VHE and XRT data, for example a constant fit ($f(x) = c, m = 0$),

7. By reapplying Step 4 for this new model obtain $\log \mathcal{L}_0$.

8. Calculate the significance of this model using the likelihood ratio test (Wilks, 1938):

$$-2 \log\left(\frac{\mathcal{L}}{\mathcal{L}_0}\right) \sim \chi^2_\nu, \tag{A.5}$$

   where ν is the difference in degrees of freedom between the two models (in this example $\nu = 1$).

In applying Steps 6-8, one acknowledges that an optimized likelihood equation often provides no useful information. To interpret the result one needs to compare the model to an alternative model. In the above case the natural null hypothesis is that there is not correlation

between the two flux bands and that the VHE flux is constant. Using nested models allows for the application of Wilks' theorem to obtain an equivalent χ^2-statistic.

Note: The above procedure only considers errors on the VHE data. To estimate the effect of the uncertainty on the X-ray data one can apply a Monte Carlo simultation, in which X-ray observations are draw from a distribution described by the observed X-ray flux and its error.

A.2.2 Example

Using the instrument response functions and Off data from the OJ 287 dataset, two sets of random data were simulated. The first dataset was drawn assuming a constant flux. The second dataset was drawn assuming a linear correlation between the VHE observations and the X-ray observations of OJ 287. A likelihood-ratio test, as described in Appendix A.2.1, was applied to both datasets to test for a correlation between the VHE and X-ray observations. This was repeated 1000 times, with the resulting equivalent χ^2-distributions shown in Figure A.2. The constant-flux distribution is well-described by a χ^2-distribution with $\nu = 1$. This indicates that the method described in Appendix A.2 can be used to distinguish between a correlated and non-correlated model.

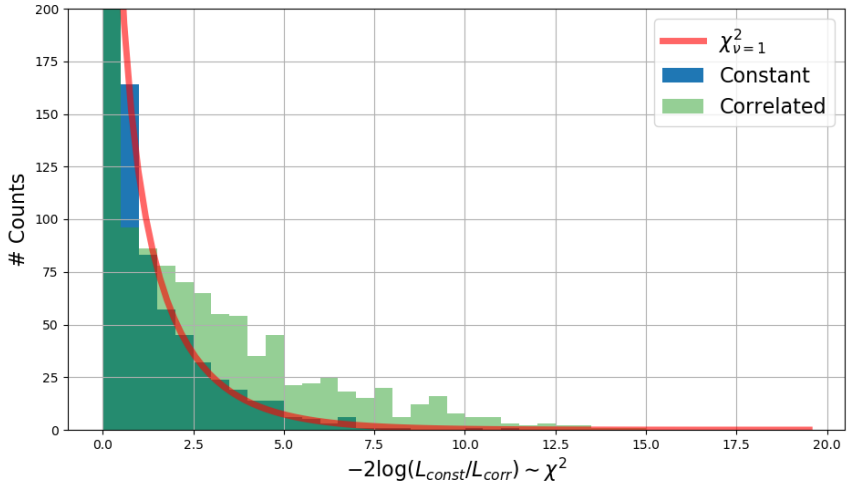

Figure A.2: Simulated likelihood-based correlation test χ^2-Distributions. The blue histogram corresponds to data simulated assuming a constant (non-correlated) relation to the X-ray data. The green histogram corresponds to data simulated assuming a correlated relation to the X-ray data. The red line corresponds to a χ^2-distribution with $\nu = 1$.

Appendix B

OJ 287 Additional Results and Figures

B.1 OJ 287 Daily *Swift*-XRT Results

Table B.1: *Swift*-XRT analysis. Column 1 shows the observation ID. Column 2 shows the date of the observation in MJD. Column 3 shows the live time of the observation in seconds. Column 4 shows the deabsorbed integral flux between 0.3 - 10 keV. Column 5 shows the best-fit power-law spectral index or α and β is the case of a log-parabola model. Columns 6 and 7 show the χ^2 and number of degrees of freedom, respectively, of the power-law fit. Column 8 shows the F-Test probability of the data being better fit by a power law model. a P_{F-Test} of "N/A" corresponds to an observations in which the log-parabola fit fails, hence a power-law model is assumed.

Obs ID	MJD	Live Time (Seconds)	ϕ (0.3 − 10 keV) $\times 10^{-11}$(ergs cm^{-2}s^{-1})	Γ (α,β)	χ^2	NDF	P_{F-Test}
00030901254	57723.318	1007.927	$\left(2.90^{+0.12}_{-0.11}\right)$	$\left(2.40^{+0.07}_{-0.06}\right)$	31.08	40	0.624
00030901255	57725.374	743.367	$\left(2.34^{+0.16}_{-0.15}\right)$	$\left(2.31^{+0.13}_{-0.13}\right)$	14.99	21	0.422
00033756090	57727.698	982.980	$\left(1.37^{+0.09}_{-0.08}\right)$	$\left(2.50^{+0.13}_{-0.13}\right)$	47.74	26	0.156
00033756091	57729.558	1097.948	$\left(0.98^{+0.08}_{-0.08}\right)$	$\left(2.03^{+0.14}_{-0.14}\right)$	22.38	24	0.863
00033756092	57731.812	1127.885	$\left(1.24^{+0.08}_{-0.07}\right)$	$\left(2.18^{+0.11}_{-0.11}\right)$	25.00	23	0.724
00033756093	57733.545	982.979	$\left(1.24^{+0.09}_{-0.08}\right)$	$\left(2.51^{+0.15}_{-0.15}\right)$	28.92	26	0.060
00033756094	57735.935	867.689	$\left(0.91^{+0.09}_{-0.08}\right)$	$\left(2.08^{+0.18}_{-0.18}\right)$	25.47	13	N/A
00033756095	57741.248	968.012	$\left(1.15^{+0.09}_{-0.09}\right)$	$\left(2.11^{+0.15}_{-0.15}\right)$	20.88	25	0.644
00033756096	57743.971	1082.975	$\left(2.34^{+0.11}_{-0.10}\right)$	$\left(2.38^{+0.08}_{-0.08}\right)$	44.71	42	0.341
00033756097	57745.769	977.650	$\left(4.07^{+0.21}_{-0.20}\right)$	$\left(2.41^{+0.17}_{-0.18}\right), \left(0.70^{+0.53}_{-0.45}\right)$	26.75	32	0.007
00033756098	57747.957	943.208	$\left(1.75^{+0.10}_{-0.10}\right)$	$\left(2.45^{+0.10}_{-0.10}\right)$	31.98	28	0.330
00033756099	57751.495	930.518	$\left(2.51^{+0.12}_{-0.12}\right)$	$\left(2.43^{+0.08}_{-0.08}\right)$	29.75	40	0.212
00033756100	57753.341	1013.099	$\left(2.49^{+0.11}_{-0.11}\right)$	$\left(2.53^{+0.08}_{-0.08}\right)$	35.61	37	0.668
00033756101	57755.015	901.594	$\left(2.86^{+0.13}_{-0.12}\right)$	$\left(2.73^{+0.12}_{-0.12}\right), \left(-0.50^{+0.36}_{-0.31}\right)$	34.49	40	0.021
00033756102	57757.934	1013.112	$\left(2.12^{+0.11}_{-0.10}\right)$	$\left(2.40^{+0.09}_{-0.08}\right)$	41.84	36	0.858
00033756103	57759.731	813.440	$\left(1.73^{+0.11}_{-0.10}\right)$	$\left(2.60^{+0.11}_{-0.11}\right)$	34.85	25	0.937

Continued on next page

Table B.1 – *Continued from previous page*

Obs ID	MJD	Live Time (Seconds)	ϕ (0.3 − 10 keV) $\times 10^{-11}$(ergs cm^{-2}s^{-1})	Γ (α,β)	χ^2	NDF	P_{F-Test}
00033756105	57763.789	805.214	$\left(1.72^{+0.10}_{-0.10}\right)$	$\left(2.37^{+0.11}_{-0.12}\right)$	26.57	24	0.367
00033756106	57768.691	978.151	$\left(0.50^{+0.09}_{-0.08}\right)$	$\left(2.24^{+0.39}_{-0.43}\right)$	20.45	14	0.071
00033756107	57770.693	1008.099	$\left(1.17^{+0.09}_{-0.09}\right)$	$\left(2.25^{+0.14}_{-0.14}\right)$	8.29	21	0.224
00033756109	57775.345	982.945	$\left(0.88^{+0.18}_{-0.15}\right)$	$\left(1.51^{+0.28}_{-0.30}\right)$	20.52	15	0.988
00033756110	57777.596	922.607	$\left(1.07^{+0.11}_{-0.10}\right)$	$\left(1.80^{+0.16}_{-0.16}\right)$	16.14	19	0.203
00033756111	57779.990	923.069	$\left(2.01^{+0.19}_{-0.17}\right)$	$\left(2.42^{+0.16}_{-0.16}\right)$	10.80	13	0.623
00033756112	57781.777	1002.492	$\left(1.83^{+0.10}_{-0.10}\right)$	$\left(2.27^{+0.09}_{-0.09}\right)$	39.69	33	0.325
00033756113	57783.372	933.200	$\left(2.68^{+0.12}_{-0.11}\right)$	$\left(2.35^{+0.07}_{-0.07}\right)$	63.90	41	0.178
00033756114	57786.360	1967.716	$\left(4.56^{+0.10}_{-0.10}\right)$	$\left(2.54^{+0.04}_{-0.04}\right)$	96.09	112	0.904
00033756115	57787.357	998.139	$\left(4.07^{+0.14}_{-0.14}\right)$	$\left(2.68^{+0.06}_{-0.06}\right)$	58.36	58	0.387
00033756116	57788.154	994.202	$\left(3.74^{+0.14}_{-0.13}\right)$	$\left(2.48^{+0.06}_{-0.06}\right)$	72.05	53	0.902
00033756117	57789.433	838.394	$\left(3.55^{+0.15}_{-0.14}\right)$	$\left(2.43^{+0.07}_{-0.07}\right)$	59.77	51	0.063
00033756118	57791.078	783.476	$\left(3.85^{+0.15}_{-0.15}\right)$	$\left(2.42^{+0.07}_{-0.07}\right)$	38.73	47	0.921
00033756119	57792.275	1215.258	$\left(3.65^{+0.12}_{-0.11}\right)$	$\left(2.56^{+0.05}_{-0.05}\right)$	67.60	67	0.804
00033756121	57796.991	1087.376	$\left(3.60^{+0.13}_{-0.12}\right)$	$\left(2.37^{+0.06}_{-0.06}\right)$	40.57	54	0.415
00034934001	57799.185	903.088	$\left(3.28^{+0.14}_{-0.13}\right)$	$\left(2.53^{+0.07}_{-0.07}\right)$	38.86	46	0.353
00033756122	57799.590	967.981	$\left(3.00^{+0.12}_{-0.12}\right)$	$\left(2.64^{+0.07}_{-0.07}\right)$	34.95	43	0.583
00034934002	57800.181	951.414	$\left(3.06^{+0.13}_{-0.12}\right)$	$\left(2.69^{+0.07}_{-0.07}\right)$	45.11	43	0.957
00034934003	57801.244	968.092	$\left(2.77^{+0.12}_{-0.11}\right)$	$\left(2.56^{+0.07}_{-0.07}\right)$	47.06	45	0.998
00034934004	57802.242	1212.745	$\left(2.42^{+0.10}_{-0.09}\right)$	$\left(2.58^{+0.07}_{-0.06}\right)$	49.80	48	0.388

Continued on next page

Table B.1 – *Continued from previous page*

Obs ID	MJD	Live Time (Seconds)	ϕ (0.3 − 10 keV) $\times 10^{-11}$(ergs cm^{-2}s^{-1})	Γ (α,β)	χ^2	NDF	P_{F-Test}
00034934005	57803.305	1017.902	$\left(2.37^{+0.11}_{-0.11}\right)$	$\left(2.55^{+0.08}_{-0.08}\right)$	27.38	33	0.477
00034934006	57804.235	1147.839	$\left(1.92^{+0.10}_{-0.09}\right)$	$\left(2.48^{+0.09}_{-0.09}\right)$	38.31	38	0.402
00034934007	57805.299	1013.063	$\left(2.07^{+0.10}_{-0.10}\right)$	$\left(2.73^{+0.13}_{-0.14}\right), \left(-0.82^{+0.37}_{-0.34}\right)$	37.24	39	0.002
00034934008	57806.296	973.146	$\left(2.11^{+0.11}_{-0.10}\right)$	$\left(2.39^{+0.09}_{-0.09}\right)$	26.56	31	0.189
00034934009	57807.292	978.137	$\left(3.10^{+0.16}_{-0.15}\right)$	$\left(2.51^{+0.09}_{-0.09}\right)$	29.00	30	0.639
00034934010	57808.289	882.378	$\left(2.73^{+0.12}_{-0.12}\right)$	$\left(2.50^{+0.08}_{-0.08}\right)$	31.52	35	0.298
00034934011	57809.285	1022.907	$\left(2.57^{+0.11}_{-0.11}\right)$	$\left(2.50^{+0.07}_{-0.07}\right)$	46.99	42	0.535
00034934012	57810.283	953.009	$\left(2.32^{+0.11}_{-0.10}\right)$	$\left(2.44^{+0.09}_{-0.09}\right)$	47.43	34	0.182
00034934013	57811.291	987.955	$\left(2.05^{+0.10}_{-0.10}\right)$	$\left(2.40^{+0.09}_{-0.09}\right)$	28.58	36	0.309
00034934018	57816.461	89.615	$\left(1.97^{+0.43}_{-0.36}\right)$	$\left(2.63^{+0.43}_{-0.50}\right)$	0.43	2	N/A
00034934020	57818.721	968.157	$\left(1.85^{+0.10}_{-0.10}\right)$	$\left(2.39^{+0.10}_{-0.10}\right)$	34.47	28	N/A
00034934021	57819.520	357.813	$\left(2.11^{+0.18}_{-0.17}\right)$	$\left(2.41^{+0.17}_{-0.18}\right)$	10.28	11	0.255
00034934022	57823.241	698.642	$\left(1.78^{+0.12}_{-0.11}\right)$	$\left(2.59^{+0.14}_{-0.14}\right)$	35.62	26	N/A
00034934023	57824.567	1110.999	$\left(1.79^{+0.12}_{-0.11}\right)$	$\left(2.50^{+0.13}_{-0.13}\right)$	15.64	22	0.850
00034934024	57825.174	963.167	$\left(1.37^{+0.09}_{-0.09}\right)$	$\left(2.40^{+0.12}_{-0.12}\right)$	21.42	23	0.735
00034934025	57826.372	1017.120	$\left(0.98^{+0.09}_{-0.08}\right)$	$\left(2.69^{+0.17}_{-0.19}\right), \left(-0.92^{+0.48}_{-0.43}\right)$	27.10	25	0.010
00034934026	57827.103	997.948	$\left(1.36^{+0.09}_{-0.09}\right)$	$\left(2.32^{+0.14}_{-0.14}\right)$	37.60	25	0.225
00034934027	57828.168	996.726	$\left(1.60^{+0.11}_{-0.10}\right)$	$\left(2.02^{+0.12}_{-0.12}\right)$	41.19	30	0.768
00034934028	57829.148	1004.554	$\left(1.52^{+0.10}_{-0.09}\right)$	$\left(2.03^{+0.12}_{-0.12}\right)$	33.53	30	0.608
00034934029	57830.212	948.177	$\left(1.53^{+0.10}_{-0.09}\right)$	$\left(2.40^{+0.12}_{-0.11}\right)$	28.07	27	0.085

Continued on next page

Table B.1 – *Continued from previous page*

Obs ID	MJD	Live Time (Seconds)	ϕ (0.3 − 10 keV) $\times 10^{-11}$(ergs cm^{-2}s^{-1})	Γ (α,β)	χ^2	NDF	P_{F-Test}
00034934030	57831.141	982.959	$\left(1.68^{+0.10}_{-0.09}\right)$	$\left(2.47^{+0.12}_{-0.12}\right)$	27.36	32	0.912
00034934031	57832.139	863.169	$\left(1.73^{+0.11}_{-0.10}\right)$	$\left(2.33^{+0.11}_{-0.11}\right)$	25.41	26	0.123
00034934032	57833.134	947.578	$\left(1.62^{+0.10}_{-0.10}\right)$	$\left(2.25^{+0.12}_{-0.12}\right)$	31.34	31	0.911
00034934033	57834.131	973.146	$\left(1.22^{+0.09}_{-0.09}\right)$	$\left(2.59^{+0.16}_{-0.18}\right), \left(-0.68^{+0.46}_{-0.42}\right)$	21.84	31	0.009
00034934034	57835.194	1027.896	$\left(1.46^{+0.09}_{-0.08}\right)$	$\left(2.38^{+0.11}_{-0.11}\right)$	24.90	29	0.639
00034934035	57836.190	1012.914	$\left(1.76^{+0.10}_{-0.09}\right)$	$\left(2.23^{+0.10}_{-0.09}\right)$	24.89	34	0.134
00034934036	57837.128	1038.035	$\left(1.64^{+0.10}_{-0.09}\right)$	$\left(2.81^{+0.11}_{-0.11}\right)$	28.49	31	0.916
00034934037	57838.183	993.117	$\left(1.24^{+0.08}_{-0.08}\right)$	$\left(2.23^{+0.12}_{-0.12}\right)$	34.85	23	0.129
00034934038	57839.190	898.268	$\left(1.22^{+0.10}_{-0.09}\right)$	$\left(1.84^{+0.14}_{-0.14}\right)$	18.61	21	0.752
00034934039	57840.178	1076.982	$\left(1.39^{+0.09}_{-0.09}\right)$	$\left(2.86^{+0.14}_{-0.15}\right), \left(-0.73^{+0.45}_{-0.39}\right)$	21.92	30	0.005
00034934040	57841.181	983.130	$\left(1.13^{+0.09}_{-0.08}\right)$	$\left(2.36^{+0.15}_{-0.15}\right)$	16.23	22	0.898
00034934041	57842.169	993.104	$\left(1.06^{+0.09}_{-0.08}\right)$	$\left(2.19^{+0.19}_{-0.19}\right)$	14.63	18	0.848
00034934042	57843.233	898.051	$\left(1.15^{+0.09}_{-0.08}\right)$	$\left(2.33^{+0.15}_{-0.14}\right)$	16.14	21	0.883
00034934043	57845.623	922.038	$\left(1.11^{+0.10}_{-0.09}\right)$	$\left(1.96^{+0.17}_{-0.16}\right)$	27.56	21	0.243
00034934044	57857.186	1008.091	$\left(1.21^{+0.15}_{-0.14}\right)$	$\left(2.41^{+0.24}_{-0.31}\right), \left(-1.03^{+0.83}_{-0.69}\right)$	10.70	17	0.023

B.2 OJ 287 Discrete Correlation Function Analysis

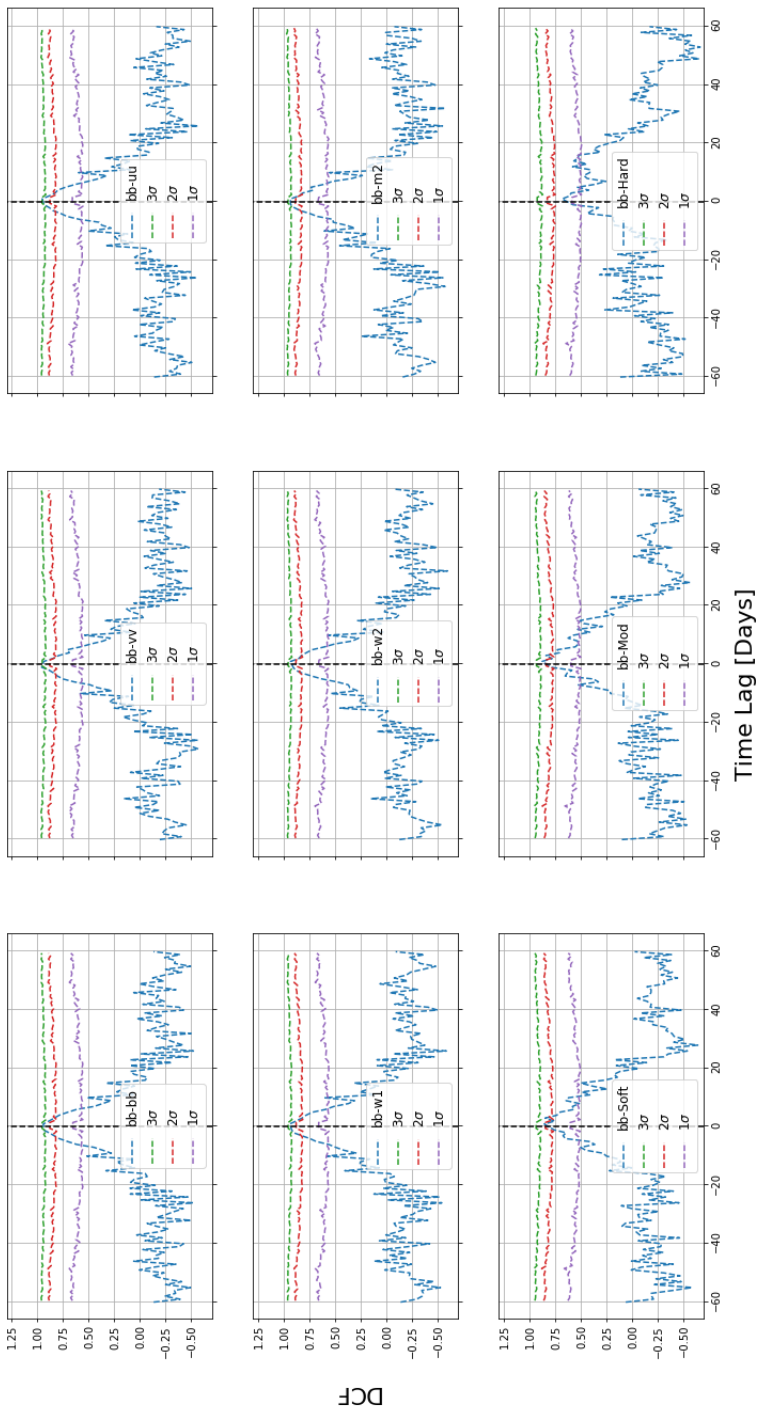

Figure B.1: Discrete correlation function analysis for *bb* filter observations. The blue points show the experimentally measured DCF values. The dashed purple, red and blue lines correspond to 1-, 2- and 3-σ confidence intervals obtained using the method described in Section 7.3.2. A negative time lag suggests a *bb* -lead, while a positive time lag suggests the *bb* data is trailing the tested energy band.

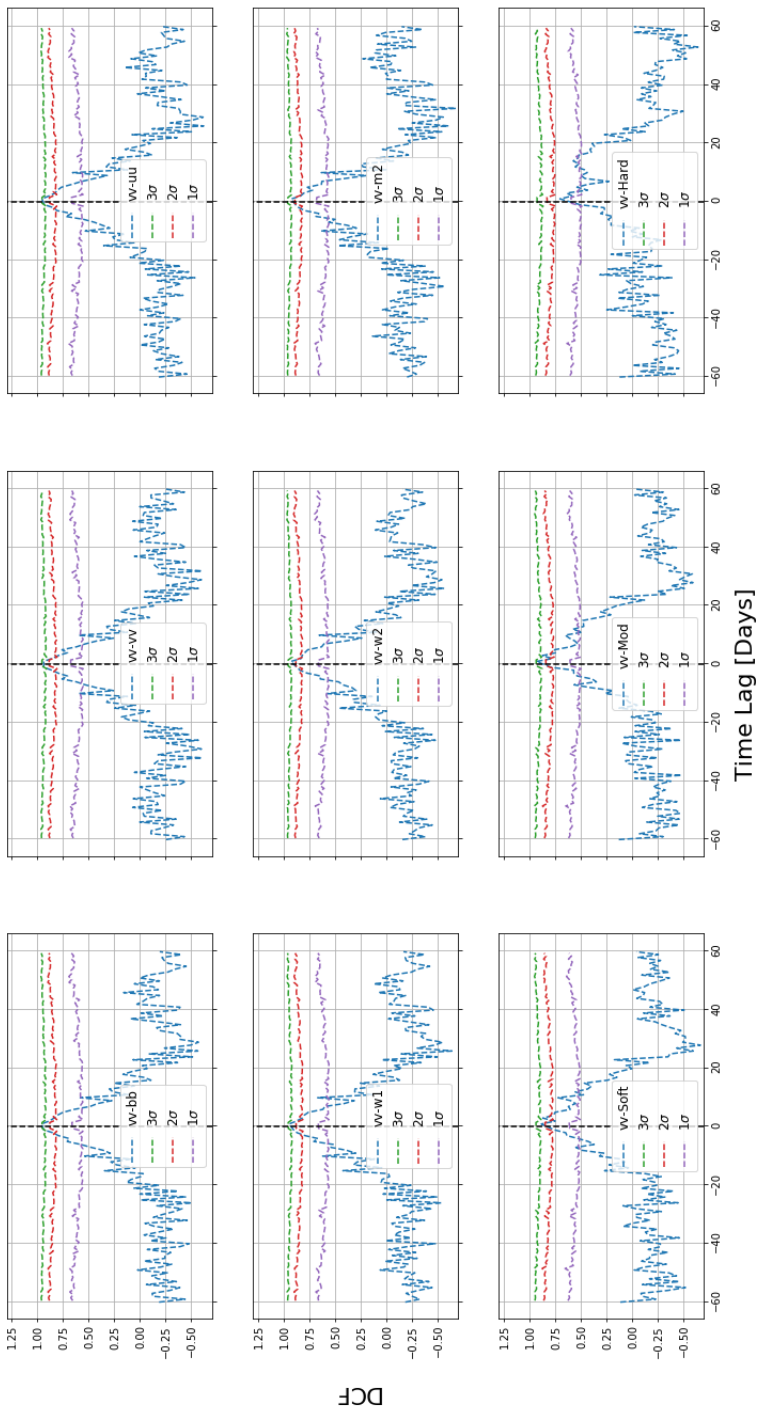

Figure B.2: Discrete correlation function analysis for $\nu\nu$ filter observations. The blue points show the experimentally measured DCF values. The dashed purple, red and blue lines correspond to 1-, 2- and 3-σ confidence intervals obtained using the method described in Section 7.3.2. A negative time lag suggests a $\nu\nu$ -lead, while a positive time lag suggests the $\nu\nu$ data is trailing the tested energy band.

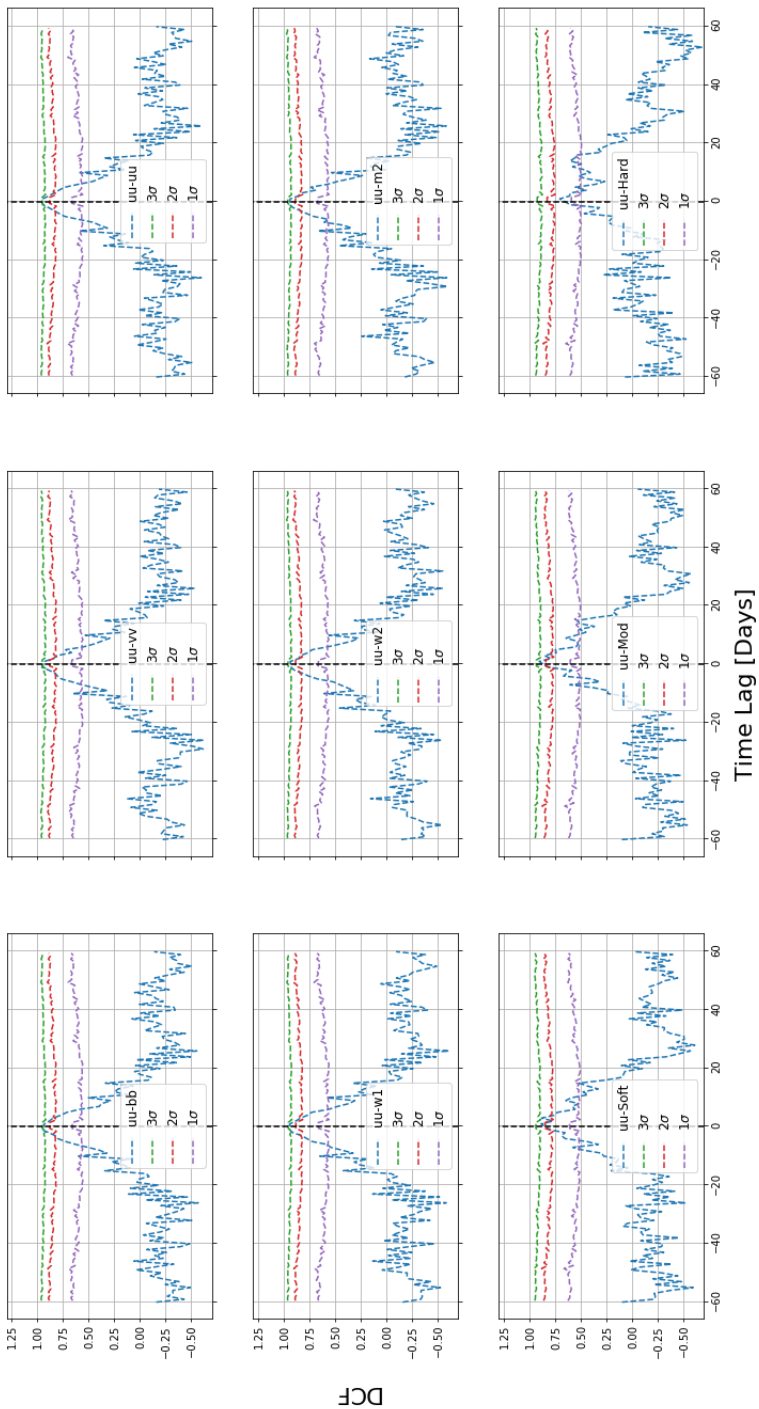

Figure B.3: Discrete correlation function analysis for *uu* filter observations. The blue points show the experimentally measured DCF values. The dashed purple, red and blue lines correspond to 1-, 2- and 3-σ confidence intervals obtained using the method described in Section 7.3.2. A negative time lag suggests a *uu* -lead, while a positive time lag suggests the *uu* data is trailing the tested energy band.

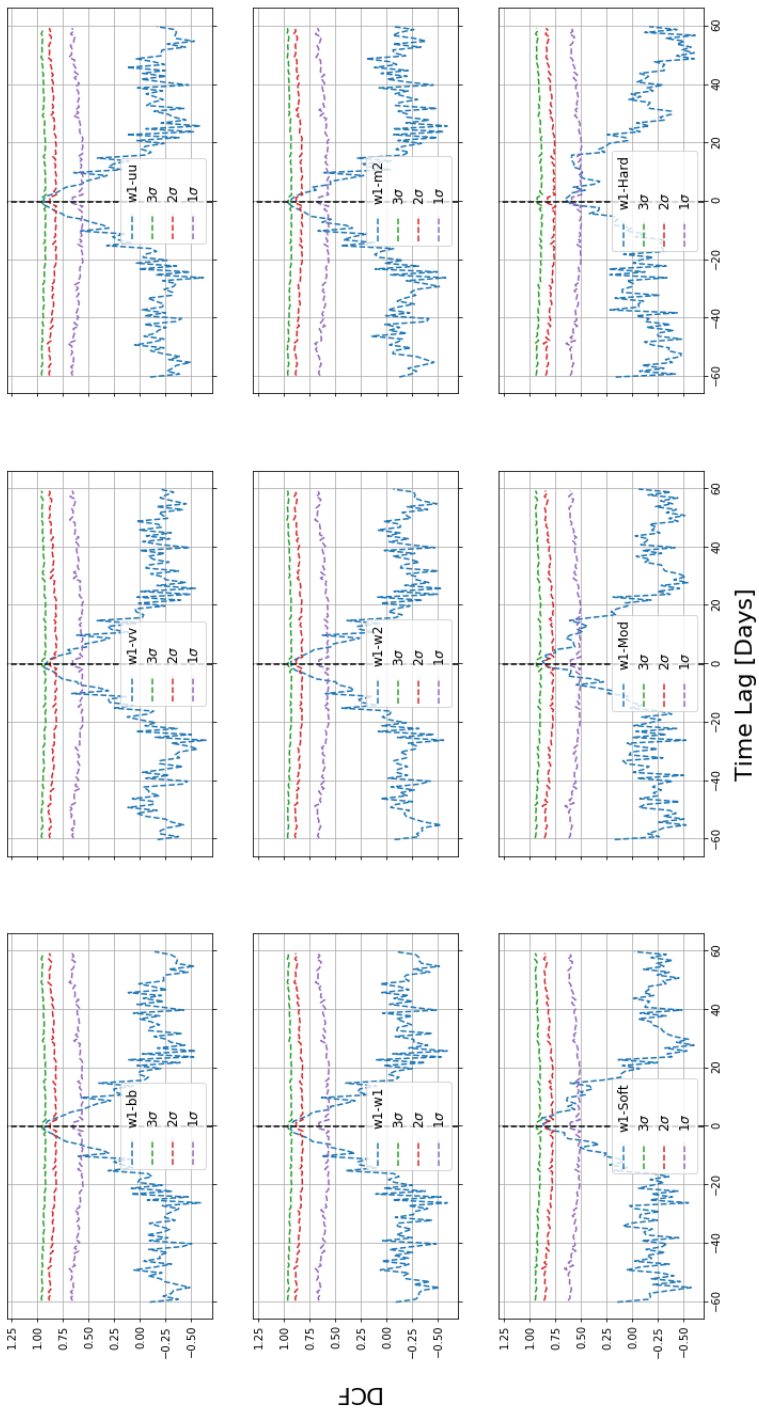

Figure B.4: Discrete correlation function analysis for *w1* filter observations. The blue points show the experimentally measured DCF values. The dashed purple, red and blue lines correspond to 1-, 2- and 3-σ confidence intervals obtained using the method described in Section 7.3.2. A negative time lag suggests a *w1*-lead, while a positive time lag suggests the *w1* data is trailing the tested energy band.

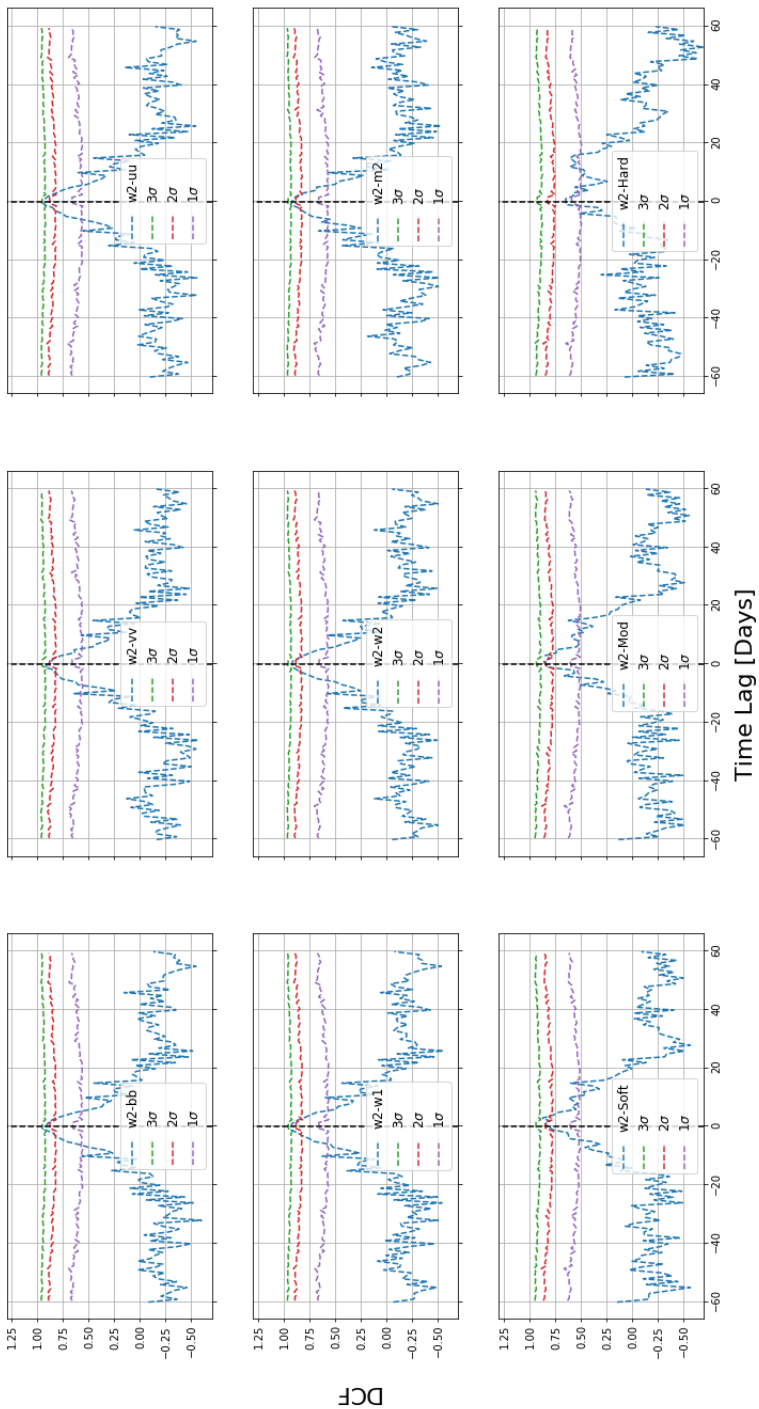

Figure B.5: Discrete correlation function analysis for $w2$ filter observations. The blue points show the experimentally measured DCF values. The dashed purple, red and blue lines correspond to 1-, 2- and 3-σ confidence intervals obtained using the method described in Section 7.3.2. A negative time lag suggests a $w2$-lead, while a positive time lag suggests the $w2$ data is trailing the tested energy band.

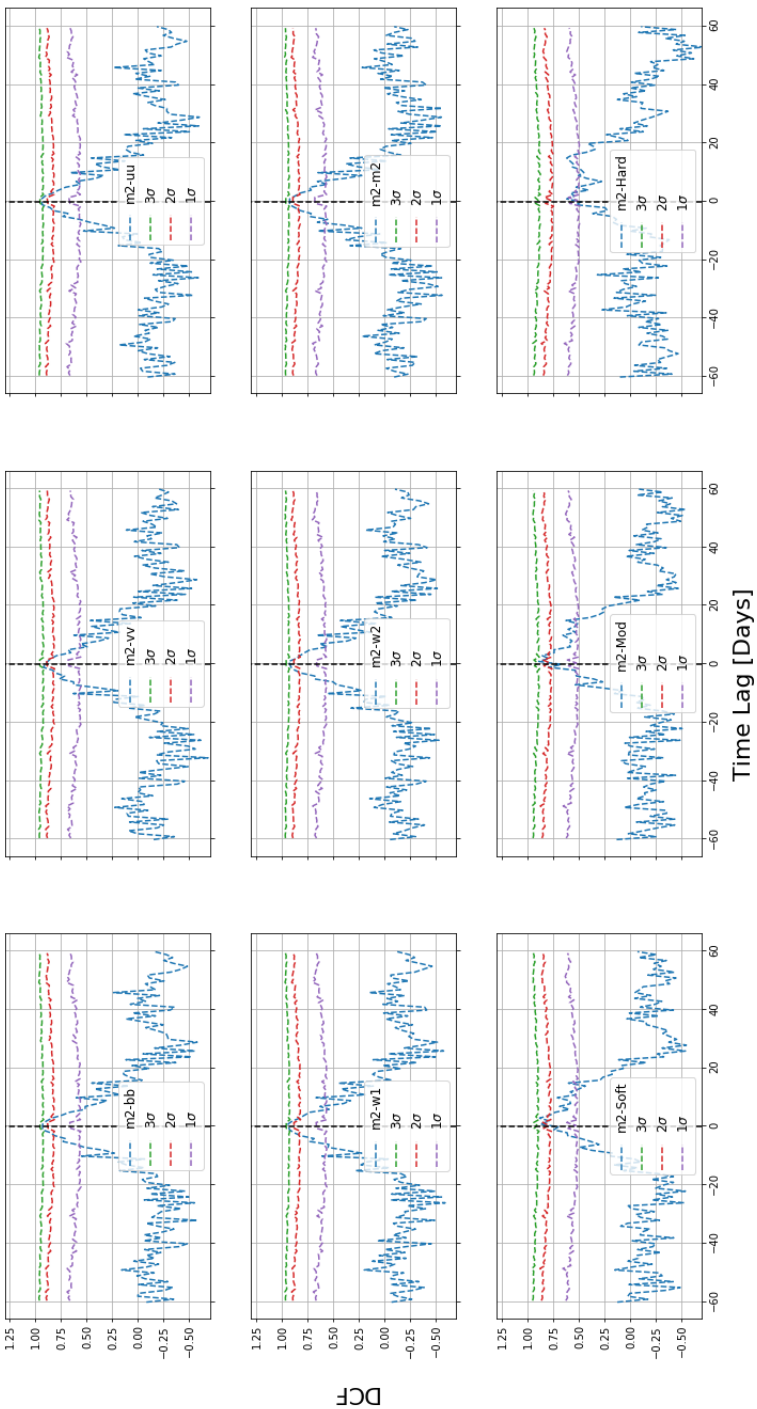

Figure B.6: Discrete correlation function analysis for *m2* filter observations. The blue points show the experimentally measured DCF values. The dashed purple, red and blue lines correspond to 1-, 2- and 3-σ confidence intervals obtained using the method described in Section 7.3.2. A negative time lag suggests a *m2*-lead, while a positive time lag suggests the *m2* data is trailing the tested energy band.

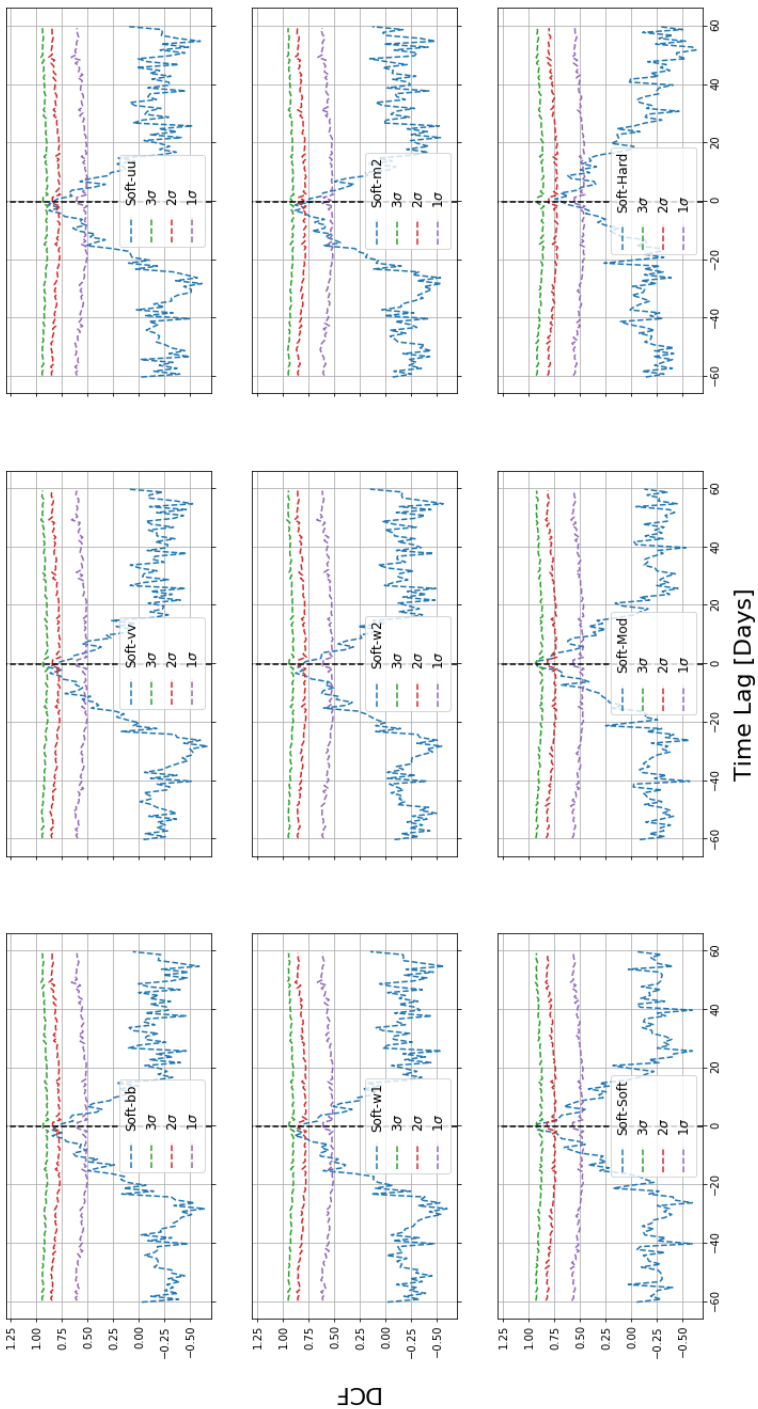

Figure B.7: Discrete correlation function analysis for soft X-ray observations. The blue points show the experimentally measured DCF values. The dashed purple, red and blue lines correspond to 1-, 2- and 3-σ confidence intervals obtained using the method described in Section 7.3.2. A negative time lag suggests a soft X-ray-lead, while a positive time lag suggests the soft X-ray data is trailing the tested energy band.

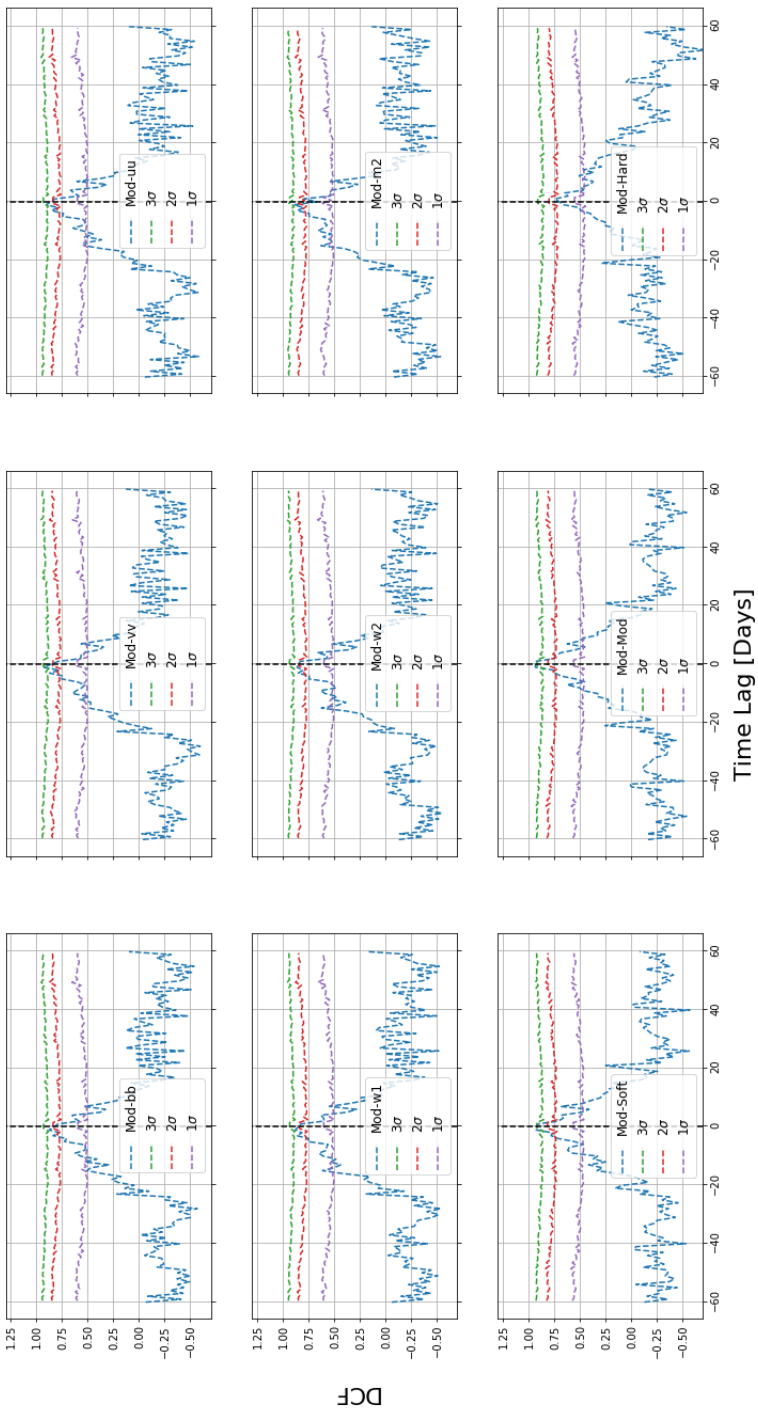

Figure B.8: Discrete correlation function analysis for moderate X-ray observations. The blue points show the experimentally measured DCF values. The dashed purple, red and blue lines correspond to 1-, 2- and 3-σ confidence intervals obtained using the method described in Section 7.3.2. A negative time lag suggests a moderate X-ray-lead, while a positive time lag suggests the moderate X-ray data is trailing the tested energy band.

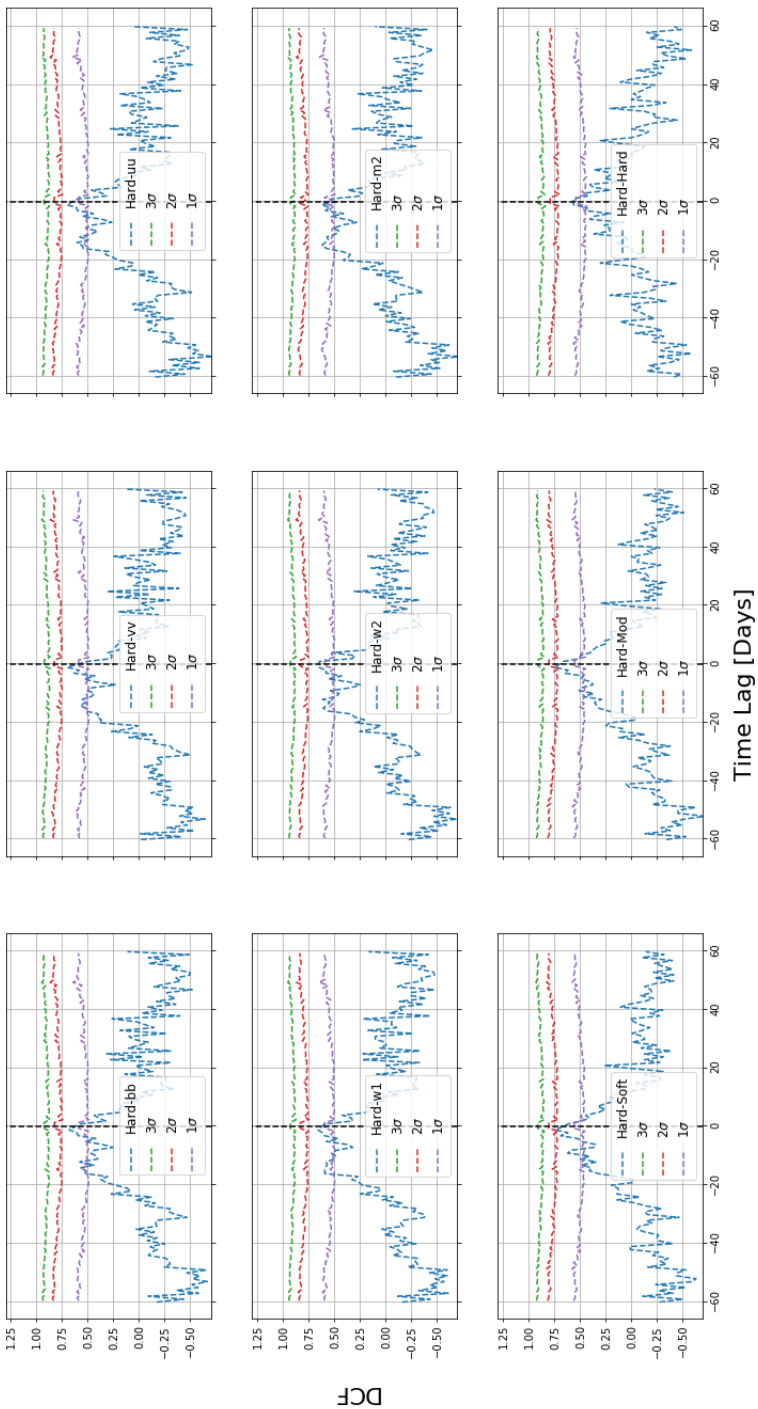

Figure B.9: Discrete correlation function analysis for hard X-ray observations. The blue points show the experimentally measured DCF values. The dashed purple, red and blue lines correspond to 1-, 2- and 3-σ confidence intervals obtained using the method described in Section 7.3.2. A negative time lag suggests a hard X-ray-lead, while a positive time lag suggests the hard X-ray data is trailing the tested energy band.

Appendix C

Constraints on the Extragalactic Background Light

C.1 EBL Upper Limits

In this section the EBL constraints for each tested model are shown. As discussed in Section 8.5, the upper limits are obtained using three different assumptions on the intrinsic energy spectra:

- No assumptions are applied to the intrinsic energy spectra. This is shown as a black line in the plots below.
- The intrinsic spectra must not be harder that the theoretical upper limit on the spectral hardness $\Gamma_{lim} = -1.5$. This is shown as a blue line in the plots below.
- The intrinsic spectra must not be harder that the observed *Fermi*-LAT spectral index, obtained from either the 3FGL catalogue or from a contemporaneous fit $\Gamma_{lim} = \Gamma_{HE}$. This is shown as a red line in the plots below. The choice of Γ_{HE} is discussed further in Section 8.5.

C.1.1 Franceschini et al. 2009 EBL Results

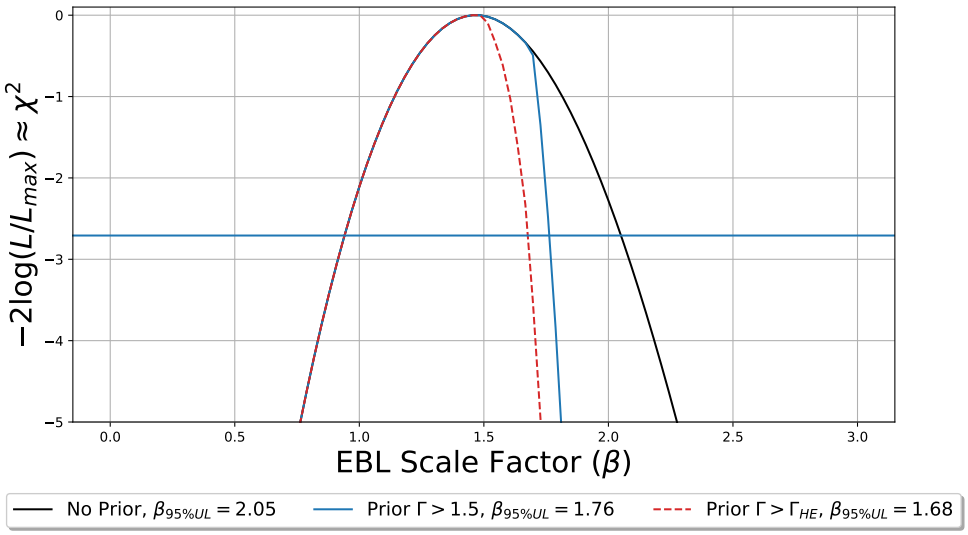

Figure C.1: Constraints on the opacity normalization (β) of an assumed Franceschini et al. (2008) EBL model. 95% confidence level frequentist upper limits are obtained using Wilks' Theorem. The upper limits are obtained by finding the value β_{UL} such that $-2\Delta \log \mathcal{L} = 2.708$.

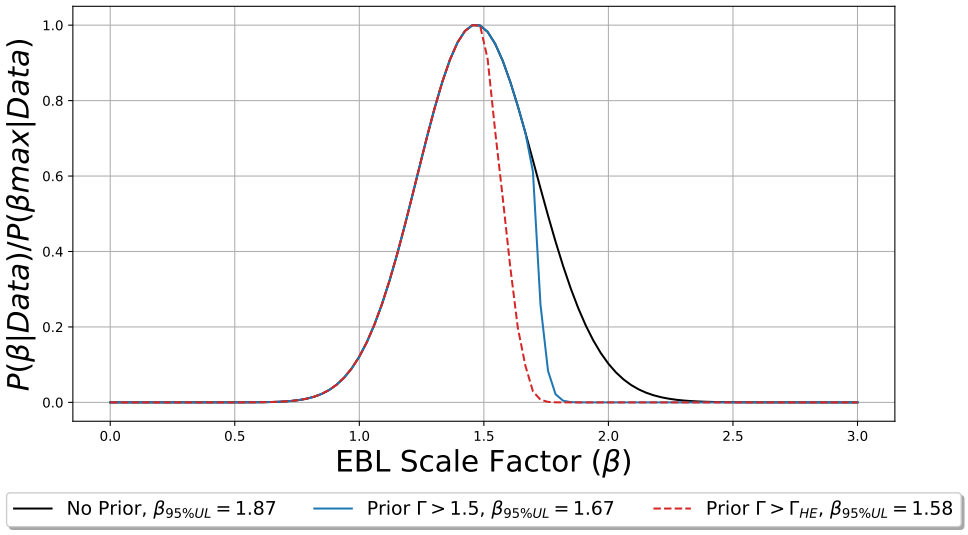

Figure C.2: Bayesian probability distribution ($P(\beta|Data)$), normalized by $P(\beta_{max}|Data)$, assuming a Franceschini et al. (2008) EBL model. 95% confidence level Bayesian upper limits are obtained using Bayes' theorem (Equation 8.21).

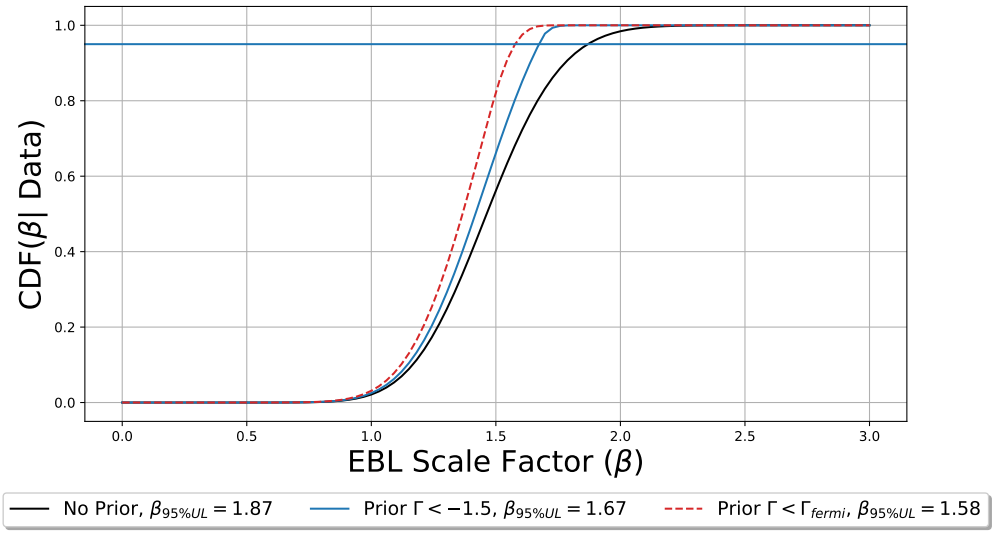

Figure C.3: Cumulative distribution function of the Bayesian probability shown in Figure C.2.

C.1.2 Finke et al. 2010 EBL Results

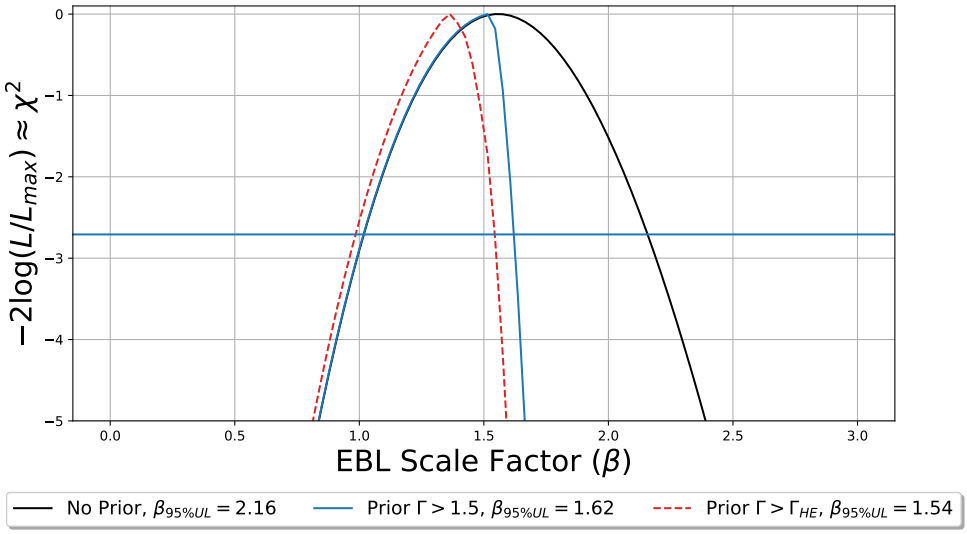

Figure C.4: Constraints on the opacity normalization (β) of an assumed Finke et al. (2010) EBL model. 95% confidence level frequentist upper limits are obtained using Wilks' Theorem. The upper limits are obtained by finding the value β_{UL} such that $-2\Delta \log \mathcal{L} = 2.708$.

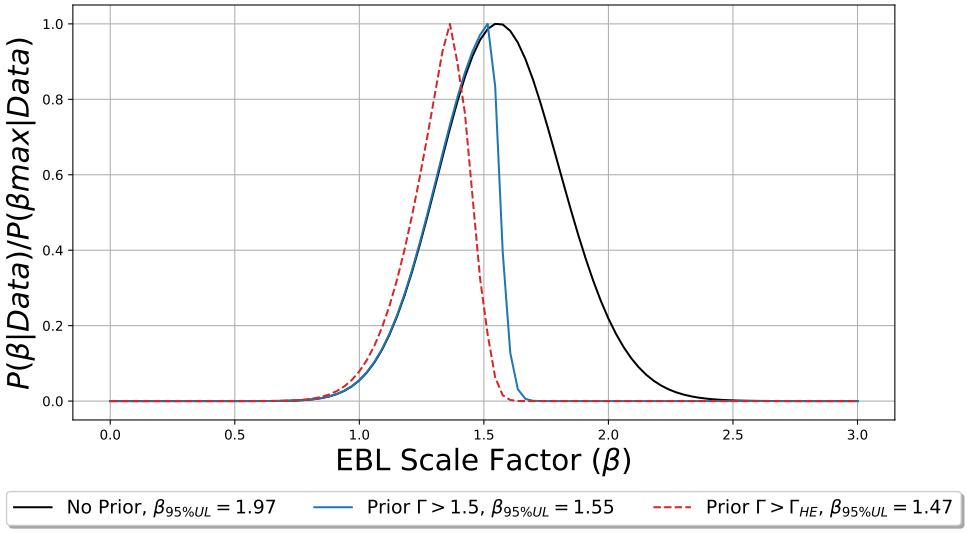

Figure C.5: Bayesian probability distribution ($P(\beta|Data)$), normalized by $P(\beta_{max}|Data)$, assuming a Finke et al. (2010) EBL model. 95% confidence level Bayesian upper limits are obtained using Bayes' theorem (Equation 8.21).

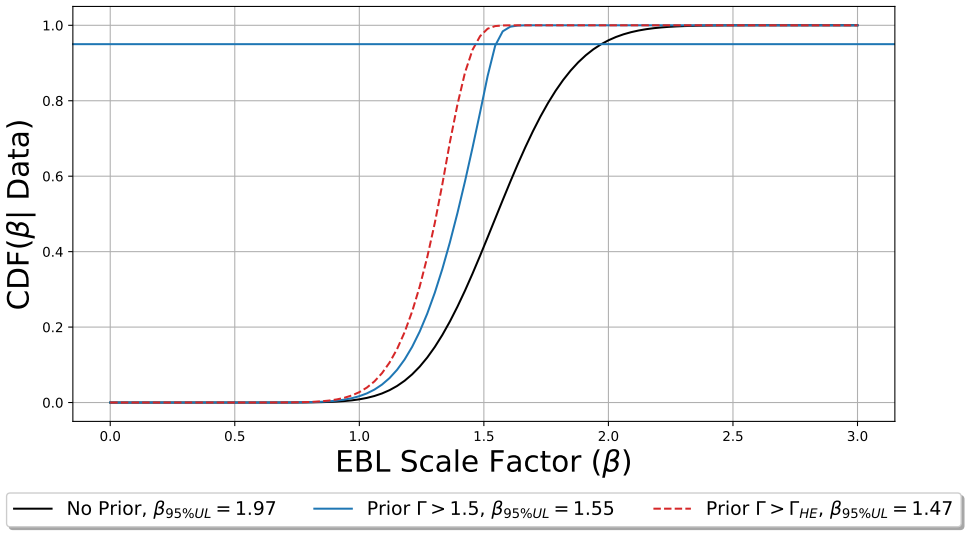

Figure C.6: Cumulative distribution function of the Bayesian probability shown in Figure C.5.

C.1.3 Dominguez et al. 2010 EBL Results

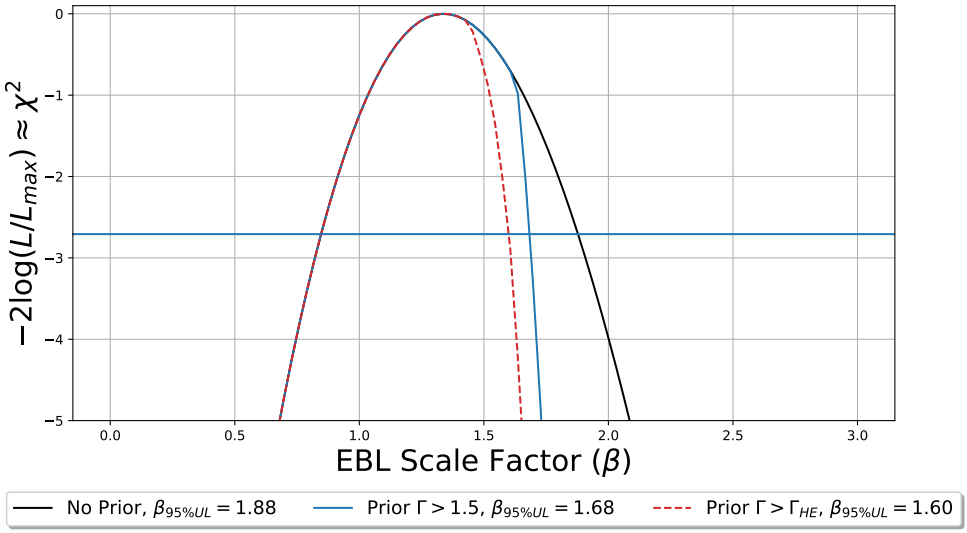

Figure C.7: Constraints on the opacity normalization (β) of an assumed Domínguez et al. (2011) EBL model. 95% confidence level frequentist upper limits are obtained using Wilks' Theorem. The upper limits are obtained by finding the value β_{UL} such that $-2\Delta \log \mathcal{L} = 2.708$.

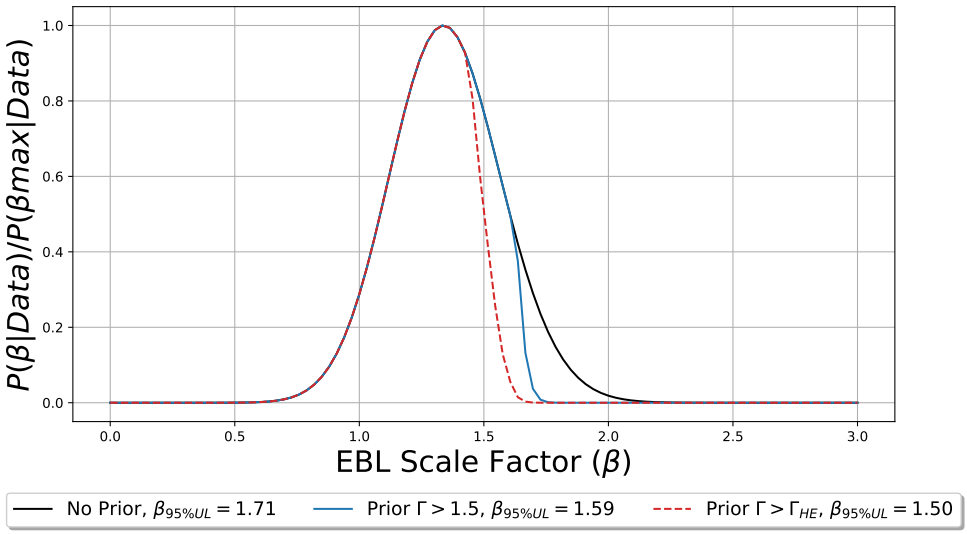

Figure C.8: Bayesian probability distribution ($P(\beta|Data)$), normalized by $P(\beta_{max}|Data)$, assuming a Domínguez et al. (2011) EBL model. 95% confidence level Bayesian upper limits are obtained using Bayes' theorem (Equation 8.21).

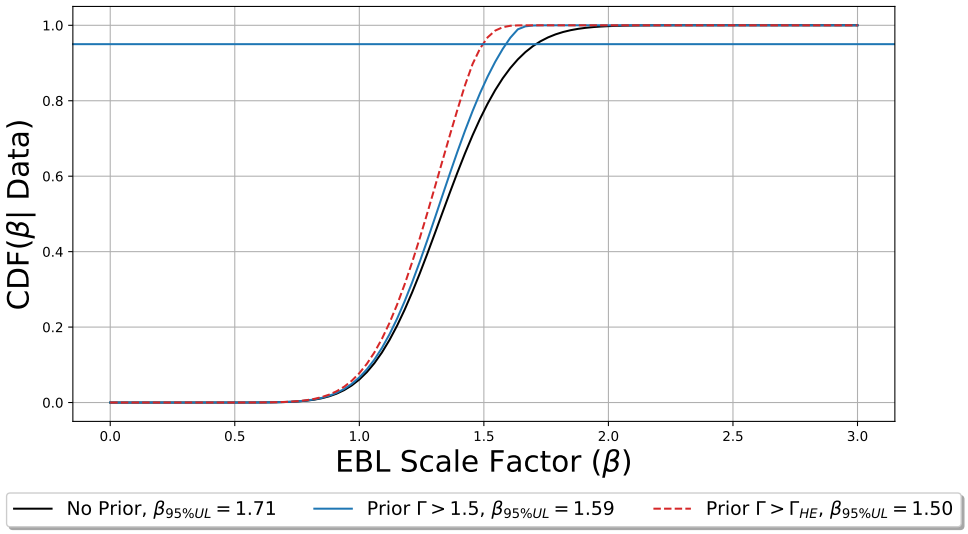

Figure C.9: Cumulative distribution function of the Bayesian probability shown in Figure C.8.

C.1.4 Gilmore et al. 2012 EBL Results

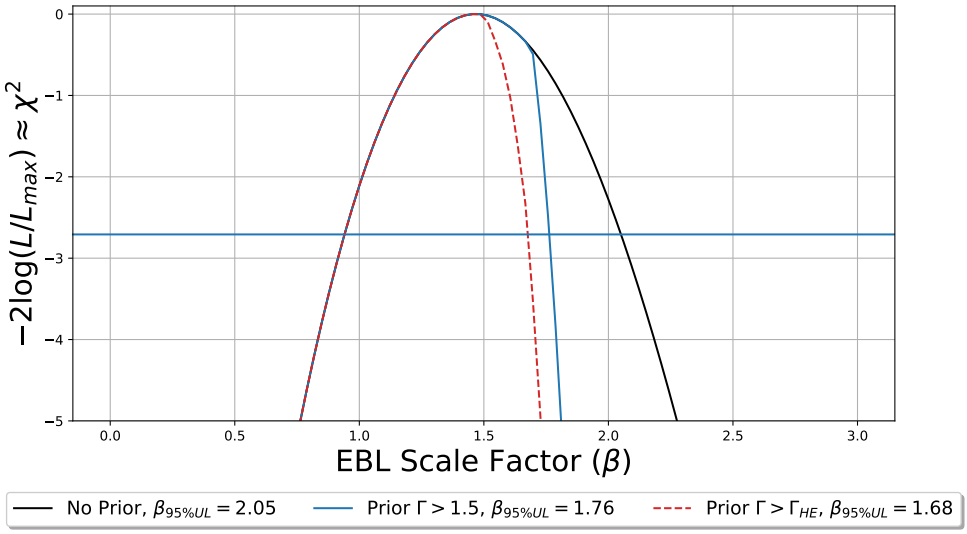

Figure C.10: Constraints on the opacity normalization (β) of an assumed Gilmore et al. (2012) EBL model. 95% confidence level frequentist upper limits are obtained using Wilks' Theorem. The upper limits are obtained by finding the value β_{UL} such that $-2\Delta \log \mathcal{L} = 2.708$.

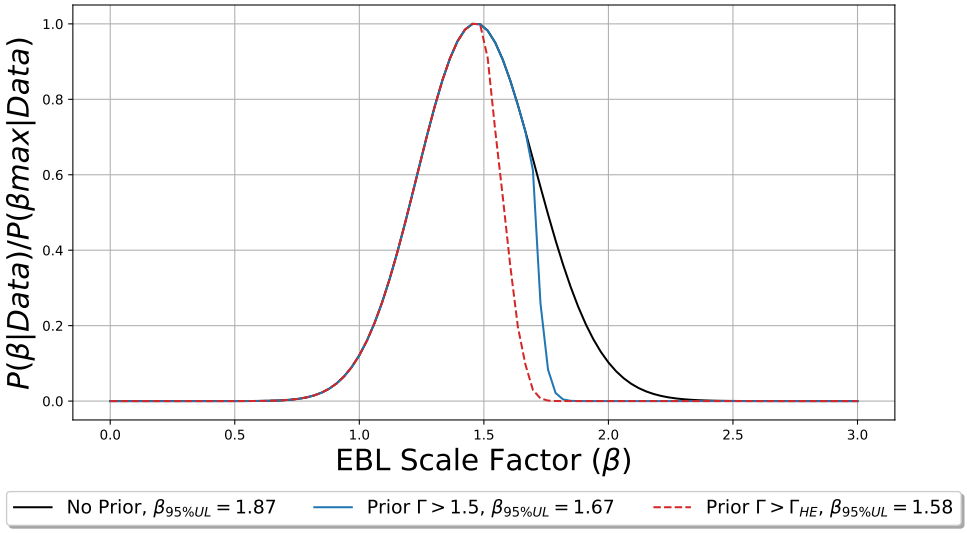

Figure C.11: Bayesian probability distribution ($P(\beta|Data)$), normalized by $P(\beta_{max}|Data)$, assuming a Gilmore et al. (2012) EBL model. 95% confidence level Bayesian upper limits are obtained using Bayes' theorem (Equation 8.21).

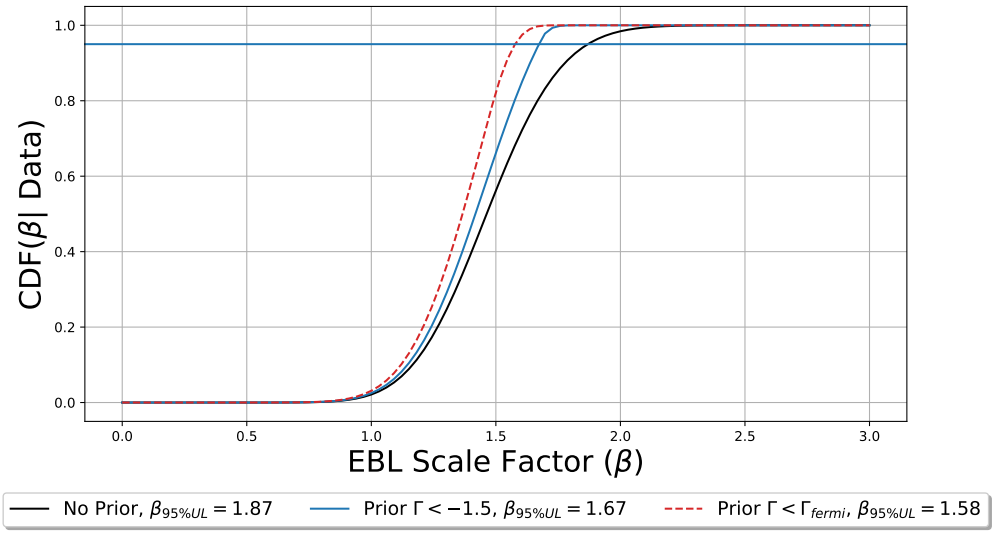

Figure C.12: Cumulative distribution function of the Bayesian probability shown in Figure C.8.

C.2 Spectral Analysis for EBL Constraints

In this section the VHE energy spectra of the sources used in the EBL constraints analysis are presented. Each of the spectra are fitted using a binned-likelihood analysis as described in Chapter A. The intrinsic energy spectra are obtained by applying a binned-likelihood fit to the intrinsic spectra assuming a Franceschini et al. (2008) EBL model. The intrinsic energy spectra are fit with both a power-law (shown in blue) and a log-parabola model (shown in red). The observed energy spectra, fitted with a power-law model, are shown in purple.

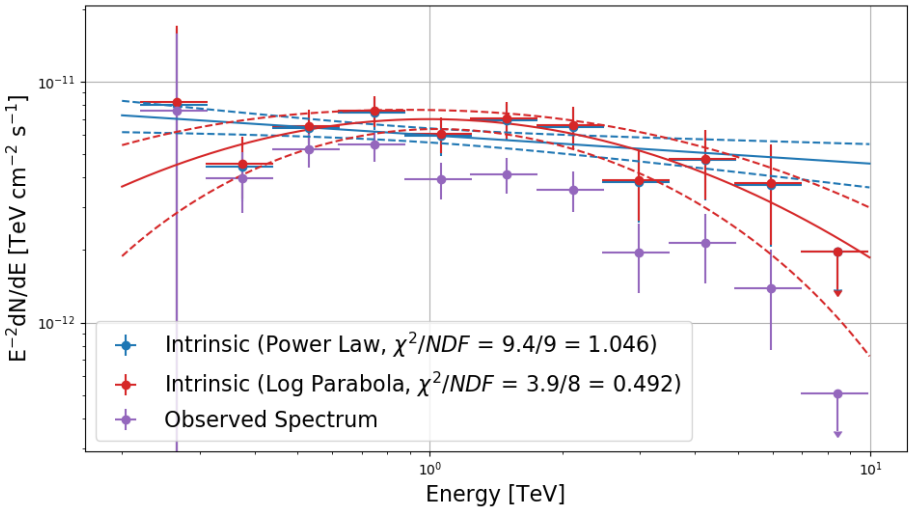

Figure C.13: VHE spectral energy distribution of 1ES 2344+514. The data analyzed here, referred to as "old" corresponds to the 2007-2008 dataset presented in Allen et al. (2017).

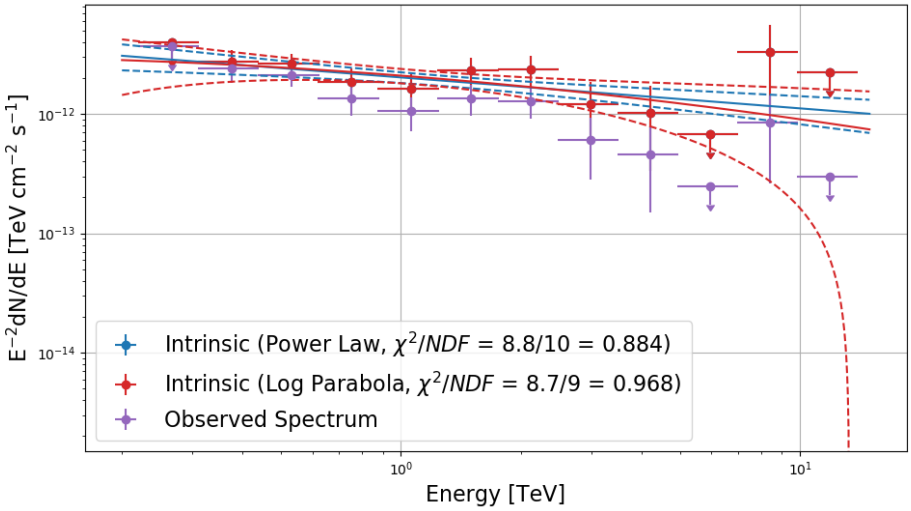

Figure C.14: VHE spectral energy distribution of 1ES 2344+514. The data analyzed here, referred to as "new" corresponds to the 2009-2015 dataset presented in Allen et al. (2017), excluding RHV observations.

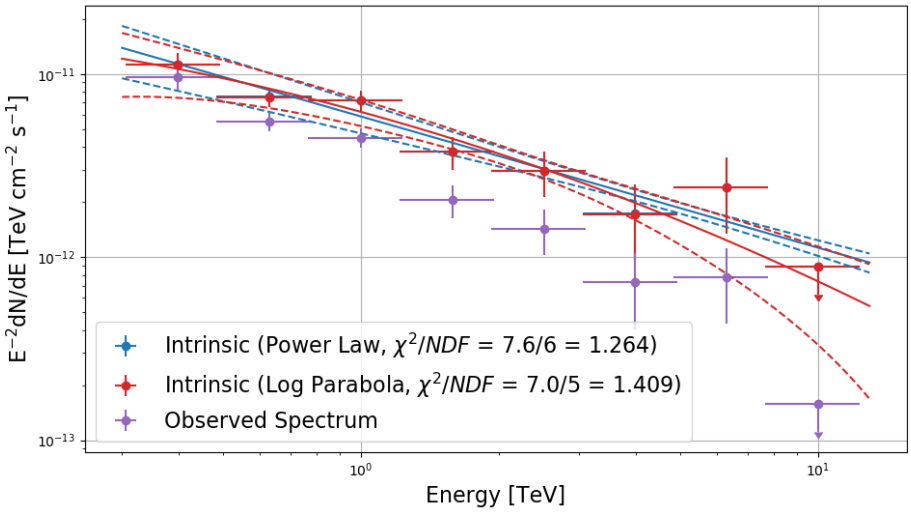

Figure C.15: VHE spectral energy distribution of 1ES 1959+650. The data analyzed here, referred to as "Low state" corresponds to the time-averaged low-state data as discussed in Section 8.3.

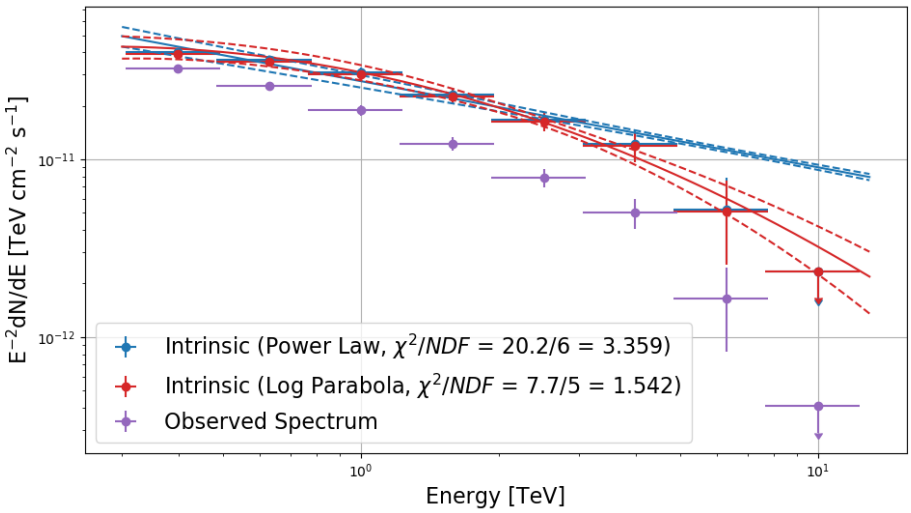

Figure C.16: VHE spectral energy distribution of 1ES 1959+650. The data analyzed here, referred to as "High state" corresponds to the time-averaged high-state data as discussed in Section 8.3.

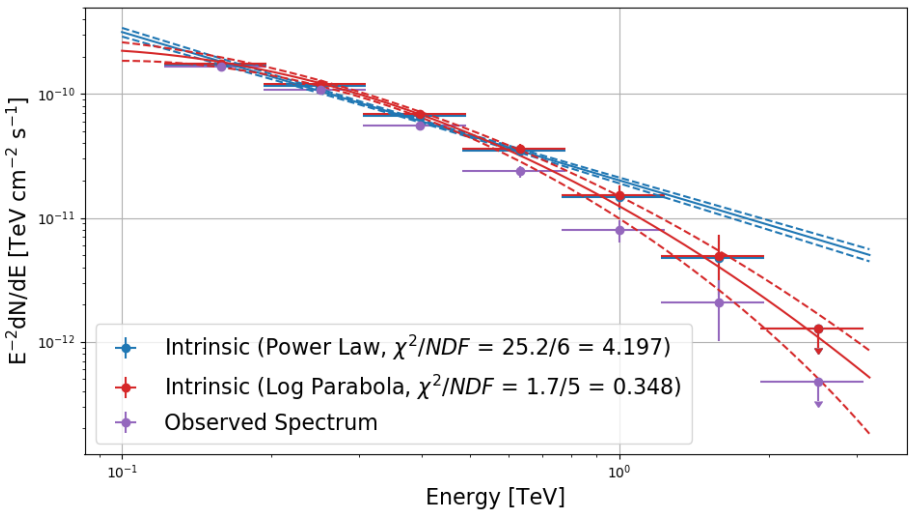

Figure C.17: VHE spectral energy distribution of BL Lac. The data analyzed here corresponds to the data presented in Abeysekara et al. (2018a).

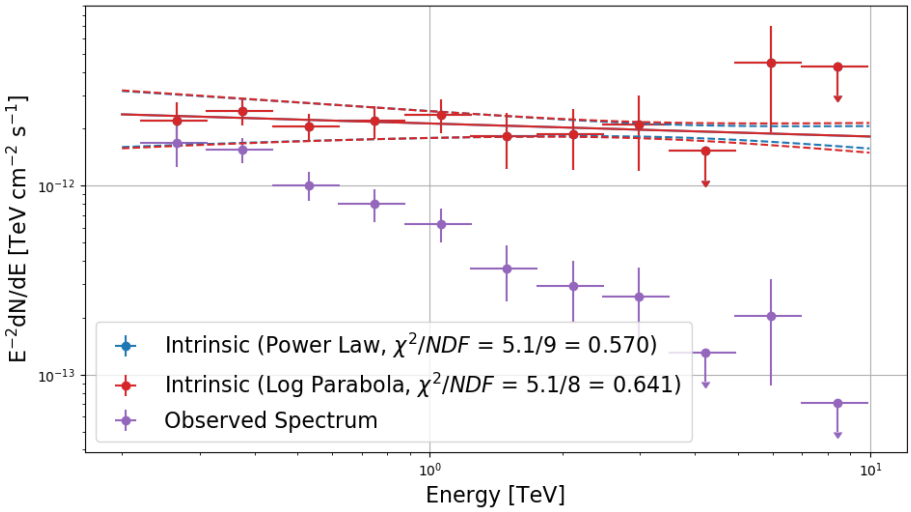

Figure C.18: VHE spectral energy distribution of RGB J0710+591.

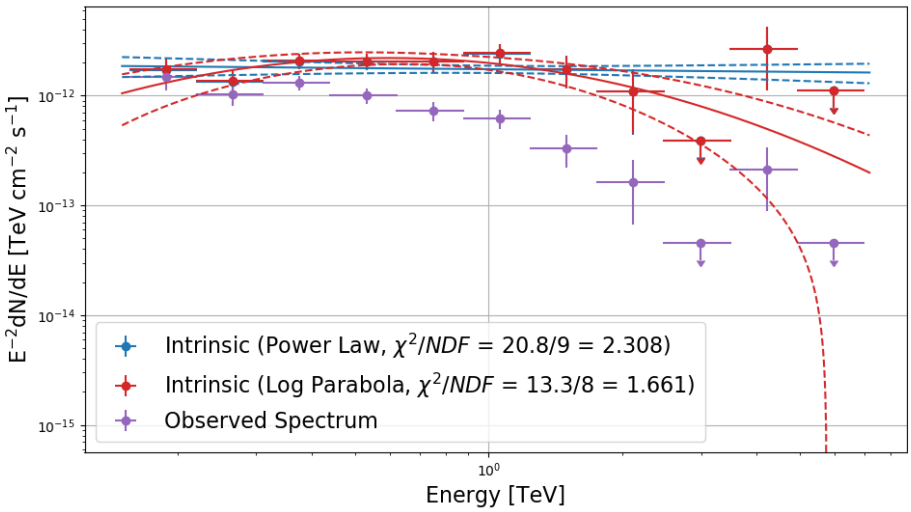

Figure C.19: VHE spectral energy distribution of H 1426+428.

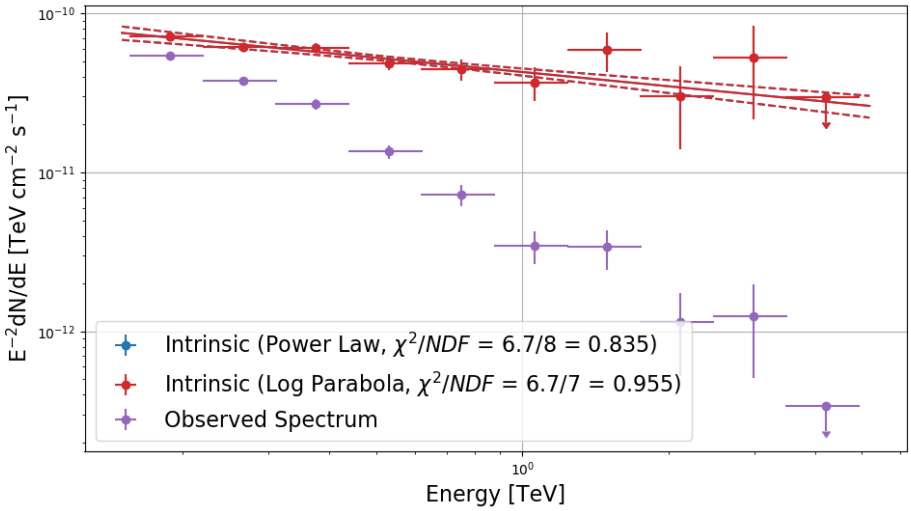

Figure C.20: VHE spectral energy distribution of 1ES 1011+496. The data analyzed here, referred to as "High state" corresponds to the time-averaged high-state data as discussed in Section 8.3.

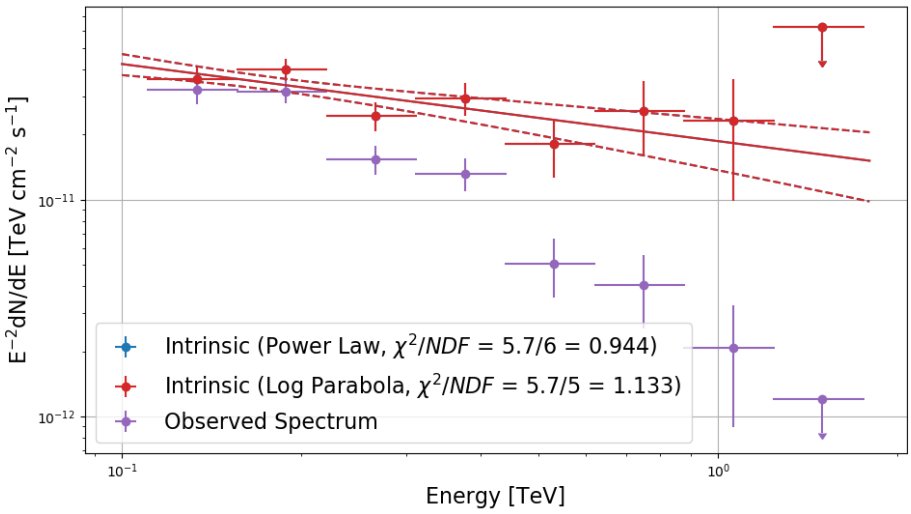

Figure C.21: VHE spectral energy distribution of MS 1221.8+2452.

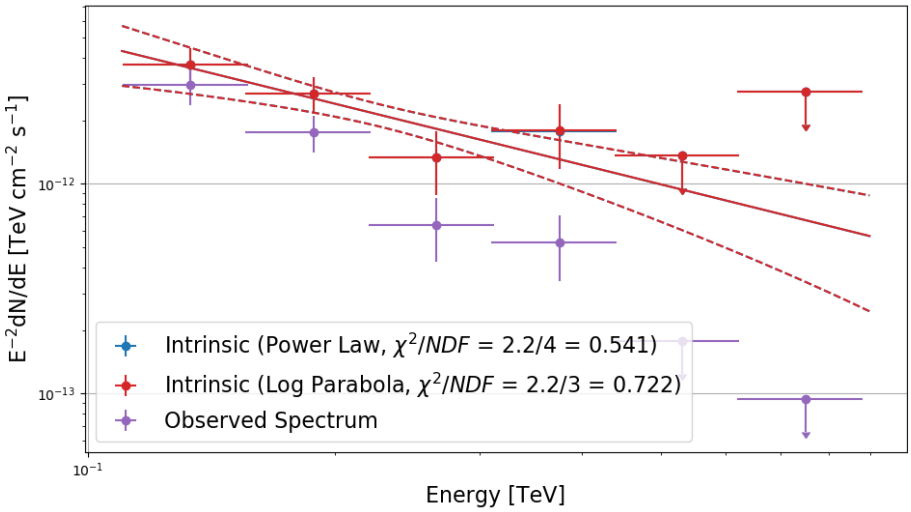

Figure C.22: VHE spectral energy distribution of OJ 287.

Bibliography

Aartsen, M. G., Ackermann, M., Adams, J., et al. 2018, Science, 361, 147

Abdalla, H., Abramowski, A., Aharonian, F., et al. 2018, A&A, 612, A1

Abdalla, H., Abramowski, A., Aharonian, F., et al. 2017, A&A, 606, A59

Abdo, A. A., Ackermann, M., Ajello, M., et al. 2009, Nature, 462, 331

Abdo, A. A., Ackermann, M., Ajello, M., et al. 2010, ApJS, 188, 405

Abeysekara, A., Alfaro, R., Alvarez, C., et al. 2013, Astroparticle Physics, 50, 26

Abeysekara, A., Benbow, W., Bird, R., et al. 2018a, ApJ, 856, 95

Abeysekara, A., Archer, A., Benbow, W., et al. 2018b, ApJ, 861, L20

Abeysekara, A. U., Archambault, S., Archer, A., et al. 2015, ApJ, 815, L22

Abeysekara, A. U., Albert, A., Alfaro, R., et al. 2017, ApJ, 843, 39

Abramowski, A., Acero, F., Aharonian, F., et al. 2013, A&A, 550, A4

Abramowski, A., Aharonian, F., Benkhali, F. A., et al. 2014, A&A, 564, A9

Acciari, V. A., Aliu, E., Arlen, T., et al. 2010, ApJ, 715, L49

Acero, F., Ackermann, M., Ajello, M., et al. 2015, ApJS, 218, 23

Acharya, B. S., Agudo, I., Samarai, I. A., et al. 2017, arXiv preprint arXiv:1709.07997

Ackermann, M., Ajello, M., Atwood, W. B., et al. 2016, in , 5

Ackermann, M., Ajello, M., Albert, A., et al. 2012a, ApJS, 203, arXiv:1206.1896

Ackermann, M., Ajello, M., Allafort, A., et al. 2012b, Science, 338, 1190

Ackermann, M., Ajello, M., Allafort, A., et al. 2013, ApJS, 209, 34

Adelman-McCarthy, J. K., & et al. 2009, VizieR Online Data Catalog

Agudo, I., Marscher, A. P., Jorstad, S. G., et al. 2012, ApJ, 747, 63

Agudo, I., Jorstad, S. G., Marscher, A. P., et al. 2011, ApJ, 726, L13

Aharonian, F., Akhperjanian, A. G., Bazer-Bachi, A. R., et al. 2007, ApJ, 664, L71

Aharonian, F., Hofmann, W., Konopelko, A., & Völk, H. 1997, Astroparticle Physics, 6, 343

Aharonian, F., Akhperjanian, A., Beilicke, M., et al. 2004, A&A, 421, 529

Aharonian, F., Akhperjanian, A., Bazer-Bachi, A., et al. 2006, A&A, 457, 899

Ahn, C. P., Alexandroff, R., Allende Prieto, C., et al. 2012, ApJS, 203, 21

Ahnen, M. L., Ansoldi, S., Antonelli, L., et al. 2015, ApJ, 815, L23

Ahnen, M. L., Ansoldi, S., Antonelli, L. A., et al. 2016, A&A, 590, A24

Ahnen, M. L., Ansoldi, S., Antonelli, L. A., et al. 2018, arXiv preprint arXiv:1807.04300

Ahnen, M. L., Ansoldi, S., Antonelli, L. A., et al. 2016, A&A, 595, A98

Ajello, M., Atwood, W. B., Baldini, L., et al. 2017, ApJS, 232, 18

Albert, J., Aliu, E., Anderhub, H., et al. 2007, ApJ, 666, L17

Albert, J., Aliu, E., Anderhub, H., et al. 2007, ApJ, 667, L21

Albert, J., Aliu, E., Anderhub, H., et al. 2007, ApJ, 669, 862

Aleksic, J., Antonelli, L. A., Antoranz, P., et al. 2011, ApJ, 729, 115

Aleksić, J., Ansoldi, S., Antonelli, L. A., et al. 2015, Journal of High Energy Astrophysics, 5-6, 30

Aleksić, J., Ansoldi, S., Antonelli, L., et al. 2016, Astroparticle Physics, 72, 76

Alexander, T. 2013, arXiv preprint arXiv:1302.1508

Aliu, E., Archambault, S., Arlen, T., et al. 2012, ApJ, 759, arXiv:1210.7224

Allen, C., Archambault, S., Archer, A., et al. 2017, MNRAS, 471, 2117

Archambault, S., Archer, A., Benbow, W., et al. 2016, arXiv.org, 142

Archambault, S., Archer, A., Benbow, W., et al. 2017, Astroparticle Physics, 91, 34

Arias, P., Cadamuro, D., Goodsell, M., et al. 2012, J. Cosmology Astropart. Phys., 6, 013

Arlen, T., Aune, T., Beilicke, M., et al. 2013, ApJ, 762, 92

Armstrong, T., Brown, A. M., Chadwick, P. M., & Nolan, S. J. 2015, MNRAS, 452, 3159

Atwood, W., Albert, A., Baldini, L., et al. 2013, ArXiv e-prints, arXiv:1303.3514

Atwood, W. B., Abdo, A. A., Ackermann, M., et al. 2009, ApJ, 697, 1071

Axford, W. I., Leer, E., & Skadron, G. 1977, International Cosmic Ray Conference, 11, 132

Barrau, A., Bazer-Bachi, R., Beyer, E., et al. 1998, Nuclear Instruments and Methods in Physics Research A, 416, 278

Barthelmy, S. D., Barbier, L. M., Cummings, J. R., et al. 2005, Space Sci. Rev., 120, 143

Beasley, A. J., Gordon, D., Peck, A. B., et al. 2002, ApJS, 141, 13

Beckmann, V., & Shrader, C. R. 2013, arXiv preprint arXiv:1302.1397

Bell, A. R. 1978, MNRAS, 182, 147

Benbow, W. 2017, in American Institute of Physics Conference Series, Vol. 1792, 6th International Symposium on High Energy Gamma-Ray Astronomy, 050001

Berge, D., Funk, S., & Hinton, J. a. 2006, A&A, 466, 13

Bevington, P. R., Robinson, D. K., Blair, J. M., Mallinckrodt, A. J., & McKay, S. 1993, Computers in Physics, 7, 415

Biland, A. 2016, The Astronomer's Telegram, 9239

Bird, R., et al. 2015, arXiv preprint arXiv:1508.07198

Biteau, J., & Williams, D. A. 2015, ApJ, 812, 60

Blandford, R. D., & Ostriker, J. P. 1978, ApJ, 221, L29

Bond, I. H., Hillas, A. M., & Bradbury, S. M. 2003, Astroparticle Physics, 20, 311

Böttcher, M. 2012, arXiv preprint arXiv:1205.0539

Böttcher, M., & Chiang, J. 2002, ApJ, 581, 127

Böttcher, M., Harris, D. E., & Krawczynski, H. 2012, Relativistic Jets from Active Galactic Nuclei (John Wiley and Sons)

Böttcher, M., Reimer, A., Sweeney, K., & Prakash, A. 2013, ApJ, 768, 54

Britzen, S., Fendt, C., Witzel, G., et al. 2018, MNRAS, 478, 3199

Brown, A. M. 2014, Monthly Notices of the Royal Astronomical Society: Letters, 442, 56

Bruggen, M., & Rosswog, S. 2007, Introduction to High-Energy Astrophysics

Burrows, D. N., Hill, J. E., Nousek, J. A., et al. 2005, Space Sci. Rev., 120, 165

Buson, S., Magill, J. D., Dorner, D., et al. 2016, The Astronomer's Telegram, 9010

Capalbi, M., Perri, M., Saija, B., Tamburelli, F., & Angelini, L. 2005

Catanese, M., Akerlof, C. W., Badran, H. M., et al. 1998, ApJ, 501, 616

Cavazzuti, E., Turriziani, S., & Giommi, P. 2007, AIP Conference Proceedings, 921, 323

Chang, Y.-L., Arsioli, B., Giommi, P., & Padovani, P. 2017, A&A, 598, doi:10.1051/0004-6361/201629487

Christiansen, J., et al. 2017, arXiv preprint arXiv:1708.05684

Ciprini, S., et al. 2015, The Astronomer's Telegram, 8193

Cogan, P. 2007, International Cosmic Ray Conference, 3, 1385

Cortina, J. 2013, The Astronomer's Telegram, 5038

Costamante, L. 2013, International Journal of Modern Physics D, 22, 1330025

Costamante, L., & Ghisellini, G. 2002, A&A, 384, 56

Cutri, R. M., Skrutskie, M. F., van Dyk, S., et al. 2003, VizieR Online Data Catalog

Daniel, M. K., Emmanoulopoulos, D., Fairbairn, M., Otte, N., & CTA Consortium, f. t. 2015, ArXiv e-prints, arXiv:1508.06622

Davis, J. M., & Cotton, E. S. 1957, Solar Energy, 1, 16

Domínguez, A., Primack, J. R., Rosario, D. J., et al. 2011, MNRAS, 410, 2556

Dorner, D., Ahnen, M. L., Bergmann, M., et al. 2015, ArXiv e-prints, arXiv:1502.02582

Dwek, E., & Krennrich, F. 2013, Astroparticle Physics, 43, 112

Edelson, R., McHardy, I., Jorstad, S., et al. 2015, The Astronomer's Telegram, 7056

Edelson, R. A., & Krolik, J. H. 1988, ApJ, 333, 646

Emmanoulopoulos, D., McHardy, I. M., & Papadakis, I. E. 2013, MNRAS, 433, 907

Fanaroff, B. L., & Riley, J. M. 1974, MNRAS, 167, 31P

Fegan, D. 1997, Journal of Physics G Nuclear Physics, 23, 1013

Feldman, G. J., & Cousins, R. D. 1998, Physical Review D, 57, 3873

Fermi, E. 1949, Physical Review, 75, 1169

Finke, J. D., Razzaque, S., & Dermer, C. D. 2010, ApJ, 712, 238

Franceschini, A., & Rodighiero, G. 2017, A&A, 603, A34

Franceschini, A., Rodighiero, G., & Vaccari, M. 2008, A&A, 487, 837

Gaia Collaboration. 2018, VizieR Online Data Catalog, I/345

Gaté, F., Alves Batista, R., Biteau, J., et al. 2017, ArXiv e-prints, arXiv:1709.04185

Gehrels, N., Chincarini, G., Giommi, P., et al. 2004, ApJ, 611, 1005

Georganopoulos, M., Perlman, E. S., Kazanas, D., & McEnery, J. 2006, ApJ, 653, L5

Ghisellini, G., & Maraschi, L. 1996, in Blazar continuum variability, Vol. 110, 436–449

Ghisellini, G., Maraschi, L., & Dondi, L. 1996, A&AS, 120, 503

Giannios, D., Uzdensky, D. A., & Begelman, M. C. 2009, MNRAS, 395, L29

Gilmore, R. C., Somerville, R. S., Primack, J. R., & Domínguez, A. 2012, MNRAS, 422, 3189

Giommi, P., Piranomonte, S., Perri, M., & Padovani, P. 2005, A&A, 434, 385

Giommi, P., Tagliaferri, G., Beuermann, K., et al. 1991, ApJ, 378, 77

Gould, R. J., & Schréder, G. P. 1967, Phys. Rev., 155, 1408

Grieder, P. K. 2010, Extensive Air Showers: High Energy Phenomena and Astrophysical Aspects-A Tutorial, Reference Manual and Data Book (Springer Science & Business Media)

Grupe, D., Komossa, S., & Gomez, J. L. 2016, The Astronomer's Telegram, 9629

Hahn, J., De Los Reyes, R., Bernlöhr, K., et al. 2014, Astroparticle Physics, 54, 25

Hall, J., Vassiliev, V. V., Kieda, D. B., et al. 2003, International Cosmic Ray Conference, 5, 2851

Hanna, D. 2008, International Cosmic Ray Conference, 3, 1417

Hauser, M. G., & Dwek, E. 2001, ARA&A, 39, 249

Hays, E. 2008, International Cosmic Ray Conference, 3, 1543

Heitler, W. 1954, The quantum theory of radiation (Courier Corporation)

Hervet, O., Boisson, C., & Sol, H. 2015, A&A, 578, A69

Hillas, A. M. 1985, International Cosmic Ray Conference, 3

Hofmann, W. 1999, Astroparticle Physics, 12, 135

Holder, J. 2005, Proceedings of the 29th ICRC, 1

Holder, J. 2011, International Cosmic Ray Conference, 12, 137

Holder, J., Atkins, R. W., Badran, H. M., et al. 2006, Astroparticle Physics, 25, 391

Holler, M., Berge, D., van Eldik, C., et al. 2015, 34th International Cosmic Ray Conference, The Hague, Id 1046

Hooper, D., & Serpico, P. D. 2007, Physical Review Letters, 99, 231102

Horan, D., Badran, H. M., Bond, I. H., et al. 2002, ApJ, 571, 753

Hudec, R., Basta, M., Pihajoki, P., & Valtonen, M. 2013, A&A, 559, 1

Hwang, H. S., Geller, M. J., Kurtz, M. J., Dell'Antonio, I. P., & Fabricant, D. G. 2012, ApJ, 758, doi:10.1088/0004-637X/758/1/25

James, F. 2006, Statistical methods in experimental physics (World Scientific Publishing Company)

Jelley, J. 1955, British Journal of Applied Physics, 6, 227

Jester, S., Harris, D. E., Marshall, H. L., & Meisenheimer, K. 2006, ApJ, 648, 900

Johnston, K. J., Fey, A. L., Zacharias, N., et al. 1995, Astronomical Journal, 110, 880

Jorstad, S. G., Marscher, A. P., Lister, M. L., et al. 2005, The Astronomical Journal, 130, 1418

Kalberla, P. M. W., Burton, W. B., Hartmann, D., et al. 2005, A&A, 440, 775

Knödlseder, J., Mayer, M., Deil, C., et al. 2016, A&A, 593, A1

Krause, M., Pueschel, E., & Maier, G. 2017, Astroparticle Physics, 89, 1

Krawczynski, H., Carter-Lewis, D. A., Duke, C., et al. 2006, Astroparticle Physics, 25, 380

Krymsky, G. 1977, in Sov. Phys. Dokl., Vol. 23, 327

Kushwaha, P., Sahayanathan, S., & Singh, K. P. 2013, arXiv.org, 2380

Kushwaha, P., Gupta, A. C., Wiita, P. J., et al. 2018, MNRAS

Lehto, H. J., & Valtonen, M. J. 1996, ApJ, 460, 207

Li, T.-P., & Ma, Y.-Q. 1983, ApJ, 272, 317

Longair, M. S. 2011, High energy astrophysics (Cambridge university press)

Loredo, T. J. 1992, in Statistical Challenges in Modern Astronomy, ed. E. D. Feigelson & G. J. Babu, 275–297

Ma, C., Arias, E. F., Eubanks, T. M., et al. 1998, The Astronomical Journal, 116, 516

Madau, P., & Phinney, E. S. 1996, ApJ, 456, 124

Madejski, G., & Sikora, M. 2016, Annual Review of Astronomy and Astrophysics, 54, 725

Maier, G., & Holder, J. 2017, International Cosmic Ray Conference, arXiv:1708.04048

Mao, L. S. 2011, New Astronomy, 16, 503

Marscher, A. P. 2016, Galaxies, 4, 37

Mazin, D., Domínguez, A., Fallah Ramazani, V., et al. 2017, in American Institute of Physics Conference Series, Vol. 1792, 6th International Symposium on High Energy Gamma-Ray Astronomy, 050037

Mazin, D., & Raue, M. 2007, AIP Conference Proceedings, 921, 240

Meagher, K. 2015, Proceedings of Science, 30-July-20, arXiv:1508.06442

Meegan, C., Lichti, G., Bhat, P. N., et al. 2009, ApJ, 702, 791

Meyer, E. T., & Georganopoulos, M. 2014, ApJ, 780, 2

Mirzoyan, R. 2014, The Astronomer's Telegram, 5887

Mirzoyan, R. 2015, The Astronomer's Telegram, 7416

Mirzoyan, R. 2017, The Astronomer's Telegram, 11061

Moralejo, A., Domínguez, A., Fallah Ramazani, V., et al. 2017, ArXiv e-prints, arXiv:1709.02238

Moretti, A., Campana, S., Tagliaferri, G., et al. 2004, in Proc. SPIE, Vol. 5165, X-Ray and Gamma-Ray Instrumentation for Astronomy XIII, ed. K. A. Flanagan & O. H. W. Siegmund, 232–240

Moretti, A., Campana, S., Mineo, T., et al. 2005, in Proc. SPIE, Vol. 5898, UV, X-Ray, and Gamma-Ray Space Instrumentation for Astronomy XIV, ed. O. H. W. Siegmund, 360–368

Mukherjee, R. 2015, The Astronomer's Telegram, 8148

Mukherjee, R. 2015, The Astronomer's Telegram, 7433

Mukherjee, R., et al. 2016, The Astronomer's Telegram, 9721

—. 2017, The Astronomer's Telegram, 10051

Mukherjee, R., et al. 2017, The Astronomer's Telegram, 11075

Neronov, A., & Vovk, I. 2011, MNRAS, 412, 1389

Nilsson, K., Takalo, L. O., Lehto, H. J., & Sillanpää, A. 2010, 60, 1

Nishiyama, T. 1999, International Cosmic Ray Conference, 3, 370

Nogués, L., Y Lin, T. T., Perennes, C., et al. 2017, ArXiv e-prints, arXiv:1710.08342

Nolan, P. L., Abdo, A. A., Ackermann, M., et al. 2012, ApJS, 199, 31

O'Brien, S., et al. 2017, arXiv:1708.02160

Otte, A. N., et al. 2011, arXiv preprint arXiv:1110.4702

Pacciani, L. 2015, The Astronomer's Telegram, 7402

Padovani, P., Alexander, D., Assef, R., et al. 2017, A&A Rev., 25, 2

Paiano, S., Landoni, M., Falomo, R., et al. 2017, ApJ, 837, 144

Park, N., et al. 2015, arXiv preprint arXiv:1508.07070

Perkins, J. S., Maier, G., & VERITAS Collaboration. 2010, 42, 719

Perlman, E. S., Stocke, J. T., Schachter, J. F., et al. 1996, ApJS, 104, 251

Peterson, B. M. 1997, An introduction to active galactic nuclei (Cambridge University Press)

Petrov, L. 2011, AJ, 142, doi:10.1088/0004-6256/142/4/105

Petrov, L. 2013, Astronomical Journal, 146, 2

Petrov, L., & Taylor, G. B. 2011, AJ, 142, 89

Piron, F., Djannati-Ataï, A., Punch, M., et al. 2001, A&A, 374, 895

Plotkin, R., Anderson, S., Brandt, W., et al. 2010, \aj, 139, 390

Prandini, E., DomÃnguez, A., Fallah Ramazani, V., et al. 2017, Frontiers in Astronomy and Space Sciences, 4, 50

Pueschel, E. 2017, AIP Conf. Proc., 1792, 060002

Raue, M., & Mazin, D. 2008, International Journal of Modern Physics D, 17, 1515

Rebillot, P. F., Buckley, J. H., Dowkontt, P., & Kosack, K. 2003, International Cosmic Ray Conference, 5, 2827

Reimer, A., Böttcher, M., & Postnikov, S. 2005, ApJ, 630, 186

Rieger, F. M., Bosch-Ramon, V., & Duffy, P. 2007, in The Multi-Messenger Approach to High-Energy Gamma-Ray Sources (Springer), 119–125

Rieger, F. M., & Duffy, P. 2004, ApJ, 617, 155

Rolke, W. A., López, A. M., & Conrad, J. 2005, Nuclear Instruments and Methods in Physics Research A, 551, 493

Roming, P. W. A., Kennedy, T. E., Mason, K. O., et al. 2005, Space Science Reviews, 120, 95

Sanchez, D. A., Fegan, S., & Giebels, B. 2013, A&A, 554, A75

Santander, M. and others. 2017, ArXiv e-prints, arXiv:1709.02365

SDSS Collaboration, Albareti, F. D., Prieto, C. A., et al. 2016, arXiv:1608.02013

Seta, H., Isobe, N., Tashiro, M. S., et al. 2009, Publications of the Astronomical Society of Japan, 61, 1011

Sikora, M., Rutkowski, M., & Begelman, M. C. 2016, MNRAS, 457, 1352

Sikora, M., Stawarz, Ł., Moderski, R., Nalewajko, K., & Madejski, G. M. 2009, ApJ, 704, 38

Sillanpaa, A., Haarala, S., Valtonen, M. J., Sundelius, B., & Byrd, G. G. 1988, ApJ, 325, 628

Sitarek, J., et al. 2017, arXiv preprint arXiv:1708.04043

Stecker, F., De Jager, O., & Salamon, M. 1996, ApJ, 473

Stroh, M. C., & Falcone, A. D. 2013, ApJS, 207, 28

Tammi, J., & Duffy, P. 2009, MNRAS, 393, 1063

Tang, B., Shang, Z., Gu, Q., Brotherton, M. S., & Runnoe, J. C. 2012, ApJS, 201, 1

Tateyama, C. E., & Kingham, K. A. 2004, ApJ, 608, 149

Tavecchio, F., & Ghisellini, G. 2008, MNRAS, 385, L98

Tavecchio, F., Maraschi, L., & Ghisellini, G. 1998, ApJ, 509, 608

Taylor, A. M., Sanchez, D., Cerruti, M., & on behalf of the H. E. S. S. collaboration. 2017, ArXiv e-prints, arXiv:1708.00775

Timmer, J and König, M. 1995, A&A, 300, 1

Trichas, M., Green, P. J., Silverman, J. D., et al. 2012, ApJS, 200, 17

Uchiyama, Y., Urry, C. M., Cheung, C. C., et al. 2006, 8, 910

Valtonen, M., & Pihajoki, P. 2013, A&A, 557, A28

Valtonen, M. J. 2007, ApJ, 659, 1074

Valtonen, M. J., Mikkola, S., Lehto, H. J., et al. 2011, ApJ, 742, 22(12)

Valtonen, M. J., Nilsson, K., Villforth, C., et al. 2009, ApJ, 698, 781

Valtonen, M. J., Zola, S., Ciprini, S., et al. 2016, ApJ, 819, 1

van Leeuwen, F. 2007, arXiv:0708.1752

Verrecchia, F., Ciprini, S., Valtonen, M., & Zola, S. 2016, The Astronomer's Telegram, 9709

Vianello, G., Lauer, R. J., Younk, P., et al. 2015, ArXiv e-prints, arXiv:1507.08343

Villata, M., & Raiteri, C. 1999, A&A, 347, 30

Völk, H. J., & Bernlöhr, K. 2009, Experimental Astronomy, 25, 173

Wakely, S. P., & Horan, D. 2008, International Cosmic Ray Conference, 3, 1341

Weekes, T. C. 1988, Physics Reports, 160, 1

Wilks, S. S. 1938, Ann. Math. Statist., 9, 60

Winston, R. 1970, Journal of the Optical Society of America, 60, 245

Wood, M., Caputo, R., Charles, E., et al. 2017, 0

Yang, J., Gurvits, L. I., Frey, S., Lobanov, A. P., & Hong, X.-Y. 2009, in Astronomical Society of the Pacific Conference Series, Vol. 402, Approaching Micro-Arcsecond Resolution with VSOP-2: Astrophysics and Technologies, ed. Y. Hagiwara, E. Fomalont, M. Tsuboi, & M. Yasuhiro, 139

Zitzer, B. 2013, The Astroparticle Physics Conference, 3